The Behaviour and Interactions of the Silica/Water Interface Studied through Nonlinear Optics

by

Benjamin Rehl

A thesis submitted in partial fulfillment of the requirements for the degree of

Doctor of Philosophy

Department of Chemistry

University of Alberta

Abstract

The chemistry of silica in contact with water is rich and diverse. These two substances are among the most ubiquitous on the surface of the Earth. Yet, despite many investigations into the interactions between silica and water, there is still more to discover. In aqueous solution, the silica surface can interact with itself, water, and ions. These interfacial processes are linked to the behaviour of water bound to the surface. Such water and related interfacial phenomena are difficult to study since silica, an insulator, is not amenable to electrochemical techniques, and conventional spectroscopic methods are overwhelmed by bulk responses. For this reason, nonlinear optical techniques, such as sum frequency generation (SFG) spectroscopy, have proven useful due to their surface specificity. This thesis focuses on understanding the response of interfacial water near silica in the presence of ions or solution pH. Sum frequency generation is primarily used in this thesis to measure the silica/water interface, however, complementary techniques such as second harmonic generation (SHG) and streaming potential are also used.

Under the model of the $\chi^{(3)}$ method, both SFG and SHG are believed to measure the amount of aligned waters at the silica/water interface, yet different pH dependent behaviours have been observed by these techniques. Through a comparison of nonresonant SHG and resonant SFG, we aimed to shed light on this difference. It was found that the nonresonant signal generated at the silica/air interface was substantial, which led to the conclusion that both the silica and aligned waters contribute strongly to the SHG signal. Furthermore, comparison of SFG spectral features and molecular dynamics simulations suggested the existence of at least two populations of water at the silica surface, which are oppositely aligned at low pH. Destructive interference to SHG signal from oppositely aligned waters may also result in the differences observed.

Although ions and pH are known to play large roles in the processes of the silica/water interface, the response of surface bound water remains elusive. To observe spectral changes arising from these surface waters, SFG spectra were deconvoluted into waters aligned by the static electric field of silica and waters aligned by hydrogen bonding to silica. To do so, complex spectra were obtained from the intensity measurements by using the maximum entropy method, and then compared to zeta potential ζ, measurements at the same interface. An orientation flip of waters resonating at low wavenumbers (less than 3200 cm^{-1}) was observed as ionic strength was increased. In a similar manner, the surface water response to changes in solution pH were investigated. A change in water orientation contributing to the lower wavenumbers in the SFG surface spectra was again observed. The surface spectral features were assigned to hydrogen bond donors and acceptors and comparisons of the pH-dependent and ionic strength-dependent trends were made to macroscopic properties such as the metastability of silica colloids near their point of zero charge.

The acetonitrile-water mixture is used in chemical separation techniques such as hydrophilic interaction chromatography (HILIC), which employs silica as a stationary phase. The structure of the interface determines the retention times of the technique. Although pH can be varied to tune the separations, it is difficult to predict the retention times of some solutes when the pH is increased to high values. SFG spectra at the silica/acetonitrile-water interface of the methyl, water, and nitrile stretching regions demonstrated a change to the interfacial structure occurring at pH 10, which was highlighted by a sudden loss in signal originating from acetonitrile. Through orientation analysis of the SFG spectra, it was found that interfacial acetonitrile did not reorient over the pH adjustment, but rather was displaced from the interface by water. These observations may aid in predicting HILIC retention times at high solution pH.

These nonlinear optical studies serve to further the knowledge and understanding of the silica/water interface. As silica is a highly studied, model surface, the observations and methodologies within this thesis may prove insightful for understanding other mineral oxides or charged surfaces in contact with water, and may improve the understanding of SHG and SFG at these interfaces.

Preface

This thesis is an original work by Benjamin Rehl. Some of the research conducted for this thesis forms part of a collaboration with other group members in the Gibbs group (University of Alberta, AB) and the Hore group (University of Victoria, BC).

Chapter 2 of this thesis has been published as Rehl, B.; Rashwan, M.; DeWalt-Kerian, E. L.; Jarisz, T. A.; Darlington, A. M. Hore, D. K.; Gibbs, J. M. New Insights into $\chi^{(3)}$ Measurements: Comparing Nonresonant Second Harmonic Generation and Resonant Sum Frequency Generation at the Silica/Aqueous Electrolyte Interface. *J. Phys. Chem. C* **2019**, *123*, 10991-11000. I was responsible for data collection, analysis and manuscript composition. Mokhtar Rashwan, Dr. Emma L. DeWalt-Kerian, and Dr. Akemi M. Darlington aided in initial data collection. Dr. Akemi M. Darlington, Dr. Emma L. DeWalt-Kerian, and Dr. Tasha, A. Jarisz aided in initial manuscript composition. Dr. Dennis K. Hore (University of Victoria) performed the molecular dynamics simulations. Dr. Julianne M. Gibbs was the supervisory author.

Chapter 3 of this thesis is an original work by me. No part of this chapter has been previously published. I was responsible for data acquisition and analysis.

Chapter 4 of this thesis is an original work by me. No part of this chapter has been previously published. I was responsible for data acquisition and analysis. Dr. Emma L. DeWalt-Kerian and Tianli Liu aided in initial SFG spectra collection and zeta potential measurements, respectively.

Chapter 5 of this thesis has been published as Rehl, B.[*]; Li, Z.[*]; Gibbs, J. M. Influence of High pH on the Organization of Acetonitrile at the Silica/Water Interface Studied by Sum Frequency Generation Spectroscopy. *Langmuir* **2018**, *34*, 4445-4454. I am joint first-author of this

paper with Dr. Zhiguo Li. I was responsible for collecting SFG spectra of the silica/ACN-H_2O interface in the methyl and nitrile stretching regions as well as the silica/ACN-D_2O interface in the methyl region. Dr. Zhiguo Li was responsible for collecting SFG spectra of the silica/ACN-H_2O interface in the methyl and water stretching regions as well as the orientation analysis. We were both responsible for spectral fitting and manuscript composition. Dr. Julianne M. Gibbs was the supervisory author.

Acknowledgements

The journey through graduate school was an arduous, yet enlightening one, and I do not regret a single moment. I thank my supervisor, Dr. Julianne M. Gibbs, for her patient mentorship and guidance, for which I would be lost without. I am thankful for my supervisory committee, Dr. Jillian Buriak and Dr. Rylan Lundgren, whose advice and lessons I take to heart, and Dr. Franz M. Geiger, for the time and effort spent reviewing this thesis. I am thankful for Dr. Jonathan G. C. Veinot's encouragement and for sending me to Germany many times. I am thankful for Dr. Dennis K. Hore, whose continual advice on nonlinear optics aided me greatly. I am extremely grateful for Dr. Qingxia Liu for his support during my final semester. I thank all of my group members for helping me through the many difficulties faced in graduate school. In particular, I want to thank Dr. Akemi M. Darlington, Dr. Zhiguo Li, and Dr. Emma L. DeWalt-Kerian for taking the time to pass their knowledge on to me. I hope I successfully passed the torch to the next generation, Mokhtar Rashwan and Shyam Parshotam. I am grateful for all of the friends I've made along the way, including those from Germany, who made the last five years truly enjoyable. I am especially grateful for Anis Fahandej-Sadi, Hezhen Xie, Kevin Hooteo, Matthew Roy, Patrick Moon, and Tobias Helbich for sharing in this experience with me. I cannot stress enough that I am truly blessed by my family. I thank my mother, Olga Rehl, my brother, Erwin Rehl, and my sister, Nathalie Denicola, whose constant love and support from afar kept me motivated. I am thankful for my father, Jakob Rehl, who brought us to Canada all those years ago, and whose words of encouragement still resonate within me. I am grateful for my friends from home, Clinton Priestley, Daniel Sheppard, Josh Denicola, Kennith Green, and Sean Smith, who are like family, since they never gave up on me. And finally, I thank my girlfriend, Hansol Park, for encouraging me and especially for taking care of me while I wrote this dissertation.

Table of Contents

List of Tables

List of Figures

Chapter 1

Introduction

1.1 The Importance of Silica

1.1.1 Silica and the Earth

Silica is one of the most abundant minerals in the Earth's crust, and therefore it is not surprising that it is deeply involved in many aspects of life on Earth. To emphasize the relevance, approximately 90% of all minerals in the Earth's crust are silicates, with quartz accounting for 12% of that abundance.[1-2] Over geological timescales, silicates play an extremely important role in the regulation of CO_2 in the atmosphere (i.e. the Earth's thermostat). This regulation is referred to as the carbonate-silicate cycle and can be summarized by two main processes.[3] The first is the weathering of silicates by carbonic acid to form carbonates and silicic acid. As the carbonic acid originates from the equilibrium of atmospheric CO_2 with water, this weathering results in the capture of CO_2. The second process is simply the reverse of the first, which is the metamorphism of carbonates back into silicates, which consumes silicic acid and generates CO_2. This metamorphism requires the extreme heat and pressure of tectonic activity. For this reason, events such as volcanic eruptions lead to the release of great amounts of CO_2 into the atmosphere. The silicic acid produced from weathering is soluble in water and enters the global silica cycle, where it finds further use before ultimately becoming buried in the ocean floor and returning to the Earth's crust. Oceanic silica largely stems from the weathering of exposed continental crust with 64% arriving by the fluvial system (rivers, ground water, etc.), 25% from aeolian movements (dust storms), and the remainder originating from the weathering of the oceanic crust.[4] The global silica cycle is linked to many other global cycles such as those of phosphate and carbon, and in particular the biological pump, which describes the conversion of atmospheric CO_2 to biomass and its return to the crust through the ocean.[5]

1.1.2 Silica and the Biological Pump

Of chief importance to the biological pump is a species of phytoplankton called diatoms. Remarkably, the photosynthetic activity of these particular organisms is responsible for 75% of coastal primary production (conversion of CO_2 to biomass) and 20% of global primary production, and by relation, a similar percentage of global oxygen production.[5-6] Diatoms consume silicic acid which is incorporated into their cell walls as solid silica.[7] This consumption can result in coastal concentrations of silica which are at least two orders of magnitude lower than in deeper parts of the ocean.[8] Furthermore, the shells of dead diatoms aid in carbon transport to the ocean floor as they can aggregate and sink small biological particulates.[6] These settled diatoms are referred to as diatomaceous earth, which finds many uses such as filtration agents and in agriculture. Seemingly, diatomaceous earth is partly responsible for the existence of the Nobel Prize as it was used as a stabilizing agent in dynamite, which contributed to Alfred Nobel's fortune. The consumption of diatoms by predators recycles silica into the food chain.

1.1.3 Silica and Plants

The transport of silica from land to the oceans is largely buffered by plants that also affects the weathering of silicates through various phenomena such as altering the residence time of water, modifying soil pH, and increasing the surface area of minerals.[4, 8] Plants absorb silicic acid through their roots and into their xylem either by passive diffusion or in some instances, specific transporter proteins.[9] The silicic acid is deposited as solid structures called phytoliths, although the shape and deposition site varies. The mechanism of this deposition is not fully understood, however it may be partly due to charge interactions between small polymerized silica structures (1

– 3 nm) and the cell walls. Similarly, silica interacts with other charged species within cells such as peptides and enzymes.[10] In the form of dissolved silicic acid or solid phytoliths, silica is involved in plant stress alleviation.[9] Phytoliths provide a physical barrier to pathogens attempting to enter the plant, as well as decreasing leaf heat load and transpiration in times of drought. Heavy metals are captured by silica to form silicates, negating their toxicity. In addition to triggering or enhancing a plant's natural response to stressors, some plants grow spines from silica which help to prevent predation.[1] Despite containing 0.1% to 10% silica by dry weight, silica is not defined as an essential nutrient of plants, although deficiency leads to growth and structural problems.[9] The silica content of plants is highest in grains such as wheat and rice and is particularly high in beer.[10] Upon plant death, the silicified remains play an important role in archaeology until they slowly dissolve and continue in the global silica cycle.[1, 10]

1.1.4 Silica and Animals

Silica is found in nearly all animal tissue with approximately one to two grams in the human body.[2] Ingested silica is absorbed by the gastrointestinal tract, processed by the kidneys, and expelled with urine, although diets containing very large quantities of silica may negatively impact calcium and magnesium absorption. As with plants, silica is not classified as an essential nutrient in humans, yet it appears to play an important role in bone health and development since it is concentrated at the mineralization front of bone.[2, 11] Silica enhances bone matrix quality, mineral density, and strength by making bone more calcifiable and initiating and accelerating bone mineralization. The mechanism of these actions is not clear, but they may be due to charge interactions of both silica and bone. Furthermore, silica may interact with the immature bone matrix due to the presence of collagen, which silica plays a role in crosslinking.[11] Although silica

plays a positive role in the body, only dissolved silica (silicic acid) does so, while solid or crystalline silica may promote certain cancers if ingested and cause silicosis if inhaled.[1-2] If not enough water is consumed, silicic acid may polymerize and can contribute to kidney stones.

1.1.5 Silica and Humans

As human activity increases, we are having decidedly large and complex effects on the global silica cycle. With increasing agriculture and subsequent increases in land exposure, an increase in the amount of silicate weathering followed by the release of more silica into global silica cycle is expected.[5] Deforestation and large-scale vegetation changes (e.g. removing trees to plant wheat) affects the terrestrial silica buffering capacity.[8] Damming rivers hinders the flow of silica from land to the ocean, which lowers the concentration of oceanic silica and in turn the primary production of diatoms and other phytoplankton.[4] While fertilizer usage results in the proliferation of diatoms and other phytoplankton, this benefit comes with increasing toxic algal blooms.[8] Furthermore, since the dawn of the industrial era, increases in greenhouse gases have led to increases in silicate weathering, ocean acidity, and global temperatures, which affects marine life (e.g. diatoms) and the rate of silica dissolution.[3] As it has been reported that the complex recycling of silica occurs largely at sediment/water interfaces,[5] it is becoming increasingly important to understand how silica interacts with water on a molecular level. This molecular information may help us to further understand processes like silicate weathering and silica aggregation that play large roles in the global silica cycle.

1.2 The Silica/Water Interface

1.2.1 Silica Structure

The actual structure of the silica/water interface, and nearly all aqueous interfaces, is largely unknown. It is difficult to measure interfacial phenomena, and most techniques only provide small pieces of a larger puzzle. As measurements are made we are able to build and improve models with which to interpret and predict interfacial behaviour. It should always be remembered that these are models that do not necessarily represent fact, but are our best representations of nature given the information available, and sometimes models are simplified for convenience. For example, to model charge densities at interfaces we sometimes estimate solid structures as smooth planes or consisting of a few well-defined molecular formations. In reality, interfacial structures are likely much more complex, consisting of a dynamic maze of atoms and bonds. As hinted earlier, interfacial phenomena are responsible for a host of processes which occur on the molecular, macro, and cosmic scale. For this reason surface specific measurements are becoming increasingly important.

The interactions between silica and water have been highly studied, yet the large volumes of research into the chemistry of silica cannot possibly fit into one thesis introduction. However "*The Chemistry of Silica*. *Solubility, Polymerization, Colloid and Surface Properties, and Biochemistry,*" by Ralph K. Iler is an excellent resource on the nature of silica. Many key points from Iler are summarized for the reader below. More in-depth explanations and mechanisms can be found within the original text.[1]

Silica consists of covalently bound silicon and oxygen in the form of siloxanes. There are many polymorphs of silica, with quartz being the most common, however our focus will be largely

on that of amorphous silica. Dehydrated silica, which consists entirely of siloxanes (Si-O-Si), is hydrophobic towards water.[12] In the presence of water, silica will very slowly hydrate to form surface silanol groups (Si-OH). It has been suggested that adsorbed surface water molecules facilitate the hydration of siloxanes to silanols.[13] In the proposed hydration mechanism, a water molecule, adsorbed to a silanol, is thought to be more dissociated than bulk water and able to attack the silicon of a neighbouring siloxane, generating another silanol. Yet, the initial silanol presented in the mechanism must form without the aid of nearby silanols, suggesting hydrophobic siloxanes can form hydrogen bonds with water. The newly formed silanols continue to aid the hydration of nearby siloxanes in an autocatalytic process until reaching a surface coverage of approximately 4.6 OH/nm^2.[1, 14-16] These hydrophilic silanols are largely responsible for the interactions between water and silica. Dehydration occurs at sufficiently high temperatures for neighbouring silanols to interact with each other and condense back into siloxanes with the formation of water.[17] This dehydration begins to occur at ~115°C with a more complete OH loss at higher temperatures up to 1000°C.

1.2.2 The Electric Double Layer

In the presence of aqueous hydroxide, silanols can deprotonate to form charged siloxides (Si-O$^-$). For silica, the point of zero charge (PZC) is observed around pH 2, but there is some variability in the reported value.[18] From these charges emanate a static electric field, which is related to the surface potential, Φ_0. In aqueous electrolyte solutions, these negative charges can attract counter ions, such as sodium cations, from the bulk. The presence of excess counter ions near the surface constitutes the so-called electric double layer (EDL, Figure 1.1). A layer of counter ions some distance away from the surface at the outer Helmholtz plane (OHP) is responsible for

neutralizing a large amount of the surface potential. Molecules within this so-called Stern layer are relatively immobile and bound to the surface. The extent of surface potential decay beyond the OHP depends on the concentration of ions and the relative permittivity of water within this layer. Water, a highly polar molecule, may orient itself to favourably align its permanent dipole with that of the static electric field. The behaviour of silica in water largely stems from this surface potential, however, for insulating mineral oxides, the surface potential is not easily measured by electrochemical measurements. Furthermore, the EDL is a phenomenon common to all charged surface/aqueous interfaces and is therefore important to understand well.

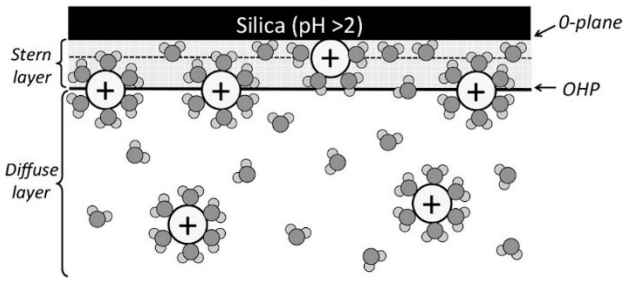

Figure 1.1 Molecular view of the silica/water electric double layer in the presence of ions. Reprinted with permission from Gibbs and coworkers.[19] Copyright 2017 American Chemical Society.

In 1853, Helmholtz theorized that a charged surface in aqueous solution stores charge electrostatically, and forms a double layer consisting of a charged surface that is neutralized by a rigid wall of counter ions.[20] In 1913, Gouy and Chapman improved Helmholtz's double layer by realizing the counter ions may not take the form of a rigid wall.[21] Rather, they suggested the counter ions exist as a diffuse cloud near the surface. The potential within this "diffuse layer" would experience an exponential decay with increasing distance from the surface. In 1924, Stern combined the Helmholtz and Gouy-Chapman models to allow for both a rigid wall of ions and a

diffuse layer, since the Gouy-Chapman model failed at high potentials.[22] An ion's distance of closest approach to the surface was then determined by its ionic radius, where the space within this distance became known as the Stern layer. Finally in 1947, Grahame realized the distance of closest approach may be governed by an ion's hydrated radius, and that some ions may shed their hydration spheres to penetrate the Stern layer, specifically adsorbing to the surface charges.[23] An implication of the Stern and diffuse layers is that the potential first decays linearly from the surface to the OHP and then exponentially as a diffuse layer of ions and solvent molecules neutralize the remaining charge. Additionally, species which do not move with the bulk solution, and are instead associated with surface, are said to lie within the slipping plane. In general, the slipping plane is thought to occur from somewhere outside the OHP within the diffuse layer. The potential at this distance is referred to as the zeta potential. The concept of specifically adsorbed ions is known as the site-binding theory, and was put forward to explain certain anomalies at the silica/water interface, such as the large difference between zeta potential and expected surface potential calculated from surface charge densities.[24]

1.2.3 Dissolution

The solubility of silica and the dissolution rate is measured with respect to the concentration of "soluble silica", $Si(OH)_4$, within solution, and are important concepts for studying the durability of glasses and siliceous materials, such as diatomaceous earth.[1] Ionic strength plays little role (with some exceptions[25]) in the total solubility of amorphous silica,[26] with saturation reaching ~100 ppm around neutral pH values.[1, 27] The solubility at pH 2 exhibits a local maximum, however, it decreases with increasing pH until pH ~7, a local minimum, and then rises rapidly with further increasing pH.[1] Beyond pH 10.7, $Si(OH)_4$ ionizes and silica begins to dissolve rapidly as

the depletion of soluble silica drives the equilibrium forward.[28] Unlike the total solubility, the dissolution rate of silica is affected by ionic strength. Initially, it is noted that silica free of impurities immersed in very pure water is highly resistant to dissolution.[1] Under such conditions, water containing silica may take weeks to reach saturation,[1] yet increasing salt concentrations have been found to increase the rate of dissolution.[29] Furthermore, impurities embedded within the silica matrix may leach out into solution over time and promote dissolution.[30] Though not all ions behave the same, for example, aluminum demonstrates unique behaviour with silica, in that the trivalent ion strongly hinders dissolution.[31] The rate of dissolution with respect to pH does not follow the same trend as solubility. Generally, the rate only increases with increasing pH above pH 2, suggesting hydroxide plays a key role. However the rate also slightly increases below pH 2, implying dissolution may also be catalyzed by acid.[32] Yet, the latter mechanism has been suggested to be related to the release of fluoride ions from an impure silica matrix that strongly promote dissolution.[33] Finally, silica deposition follows a similar mechanism and is affected by pH and ionic strength in the same manner as dissolution, with the exception of high pH above 10.7 due to the ionization of soluble silica.

1.2.4 Stability

The stability of silica in solution can be considered in terms of resistance to aggregation, which induces particle growth, and is affected by solution pH and the presence of ions. Silica particles may grow from soluble silica as it polymerizes with itself in the presence of hydroxides to form monomers, which then form dimers, and then trimers, and so on.[1] The continual deposition of silica on these structures results in the formation of small particles, which eventually aggregate into larger particles through gelation and coagulation. As nucleation of particles is ongoing,

Ostwald ripening suggests that smaller particles will tend towards dissolution, favouring the growth of larger particles to minimize total surface energy. Aggregation rates lessen with increasing pH because of charge repulsion from siloxides.[1] Furthermore, coagulation is believed to be facilitated by salt through a bridging mechanism, where an ion, such as sodium, exchanges one water from its hydration sphere with water from a silanol, or the silanol itself.[1] A second coordination event at the same ion from another silica particle links the two particles together. In a similar light, an increase in ionic strength is associated with a decrease in aggregation rate as charge screening minimizes some of the repulsion between particles.[34-35] A unique property of silica among other colloids is the enhanced stability observed near the PZC, whereas other particles require relatively high potentials to remain suspended in solution.[1] The gelation time of silica is also pH dependent, and exhibits similar trends as the solubility. Local maxima in gelation times are observed near pH 2 and beyond pH 7. However, around pH 6-7, silica gels relatively quickly, indicating reduced stability.[1] The enhanced stability near the PZC may be due to low concentrations of hydroxide ions, which facilitate aggregation, at pH 2. However, below pH 2, an increase in aggregation times are observed, indicating a possible link to hydronium as well. Of particular note, the enhanced stability around pH 2 has been inferred to be related to the hydration waters of silica, since ions should play a minor role at the PZC.[1] Through viscosity measurements, this surface water layer has been shown to be only one monolayer thick.[36]

1.2.5 Analytical Methods

As silica is an insulator, the silica/water interface cannot be studied by electrochemical methods (although single crystal quartz electrodes may yield some advancement in this area[37]). Therefore, optical methods such as infrared (IR) absorption,[38-39] nuclear magnetic resonance,[16] and

X-Ray photoelectron spectroscopies,[40-42] have been used to study the silica/water interface. Thermogravimetric analysis has been coupled with IR absorption to follow spectral changes with temperature.[43] Atomic force microscopy,[44] electrokinetic measurements,[45-50] potentiometric titrations,[51-53] and colourimetric methods[1, 54] are also useful for studying the silica/water interface. Among the analytical methods used to study the silica/water interface, many are designed for the colloid/water interface, rather than a planar/water interface. This may in part be due to the difficulty in differentiating between bulk and surface responses; silica colloids have high surface area and therefore more of the response will be due to the interface. However, some particle size studies can be extrapolated to the infinite regime (planar geometry). Yet it is clear that studying the silica/water interface, which under certain conditions may contain only a single monolayer of water in contact with the silica surface, is difficult. With this in mind, nonlinear optical techniques such as sum frequency generation (SFG) and second harmonic generation (SHG) spectroscopies, due to their surface selectivity, have proven useful in studying the interactions between silica and water.

1.3 Nonlinear Optics

1.3.1 The Nonlinear Susceptibilities

Nonlinear optics (NLO) is the study of nonlinear interactions of light with matter. Very strong electric fields are required to induce these nonlinear effects, and therefore the development of NLO followed closely after the invention of the laser. The general theory of NLO and its relation to SHG and SFG are summarized in Sections 1.2.1 to 1.2.4 under the electric dipole approximation and following from the text, "*Nonlinear Optics,*" by Robert W. Boyd.[55]

Matter will become polarized when interacting with the electric field of light. This polarization stems from the induced oscillation of electrons within the molecules and results in the generation of an electric field at the frequency of the original oscillation. The nature of this interaction, and the resulting polarization, is described by the susceptibilities of the medium. It is intuitive to write this relation as the following

$$P = P^{(1)} + P^{(2)} + P^{(3)} + \cdots + P^{(i)} \ldots = \chi^{(1)}E + \chi^{(2)}E^2 + \chi^{(3)}E^3 + \cdots + \chi^{(i)}E^i, \quad (1.1)$$

where P is the sum of i induced polarizations, $P^{(i)}$, E is the electric field of the incident light, $\chi^{(1)}$ is the linear susceptibility, $\chi^{(2)}$ is the second-order nonlinear susceptibility, $\chi^{(3)}$ is the third-order nonlinear susceptibility, and so on. Since the electric field can be described as a wave oscillating at its fundamental frequency, ω, $P^{(1)}$ is the induced polarization due to electrons oscillating at the same frequency. However, $P^{(2)}$ and $P^{(3)}$ are the induced polarizations due to electrons oscillating at twice (2ω) and triple (3ω) the fundamental frequency, respectively (Figure 1.2). These higher order, nonlinear, polarizations are therefore responsible for generating electric fields oscillating at the higher order harmonics of the fundamental frequency. From equation 1.1, doubling the strength of the electric field will double $P^{(1)}$, quadruple $P^{(2)}$, octuple $P^{(3)}$, and so on. The term, nonlinear optics, arises from this phenomenon as an increase in higher order polarizations is not linear with respect to an increase to the electric field. In particular, it is the first two nonlinear terms, $\chi^{(2)}$ and $\chi^{(3)}$, on which we focus the remainder of Section 1.2, and what we aim to measure by SFG and SHG.

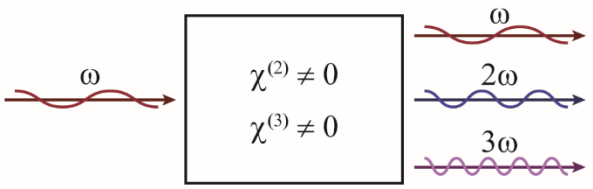

Figure 1.2 Depiction of a nonlinear medium converting light of frequency ω, to the second and third harmonics, 2ω and 3ω, respectively.

Furthermore, the unique ability of sum frequency and second harmonic generation spectroscopies to probe buried interfaces arises from their selection rules, which require a noncentrosymmetric medium. This selection rule stems from the anharmonic oscillations of electrons, and is the reason high laser powers are required to observe nonlinear processes. However, whereas $\chi^{(2)}$ is zero in centrosymmetric media (Figure 1.3), $\chi^{(3)}$ is not. Simplistically, for a centrosymmetric system, an electric field inversion will result in a corresponding polarization inversion, or, $\left(-P^{(2)}\right) + \left(-P^{(3)}\right) = \chi^{(2)}(-E)^2 + \chi^{(3)}(-E)^3$. Since $\chi^{(2)}$ does not invert because it is a physical property, and the square of a negative number is a positive one, the only solution to the above and equation 1.1 is that $\chi^{(2)} = 0$. In a similar manner, the cube of a negative number remains negative, and therefore $\chi^{(3)}$ does not necessarily equal zero in a centrosymmetric medium.

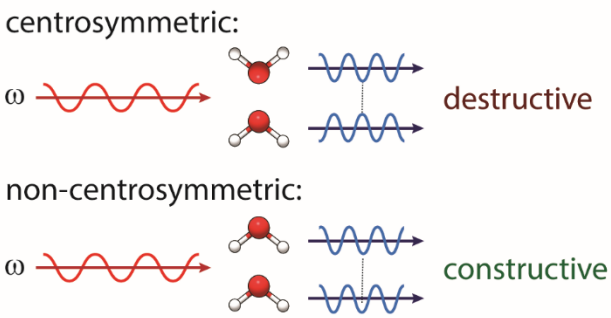

Figure 1.3 Depiction of centrosymmetry leading to complete destructive interference of second harmonic signals, and non-centrosymmetry leading to constructive interference of second harmonic signals.

It is useful to describe the surface selectivity of the second-order nonlinear susceptibility by the following equation

$$\chi^{(2)} = N\langle\beta\rangle, \tag{1.2}$$

where N is the number density of oscillators, and β is the hyperpolarizability of those oscillators. The hyperpolarizability is to a molecule as the nonlinear susceptibility is to a medium. The angled brackets indicate an average over all molecular orientations, and therefore a completely random distribution of orientation leads to $\langle\beta\rangle = 0$, and therefore a $\chi^{(2)}$ of zero. Furthermore, an increase in the net alignment of a medium will increase $\chi^{(2)}$. Similarly, a displacement of oscillators (i.e. decrease in number density) will decrease $\chi^{(2)}$, and vice versa.

1.3.2 Second Harmonic Generation

Second harmonic generation involves the annihilation of two photons at frequency, ω, and the simultaneous creation of one photon at frequency 2ω, and is the simplest case of nonlinear

optics. The efficiency of this process is the second-order nonlinear susceptibility, and depends on the number of oscillators, their net alignment, and the strength of the hyperpolarizabilities involved (equation 1.2). Furthermore, the hyperpolarizability, and therefore SHG, is significantly enhanced when either the fundamental frequency or the second harmonic is on resonance with an energy transition. On this note, SHG is often used to probe electronic transitions because of the high energy photons generated by the lasers typically used (i.e. visible to near-IR). When considering nonresonant SHG, an electron is excited to a virtual state, from which it relaxes and emits light at the second harmonic frequency (Figure 1.4). This process, first observed by Franken and coworkers in 1961 through crystalline quartz,[56] has since become a useful tool in both research and application. For example, common green laser pointers usually contain a near-IR light emitting diode (1064 nm) which is converted to its second harmonic (532 nm) through a doubling crystal, which has a very large $\chi^{(2)}$.

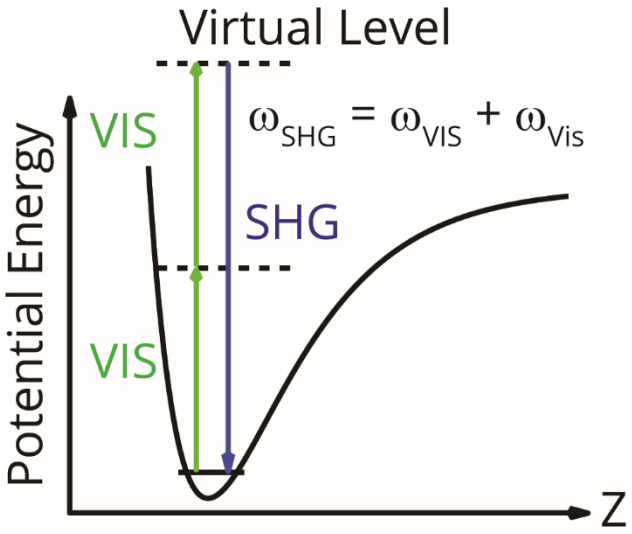

Figure 1.4 Energy transition involved in nonresonant second harmonic generation. Virtual states are shown as dashed lines, and the ground state is shown as a solid straight line. The curved solid line is the potential energy of a molecule as a function of internuclear distance in the z-direction.

1.3.3 Sum Frequency Generation

A more general case of nonlinear optics is sum frequency generation, where more than one fundamental frequency of light is used. Since each electric field can result in the processes described in equation 1.1, and additional processes involving the interplay of the two electric fields, E_{ω_1}, and E_{ω_2}, we have the following

$$P = \chi^{(1)}E_{\omega_1} + \chi^{(1)}E_{\omega_2} + \chi^{(2)}E_{\omega_1}^2 + \chi^{(2)}E_{\omega_2}^2 + \chi^{(2)}E_{\omega_1}E_{\omega_2} + \cdots, \quad (1.3)$$

where the first four terms are the linear and second harmonic responses of the medium with the two electric fields, and the last term is the sum frequency generation. Other second order terms (i.e. difference frequency generation), and higher order terms (e.g. third harmonic generation) are excluded for simplicity. It is important to emphasize that all optical processes (including those not shown) may occur simultaneously and result in unique oscillation frequencies, however, the magnitudes of nonlinear susceptibilities generally decrease with increasing order (i.e. $\chi^{(2)} >> \chi^{(3)} >> \chi^{(4)}$, etc.) Yet, with proper phase matching conditions, the efficiency of some processes can be enhanced relative to others. Sum frequency generation results from the oscillation of electrons at the sum frequency, $\omega_1 + \omega_2$. The same selection rules of SHG apply for SFG, although for the latter, it is more common for one electric field to be on resonance with either a vibrational or electronic transition. When one laser beam is in the mid-IR range, vibrational resonances result in the enhancement of the SFG signal. In general, an electron is excited by an IR photon to a higher vibrational mode and upconverted to a virtual state by the photon from another laser beam (Figure 1.5). These excitations can occur simultaneously, or given the lifetime of the vibrational state, the excitation from the pump beam can occur sometime after the vibrational excitation. An additional selection rule for vibrational sum frequency generation (vSFG) is that an SFG-active resonance

must be both Raman- and IR-active, which can be seen in the description of the resonant hyperpolarizability β, for vSFG,

$$\beta = \alpha \times \mu, \tag{1.4}$$

where α is the polarizability and μ is the transition dipole moment.

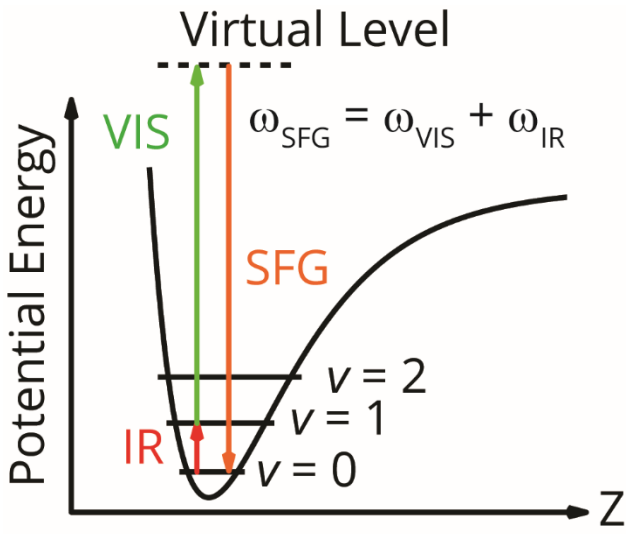

Figure 1.5 Energy transition involved in resonant, vibrational sum frequency generation. In this case, the IR light is on resonance with a vibrational mode, while the visible is off resonance. Virtual states are shown as dashed lines, and the ground and vibrational states are shown as a straight solid lines. The curved solid line is the potential energy of a molecule as a function of internuclear distance in the z-direction.

1.3.4 Polarization Resolved SFG

The oscillation orientation (e.g. horizontal, vertical, etc.) of the resulting SFG electric field is highly dependent on the orientation of the oscillators. In reality, the resulting oscillation can be in all directions, with varying degrees of magnitude. By measuring specific polarization

orientations through the use of optical filters (i.e. polarizers), molecular orientations can be determined.[57-58] These orientations are usually defined as being parallel or perpendicular to the plane of incidence, which is the plane between the surface normal and incident electric fields, and are abbreviated by 'P' and 'S' (derived from the German words for parallel and perpendicular, *parallel* and *senkrecht*). The orientational nonlinear susceptibility depends on the orientation of the input electric fields and can be denoted as $\chi_{ijk}^{(2)}$, where *i, j,* and*, k* constitute the polarization combination, which by convention, are listed in order of decreasing energy. For example, SSP indicates S-polarized sum frequency light, S-polarized visible light, and P-polarized IR light (Figure 1.6). Under the geometry defined in Figure 1.6, and the $C_{\infty v}$ symmetry present at interfaces, only seven of these $\chi^{(2)}$ polarization combinations are nonzero, and three of these are equivalent to others, leaving only four, unique, nonzero polarization combinations: ssp, pss, sps, and ppp.

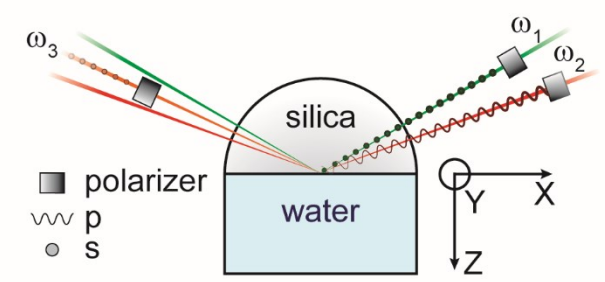

Figure 1.6 Schematic of sum frequency generation in ssp polarization combination where s and p are defined with respect to the plane of incidence (xz-plane). ω_1, ω_2, and ω_3 are visible, infrared, and sum frequency light, respectively.

1.3.5 The $\chi^{(3)}$ Method

The first nonlinear optical study of the silica/water interface, by Eisenthal and coworkers,[59] led to what is known as the $\chi^{(3)}$ method. Because of the surface specificity of SHG, Eisenthal and coworkers expected to generate signal from the silica/water interface largely from the terminal silanols, which inherently lack inversion symmetry. The deprotonation of silanols was expected to change the SHG signal on the assumption that the hyperpolarizability of silanols differ from that of siloxides. They observed a signal increase (Figure 1.7a) with increasing pH, leading to the initial theory that $\beta_{SiO^-} > \beta_{SiOH}$.

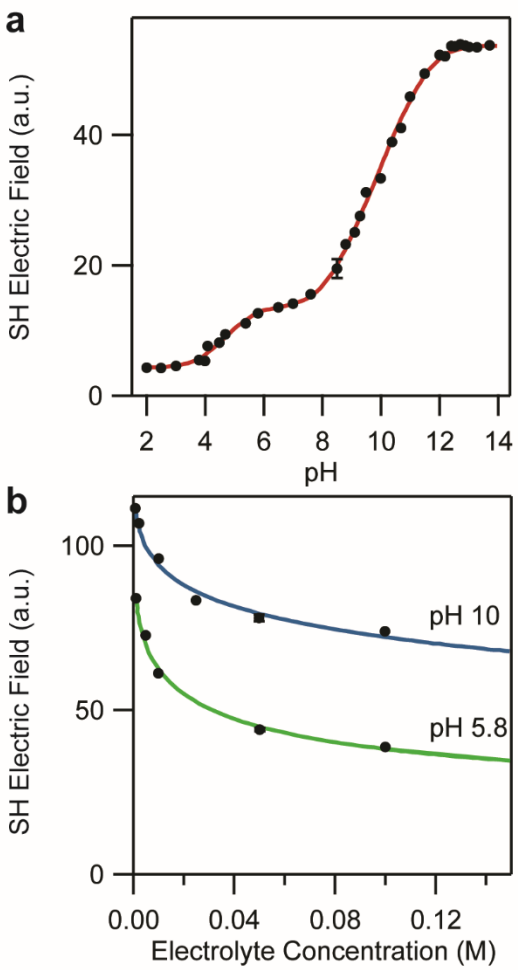

Figure 1.7 (a) SH electric field at the silica/water interface in the presence of 500 mM NaCl from pH 2-14, and at increasing electrolyte concentrations at (b) pH 5.8 and pH 10. Solid lines are fits from a constant capacitance model. Adapted from Eisenthal and coworkers, Copyright 1992,[59] with permission from Elsevier.

To test their theory, they added electrolytes to the solution, which are known to affect the surface charge density at the surface.[1] With an increase in electrolyte concentration, they expected more silanols to become deprotonated and the SHG signal to increase. However, in direct opposition to their hypothesis, they observed the SHG signal decrease with increasing ionic strength at both pH 5.8 and 10 (Figure 1.7). In order to account for these results, they developed a

new theory contributing the dominant signal generators at the silica/water interface to the water molecules, rather than the silica. Bulk water, although of C_{2v} symmetry and intrinsically lacking an inversion centre, is randomly oriented in bulk solution and should not generate net signal via second harmonic generation. However, due to hydrogen bonding with the silanols and siloxides at the surface, water may become oriented in a preferential direction and lead to a nonzero, orientationally averaged hyperpolarizability, $\langle\beta\rangle$, and therefore a nonzero nonlinear susceptibility. Furthermore, the static electric field from charged siloxides may align water molecules through their molecular dipoles, and in addition, polarize their electrons. The polarization of waters aligned by this additional electric field is described by a third-order nonlinear susceptibility, $\chi^{(3)}$, however since a static electric field has no oscillation frequency, the resulting polarization frequency is also at the second harmonic. Recalling that $\chi^{(3)}$ does not require a lack of inversion symmetry to be nonzero, even centrosymmetric bulk waters may generate second harmonic light if they become sufficiently polarized by the static electric field. Therefore the static electric field contributes to the total second harmonic signal in two ways: the alignment of water molecules through interaction with their permanent dipoles, and the polarization of water molecules. The former process contributes via the hyperpolarizability, β, while the latter described by the second hyperpolarizability, γ. Therefore we come to the $\chi^{(3)}$ method which is summarized as

$$\sqrt{I_{2\omega}} \propto P_{2\omega} = \chi^{(2)}E_{\omega}E_{\omega} + \chi^{(3)}E_{\omega}E_{\omega}\int_0^{\infty} E_o dz, \tag{1.5}$$

where $I_{2\omega}$ is the intensity of the second harmonic signal, the square root of which is equal to the second harmonic electric field, $E_{2\omega}$. E_o is the static electric field which is integrated over all distance along the surface normal (z-direction) to yield the surface potential, Φ_0, and $\chi^{(3)}$ can be written as

$$\chi^{(3)} = N(\frac{\mu\beta}{bkT} + \gamma). \quad (1.6)$$

Here, μ is the permanent dipole of water, k is the Boltzmann constant, T is the temperature, and b is a constant determined by the experimental conditions. It can be seen from equation 1.5 that the term containing $\chi^{(3)}$ is modulated by the strength of the electric field, which ultimately arises from the presence of surface charges and is therefore related to the surface potential. Therefore if $\chi^{(2)}$ and $\chi^{(3)}$ are known, it may be possible to indirectly measure the surface potential of silica and other mineral oxides. This theory sparked large interest in the SHG technique.

1.4 SFG at the Silica/Water Interface

1.4.1 OH Bond Stretching

At the heart of the $\chi^{(3)}$ method is the assumption that the interfacial waters are contributing to the nonlinear polarization. Therefore vibrational sum frequency generation on resonance with water vibrations should reflect those trends observed by Eisenthal and coworkers. In 1994, the first vSFG spectra of the silica/water interface, on resonance with the stretching of water, were collected by Shen and coworkers.[60] Indeed, the water stretching region did exhibit SFG signal indicating a net alignment of water molecules at the silica surface. The observed trends, with respect to solution pH, did not follow those reported with nonresonant SHG,[59] however an explanation was not provided as to why the trends differed. Where Eisenthal and coworkers reported a monotonic increase in signal from low to high pH, Shen and coworkers observed an initial decrease in the net SFG signal from low to mid pH, followed by an increase in signal at higher pH (Figure 1.8). The bimodal behaviour was attributed to the competition between water alignment through hydrogen

bonding and from dipole interactions with the static electric field. It was assumed that at a neutral surface (pH 2), water would be preferentially oriented with their hydrogens pointed away from the surface by accepting hydrogen bonds from silanols. Conversely, the static electric field was assumed to align waters with their hydrogens pointing towards the surface. As the static field became stronger with increasing pH, the potential induced alignment was suggested to dominate over alignment by hydrogen bonding, with a minimum in net alignment observed around pH 4. The addition of 0.5 M NaCl at pH 1.5 did not appreciably change the net signal, and the addition of 0.1 M NaCl at pH 5.6 changed the lineshape but the total intensity remained similar. Yet, at pH 12.3, a decrease in SFG intensity was observed with salt addition. The spectrum of silica/ice (Figure 1.8f) was used to help assign vibrational modes to the spectra.

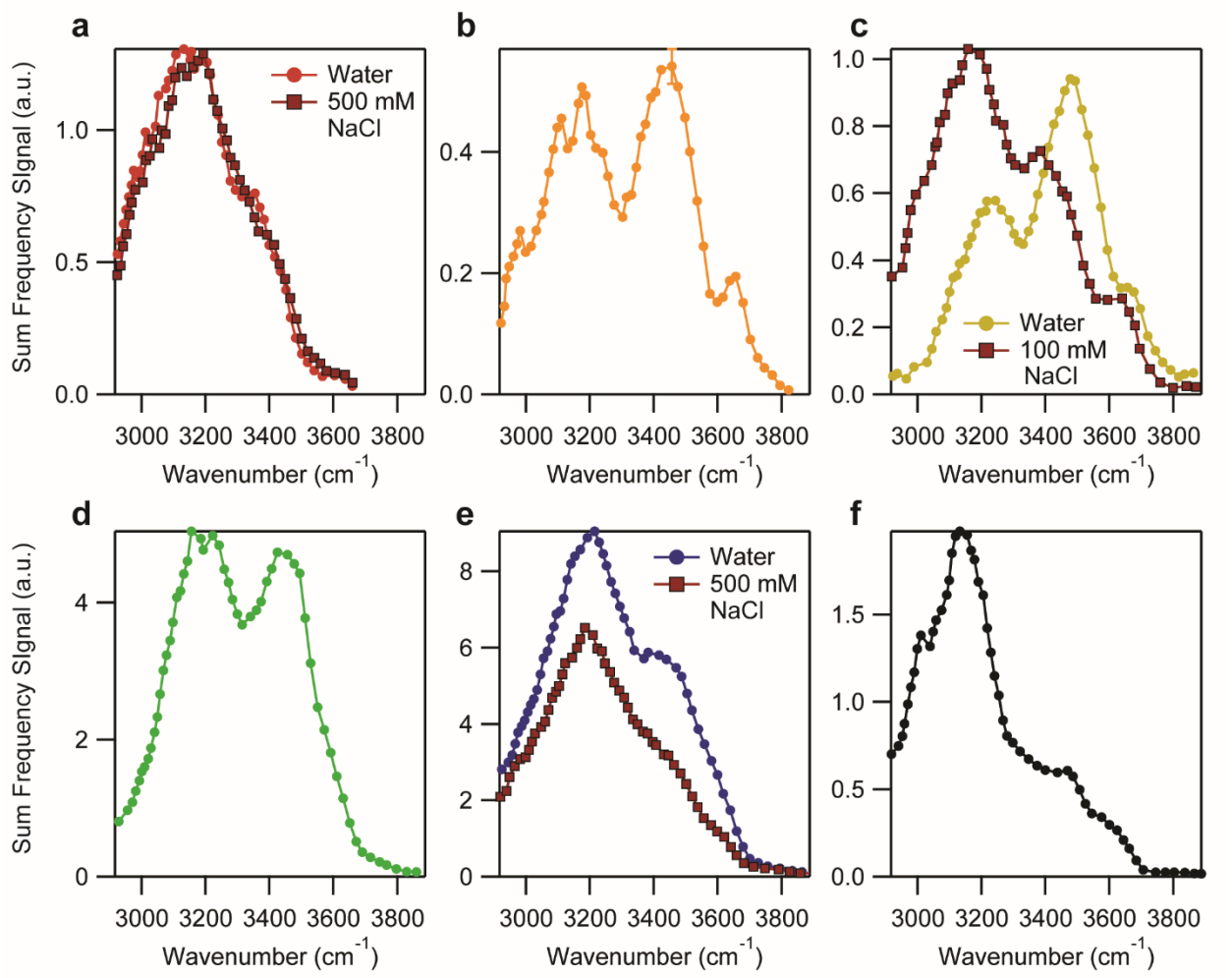

Figure 1.8 SFG spectra of the fused quartz/water (circles) and quartz/$NaCl_{(aq)}$ (squares) interfaces in the OH stretching region at (a) pH 1.5, (b) pH 3.8, (c) pH 5.6, (d) pH 8.0, (e) pH 12.3, and (f) SFG spectra at the fused quartz/ice interface. Data was digitized from Shen and coworkers.[60]

1.4.2 Hydrogen Bonding

The extent of hydrogen bonding in water affects the OH stretching frequency, which generally redshifts with increasing H-bond strength and can be characterized by a decreasing H-bond length.[61-62] Additionally, an increasing H-bond angle leads to blueshifting of the stretching

frequency.[63] Molecular dynamics (MD) simulations have shown that approximately 70% of these redshifts are due to a water molecule's first water neighbor, while the remaining 30% of the shift is due to the remaining liquid.[63] The diverse nature of hydrogen bonding in water leads to many H-bonding configurations which each exhibit a distribution of stretching frequencies. MD simulations also demonstrate that configurations with more H-bonds (e.g. 2 H-bonds to the water oxygen, and 1 H-bond to each water hydrogen) lead to lower frequencies while those with less H-bonds (e.g. 1 H-bond to the water oxygen, and 1 or 0 H-bonds to the water hydrogens) lead to higher frequencies.[62, 64-65] In all cases the lack of an H-bond to a water hydrogen leads to significantly blueshifted frequencies and narrow frequency distributions than their H-bonded counterparts.[62, 64-65] On average, each water molecule participates in 3.2 – 3.4 H-bonds,[66] where approximately 10 – 15% of the time a water hydrogen is not H-bonded.[63, 65] This free-OH configuration is unstable and leads to the reorientation of the hydrogen bond network, which involves the breakage and formation of H-bonds.[65] These reorientations in bulk solution occur on the 1 – 1.5 ps timescale in total,[62, 66-67] and exhibit a frequency dependence.[62, 67] In particular, strong H-bonds appear to reorient faster (~200 fs) than weak H-bonds (~1 ps).[67] As the uncertainty principle suggests energy is inversely proportional to time, these shorter timescale dynamics may lead to wider distributions in their stretching frequencies.

1.4.3 Silanols and Hydrophobicity

In addition to spectral changes caused by pH changes and salt addition, Shen and coworkers observed three broad modes centred around 3200 cm^{-1}, 3400 cm^{-1}, and 3680 cm^{-1}.[60] The assignment of these modes are, unfortunately, controversial. A comparison of spectra from hydrophilic and hydrophobic surfaces initially led to the theory that the 3680 cm^{-1} mode was an

indication of hydrophobicity.[68] A strong, sharp peak observed around the same frequency at the intrinsically hydrophobic air/water interface was assigned to the dangling OH of water extending out into air.[69] The lack of hydrogen bonding available to these dangling, or so-called free-OH, bonds resulted in its high wavenumber resonance and narrow lineshape. A similar mode was observed at the octadecyltrichlorosilane and octyltrichlorosilane functionalized silica surfaces in contact with water,[68, 70-72] and was given to water OH bonds dangling into the hydrophobic monolayer. However, later SFG studies at the silica/air and silica/water interfaces following either air-plasma or heat treatments (1000°C) suggested this mode to be due to the silanols themselves.[73] A sharp band at 3750 cm^{-1} observed at the silica/air interface, was attributed to the vibrations of isolated silanols,[73-74] and suggested to redshift when in contact with water due to an increase in hydrogen bonding.[73] Additionally, both the 3680 cm^{-1} mode under water and the 3750 cm^{-1} mode in air exhibited the same behaviour to air plasma and heat treatments, supporting this argument.[73] Yet, recent time-resolved SFG studies coupled with MD simulations have again suggested the mode around 3680 cm^{-1}, from silica in contact with water to be due to water interacting with relatively hydrophobic surface sites (i.e. siloxanes).[75] The vibrational dynamics of this mode were found to occur on the order of 1 ps, which are much faster than those of isolated silanols at ~100 ps.[75] Furthermore, water contact angles appeared to increase with increasing 3680 cm^{-1} mode strength.

1.4.4 Strongly and Weakly Coordinated Water

For the 3200 cm^{-1} and 3400 cm^{-1} SFG modes at the silica/water interface,[60] Shen and coworkers adopted their previous assignment of vibrations at the air/water interface[69] derived from Raman spectra of bulk water.[76] In short, the 3200 cm^{-1} peak was attributed to the symmetric stretch of tetrahedrally (strongly) coordinated water molecules, and higher wavenumber modes to symmetric stretches of less than tetrahedrally (weakly) coordinated waters and asymmetric stretches.[60] This assignment was adopted and refined, leading to the 3400 cm^{-1} mode being attributed to both the asymmetric stretching of tetrahedrally coordinated waters and the symmetric stretching of weakly coordinated waters.[77-80] Intensity around 3500 cm^{-1} was then assigned to the asymmetric stretching of the weakly coordinated waters. Furthermore, the 3200 cm^{-1} mode is often called the "ice-like" peak and the 3400 cm^{-1} mode is often called the "liquid-like" peak,[60, 81-82] because it is similar to the 3200 cm^{-1} mode in the SFG spectrum of the silica/ice interface.[60, 83-84] However some discretion to these particular assignments of "ice-like" or "liquid-like" is advised because of inter- and intramolecular coupling.

1.4.5 Inter- and Intramolecular Coupling

The diverse H-bonding environment of water leads to broadening and redshifting of the vibrational modes (i.e. intermolecular coupling), which can lead to difficulty in their assignments. The intramolecular coupling, from which arises the splitting of OH vibrations into symmetric and asymmetric modes may be more substantial than originally realized when the "ice-like" and "liquid-like" assignments were suggested. Through isotopic dilution with deuterium, the stretching is uncoupled, resulting in independent OH and OD oscillators. At the air/water interface, this

procedure revealed the 3200 cm^{-1} and 3400 cm^{-1} bands to be almost entirely due to intramolecular coupling, leaving mostly a single resonance at the air/HOD interface (Figure 1.9).[85-86] Furthermore, the bending vibration of water, which is difficult to measure at the silica/water interface due to IR absorption from silica,[87] leads to an overtone which is expected to occur at similar frequencies as the stretching modes, resulting in additional peak splitting through a Fermi resonance.[88] The implication of this coupling is that the observed peaks in SFG spectra may not be necessarily due to different structural arrangements of water, rather they may be from one population exhibiting coupling. At the silica/water interface, isotopic dilution also reduced the strength of some modes, however, more structural heterogeneity (i.e. distinct spectral features) remained at the silica/HOD interface than at the air/HOD interface.[89-90] This heterogeneity, clearly observed in the phase-sensitive measurements of the silica/HOD interface as oppositely signed modes,[82, 90] indicates that distinct populations of water do indeed exist at the silica/water interface.

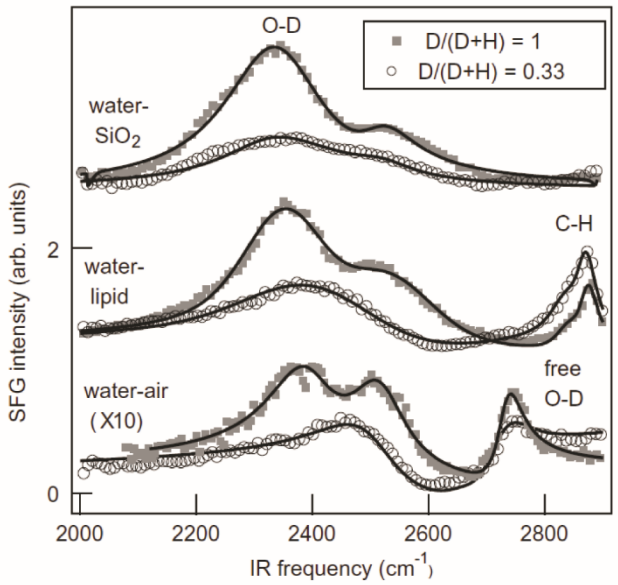

Figure 1.9 SFG spectra of the silica/D_2O, charged lipid/D_2O, and air/D_2O interfaces at pD 11.5 with no (squares) and 33% (circles) isotopic dilution with hydrogen. Reprinted from Bonn and coworkers,[89] Copyright 2009, with permission from Elsevier.

1.4.6 H-Bond Donors and Acceptors

In particular, water can interact with the underlying silica in at least two ways: as H-bond donors to the oxygens of silanols and siloxides, and as H-bond acceptors to the hydrogens of silanols. These two possibilities, which may result in opposite water alignment, are borne out of the molecular dynamics simulations of water in contact with either neutral or charged silica surfaces.[91-95] This was supported by phase measurements of the neutral silica surface in contact with water at pH 2, where there should be little to no static electric field, which revealed two oppositely signed modes as mentioned previously.[82, 90] The interpretation of H-bond donor and acceptor waters is in general agreement with the idea of strongly and weakly coordinated water molecules near the surface. Water molecules acting as H-bond acceptors from silanols would be

oriented with their hydrogens towards the bulk solution and experience strong H-bonding. The water molecules H-bond donating to silanols would be oriented with at least one hydrogen pointed down towards the surface, while the other might point up or down, depending on the rotation about the H-bond to the silanol and the local H-bonding environment. Furthermore, such a water may be slightly decoupled due to the interaction of OH with a silanol and the OH with bulk water, leading to greater asymmetric character. Conversely, the H-bond acceptor waters would exhibit both symmetric and asymmetric stretching, which may contribute to the differences between SFG spectra of the silica/water and silica/HOD interfaces at pH 2.[90]

The culmination of these assignments aid in building models with which to interpret the SFG signal and assess the interfacial processes. These fundamental models are of great importance for interpreting highly applicable NLO studies, such as the specific ion effects at charged aqueous interfaces,[19, 96] which are of extreme importance for many areas of science such as interfacial processes occurring on enzymes and DNA.[97-98] However, differences in physical models can lead to different interpretations of the interfacial processes occurring.[99-100] Therefore it is important for the physical interpretation of SFG spectra at the silica/water interface, to dissect the possible contributions to the signal.

1.4.7 Diffuse Layer Contributions

Large changes in SFG intensity are due to changes in the net alignment of diffuse layer water molecules. The extent of this alignment stems from the strength of the static electric field emanating into the bulk, which ultimately arises from the surface charge density at the surface. This static electric field can extend into solution from less than one Angstrom at high ionic strength,

to more than a micron at very low ionic strength, depending on the concentration of counter ions present in solution. Furthermore, the surface charge density can be manipulated by the dissociation of silanols.

As described above, the alignment of diffuse layer waters originates from the interactions of water dipoles with the static electric field from silica. This definition is the same as given by the $\chi^{(3)}$ method for $\chi^{(3)}$ itself,[59] and therefore we can consider the alignment of diffuse layer waters to contribute via a $\chi^{(3)}$ process. However according to MD simulations (for which experimental support is still needed), contrary to nonresonant SHG, the contribution of $\chi^{(3)}$ to resonant SFG is primarily through the reorientation of molecules, rather than the polarization of molecules (i.e. $\beta_{\text{resonant}} \gg \gamma_{\text{resonant}}$).[92] Tian and coworkers suggested that the lineshape of $\chi^{(3)}$ is independent of the underlying substrate and rather a property of bulk water,[101] and has since been experimentally extracted and simulated at various interfaces (Figure 1.10). Furthermore, since the magnitude of the $\chi^{(3)}$ contribution to SFG spectra is dependent on the strength of the static electric field, it may be a useful tool in describing the properties of the diffuse layer.[102] Although similar between interfaces, $\chi^{(3)}$ is expected to be affected by changes to the diffuse layer H-bond network. It has been shown by electronic second harmonic scattering (SHS) that bulk water experienced an increase in molecular ordering when the ionic strength was increased from 1 μM to 1 mM and then remained constant up to 100 mM.[103] This trend was invariant of cation or halide identity and appeared to correlate well with surface tension. Perhaps this ordering was reflected in the molecular dynamics simulations of aqueous sodium chloride solutions which demonstrated a slight redshift in $\chi^{(3)}$ lineshape from pure water to 100 mM ionic strength.[104] Although this redshift was minor in comparison to the changes observed beyond 100 mM, which in general was a decrease in $\chi^{(3)}$ magnitude. Additionally, an increase in temperature resulted in

a blueshift and a decrease in $\chi^{(3)}$ magnitude, as higher thermal energy should disorder water. These effects were also correlated to the dielectric constant of the diffuse layer.[105]

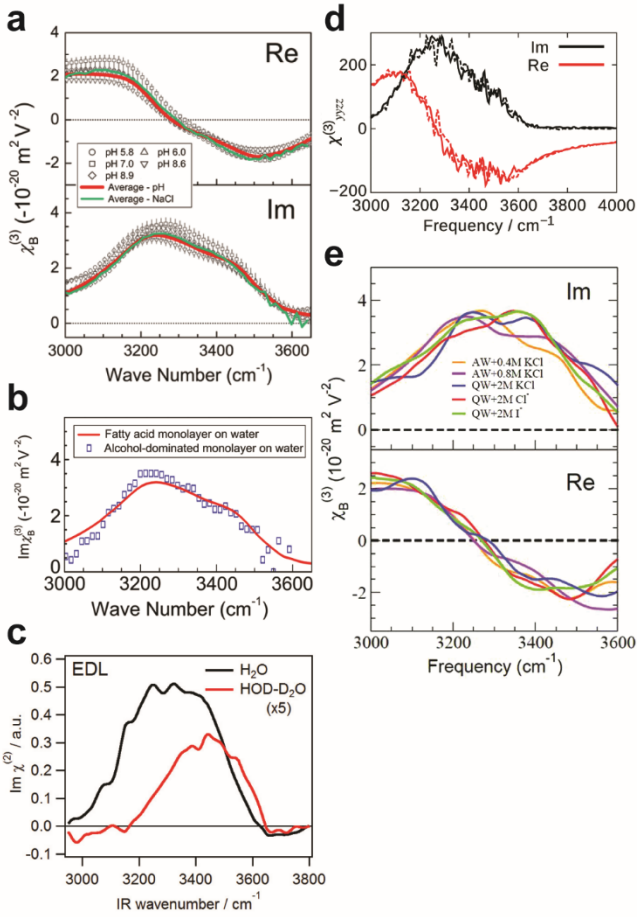

Figure 1.10 Complex spectra of the third order nonlinear susceptibility extracted from (a) the lignoceric acid/water interface,[101] (b) the octadecanol/water interface,[101] (c) the silica/water and silica/HOD interfaces,[100] simulated bulk water under an applied electric field,[92] and simulated air/water and quartz/water interfaces.[94] (a) and (b) are adapted with permission from Tian and coworkers,[101] Copyright 2016 American Physical Society. (c) is reprinted with permission from Tahara and coworkers,[100] Copyright 2018 American Chemical Society. (d) and (e) are adapted with permission from Morita and coworkers,[92] and Gaigeot and coworkers,[94] respectively. Published by the PCCP Owner Societies.[92, 94]

1.4.8 Screening and Interference

In general, an increase in counter ion concentration is accompanied by interfacial charge screening, as evidenced from potential measurements.[41, 47-50, 106] As the negative interfacial charges are screened by cations, the Debye length decreases and leads to an increasingly smaller volume of water molecules interacting with the static electric field, resulting in a smaller amount of aligned waters in the diffuse layer. In other words, since SFG signal is proportional to the number density of aligned oscillators (equation 1.2), the signal from diffuse layer waters is expected to decrease when ionic strengths are increased. Yet special considerations must be made for ionic strengths below 1 mM due to phase matching conditions.

The coherence length of the SFG process from an interface depends on the wavevectors of the incoming electric fields and the refractive indices of the two media (i.e. silica and water). SFG will still occur some distance beyond the coherence length, however, the signal will begin to be generated out of phase from, and destructively interfere with, signal generated within the coherence length.[107-108] This phenomenon becomes significant when the Debye length is relatively long, which for typical SFG experiments in reflection geometry occurs below 1 mM ionic strength. Therefore, the SFG signal will increase with the addition of salt into pure water until approximately 1 mM ionic strength and then decrease beyond this concentration due to dominating screening effects (Figure 1.11). This phase change has been shown to significantly affect the final measured SFG lineshape, which is a combination of waters aligned by the static electric field (diffuse layer) and waters aligned by hydrogen bonding to the surface.[92, 109-110] However, screening and interference are not sufficient to explain all signal changes observed in SFG and SHG at the silica/water interface by SFG.

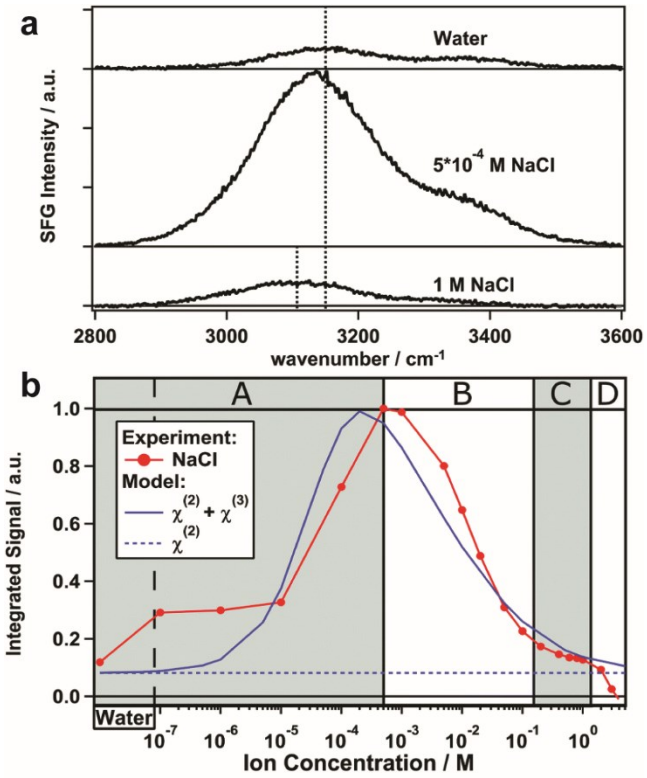

Figure 1.11 (a) Raw SFG spectra of the silica/water interface at increasing ionic strength. Dashed lines indicate peak maxima. (b) Integrated intensities of the SFG spectra of the silica/water interface with increasing ionic strength. Shaded regions A-D indicate different regions of spectral behaviour. Published by the PCCP Owner Societies.[108]

1.4.9 Specific Ion Effects

The surface-hydrating waters within the Stern layer, sometimes referred to as the bonded interfacial layer,[101] play a large role in SFG and SHG signal generation but their behaviour does not always follow the trends expected by screening and interference. In addition to ion adsorption,[111-114] specific ion effects highlight these phenomena, since ions of the same valency within the diffuse layer should screen charges with the same efficacy. Yet differences in the

amount of aligned waters are apparent and are attributed to the ions' ability to perturb the hydrogen bonding structure of water in contact with the surface. Monovalent cations generally follow a direct Hofmeister trend at natural pH values (~pH 5.8), with kosmotropes (order-makers), like Na^+ and Li^+, attenuating the signal the least, and chaotropes (disorder-makers), like Cs^+ and K^+, attenuating the signal the most.[19, 115-117] The degree of attenuation has been related to many properties of the salts including the ionic radii,[115] the dissociation constant of the cation's respective acid,[116] and cation hydration energies.[19] At high[19, 117] and low[19] pH, a reversal of the Hofmeister series has been observed, where kosmotropes exhibited the greatest signal attenuation and vice versa for the chaotropes. Higher valency ions, like Mg^{2+} and Ca^{2+}, demonstrate even greater H-bond disruption than monovalent ions.[116-117] Although divalent ions are expected to exhibit stronger surface charge screening, it has been suggested that they can more easily displace surface waters in exchange for their own cation hydration waters, compared to monovalent ions.[116] Anions were also demonstrated at high pH to follow a direct Hofmeister series which was attributed to matching water affinities between surface and anion hydration waters.[118] It is interesting to note that in most cases,[19, 99, 115, 117] the greatest perturbation was observed in the low wavenumber mode (3200 cm^{-1}) and in some form attributed to the presence of charged siloxides, as SHG and electrokinetic measurements on mesoporous silica indicate silanol deprotonation is completely compensated by cation adsorption.[119]

The deprotonation of silanols is thought to originate from more than one type of silanol, which are distinguished by their hydrogen bonding environment. From the bimodal SHG signal observed at the silica/water interface over a broad pH range of 2 to 14 (Figure 1.7a),[59] at least two types of silanols were identified: "more-acidic" with lower pK_a's and "less-acidic" with higher pK_a's. Using a method developed by Eisenthal and coworkers,[120] cations were found to shift the

pK_a's of these silanols to lower or higher values depending on the cation identity,[121] and the magnitude of the shift was dependent on the cation concentration.[122] Furthermore, anions shifted the "more-acidic" pK_a's to lower pH and the "less-acidic" pK_a's to higher pH,[123] which depended on the halide size and not the concentration.[122] From these trends were inferred positive cooperativity between anions and the "more-acidic" silanols, and negative cooperativity the "less-acidic" silanols.[123] Therefore, the waters in direct contact with the silica surface or those of adsorbed ion hydration spheres are expected to behave differently from those aligned in the diffuse layer. Yet it should be noted that earlier studies at low salt concentrations had not accounted for the interference effects as discussed above, and may benefit from a reinterpretation to isolate the specific ion effects on the bonded interfacial layer.

1.4.10 Disentangling Surface Contributions

It is challenging to measure these buried surface waters because of the large number of aligned molecules within the diffuse layer. Early investigations to disentangle the contributions of the surface from the diffuse layer used salt concentration as a tool to systematically reduce the Debye length.[124-125] As the Debye length was reduced, a predominantly surface contribution was expected to be probed by SFG. However, it was recognized that as the concentration was increased, changes to the surface hydrogen bond structure and surface charge densities may occur, altering the apparent surface spectral lineshapes. A similar trend in intensities was observed using SHG at the silica/graphene/water interface capturing the initial increase in signal with low ionic strengths.[126] The increase was attributed to changes in $\chi^{(2)}$ and $\chi^{(3)}$ with the formation of the EDL. Later, using α-quartz as an internal phase reference, it was demonstrated by SHG that the $\chi^{(3)}$

component of the signal interfered with the bulk $\chi^{(3)}$ response of the quartz, which was purely imaginary.[127] This interference indicated a phase change in the water $\chi^{(3)}$ response and possible interference within the diffuse layer. At the same time emerged a report detailing the $\chi^{(3)}$ phase change from the silica/water interface and resulting destructive interference within the diffuse layer.[107] It was demonstrated that the observed increase and decrease in signal (Figure 1.11a) was largely optical in origin and not indicative of changes to H-bonding structure at the interface. Simultaneously, a methodology was developed by Tian and coworkers to deconvolute the spectral contributions of waters aligned by hydrogen bonding with the surface (Figure 1.12) and by the static electric field (Figure 1.10a).[101] In short, under the assumption of an unchanging surface water structure between two different SFG spectra (e.g. over a salt or pH titration), the change in SFG signal must be completely due to a change in the potential-aligned component, $\chi^{(3)}\Phi$, where Φ is the surface potential (equation 1.5). As discussed earlier, it was shown that $\chi^{(3)}$ is independent of the surface and therefore the difference can be attributed to changes in the potential. With some knowledge of the potential, the diffuse layer component can be removed from the total spectra, where the remainder is the signal from waters aligned by other forces (i.e. hydrogen bonding). This methodology, which requires accurate phase referencing, was well received and variations of the analysis have been applied to the silica/water interface using SFG,[90, 94, 100, 128-130] SHG,[131-132] and SHS.[133] These studies have yielded a wealth of insight into the behaviour of waters in the so-called bonded interfacial layer.

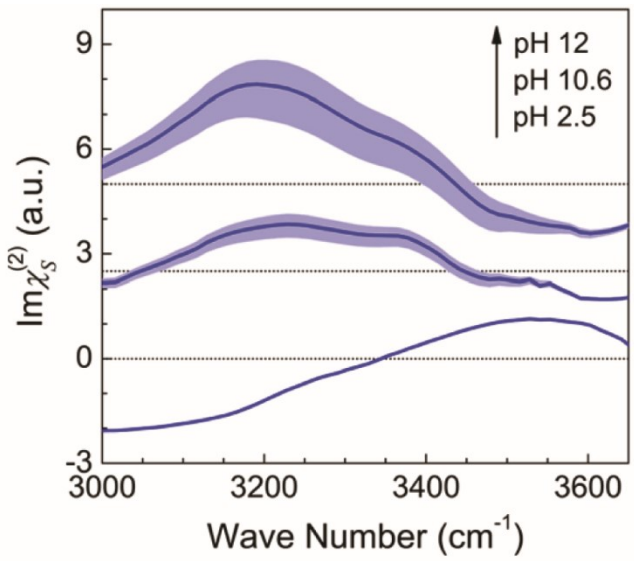

Figure 1.12 Imaginary surface component of the sum frequency spectra at the charged lipid/water interface from low to high pH. Spectra are offset for clarity. Dashed lines and shading denote zero and uncertainty, respectively. Reprinted from Tian and coworkers,[101] Copyright 2016 American Physical Society.

1.4.11 Dissolution and Hysteresis

Ultimately, the organization of surface bound waters is directly linked to the structure and chemistry of the underlying silica surface. In time evolution studies at the silica/water interface, it was shown that the SFG signal was very different after soaking in pure water than after soaking in basic water.[44] In pure water, the spectra after soaking demonstrated a drastic change in lineshape, but in basic water, the spectra were barely affected. The change in pure water was attributed to water molecules penetrating the silica surface and inducing swelling, which was supported by AFM surface roughness measurements. The resistance to swelling at high pH was attributed to an electrostatic barrier protecting the surface from attack by water. This stabilization behaviour was

reflected in the SFG studies by Borguet and coworkers in the presence and absence of salt at various solution pH.[134] It was observed that the SFG signal, and by association, the silica/water interface, was most susceptible to salt addition at pH values from 6 to 10, whereas relative resistance to salt addition was observed at lower and higher pH values. This behaviour was compared with the trend of quartz dissolution in salt water, which was predicted to depend on the motion and orientation of surface-solvating waters.[135] Furthermore, silica dissolution was studied by vSFG by taking advantage of the interference effect discussed earlier.[136] The submillimolar concentrations of silicic acid ions released into solution resulted in a detectable signal increase from pure water and indicated that silica dissolution occurred on the order of hours. The dissolution was determined to be autocatalytic, where silicic acid was suggested to further promote the dissolution of silica. In another dissolution study, flow of near neutral water across silica decreased the total SFG signal which was attributed to a loss in surface charge density.[137] This loss was suggested to arise from the dissolution reaction of silica where a partially cleaved siloxane reacts with water to form charged silicic acid and a neutral silanol. Flow conditions would remove the silicic acid and drive the equilibrium forward. At low pH, flow did not affect the surface charge because of less availability of cleaved siloxanes. At high pH, a competition between flow-induced charge loss and silica deprotonation due to the basic conditions resulted in a minimal overall change in the SFG signal. The return to equilibrium after flowing at neutral pH required nearly half an hour. Similar delays in establishing equilibria were observed at the silica/water interface using SHG at various salt concentrations and pH values.[138] Depending on the salt concentration, equilibrium conditions under flow were prevented by up to an hour, depending on the cation hydration energy and anion polarizability.

The behaviour of the silica/water interface also depends on the hysteresis of the sample. It was shown by SHG that the number and relative proportion of silanol sites may depend on the initial pH of a titration.[139] When initialized at pH 12 and titrated to pH 2, three pK_a's were observed, rather than the two when the titration was started at pH 7 or 2. Similarly, a salt titration from low to high concentrations yielded relatively lower SHG intensities than a titration in the reverse direction.[105] However, an initial titration from low concentration did not affect the trend of a subsequent titration from high concentration. Additionally, relative proportions of modes observed in the stretching region of water by SFG were different when silica was pretreated with air plasma or heat.[73] Furthermore, acid leaching treatments of impurity-containing silicas resulted in porous-rich surface layers which exhibited different water hydrogen bonding structure than before the treatment.[74] Finally, sodium silicate was demonstrated to irreversibly bind to the silica surface when introduced at either pH 5 or 9 and also resulted in a change to the water hydrogen bond structure.[140]

1.4.12 Summary

In summary, water and silica present one of the most prevalent interfaces on the surface of the Earth. The ubiquitous silica/water interface serves as a highly studied model for other charged interfaces. The behaviour of water hydrating with, and electrostatically attracted to, the silica surface has been recognized to be of clear importance to further our understanding of the interplay between these two common, yet complex substances. Nonlinear optical techniques such as SHG and SFG have proven invaluable in understanding interfacial processes at the silica/water interface. However, the interpretation of such studies is sometimes controversial due to the complexity of the interface and contributions to the NLO signal. While this introduction covers the investigation

of the silica/water interface by nonlinear optics, there are also excellent reviews of NLO studies on various charged and neutral surface/solution interfaces.[141-147]

1.5 Thesis Organization

This thesis mainly focuses on studying the interactions of water with silica using SFG. Ionic strength, solution pH, and beam polarizations are used as tools to investigate the behaviour of the silica/water interface. Complementary techniques, including SHG and streaming current/potential are applied alongside SFG to gain further insight.

Chapter 2 is a study comparing the pH dependent trends observed by SFG and SHG at the silica/water interface in the presence of high salt concentrations. The difference in trends observed, as highlighted in Section 1.3.1, have never been directly addressed. The pH dependent behaviour observed by resonant SFG exhibited a minimum near neutral pH, while that by nonresonant SHG did not, despite the $\chi^{(3)}$ method suggesting the dominant signal contribution to SHG is from the waters. Measurement of the silica/air interface by SHG suggested the silica to yield a much larger contribution to the overall signal than previously thought, and is partly responsible for the lack of signal increase at low pH. Comparisons of the behaviour of vibrational modes observed by SFG and molecular dynamics simulations (performed by Dr. Hore at the University of Victoria), suggested a net flip in water molecules contributing to the lower wavenumbers of the spectra. Since SHG cannot resolve such contributions, destructive interference between oppositely aligned populations of water was suggested to also be responsible for the continual decrease in SHG signal with decreasing pH. An outcome of this study is that signal loss in nonresonant SHG does not

necessarily imply disorder, rather local populations can increase in order, even if the net alignment diminishes.

Chapter 3 investigates changes to the water structure hydrating silica induced by increasing salt concentration. In addition to collecting SFG spectra, the zeta potential of the interface is measured and used in the analysis. The change in surface water structure due to the presence of ions is sometimes overlooked in SFG analyses which may lead to incorrect interpretations of the SFG spectra regarding the behaviour of the silica/water interface. Therefore we aimed to extract the spectral contributions of the surface waters over an increasing ionic strength. The maximum entropy method was used to retrieve the phase information required for the deconvolution method described in Section 1.3.9, which was lost in the intensity measurement. The third order nonlinear susceptibility, or diffuse layer spectrum, is then extracted from the spectra, which was used to calculate the surface contributions of water with increasing ionic strength. A sign reversal at low wavenumbers of the surface spectra with increasing ionic strength demonstrated a net reorientation of some water populations at the surface. As the study was performed at a single pH, that of CO_2 equilibrated water, the reversal was found to be completely induced by ions. The obtained surface spectra were similar when a calculated surface potential was used, rather than the measured zeta potential, the implications of which were discussed.

Chapter 4 aims to dissect the surface water contribution from the total SFG signal at the silica/water interface from high to low pH. Using the same methodology as Chapter 3, the phase information of the intensity spectra were obtained. However, because of silanol dissociation over the pH range studied, the underlying assumption of an unchanging surface does not hold between any of the pH points studied. Therefore the diffuse layer spectrum from Chapter 3 was used, along with the measured zeta potentials over the pH range, to extract the surface contributions. A net

reorientation of surface waters contributing to lower wavenumbers was again observed. The trend in surface water alignment was found to mirror the pH dependent behaviour of other properties of silica such as solubility and aggregation rate. A model was suggested to explain the observed spectral behaviour which involves the increasing number of charged siloxides.

Chapter 5 is a study on the behaviour of the silica/water interface in the presence of acetonitrile with increasing pH. This interface is common in hydrophilic interaction chromatography, however, it becomes difficult to predict retention times at high pH. The methyl, water, and nitrile stretching regions were measured using SFG. As pH was increased, a sudden drop in aligned acetonitrile molecules was observed. Through orientation analysis, it was determined the drop in acetonitrile signal was not due do a reorientation, but rather a displacement of acetonitrile molecules from the surface. The displacement was suggested to result from a silica preference of water over acetonitrile at high pH. These observations may shed light on the retention times observed in hydrophilic interaction chromatography at high pH. Furthermore, the increase in signal of the water stretching region supported this claim.

Chapter 6 is the conclusion to this thesis. Areas of future work regarding the silica/water interface are discussed. Some of the author's perspectives regarding data collection and analysis are given.

Chapter 2

New Insights into $\chi^{(3)}$ Measurements: Comparing Nonresonant Second Harmonic Generation and Resonant Sum Frequency Generation at the Silica/Aqueous Electrolyte Interface

"*New Insights into $\chi^{(3)}$ Measurements: Comparing Nonresonant Second Harmonic Generation and Resonant Sum Frequency Generation at the Silica/Aqueous Electrolyte Interface*" **Rehl, B.**; Rashwan, M.; DeWalt-Kerian, E. L.; Jarisz, T. A.; Darlington, A. M. Hore, D. K.; Gibbs, J. M. *J. Phys. Chem. C* **2019**, *123*, 10991-11000.

2.1 Introduction

Nonlinear optical techniques (NLO) such as second harmonic generation (SHG) and sum frequency generation (SFG) are powerful methods for studying buried interfaces due to their surface specificity.[148-151] These techniques have been used to enhance understanding of dielectric interfaces such as mineral oxides in contact with water.[44, 141, 143, 147, 152] Silica, one such mineral oxide, is one of the most abundant minerals in the Earth's crust and for this reason receives a tremendous amount of attention.[1] As such, nonresonant SHG and vibrational SFG have both been utilized to probe the silica/water interface in the presence of different ions[19, 80, 115-118, 121-125] and at different pH.[59-60, 73, 81-82, 119, 134] These studies have revealed that silica is able to affect the order, alignment, and structuring of water molecules due to both electrostatic interactions between the water and charged siloxide sites at the surface that dominate above pH 2 and hydrogen-bonding interactions between water and surface sites.[59-60]

The sensitivity of nonresonant SHG to the presence of surface charges on mineral oxides was first proposed by Eisenthal and co-workers in their seminal paper in 1992.[59] These early studies were conducted at the silica/aqueous electrolyte interface and suggested that the nonresonant second harmonic signal intensity could be explained by the alignment or polarization of water molecules interacting with an interfacial potential (Φ_0) that originated from the charged silica surface. As such, a new $\chi^{(3)}$ model of SHG was invoked where the electric field oscillating at the second harmonic frequency ($E_{2\omega}$) could be related both to the second-order nonlinear susceptibility $\chi^{(2)}$ and the product of the third-order susceptibility $\chi^{(3)}$ and the interfacial potential Φ_0 according to:

$$E_{\omega_1+\omega_2} \propto \chi^{(2)} E_{\omega_1} E_{\omega_2} + \frac{\kappa}{\sqrt{\kappa^2+(\Delta k_z)^2}} e^{i\varphi} \chi^{(3)} E_{\omega_1} E_{\omega_2} \Phi_0 \quad (2.1)$$

E_{ω_1} and E_{ω_2} are the incident electric fields from the laser source oscillating at frequencies ω_1 and ω_2, respectively, and SHG describes the specific case when $\omega_1 = \omega_2$. Equation 2.1 also reveals the dependence of the relative phase of $\chi^{(2)}$ and $\chi^{(3)}$ on the salt concentration owing to the relationship between the ionic strength and the Debye length. Here κ is the inverse of the Debye screening length, Δk_z is the inverse of the coherence length, and φ is the $\chi^{(3)}$ phase angle described by $\varphi = \tan^{-1}(\Delta k_z/\kappa)$.[101, 105, 107-110, 127] In nonresonant SHG where neither the incident light frequency nor the SH frequency are on resonance with any electronic or vibrational transition, $\chi^{(2)}$ contains contributions from every molecular species that is non-centrosymmetrically assembled at the silica/water interface. In contrast, $\chi^{(3)}$ describes only the contributions of water based on interactions with the interfacial potential Φ_0.[59]

In the original experiments by Eisenthal and co-workers at the silica/aqueous electrolyte interface the pH was varied from pH 2 to pH 14, and the magnitude of the SHG signal was found to be smallest at pH 2.[59] This low pH corresponded to the expected point of zero charge (PZC) of silica that would result in an interfacial potential of zero. Therefore, the authors proposed that at pH 2 the contribution from the $\chi^{(3)}\Phi_0$ term was zero and the signal stemmed from $\chi^{(2)}$, which was assumed to be independent of potential.[59] Moreover, as the SHG intensity was very low at pH 2, the authors concluded the intrinsic $\chi^{(2)}$ response of the silica/aqueous salt interface was small and not important in the discussion of the pH-dependent behaviour at intermediate and high pH.[59] Increasing the pH from 2 to ~14 led to significant changes in signal intensity (150 fold increase), which the authors attributed to an increase in SH response from water molecules based on interactions between the water and the surface potential as a result of the increasingly negative surface.[59] This argument that pH-dependent trends in SHG intensity originated from the interaction of the surface potential (or surface static field) with water (i.e. the $\chi^{(3)}$ term) was subsequently used

in a significant amount of NLO studies on charged surfaces including silica,[119, 121-123, 138, 153-155] alumina,[156-157] and titania.[158]

The $\chi^{(3)}$ method has also been used to describe another second-order nonlinear optical process, vibrational SFG, for various charged interfaces.[19, 92, 107-108, 124, 134, 143, 145, 159-161] The expressions for the SFG intensity are very similar as SFG has the same symmetry requirement of a non-centrosymmetric system as nonresonant SHG (equation 2.1). For vibrational SFG of water, ω_1 corresponds to visible light (λ = 800 nm) and ω_2 is in the infrared such that the IR electric field is on resonance with the O-H stretch of water, thereby reporting specifically on water aligned near the surface.[159-161] Therefore, for vibrational SFG both $\chi^{(2)}$ and $\chi^{(3)}$ originate exclusively from water unlike nonresonant SHG that could theoretically depend on other interfacial species. Nevertheless, nonresonant SHG is generally thought to report mainly on the amount of ordered or polarized water owing to the apparently small contribution from the neutral silica surface (at pH 2) in the original Eisenthal experiments.[143, 145]

Despite the general understanding that both techniques are influenced by the amount of net ordered water, inconsistencies between SHG and SFG have arisen when comparing experiments on silica at high electrolyte concentrations.[19, 60, 99] As mentioned, in the original nonresonant SHG experiments at the silica/water interface $\chi^{(2)}$ was assumed to be small[59] and in all SHG studies at this interface the pH dependent trend only decreased from high to low pH,[59, 121-122, 138-139] while resonant SFG experiments at the same interface exhibited non-monotonic behaviour.[19, 60, 99] If interference between $\chi^{(2)}$ and $\chi^{(3)}\Phi$ is invoked to explain this difference as was applied in studies of interfacial water on alumina,[156-157, 162-163] titania,[158, 164] LB thin films,[165-166] and polymer particles,[167] then SHG intensity should also display non-monotonic pH-dependent behaviour since $\chi^{(2)}$ at the silica/water interface was assumed to be small, yet it does not.

To address the question of whether SHG and SFG both primarily measure water at the silica/water interface, which lies at the heart of the original description of the $\chi^{(3)}$ method, here we compare the nonresonant SHG from the silica/water interface in the presence of 0.5 M NaCl with resonantly enhanced SFG using different polarization combinations. At this high salt concentration, we demonstrate that the pH-dependent trends observed for the two techniques exhibit distinct dissimilarities below ~pH 6 and postulate three possible causes for the differences observed. These postulates provide a new framework for considering the origin of both non-resonant SHG and resonant SFG and how each measurement relates to the amount of net ordered water at the silica interface.

2.2 Experimental Section

2.2.1 Laser Assembly – Sum Frequency Generation

Our regeneratively amplified laser (Spectra-Physics, Spitfire Pro, 1kHz, 120fs, 3.3W) is seeded and pumped, respectively, by a Ti-sapphire oscillator (Spectra-Physics, Maitai, 80 MHz) and a Nd:YLF laser (Spectra-Physics, Empower) to produce 800 nm light. This light is passed through a 30/70 beam splitter to direct 2.3 W to pump a noncollinear optical parametric amplifier (TOPAS-C/NDFG, Light Conversion) to generate tunable, broadband IR light (FWHM ~ 120 cm^{-1}). A filter is used to remove any signal and idler from the OPA from the IR beam which is then passed through a zero-order, tunable half-wave plate (Alphalas), a CaF_2 focusing lens (focal length = 500 mm, Thorlabs), and a polarizer (Thorlabs, LPMIR050-MP2) before reaching the sample. The remaining 1.0 W of 800 nm light from the Spitfire Pro was passed through an air-spaced Fabry-Perot Etalon (TecOptics) to generate narrow picosecond pulses (FWHM ~ 10 cm^{-1}). The

visible light is then passed through a polarizer (Thorlabs, LPVIS050-MP2), a zero-order half-wave plate (Thorlabs, λ/2 @ 808 nm), and a BK7 focusing lens (focal length = 500 mm, Thorlabs) before reaching the sample. The visible beam (10-20 μJ/pulse) and IR beam (~14 μJ/pulse) were directed at the sample, an IR-grade fused quartz hemisphere (Almaz Optics, IR grade fused quartz (KI), 25.4 mm diameter), at incident angles of 61° and 67° with respect to the surface normal, respectively, and slightly defocused to avoid beam-induced sample damage. These two beams were spatially and temporally overlapped at the sample interface to generate the sum frequency light. The SFG reflection beam was passed through a BK7 recollimating lens (focal length = 400 mm, Thorlabs), a polarizer (Thorlabs), a BK7 focusing lens (focal length = 100 mm, Thorlabs) and a filter (Thorlabs, FES0750) to remove any residual visible light before entering a spectrograph (Acton SP-2556 imaging spectrograph, grating: 1200 grooves/mm and 500 nm blaze wavelength) connected to a thermoelectrically cooled (-75 °C), back-illuminated, charge-coupled device camera (Acton PIXIS 100B CCD digital camera system, 1340 x 100 pixels, 20 μm x 20 μm pixel size, Princeton Instruments).

2.2.2 Laser Assembly – Second Harmonic Generation

The beam from a Ti-Sapphire oscillator (Spectra-Physics, Maitai, 80 MHz, 350 mW average power) was passed through a Glan-Thompson polarizer (B. Halle, UV-grade calcite, PGT 4.10), a half-wave plate (Thorlabs, λ/2 @ 400 – 800 nm) and finally a BK7 focusing lens (Thorlabs, focal length = 100 mm) directed at our sample at an incident angle of 60°, with respect to the surface normal. The reflected SHG was passed through, a BK7 recollimating lens (Thorlabs, focal length = 100 mm), a filter (Thorlabs, FB400-40, CWL = 400 nm, FWHM = 40 nm) to remove residual 800 nm light, a focusing lens, and a Glan Thompson polarizer (B. Halle) before entering

a monochromator (Optometrics, Corp, Mini-Chrom MC1-02) and a photomultiplier tube (Hamamatsu Photonics). The electrical response from the PMT was amplified and counted by a gated photon counter (Stanford Research Systems). The wavelength and quadratic power dependence of the SHG signal was verified prior to each experiment.

2.2.3 Materials

NaCl (99.99%, Alfa Aesar) was used to prepare salt solutions. NaOH (99.99%, Sigma-Aldrich) and HCl (trace metal grade, Fisher Chemical) were used to adjust pH. Sulfuric acid (95.0 – 98.0%, Caledon Laboratories) and hydrogen peroxide (30% w/w in H_2O, Sigma-Aldrich) were mixed in 3:1 or 4:1 ratios and used for piranha cleaning. All materials were used without further purification. Ultrapure deionized water (18.2 MΩ•cm) was used after deionization from a milli-Q-Plus ultrapure water purification system (Millipore). All experiments were performed with freshly prepared solutions.

2.2.4 Sample Preparation

Prior to each experiment, an IR-grade fused silica hemisphere (Almaz Optics, 1-inch diameter) was washed and sonicated (5 min) and washed again in ultrapure water. The hemisphere was immersed in piranha solution (3:1 or 4:1 mixture of H_2SO_4 and H_2O_2, 1 hour) and then rinsed thoroughly with ultrapure water. The hemisphere was then subjected to four rinse/sonication (5 min) cycles with ultrapure water before drying in an oven at 110°C (30 min). NaCl (1.461g) was dissolved in ultrapure water (50 mL) to yield a 500 mM NaCl solution. This salt solution was used to prepare acidic and basic solutions by the addition of HCl and NaOH, respectively, for the

adjustment of solution pH. Strongly acidic salt solution was prepared by dissolving NaCl (0.5844g) in ultrapure water (10 mL) followed by the addition of concentrated HCl (34-37%, 10 mL). Fresh solutions was prepared prior to each experiment. The fused silica hemisphere was removed from the oven and immediately mounted on a custom-built Teflon cell with the flat side of the silica perpendicular to the laser table and in contact with the sample solution. The top of the Teflon cell was exposed to allow for the adjustment of solution pH. A pH probe (Orion^{TM} ROSS Ultra^{TM} Low Maintenance pH/ATC Triode^{TM} combination electrode, 8107UWMMD) was inserted into the exposed opening and used to measure the pH of the solution while adjusting the solution pH and only until a stable pH reading was achieved in order to minimize the effect of probe leakage. The exposed opening was covered with a clean, glass slide while the probe was not inserted into the cell.

2.2.5.1 SHG Experiments

A freshly cleaned, oven-dried, fused silica hemisphere was mounted to the sample cell and the laser was aligned to the SHG response from the silica/air interface and SHG was collected. The cell was filled with ultrapure water and the sample was allowed to equilibrate for 30 min before collecting SHG. The water was replaced with 500 mM NaCl solution (pH 5.8) and allowed to equilibrate for 15 min before collecting SHG. The pH of the solution was adjusted with acidic or basic solutions made from the freshly prepared stock salt solution. The reported SHG signal was the average intensity of 60 measurements (2 second collection per measurement) after the 5 minutes of equilibration. For very low solution pH, the already acidic solution (pH ~0) was replaced with a strongly acidic salt solution (pH < 0) and the sample was allowed to equilibrate for 30 min before collecting SHG. SHG was collected in p-in, p-out (ppp) and s-in, p-out (pss)

polarization combinations. Intensities were corrected for local field effects and normalized to each experiment's silica/500 mM NaCl intensity at initial pH (pH ~5.8). Solution pH values were measured immediately after equilibration before both ppp and pss polarization combinations. The SHG counts per second and solution pH over time are provided for a representative high and low pH titration (Figure 2.1). The high pH titration depicts the measured counts per second from the silica/air (0 seconds), silica/water (560 seconds), and silica/$NaCl_{(aq)}$ (2430 seconds) interfaces. The low pH titration depicts only the measured counts per second for the silica/$NaCl_{(aq)}$ interface for simplicity.

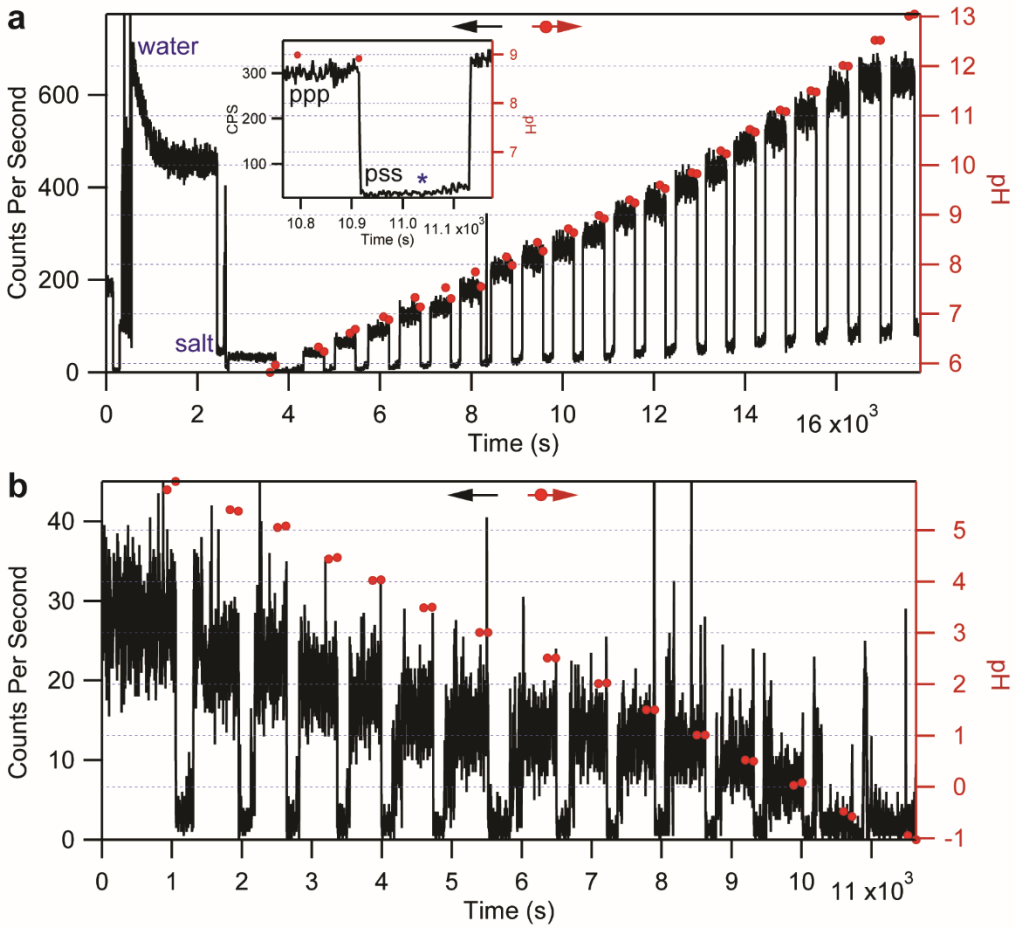

Figure 2.1 SHG counts per second (black lines) and solution pH (red circles) over time for a representative (a) high and (b) low pH titration. SHG was measured in both ppp (larger values)

and pss (smaller values) polarization combinations for a given pH. Inset: Expanded view to highlight intensity change upon pH adjustment (blue asterisk).

2.2.5.2 Notes on Experimental Differences Between the Current and Previous SHG Studies

Some of the SHG intensity trends of the current study were found to be different from what we had previously observed.[121-123, 139] In the current study the SHG intensity decreased to ~45 % its value at pH 5.8 when we lowered the pH to 2, where previously it had decreased to ~15 % of its value at pH 5.8 when we lowered the pH to 2. Additionally we did not observe a striking bimodal feature centred around pH 6, rather a very minor plateau (if any) was observed around pH 8. We take note of this study's method of pH adjustment because it was different than in previous experiments in which the pH was adjusted in slightly smaller increments and data collection began as soon as the pH reading stabilized.[121-123, 139] In the current work the pH was adjusted in slightly larger increments and continually adjusted until the pH reading was stable and did not drift, afterwards the sample was allowed to equilibrate for 5 min before collecting SHG. In more detail, for the current study the pH was adjusted until the reading stabilized with a drift of no more than ~0.01 pH points per several seconds and then allowed to equilibrate for 5 minutes. We deemed this method of pH adjustment necessary in order to make the comparison to SFG due to the long measurement times at a single pH value. Additionally, the starting pH was not manually preadjusted to pH 7 prior to the experiment, rather, the solution's natural starting pH of ~5.8 was used. The solution was never adjusted in the reverse direction (i.e. acid was never added to a base titration and base was never added to an acid titration). Furthermore, the pH probe used to measure solution pH was only left in solution until a stable, reading (of minimal drift) was achieved and then removed and stored in excess 500 mM NaCl stock salt solution to prevent sample

contamination from the probe electrolyte solution, whereas in previous work the probe was allowed to sit in solution for the durations of the entire experiment. Finally, a clean glass slide was used to cover the opening of the cell while the pH probe was not inserted to help minimize interaction with CO_2.

2.2.6 SFG Experiments

A gold-coated fused silica hemisphere (IR-grade) was mounted to the sample cell and used to align the laser and optimize the SFG response before collecting a set of gold reference spectra at ~2900 cm^{-1}, ~3000 cm^{-1}, ~3100 cm^{-1}, ~3200 cm^{-1}, ~3300 cm^{-1}, and ~3400 cm^{-1}. These six frequencies were used to measure SFG at all interfaces and solution pH values. Measured wavenumbers were calibrated through the use of a polysterene reference by passing the IR beam through a polystyrene film, collecting a reference spectrum from the gold/air interface, and comparing the measured SF wavenumbers to the known polystyrene aromatic C-H absorptions at 3026 cm^{-1}, 3059 cm^{-1}, and 3081 cm^{-1}. The gold-coated hemisphere was then replaced with a freshly cleaned, oven-dried, fused silica hemisphere and SFG from the silica/air interface was collected. The remainder of the experiment was carried out in the same manner as SHG following filling the cell with ultrapure water. SFG was collected in ppp, pss and ssp polarization combinations (for example pss denotes p-polarized sum frequency light, s-polarized visible light, and s-polarized IR light, respectively). Sample spectra were acquired for 30s for ppp and 120s for ssp and pss polarization combinations, while gold reference spectra were collected over 1s acquisition times. Background spectra were collected by blocking the IR beam before reaching the sample which were then subtracted from the raw gold reference and sample spectra. The background corrected spectra from the sample were then divided by the background corrected gold reference spectra and

plotted against the IR wavenumbers used. These processed spectra were then integrated from 2850 to 3550 cm^{-1} and normalized to the integrated value at initial pH (pH ~5.8). A set of high and low pH titration spectra were then normalized to the maximum intensity at high pH. Data were analyzed using the software Igor Pro 7.05. The spectra shown in the figures are representative of at least two experiments.

2.2.7 Molecular simulations

As we are interested in evaluating the relative population of 3200 cm^{-1} and 3400 cm^{-1} intensity in the SFG spectra, we have performed molecular dynamics simulations of water next to an uncharged hydrophilic interface. A 3.945 nm × 3.796 nm surface was created from a base layer of 10 OPLS/AA methylene united atoms in a hexagonal array (a = 0.438 nm, c = 0.160 nm lattice constants) terminated with an OH group oriented 71.5º from the normal with random azimuth. 100% of the surface sites have an OH group, resulting in a hydroxyl density of 0.0415 nm^{-2}. We have taken care to equilibrate a large enough system to ensure a bulk water density of 1.0 g/mL in the centre of our 10 nm deep box. The resulting density profile and distance-dependent order parameters show significant structuring up to approximately 1 nm into the aqueous phase.[91] 1980 SPC/E water molecules were then added to a total box depth of 10 nm. GROMACS 4.5.5 was used to run the simulations, employing Berendsen temperature coupling at 300 K, three-dimensional periodic boundary conditions, van der Waals interactions cut at 1.2 nm, PME electrostatic interactions with a real-space equivalent cut-off of 1.2 nm. Following energy minimization and equilibration, one out of every 50 frames were sampled from a 10 million frame trajectory with a timestep of 1 fs to yield 200 000 snapshots for analysis, recording Cartesian coordinate and force data. Following the instantaneous normal mode approach developed by Morita and Hynes, the net

force along each OH bond was determined. This was then mapped onto a result parameterized from previous electronic structure calculations[77] to arrive at the uncoupled OH stretching frequencies of the hydrogen-bonding environment specific to each OH oscillator. The two OH frequencies were then coupled to arrive at the low- and high- energy eigenmodes, analogous to the symmetric and antisymmetric modes in gas-phase spectra. We then consider any species whose low energy mode fell into the 3150–3250 cm^{-1} window to be associated with the 3200 cm^{-1} intensity, and species in the 3350–3450 cm^{-1} region as belonging to the 3400 cm^{-1} peak. This enabled comparison of populations in these two distinct spectral regions, irrespective of the associated hyperpolarizability values or the contributing molecular orientations.

2.3 Results and Discussion

2.3.1 Local Field Effects at the Silica/Water and Silica/Air Interfaces

In order to make a meaningful comparison between resonant sum frequency generation and nonresonant second harmonic generation at various interfaces, we corrected the intensities for local field effects. This correction is particularly important for the comparisons made between the silica/water and silica/air interfaces. The correction involves the Fresnel coefficients which are calculated according to the following equations:[57]

$$L_{XX}(\omega_i) = \frac{2n_1(\omega_i)\cos\gamma_i}{n_1(\omega_i)\cos\gamma_i + n_2(\omega_i)\cos\alpha_i}, \tag{2.2}$$

$$L_{YY}(\omega_i) = \frac{2n_1(\omega_i)\cos\alpha_i}{n_1(\omega_i)\cos\alpha_i + n_2(\omega_i)\cos\gamma_i}, \tag{2.3}$$

$$L_{ZZ}(\omega_i) = \frac{2n_2(\omega_i)\cos\alpha_i}{n_1(\omega_i)\cos\gamma_i + n_2(\omega_i)\cos\alpha_i}\left(\frac{n_1(\omega_i)}{n'(\omega_i)}\right)^2, \tag{2.4}$$

where n_1, n_2, and n' are the frequency dependent refractive indices of fused silica, water (or air), and the interfacial layer, respectively. The angles of incidence/reflection are given by α_i (i = SFG, visible, and IR) and the angles of refraction are given by γ_i (i = SFG, visible, and IR) which are calculated using Snell's Law. These Fresnel coefficients are then used to calculate the nonzero tensor elements according to the following equations assuming a rotationally isotropic surface of $C_{\infty v}$ symmetry:[57]

$$\chi_{eff}^{(2),ssp} = L_{YY}(\omega_{SFG})L_{YY}(\omega_{Vis})L_{ZZ}(\omega_{IR}) \sin\alpha_{IR}\, \chi_{XXZ}^{(2)}, \tag{2.5}$$

$$\chi_{eff}^{(2),pss} = L_{ZZ}(\omega_{SFG})L_{YY}(\omega_{Vis})L_{YY}(\omega_{IR}) \sin\alpha_{SFG}\, \chi_{ZXX}^{(2)}, \tag{2.6}$$

$$\begin{aligned}\chi_{eff}^{(2),ppp} = {} & -L_{XX}(\omega_{SFG})L_{XX}(\omega_{Vis})L_{ZZ}(\omega_{IR}) \cos\alpha_{SFG} \cos\alpha_{Vis} \sin\alpha_{IR}\, \chi_{XXZ}^{(2)} \\ & -L_{XX}(\omega_{SFG})L_{ZZ}(\omega_{Vis})L_{XX}(\omega_{IR}) \cos\alpha_{SFG} \sin\alpha_{Vis} \cos\alpha_{IR}\, \chi_{XZX}^{(2)} \\ & +L_{ZZ}(\omega_{SFG})L_{XX}(\omega_{Vis})L_{XX}(\omega_{IR}) \sin\alpha_{SFG} \cos\alpha_{Vis} \cos\alpha_{IR}\, \chi_{ZXX}^{(2)} \\ & +L_{ZZ}(\omega_{SFG})L_{ZZ}(\omega_{Vis})L_{ZZ}(\omega_{IR}) \sin\alpha_{SFG} \sin\alpha_{Vis} \sin\alpha_{IR}\, \chi_{ZZZ}^{(2)}.\end{aligned} \tag{2.7}$$

The effective tensor elements are calculated from the intensities based on the following equation:[57]

$$I(\omega_{SFG}) = \frac{8\pi^3\omega_{SFG}^2 \sec^2\alpha_{SFG}}{c^3 n_1(\omega_{SFG}) n_1(\omega_{Vis}) n_1(\omega_{IR})} \left|\chi_{eff}^{(2)}\right|^2 I(\omega_{Vis}) I(\omega_{IR}), \tag{2.8}$$

where ω_{SFG} is the frequency of the sum frequency light, c is the speed of light in a vacuum, and $I(\omega_{SFG})$ is the frequency-dependent beam intensity. The prefactor of equation 2.8, $\frac{8\pi^3\omega_{SFG}^2 \sec^2\alpha_{SFG}}{c^3 n_1(\omega_{SFG}) n_1(\omega_{Vis}) n_1(\omega_{IR})}$, and the intensities of the visible and infrared beams are accounted for by

normalizing the sample spectra (silica/water or silica/air) to that of the strong nonresonant of silica/gold. After normalization, equation 2.8 is reduced to

$$I'(\omega_{SFG}) = \left|\chi_{eff}^{(2)}\right|^2, \tag{2.9}$$

where $I'(\omega_{SFG})$ are the arbitrary units obtained after dividing $I\left(\omega_{SFG_{sample}}\right)$ by $I\left(\omega_{SFG_{gold}}\right)$. For simplicity, we refer to $I'(\omega_{SFG})$ simply as the intensity, or $I(\omega_{SFG})$. The refractive indices of silica, n_1, for the visible wavelength (800 nm) was 1.453, while for the IR and SFG wavelengths were calculated using the Sellmeier equation with coefficients of $B_1 = 0.696$, $B_2 = 0.408$, $B_3 = 0.897$, $C_1 = 0.00468$, $C_2 = 0.0135$, and $C_3 = 97.93$. The refractive indices of water, n_2, for the visible and SFG wavelengths were 1.33, while for the IR wavelengths those measured by Segelstein[168] were used. The refractive index of air was 1.00 for all wavelengths used. The interfacial refractive index, n', was approximated to be 1.4 for the silica/water interface[73] and 1.23 for silica/air interface. As we chose frequency-independent values for n', and since we normalized integrated SFG intensities and SHG intensities to the same pH, the exact values used will not affect the comparison between the two techniques. However, a comparison between the silica/air and silica/water interfaces may be affected by our choice of n' values.

The effect of correcting SFG spectra for local field effects in ppp, ssp, and pss polarization combinations can be seen in Figures 2.2, 2.3, and 2.4, respectively.

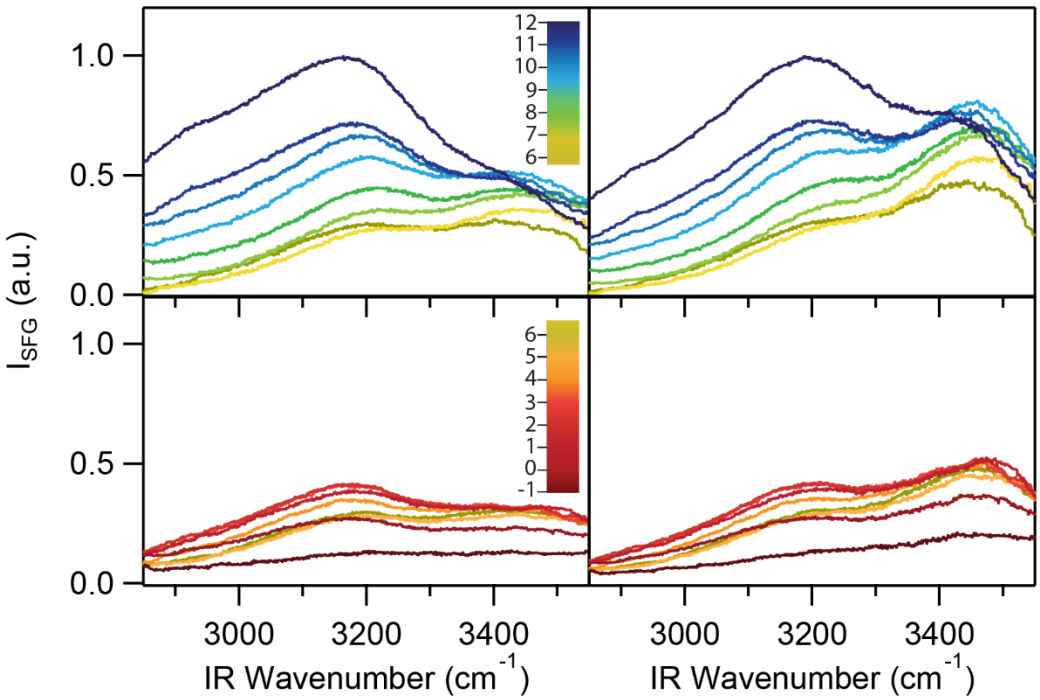

Figure 2.2 ppp-SFG spectra from 2850 – 3550 cm^{-1} measured at the silica/water interface at 500 mM NaCl over a pH range of 5.8 to 12 (top panel) and 5.8 to below 0 (bottom panel). Spectra are compared without local field corrections (left) and with local field corrections (right). Intensities are normalized to the maximum at high pH. Reprinted with permission from Gibbs and coworkers,[169] Copyright 2019 American Chemical Society.

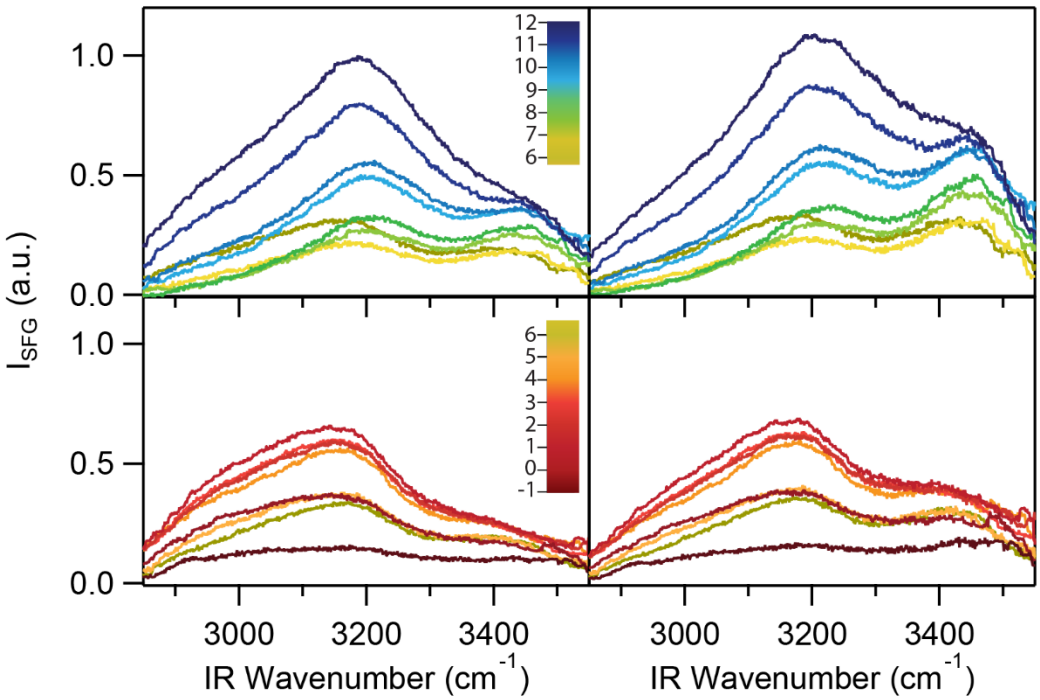

Figure 2.3 ssp-SFG spectra from 2850 – 3550 cm^{-1} measured at the silica/water interface at 500 mM NaCl over a pH range of 5.8 to 12 (top panel) and 5.8 to below 0 (bottom panel). Spectra are compared without local field corrections (left) and with local field corrections (right). Intensities are normalized to the maximum at high pH. Reprinted with permission from Gibbs and coworkers,[169] Copyright 2019 American Chemical Society.

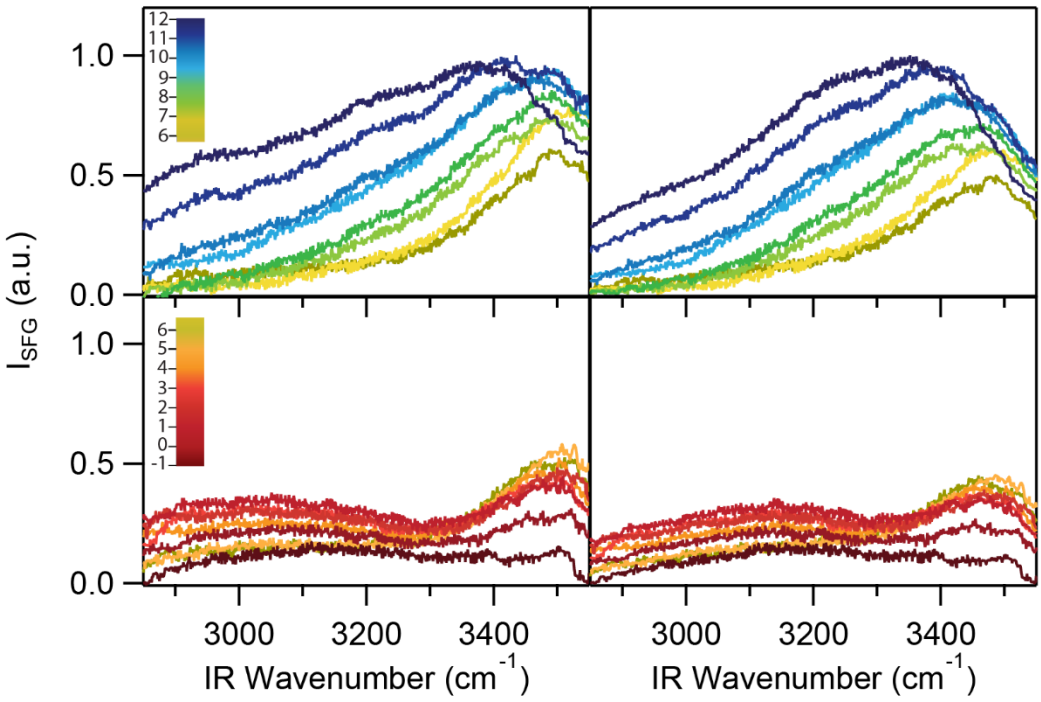

Figure 2.4 pss-SFG spectra from 2850 – 3550 cm^{-1} measured at the silica/water interface at 500 mM NaCl over a pH range of 5.8 to 12 (top panel) and 5.8 to below 0 (bottom panel). Spectra are compared without local field corrections (left) and with local field corrections (right). Intensities are normalized to the maximum at high pH. Reprinted with permission from Gibbs and coworkers,[169] Copyright 2019 American Chemical Society.

2.3.2 Sum Frequency and Second Harmonic Generation at the Silica/Water Interface in the Presence of 500 mM NaCl Over the pH Range of 2-12

Figure 2.5a illustrates the *ssp*-SFG spectra (s-polarized SFG, s-polarized E_{ω_1} (E_{VIS}), p-polarized E_{ω_2} (E_{IR})) at the silica/aqueous sodium chloride interface (500 mM) from pH 0 that lies below the point of zero charge of silica, to pH 12 where silica is very negatively charged. At this high ionic strength we note two specific effects at the silica/aqueous electrolyte interface: salt

addition is known to induce changes to the surface charge density of silica,[52, 54, 119] and screening of surface charges by sodium cations results in a short Debye length.[23] Given the concentration of NaCl used in this study, the total ionic strength change due to the pH adjustments was small (2% increase from initial pH to either pH 2 or 12) relative to the initial concentration. We also note at this high ionic strength, which corresponds to a short Debye length (~4 Å at 500 mM ionic strength[170]), the phase mismatch term between $\chi^{(2)}$ and $\chi^{(3)}$ shown in equation 2.1 is small (i.e. $\frac{\kappa}{\sqrt{\kappa^2+(\Delta k_z)^2}} = 0.99997$) and the $\chi^{(3)}$ phase angle, φ, is close to zero degrees (0.4°). Therefore we assumed the phase mismatch factor was equal to 1 and φ was equal to 0° for the current analysis. This approximation is consistent with previous vibrational SFG studies that suggested that the phase factor could be ignored for salt concentrations greater than 0.4 M,[94] while for SHG the phase factor only became critical below 1 – 10 mM ionic strength.[107] In order to more closely analyze the pH-dependent trends of the silica/water interface studied by SFG and compare them with nonresonant SHG, the integrated sum frequency signal from 2850 – 3550 cm^{-1} and the second harmonic signal are compared (Figure 2.5b). From the integrated intensities of the SFG we see that the total SF signal exhibited a local minimum at ~ pH 6, consistent with our earlier work,[99] and a local maximum at ~ pH 2, which is the expected point of zero charge.

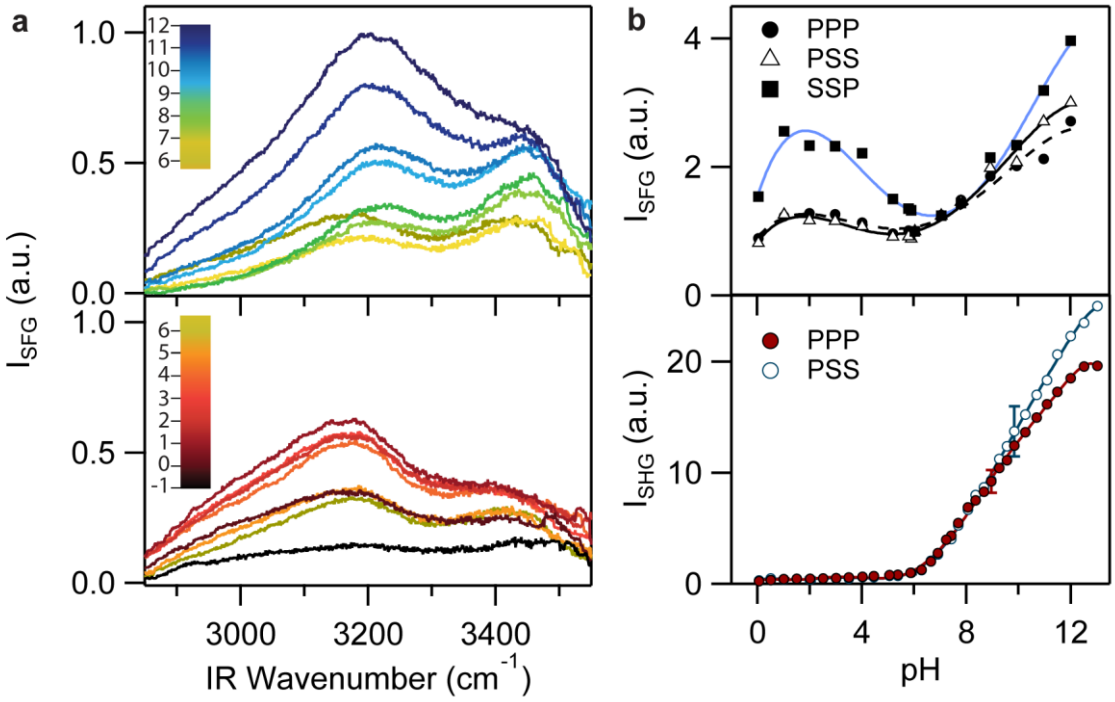

Figure 2.5 (a) ssp-SFG spectra from 2850 – 3550 cm^{-1} measured at the silica/water interface at 500 mM NaCl over a pH range of 5.8 to 12 (top panel) and 5.8 to below 0 (bottom panel). SFG spectra are corrected for local field effects and normalized to maximum intensity at high pH. (b) Integrated SFG intensities at the ssp, pss, and ppp polarization combinations (top) and the SHG intensity at the p-in/p-out (ppp) and s-in/p-out (pss) polarization combinations over the pH range studied. Integrated SFG intensities and SHG intensities are normalized to their values at pH 6. Smooth lines are guides for the eye. Reprinted with permission from Gibbs and coworkers,[169] Copyright 2019 American Chemical Society.

In previous SFG experiments, the non-monotonic trend in water response with varying pH was associated with a flip in water that occurred approximately at the pH where the minimum in SF intensity was observed.[82, 99, 162-164] In our previous work, we had also noted that the low wavenumber region that dominated the ssp and ppp-SFG spectra exhibited the non-monotonic

behaviour while the high wavenumber region did not but decreased systematically with decreasing pH.[99] Our analysis and supporting simulations found that the waters contributing to the low wavenumber range flipped upon decreasing the pH from 12 to 2, whereas those contributing to high wavenumber range did not. In support of this analysis, a change in sign of the imaginary part of the SFG response ($Im\chi^{(2)}$) has been observed only for the low wavenumber region at the silica/water interface upon passing from high to low pH, consistent with flipping of only those corresponding water molecules.[82, 90]

2.3.3 The Effect of Experimental Conditions on the pH Dependent SHG Intensities

However, these non-monotonic intensity trends were never observed for the SHG intensities (Figure 2.5b), which simply decreased in magnitude from high to low pH for both polarization combinations. This general decrease in SHG with decreasing pH is consistent with our previous work[121-122] and that of Eisenthal,[59] yet a distinct bimodal feature (double sigmoid) was formerly observed in these surface titrations. We performed systematic experiments to identify why this was absent in our new observations. To determine the cause of the intensity drop difference at low pH and the absence of an obvious bimodal feature, we systematically tested experimental conditions for their effect on the SHG intensity (Figure 2.6). The conditions we tested, summarized in Table 2.1, were the beam polarizations, salt/acid purity, silica grade, cleaning procedure, and preadjustment of solution pH. The initial conditions included a polarization of s-in/p-out (pss), high purity salts/acids, IR-grade silica, a piranha cleaning procedure, and no pH preadjustment. Removal of the polarizer after the sample (s-in/all-out) resulted in a slightly higher intensity, but not a significant difference in the overall trend. Using lower purity salts and acids caused the signal to drop slightly. Using UV-grade silica, which is known to have a much greater

hydroxide content, caused the signal to drop significantly at low pH. Cleaning the substrate with Nochromix and air plasma instead of piranha solution demonstrated no difference in trend. Finally, preadjusting the solution pH from 5.8 to 7 prior to the experiment resulted in a large drop in intensity at low pH. We note that the method of solution pH preadjustment for the current study follows that described in the experimental section (adjusted until no significant pH drift occurred and then equilibrated for 30 minutes as reactions may be stalled at interfaces[138]), whereas in previous studies the pH was adjusted to an initial value of 7 with no further perturbation and then allowed to equilibrate for 30 minutes resulting in the lower recorded pH (~pH 6.3) as seen in Figure 2.6. In summary, the difference in shape of the SHG pH titration in these experiments appears to arise from the use of IR-grade silica instead of UV-grade silica, as well as the influence of different starting pH owing to hysteresis, which is significant in pH titrations for silica.[44, 139] Nevertheless, for this study, direct comparisons between SHG and SFG can be made as the same samples were used as well as the same experimental procedures.

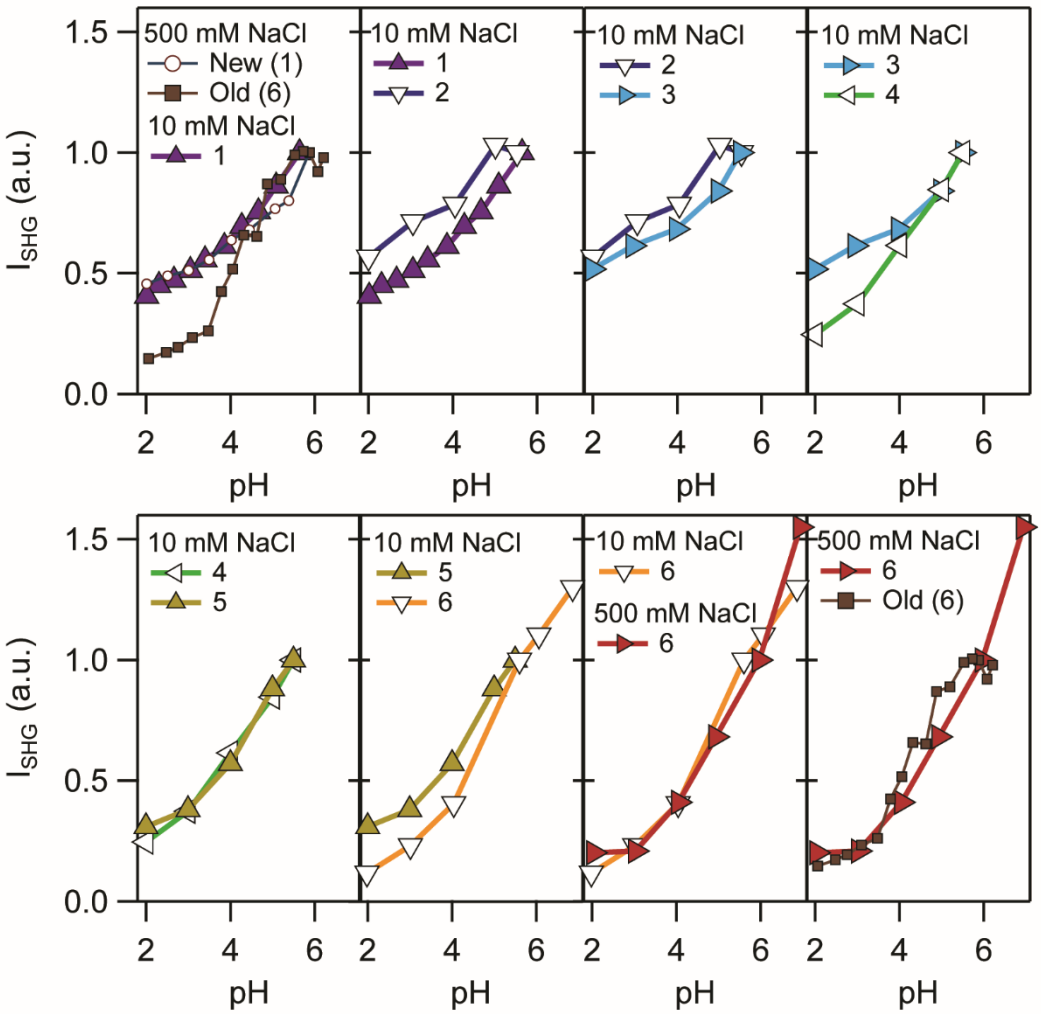

Figure 2.6 pH-Dependent SHG intensities over a pH range of 6 to 2 as a function of changing experimental conditions given by Table 2.1. SHG data from previous work[121] (Old) is contrasted to the SHG data of the current study (New). All SHG intensities are normalized to their respective values at pH 5.8. Adapted with permission from Gibbs and coworkers,[169] Copyright 2019 American Chemical Society.

Table 2.1 Experimental conditions for the SHG experimental investigations of Figure 2.6.

Condition	Polarization	Salt/Acid Purity	Silica Purity	Cleaning Procedure	Initial pH
1	pss	High[a]	IR grade	Piranha	5.8
2	s-in/all-out	High[a]	IR grade	Piranha	5.8
3	s-in/all-out	Low[b]	IR grade	Piranha	5.8
4	s-in/all-out	Low[b]	UV grade	Piranha	5.8
5	s-in/all-out	Low[b]	UV grade	Nochromix/Plasma[c]	5.8
6	s-in/all-out	Low[b]	UV grade	Nochromix/Plasma[c]	7

[a] Trace metal grade 99.99% NaCl (Alfa Aesar). Trace metal grade HCl (Fisher Chemical). [b] ≥ 99.0 % NaCl (Sigma Aldrich). Reagent grade HCl (Caledon Laboratories). [c] The flat surface of the hemisphere was covered in a 5 % (w/v) solution of Nochramix (Godax Laboratories) in H_2SO_4 instead of submersion in piranha. A MeOH rinse/sonication was included before and after Nochramix treatment with additional ultrapure water rinsing/sonication. After drying (110°C) the sample was subjected to plasma cleaning (Harrick Plasma, PDC-32G, 1100 mtorr, 2 min).

2.3.4 The Nonresonant SHG Nonlinear Susceptibility at the Silica/Air Interface and Estimating the SHG Water Response

To determine whether silica contributed significantly to the nonresonant SHG, the second harmonic signal was measured at the silica/air interface and compared with that at the silica/water interface after accounting for the local field effects of the pss polarization combination in both experiments. From this comparison, it is seen that the second harmonic electric field from the silica/air interface equals that of the silica/water interface at pH ~6.5 (Figure 2.7a). Below this pH, we observe greater SHG from the silica/air interface than from the silica/aqueous interface. We cannot state that the $\chi^{(2)}$ of silica in contact with water would be precisely the same as that observed in air; nevertheless it would seem unlikely that such a large signal vanishes entirely upon interaction with water. As the true value of n' is unknown, we calculate the relative SHG response

from the silica/water and silica/air interfaces over a range of n' values (Figure 2.7b). We find that n' values between that of silica and water or that of silica and air lead to a second harmonic electric field from the silica/air interface that is approximately equal to the second harmonic electric field from the silica/$NaCl_{(aq)}$ interface from pH 4 to 7.

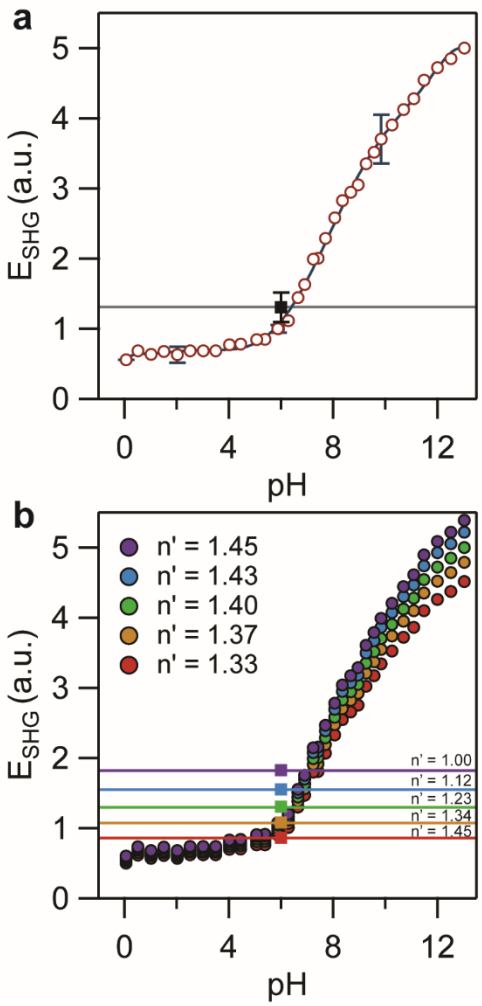

Figure 2.7 (a) Comparison of pss-SHG electric field at the silica/water interface (500 mM NaCl, circles) to the pss-SHG electric field at the silica/air interface (square and horizontal line). Error bars represent the standard deviation between multiple experiments. The smooth line is a guide for the eye. Reprinted with permission from Gibbs and coworkers,[169] Copyright 2019 American

Chemical Society. (b) pss-SHG electric fields calculated with varying values of n' for the silica/water (circles) and silica/air (squares and horizontal lines) interfaces.

Recently, Bonn and coworkers suggested that the SHG signal from the air/membrane monolayer/aqueous interface arose from a convolution of contributions from the water and the membrane surface, with an additional component being hyper-Rayleigh scattering.[166] For a composition of the mixed monolayer that was neutral, the water response was very small according to phase-sensitive ssp-SFG experiments, yet the SHG intensity was substantial. Furthermore, the imaginary component of the SFG response of water changed sign upon transitioning from a negatively charged membrane to a positively charged membrane. Therefore, the authors proposed that $\chi^{(2)}$ stemmed from the SHG response of the membrane which was significant and remained constant with pH while the $\chi^{(3)}\Phi$ term stemmed from the amount of water, which could be determined independently by integrating the ssp-SFG imaginary spectra. At the positively charged interface, $\chi^{(2)}$ from the substrate interfered destructively with the water response manifested in $\chi^{(3)}\Phi$. This destructive interference between the $\chi^{(2)}$ and $\chi^{(3)}\Phi$ terms has also been proposed for SHG measurements at titania[158] and alumina[156-157] surfaces at pH values below the PZC.

To test this SHG model for the silica/aqueous interface where $\chi^{(2)}$ stemmed from the substrate and the $\chi^{(3)}\Phi$ response could be approximated by the integrated ssp-SFG response of water, we first determined the SHG response stemming exclusively from the water. This was achieved by subtracting the square root of the local field corrected SHG intensity at the silica/air interface from the square root of the local field corrected SHG intensity at the silica/aqueous interface. This analysis was based on our approximation of the $\chi^{(3)}$ phase angle to be 0° (or 180°) among all contributing terms (i.e. $\chi^{(2)}_{silica}$, $\chi^{(2)}_{H_2O}$, and $\chi^{(3)}_{H_2O}\Phi_0$). Moreover we assumed that the silica response under water was unchanging with varying pH and equivalent to what was measured

at the silica/air interface. The resulting SH water response should be proportional to $\left|\chi^{(2)}_{H_2O} + \chi^{(3)}_{H_2O}\Phi_0\right|$ (Figure 2.8a). We also include the square root of the integrated SFG intensity after local field corrections, which provides an estimate of the SF water response as it does not take into consideration the non-resonant contribution or interfering modes. To determine how much the intensities varied for the two different measurements, we also squared the SH water response value resulting in the SHG intensity that should stem from water. This value is compared with the integrated SFG intensity after local field corrections for the ssp and pss polarization combinations (Figure 2.8b).

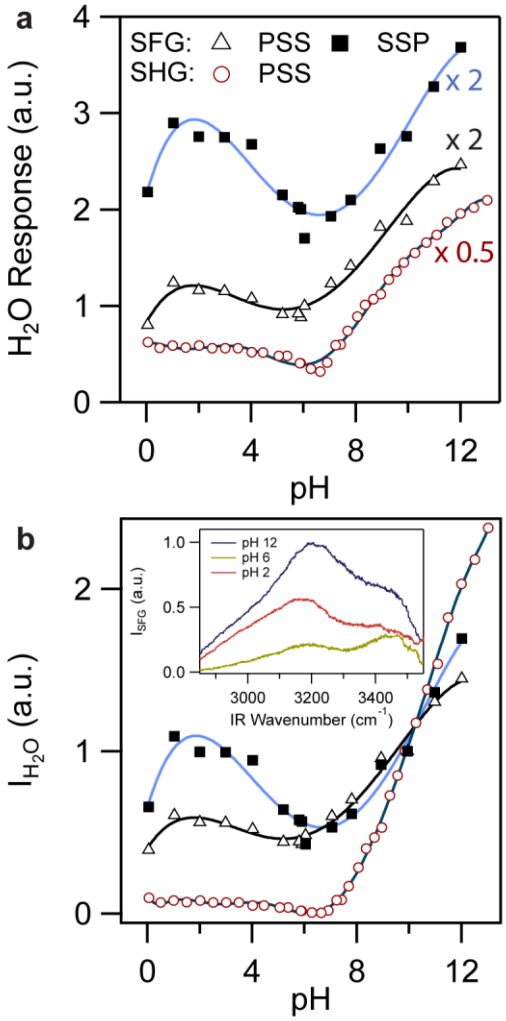

Figure 2.8 (a) The water response proportional to $\left|\chi^{(2)}_{H_2O} + \chi^{(3)}_{H_2O}\Phi_0\right|$ calculated from SHG and integrated SFG. Data are offset and multiplied for clarity. (b) The integrated SFG intensities compared to the square of the second harmonic water response. Intensities are normalized to their values at pH 10. (inset: SFG spectra at the silica/aqueous sodium chloride interface at pH 12, 6, and 2. Smooth lines are guides for the eye). Reprinted with permission from Gibbs and coworkers,[169] Copyright 2019 American Chemical Society.

Firstly, the minimum in the SHG response from water occurred at a pH near the pH were the minimum in the SFG response of water was observed (Figure 2.8a). This observation supports

the Bonn model for interpreting SHG, where the $\chi^{(2)}$ stemmed from the substrate and the $\chi^{(3)}\Phi$ term was captured by the integrated ssp-SFG imaginary spectra of water. Next we compared the minimum in intensity stemming from water for SHG and SFG with both measurements normalized to their respective values at pH 10. For SHG, the water response was zero at the minimum (~pH 7), which is consistent with the SHG from the silica/air interface being greater in magnitude than that measured at lower pH for the silica/aqueous interface (Figure 2.8b). Yet for the SFG, we observed a significant amount of SF response at this pH compared to what was observed at higher and lower pH (Figure 2.8b). Furthermore, the SFG intensity spectrum for the silica/aqueous electrolyte interface at pH 6 exhibited pronounced peaks at 3200 cm^{-1} and 3400 cm^{-1}, suggesting a significant amount of ordered water at this pH (Figure 2.8b, inset). Additionally, the increase in water intensity for ssp-SFG in the low pH region suggested that the amount of aligned water at ~pH 2 was approximately equal to that observed at pH 10 (Figure 2.8b). In contrast, the SHG water intensity at pH 2 was twelve times lower than that at pH 10 indicating that the amount of aligned water contributing to the SHG differed from that contributing to the ssp-SFG. These observations suggested that the differences in SHG and SFG were not completely captured by the SHG from the silica alone and the integrated ssp-SFG spectra, which leads to the second proposed difference in the two measurements.

2.3.5 A Comparison of Dominant Water Modes Measured by Resonant SFG at the Silica/Water Interface

The trend observed by SHG may also be explained by interference between the signals originating from the water populations that primarily contribute to the 3200 cm^{-1} and 3400 cm^{-1} modes in SFG (Figure 2.9). As previously mentioned, phase-sensitive measurements at the

silica/water and silica/HOD interface as a function of pH and at low salt concentration found that the low wavenumber region exhibited a change in sign of $Im(\chi_{eff}^{(2)})$ upon decreasing from pH 12 to 7 to 2, while the high wavenumber region did not.[82, 90] Furthermore, at high pH the $Im(\chi_{eff}^{(2)})$ spectrum was entirely positive whereas at low pH, the low wavenumber region was negative while the high wavenumber region remained positive. We also proposed a flip in orientation of only the water contributing to the low wavenumber region based on our simulations of the SFG response of a hydrophilic surface/water interface and the observed pH dependent trends at both high and low wavenumbers.[99] Additionally, the phase-sensitive measurements on silica revealed that at low pH the water populations were opposite in orientation, which for our experimental conditions should occur below pH 6.5, where the minimum in SFG intensity was observed (Figure 2.9).

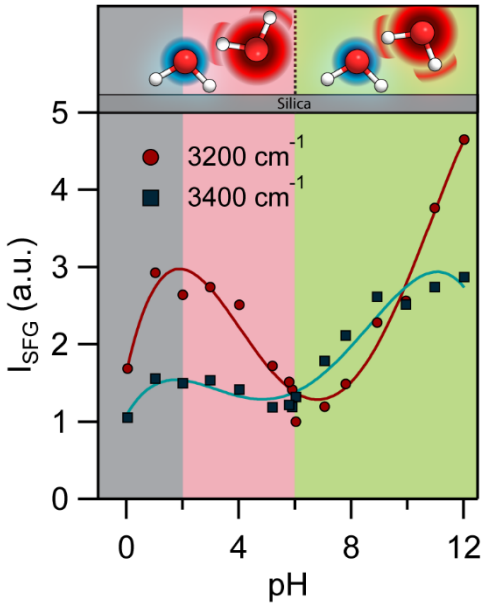

Figure 2.9 Intensities of ssp-SFG at a) 3185 cm^{-1} and b) 3455 cm^{-1} normalized to the intensity at 3185 cm^{-1} measured at pH 6. Green and red shading indicate possible constructive and destructive interference between water populations, respectively. Smooth lines are guides for the eye. Top:

Illustration of flipping water molecules contributing to the low wavenumber region. Reprinted with permission from Gibbs and coworkers,[169] Copyright 2019 American Chemical Society.

As SHG measures the orientational average of all water molecules, cancellation between populations that are oriented in opposite directions could result in lower SHG, unlike SFG which separates populations based on their different resonant OH vibrations. Consequently, even if water assemblies were oppositely oriented they could contribute to the SFG intensity if the assemblies had significant differences in their resonant frequencies, which would be the case for the waters contributing at low (3200 cm^{-1}) and high (3400 cm^{-1}) wavenumber. This scenario would explain why the SHG was much lower in intensity below pH 6.5 than the integrated SFG, as the cancellation of oppositely oriented water populations should occur for the former at lower pH.

2.3.6 Molecular Dynamics Simulations of a Neutral, Hydrophilic Surface in Contact with Water

When integrating the SFG to approximate the amount of ordered water, another underlying assumption is that the orientationally averaged resonant molecular hyperpolarizabilities of the modes contributing at 3200 cm^{-1} ($\langle\beta_{3200}\rangle$) and at 3400 cm^{-1} ($\langle\beta_{3400}\rangle$) are roughly equivalent. Accordingly, the intensity at low and high wavenumber would reflect the number of aligned waters.

To determine whether the SFG activity of waters contributing at low and high wavenumber were roughly equivalent on a per molecule basis, we performed MD simulations of the average molecular hyperpolarizabilities of water in contact with a polar surface and determined the average hyperpolarizability at 3200 cm^{-1} and 3400 cm^{-1}. Although there have been simulations with explicit silica surfaces,[171-173] we have opted for our simplified model hydrophilic surface described in the

experimental section as we have extensively compared its resulting interfacial water structure and generated model SFG spectra from this system[91, 99, 174] in comparison to experimental homodyne and phase-resolved spectra.[72, 82, 90, 100-101] In Figure 2.10a, c and e, we report the log of the ratio of these 3200 cm^{-1} and 3400 cm^{-1} hyperpolarizability per molecule values as a function of twist and tilt angle for ppp, ssp and pss polarization combinations, respectively. Although the log ratio values vary considerably depending on the twist and tilt angle, we see that overall the vast majority of twist and tilt angles lead to log ratio values greater than 0 for the ssp and ppp polarization combinations (Figure 2.10b, and f, respectively), which corresponds to $\langle\beta_{3200}\rangle$ greater than $\langle\beta_{3400}\rangle$. This indicates that the water contributing at 3200 cm^{-1} is intrinsically more SFG active at most twist and tilt angles for the ssp and ppp spectra. Moreover, the simulations of the ssp-SFG found that the 3400 cm^{-1} region contained a greater number of contributing oscillators than the 3200 cm^{-1} region by a factor of 1.8, despite the greater intensity observed at 3200 cm^{-1} and 3400 cm^{-1} in the simulations[91] (which is consistent with the experimental results observed at low pH and low salt concentration[19, 81-82, 90, 99, 164]). These simulations suggest that using the integrated ssp or ppp-SFG spectra to understand the amount of aligned water in the system exaggerates the contributions from water contributing to the low wavenumber region, which are lower in number but greater in SFG activity. In contrast, as SHG is a nonresonant measurement in our experimental configuration, to a first approximation the nonresonant hyperpolarizabilities behind these two resonant features should be the same (in other words we are assuming changes in hydrogen bonding does not substantially change the non-resonant hyperpolarizability of water). As such, SHG should be most sensitive to the total number of water molecules that are aligned by the field unlike SFG, which spectrally resolves the different water populations and is sensitive to their intrinsic SF activity.

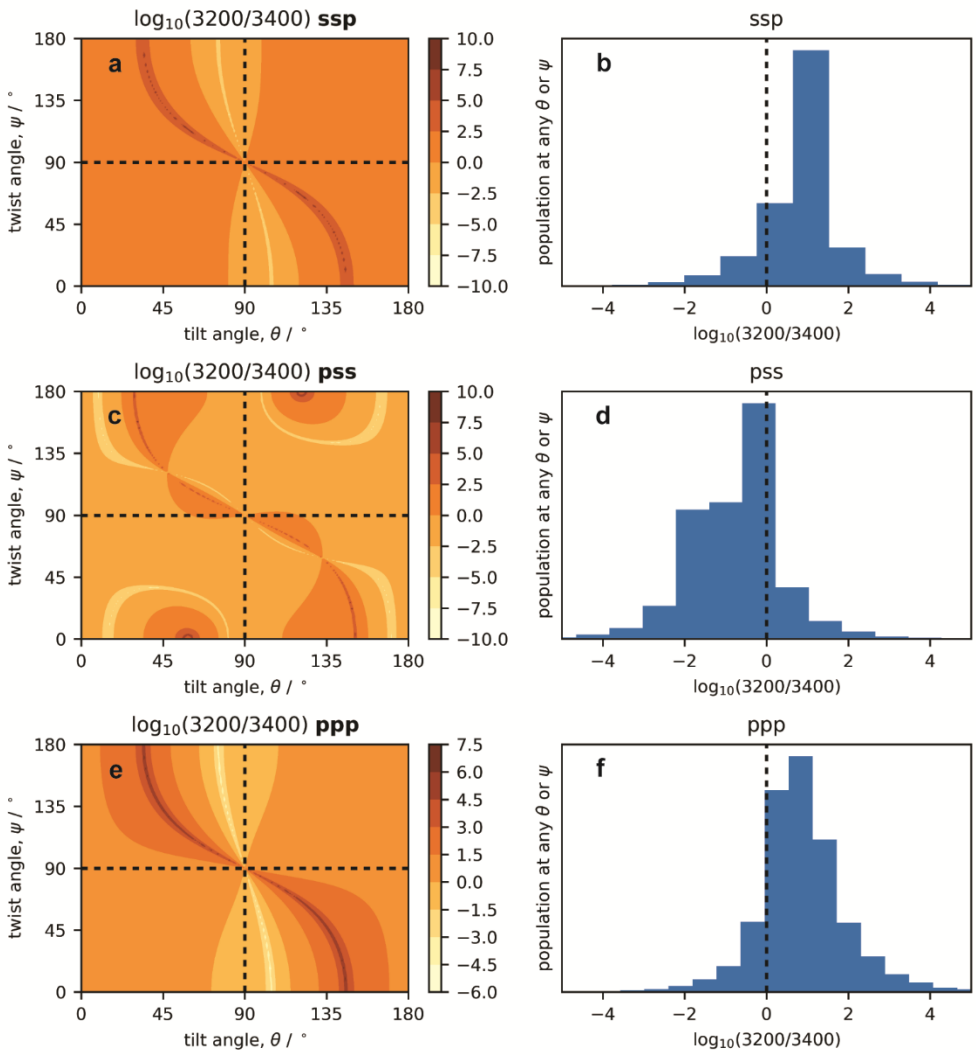

Figure 2.10 Log ratios of β_{3200} and β_{3400} at all possible twist and tilt angles calculated for the (a) ssp, (c) pss and (e) ppp polarization combinations. Histograms of the frequency that each log ratio value occurred in the corresponding twist and tilt maps are shown for the (b) ssp, (d) pss and (f) ppp polarization combinations. Reprinted with permission from Gibbs and coworkers,[169] Copyright 2019 American Chemical Society.

2.4 Conclusion

In summary, the pH dependence of the silica/water interface measured by nonresonant SHG and vibrational SFG exhibit substantial differences. We attribute these differences to three possible origins: 1) the underlying silica substrate contributes significantly to the SH signal but not SFG owing to resonant enhancement of the water for the latter; 2) destructive interference arises in SHG from different populations of oriented water at lower pH that are spectrally resolved in SFG and therefore do not lead to cancellation of signal; and 3) SHG is sensitive to the number density of aligned water whereas SFG is strongly influenced by the different intrinsic SFG activities of water populations experiencing different chemical environments. None of these possibilities are mutually exclusive and several may contribute to the observed differences between measurements performed using SHG and SFG spectroscopy. Nevertheless, from this investigation we propose that care must be taken in using the integrated ssp-SFG or ppp-SFG since the amount of net ordered water in the system contributing to the high wavenumber region of the ssp and ppp-SFG water spectra, which has lower intensity, actually contains the greatest number of aligned water molecules. Furthermore, spectral resolution of SFG allows water populations of opposite orientation to contribute substantial intensity making it difficult to relate the SFG intensity to the net amount of ordered water. With respect to interpreting SHG results, attention must also be paid when interpreting the SHG intensity at the solid/liquid interface as directly proportional to the net amount of aligned water. Specifically, the $\chi^{(2)}$ contribution from the substrate must be known; if the observed signal intensity is lower than that observed for the bare substrate, this suggests destructive interference is occurring between the signal arising from the net alignment of water and that of the substrate. Accordingly, a decreasing signal intensity could be indicative of *more* rather than less aligned water, owing to such destructive interference. In particular, for the mineral

oxide/water interface, destructive interference between the substrate response and that of the net aligned water should be considered when the SHG intensity becomes very small, which for silica occurs at high salt concentration and lower pH.

Chapter 3

On the Role of Ionic Strength on Surface Bound Water Structure at the Silica/Water Interface

3.1 Introduction

Ions are known to play a large role in the behaviour of the silica/water interface, from screening surface charges[49-50, 106] to inducing dissolution[51, 54] and altering acid-base equilibria[47, 52-53, 175]. Yet there are still questions regarding the effect of ions on the behaviour of waters directly bound to the silica surface. These waters are difficult to measure by conventional spectroscopic techniques or electrochemical methods due to the overwhelming response of bulk molecules and the insulating nature of silica, respectively.

Sum frequency generation (SFG) spectroscopy is one technique that is well suited to study such buried interfaces, owing to its selection rule that requires a break of inversion symmetry for SFG to occur. Indeed, SFG has been used to study many charged surface/aqueous interfaces,[79, 142-144, 147, 162, 164, 176-179] with silica being the first.[60] SFG fails, however, to disentangle the response of the surface-bound waters from those further away from the surface which are aligned due to interactions with the static electric field emanating from a charged surface. Recent studies have suggested the latter can be significant depending on the surface charge density of the surface and the ionic strength.[92, 101, 108, 124]

As discussed in Chapter 1, it was shown in 2016 that the spectral behaviour of the bound "surface" waters can be separated from that of their bulk counterparts using the $\chi^{(3)}$ method.[101] This $\chi^{(3)}$ method, originally proposed by Ong et al.,[59] and widely accepted,[92, 107-108, 124, 131, 159, 166, 169] separates the sum frequency electric field into two origins: water assembled non-centrosymmetrically due to hydrogen bonding or ion hydration at the surface, given by the second-order nonlinear susceptibility, $\chi^{(2)}$, and waters which are aligned or polarized by the static electric field emanating into the bulk from the charged surface, given by the product of the third-order

nonlinear susceptibility, $\chi^{(3)}$, and the interfacial potential, Φ_0. For vibrational SFG, this relation is shown by the following equation

$$\sqrt{I_{SFG}} \propto E_{SFG} \propto \chi^{(2)} E_{Vis} E_{IR} + \chi^{(3)} E_{Vis} E_{IR} \int_0^\infty E_0(z) e^{i\Delta kz} dz, \quad (3.1)$$

where I_{SFG} is the SFG intensity, E_{Vis} and E_{IR} are the electric fields of the visible and infrared laser light sources incident on the silica surface, Δk is the wavevector mismatch of the sum frequency, visible, and infrared electric fields, and E_{SFG} is the electric field of the sum frequency light generated at the interface. The static electric field emanating in the z-direction (along the surface normal) is given by $E_0 = -\frac{d\Phi(z)}{dz}$, where $\Phi(z)$ is the electrostatic potential.[180]

By performing phase-sensitive SFG measurements as a function of ionic strength and pH at a Langmuir-Blodgett monolayer, Tian, Shen and coworkers separated the surface $\chi^{(2)}$ contribution from the $\chi^{(3)}$ response. They proposed that the measured $\chi^{(3)}$ spectrum is a property of the bulk liquid, and relatively constant from interface to interface, which was demonstrated valid up to approximately 100 mM ionic strength by MD simulations.[104] As such, this framework provides means to extract the surface contribution from the total signal if the surface potential and phase information is known. However, phase-sensitive SFG presents experimental challenges and is very sensitive to proper phase referencing.[82, 181] Consequently, intensity SFG measurements are still more common than the phase measurements for probing buried solid/liquid interfaces like the silica/water interface.[75, 108, 116, 128, 169] Additionally, surface potentials are difficult to determine experimentally at insulating interfaces like that of silica. Accordingly, a recent $\chi^{(3)}$ analysis aimed at separating $\chi^{(2)}$ (the surface contribution) and $\chi^{(3)}$ (the bulk–like contribution) at the silica/water interface used pKa values for surface sites or assumed a surface charge density at a given pH based on previous reports in the literature.[100] As different surface preparations and

samples for mineral oxides can influence the SFG spectra of water,[73-74, 139] independently measuring the surface potential would be ideal. Moreover, despite the strong evidence of the role that ions play at charged aqueous interfaces,[1, 19, 49, 117] it is often assumed that $\chi^{(2)}$ does not change with increasing salt concentration.[100, 107, 182]

Herein we demonstrate the effect of ionic strength on the SFG spectra of the surface-bound waters at the silica/water interface through the methodology described above. In lieu of a calculated surface potential, we measure the zeta potential, which has been related to both SFG and second harmonic generation,[42, 154, 183] but has not been used to deconvolute the $\chi^{(2)}$ and $\chi^{(3)}$ contributions. Using the reported phase-sensitive spectra of SFG at the silica/water interface as guides, we apply the maximum entropy method (MEM) to our measured SFG intensities to obtain the complex valued SFG spectra required for the analysis, which has been shown to be an accurate method to estimate the phase.[184-186] Using these complex spectra and the measured zeta potentials, we determine the $\chi^{(3)}$ spectrum at the silica/water interface, which agrees well with that of Tian, Shen and coworkers. Moreover, we observe significant changes in the surface bound water $\chi^{(2)}$ imaginary spectra with increasing salt concentration near the natural pH of 6. In particular, we observe a change in sign in the low wavenumber mode with increasing salt concentration, indicative of a flip in the oriented water that contributes at this wavenumber.

3.2 Experimental Section

3.2.1 Materials

NaCl (99.99%, trace metals basis, Alfa Aesar) was used to prepare salt solutions and KCl (99.999%, trace metals basis, Acros Organics) was used to calibrate the SurPASS instrument.

HPLC-grade MeOH (Fisher Chemical) was used for substrate cleaning. Sulfuric acid (95.0-98.0%, Caledon Laboratories) and hydrogen peroxide (30% w/w in H_2O, Sigma-Aldrich) were mixed in a 3:1 ratio and used for piranha cleaning substrates. All materials were used without further purification. Ultrapure deionized water (18.2 MΩ·cm) was used after deionization from a Milli-Q Direct 8 Water Purification System (Millipore, ZR0Q008WW). IR-grade fused quartz hemispheres (Almaz Optics, KI, 1 in. diameter) were used for SFG experiments. IR-grade fused quartz windows (Almaz Optics, KI, 2.5 in. diameter, 8 mm thickness) were used for zeta potential experiments. Sealing and spacer foils (Anton Paar, 97835 and 97834) were used to construct the flow channel along the fused quartz windows in the SurPASS clamping cell (Anton Paar, 22653).

3.2.2 Sample Preparation

Prior to an SFG experiment, an IR-grade fused quartz hemisphere was rinsed and sonicated (5 min) in ultrapure water, HPLC-grade MeOH, ultrapure water, and then ultrapure water again before being immersed in piranha solution (3:1 H_2SO_4:H_2O_2, 1 h). The hemisphere was then washed by the same water/MeOH rinse/sonication cycles as mentioned above followed by drying in an oven at 110°C (15 min) and then drying in the atmosphere while covered in a clean, glass petri dish (15 min). A Teflon sample cell, built in-house and described elsewhere,[121] was rinsed and sonicated in ultrapure water, HPLC-grade MeOH, and ultrapure water again before being allowed to dry in open atmosphere. Prior to a zeta potential experiment, two IR-grade fused quartz windows were cleaned in the same way as described above. One window was modified in-house by drilling two holes through, aligned to the specifications of the SurPASS clamping cell, to facilitate the measurement. The clamping cell insert (Anton Paar, 21411) was rinsed and sonicated in ultrapure water, HPLC-grade MeOH, and ultrapure water again before being allowed to dry in

open atmosphere. Onto the clean, dry clamping cell insert was placed a sealing foil. The clean, dry, modified fused quartz window was then placed on top of the sealing foil with the holes aligned. A spacer foil was then carefully placed on top of the window with the holes and channel aligned. Finally, a second fused quartz window was placed on top of the spacer foil to complete the channel. On top of the second fused quartz window was placed a support plate (Anton Paar, 84439) and the whole stack was placed within the clamping cell and tightened. A set of SurPASS Ag/AgCl electrodes (Anton Paar, 22667) were then connected through the clamping cell insert. Two concentrations of NaCl solution (10 mM and 1 M) were used to increase the sample solution ionic strength. Solutions were prepared fresh and stored open to atmosphere for approximately 3 hours before data collection. Solutions for zeta measurements were prepared by diluting the 1 M NaCl solution.

3.2.3 Laser Assembly

Some modifications to the laser assembly were made after the collection of data in Chapter 2. The modified system is as follows. A regeneratively amplified laser (Spectra-Physics, Spitfire Pro, 1 KHz, 94 fs, 3.3 W) was seeded and pumped, respectively by a Ti-sapphire oscillator (Spectra-Physics, MaiTai, 80 MHz) and a Nd:YLF laser (Spectra-Physics, Empower 30) to generate high peak power 800 nm pulses. This 800 nm was passed through a 35% beam splitter (Newport) directing 2.3 W to pump a noncollinear optical parametric amplifier (TOPAS-C/NDFG, Light Conversion) to produce a tunable, broadband IR light (FWHM = ~90 cm^{-1}). An infrared longpass filter (Edmund Optics, 2.40 μm, 68-653) was used to remove any residual signal and idler contribution from the IR beam, which was then passed through a polarizer (Thorlabs, LPMIR050-MP2), a zero-order, tunable half-wave plate (Alphalas), and a CaF_2 focusing lens (Thorlabs, f =

500 mm) before reaching the sample. The remaining 1.0 W of 800 nm light from the Spitfire Pro was passed through an air-spaced Fabry-Perot Etalon (TecOptics) to generate narrow, picosecond pulses (FWHM = ~7 cm^{-1}). The visible light was then passed through a delay stage, a polarizer (Thorlabs LPVIS050-MP2), a zero-order, half-wave plate (Thorlabs, λ/2@808 nm), and a BK7 focusing lens (Thorlabs, f = 500 mm) before reaching the sample. The visible (~10-20 μJ/pulse) and IR (~18 μJ/pulse) beams were directed at the sample cell at incident angles of 61° and 67°, respectively, relative to the surface normal. The beams were slightly defocused to avoid beam-induced sample damage while spatially and temporally overlapped at the sample interface to generate sum frequency light. The SFG reflection beam was passed through a BK7 recollimating lens (Thorlabs, f = 400 mm), a half-wave plate (Thorlabs, λ/2@808 nm), a Glan-Thompson calcite polarizer (Thorlabs, GTH10M), a BK7 focusing lens (Thorlabs, f = 100 mm), and a filter (Thorlabs, FES0750) before entering a spectrograph (Princeton Instruments, Acton SP-2556 imaging spectrograph, grating: 1200 grooves/mm, 500 nm blaze wavelength) connected to a thermoelectrically cooled (-75°C), back-illuminated, charge-coupled device camera (Princeton Instruments, Acton PIXIS 100B CCD digital camera system, 1340 x 100 pixels, 20 um x 20 um pixel size).

3.2.4 SFG Experiments

A fused quartz hemisphere (Almaz Optics, KI, 1 in. diameter) with a gold-coated planar side (200 nm) was mounted to the clean sample cell. The laser was aligned and the SFG signal was optimized using the signal from the silica/gold interface. A nonresonant reference spectrum was collected at a single delay setting using 6-7 IR pulses with centres ranging from ~2900-3500 cm^{-1}. A polystyrene calibration film (International Crystal Laboratories, 38 μm thick) was used to

calibrate the detected frequency by comparison to three known polystyrene aromatic C-H absorptions centred at 3026, 3059 and 3081 cm^{-1}. The gold-coated hemisphere was then exchanged for a freshly cleaned fused quartz hemisphere. The cell cavity was rinsed five times with ultrapure water and then allowed to equilibrate in ultrapure water for 30 minutes. NaCl solution was then added by micropipette to achieve the lowest ionic strength solution in the cell and allowed to equilibrate for 30 minutes. After measurement, the ionic strength was further increased through the addition of concentrated NaCl by micropipette (Gilson, calibrated by Transcat, Inc.). Each subsequent solution was allowed to equilibrate with the fused quartz surface for 15 minutes before measurement. After collecting all sample spectra, the hemisphere was exchanged once more for the gold-coated hemisphere and a reference spectra was collected. Sample spectra were collected in ssp polarization (s-sum frequency, s-visible, p-infrared) for 120 s at each frequency used for the nonresonant reference. Reference spectra were collected in ppp polarization for 1s per centre frequency averaged over 10 acquisitions. All spectra were background corrected by subtraction with a background spectrum collected immediately prior to each sample or reference spectrum. Background spectra were collected by blocking the IR laser and acquiring signal at a single pulse.

3.2.5 Zeta Potential Experiments

Zeta potential measurements were performed on a SurPASS Electrokinetic Analyzer (Anton Paar) using the clamping cell. The conductivity probe (Anton Paar, 18116) was calibrated prior to each experiment with 0.1 M KCl solution. Before setting up the clamping cell, the electrodes were connected by connection tube (Anton Paar, 100083) and the instrument was cleaned with ultrapure water four times (300 s for each cleaning cycle). After mounting the clamping cell to the instrument and connecting the electrodes, the instrument was filled with

ultrapure water (200 s fill time) and a flow check was performed (500 mbar) to confirm linear flow rate with respect to pressure and to check for cell leakage. The cell was then rinsed with ultrapure water (500 mbar for 500 s) and allowed to equilibrate for 30 minutes. Higher ionic strength solutions were prepared, as described above, while the fused quartz window equilibrated under the current solution. Each solution was filled (200 s) into the instrument, followed by rinsing (500 mbar for 500 s) and equilibrated for at least 15 minutes before measurement, except for the initial introduction of NaCl which was allowed to equilibrate for at least 30 minutes. Measurements were performed under streaming current mode with a rinse target pressure of 500 mbar for 180 s and a ramp target pressure of 400 mbar for 20 s. The clean, calibrated conductivity probe was allowed to sit in the sample solution during the entire experiment.

3.3 Results and Discussion

3.3.1 Sum Frequency Spectra and Zeta Potentials of the Silica/Water Interface in the Presence of Increasing Sodium Chloride Concentrations

SFG intensity spectra were collected at the silica/water interface in the presence of increasing sodium chloride ionic strength (Figure 3.1a). In the spectral window, two large peaks were observed which we refer to as the 3200 cm^{-1} and 3400 cm^{-1} modes. The exact origin of these two modes remains a subject of debate,[60, 82, 85, 92, 99-100, 130] but in general it is accepted that the lower wavenumber mode arises in part from strongly hydrogen bonded water and the higher wavenumber mode from weakly hydrogen bonded water near the surface, although a fermi resonance also contributes to the intensity in both regions.[81] Consistent with earlier work,[108, 128] the overall intensity of the SFG signal increased with ionic strength until approximately 1 mM,

and then decreased with stronger ionic strengths, as seen in Figure 3.1b. This non-monotonic behaviour has been mainly attributed to an interplay between the screening of surface charges,[80, 115, 124-125, 134] and interference between $\chi^{(2)}$ and $\chi^{(3)}$.[107-108, 128] The former is proposed to be responsible for the decrease in signal observed beyond 1 mM ionic strength, as the increase in cations screen surface charges reducing the interfacial potential and the Debye length. With both surface potential and Debye length reduced, the alignment and polarization of water molecules should decrease, resulting in a smaller SFG signal. The relative strength of the surface potential is reflected in the behaviour of the zeta potential over this salt concentration range, which generally decreases with increasing ionic strength.

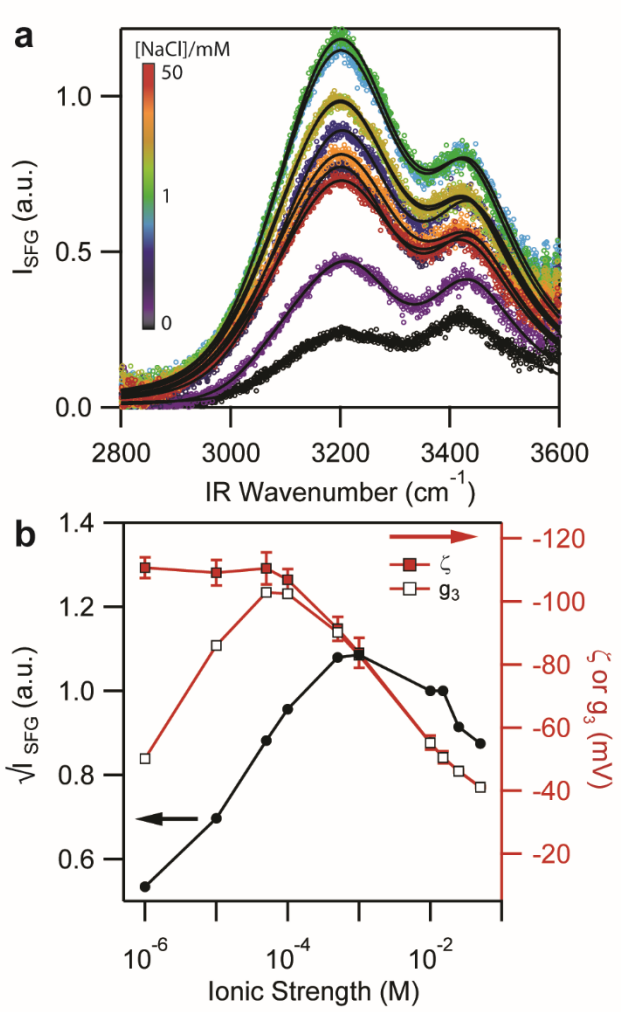

Figure 3.1 (a) SFG intensity corrected for local field effects from 2800 to 3600 cm^{-1} at the silica/water interface over a NaCl concentration range of pure water (black) to 50 mM NaCl (red) and (b) the square root of the integrated SFG intensity compared to the ζ potentials and g_3 values at the same interface, where error bars on the ζ potentials are the range between multiple measurements.

3.3.2 Accounting for Wavevector Mismatch at Low Ionic Strengths

The increase in SFG signal from pure water to 1 mM ionic strength is attributed, in part, to the contribution of interference and stems from the long Debye length present at low salt concentration. As the ionic strength decreases, waters aligned by the static electric field further away from the surface than the coherence length of the SFG process leads to significant destructive interference within the $\chi^{(3)}$ response, leading to an overall phase change. Noticeable destructive interference occurs below 1 mM NaCl, and can be modeled by the following equation,

$$g_3 = \Phi_0 + i\Delta k \int_0^\infty \Phi(z) e^{i\Delta k_z} \, dz, \tag{3.2}$$

where the interference is incorporated into the potential as a function of distance from the surface in the z-direction (normal to the surface) and depends on the wave vector mismatch, Δk, of the SF, visible, and IR electric fields.[128] The solution to this integral can be estimated for relatively low potentials (i.e. below 25 mV) as $\Phi_0 \left[\frac{\kappa}{\kappa - i\Delta k_z}\right]$, also known as $\Phi_0 f_3$,[110] but for larger potentials equation 3.2 should be solved numerically or using a series expansion according to the following[128]

$$g_3 = \Phi_0 - \frac{4ik_bT\Delta k}{e} \sum_{n=1}^{\infty} \frac{\xi^{2n-1}}{(2n-1)(i\Delta k - \kappa(2n-1))}, \tag{3.3}$$

$$\xi = \tanh \frac{e\Phi_0}{4k_bT}. \tag{3.4}$$

The Debye length, κ^{-1}, wavevector mismatch, Δk, and individual wavevectors, k_i, are given by

$$\kappa^{-1} = \sqrt{\frac{\varepsilon_R \varepsilon_0 RT}{2F^2 C \times 1000}}, \tag{3.5}$$

$$\Delta k = k_{vis} + k_{IR} + k_{SFG}, \tag{3.6}$$

$$k_i = \frac{2\pi\nu_i}{c} n_{H_2O,i} \cos\gamma_i. \tag{3.7}$$

Here ε_R is the relative permittivity of water, for which a value of 78 was used,[110] ε_0 is the vacuum permittivity, R is the ideal gas constant, F is Faraday's constant, and C is the concentration. Note that equation 3.5 is the simplified form for monovalent ions and that equation 3.6 uses the opposite sign convention for k_{SFG} because of the reflection geometry. The wavevectors, k_i, where i = SFG, visible, and infrared, depend on the frequency, ν_i, of the ith light, the speed of light, c, the frequency dependent refractive indices of the aqueous medium, $n_{H_2O,i}$, and the refracted angle, γ_i, of the ith laser. As demonstrated recently,[128] it is important to calculate the complex wavevectors, given by the complex refractive indices and complex refraction angles, to properly account for dispersion/absorption into the medium. Regarding the form used to solve equation 3.2, Hore and Tyrode demonstrated that the series expansion presented in equation 3.3 at n = 1000 yields a result which is indistinguishable from the numerical solution within the relevant ionic strength range.[128]

After incorporating the effect of interference into our measured zeta potentials, we compare g_3 to the square root of the SFG intensity. If the $\chi^{(2)}$ surface response is constant with increasing salt concentration, the trend in $\sqrt{I_{SFG}}$ should match that of g_3. Yet, from Figure 3.1b it is evident the SFG electric field is not linear with g_3, and therefore the $\chi^{(2)}$ stemming from the surface bound waters must be changing. Indeed, recent work by Hore and Tyrode revealed that the magnitude of $\chi^{(2)}$ had to change significantly to account for their salt variation SFG experiments, like that shown in Figure 3.1b, measured as a function of incident angles based on the data integrated from 2800-3800 cm^{-1}.[128]

3.3.3 Estimating the Complex Nonlinear Susceptibility from the Maximum Entropy Method

To determine the spectral changes in $\chi^{(2)}$, rather than just the changes in magnitude, with changing salt concentration the complex valued spectra are required. Since SFG intensity is related to the square of the nonlinear susceptibility, the phase information is not acquired by the measurement. However it has been shown that the maximum entropy method (MEM) is adequate in predicting this phase from intensity measurements. Described here is a brief overview of the maximum entropy method; in-depth descriptions can be found elsewhere.[184, 186-187] In regards to finding the complex valued spectra from the intensity, the maximum entropy method estimates the most probable solution to the phase without adding new information. To do so, we first consider the spectral entropy, h

$$h \propto \int_0^1 \log I(v) dv, \tag{3.8}$$

where I is the intensity spectrum, and v is a rescaled frequency (from 0 to 1, for ease of analysis) given by

$$v = \frac{\omega - \omega_1}{\omega_2 - \omega_1}, \tag{3.9}$$

As information is added to a system, the spectral entropy decreases (i.e. becomes more negative). Therefore the most probable solution of the phase to the intensity which does not add new information to the system will be the one which has the highest spectral entropy (i.e. maximum entropy method). By constraining the spectral entropy to be constant, and forbidding the growth of resonances over time, through variational calculus and the method of Lagrange multipliers, one eventually arrives at:

$$I(v) = \frac{|b|^2}{\left|1 + \sum_{m=1}^{M} a_m e^{i2\pi m v}\right|^2}, \tag{3.10}$$

where the a_m and b coefficients are solved from the following Toeplitz system for 2M+1 data points

$$\begin{bmatrix} R(0) & R(-1) & \dots & R(-M) \\ R(1) & R(0) & \dots & R(1-M) \\ \vdots & \vdots & \ddots & \vdots \\ R(M) & R(M-1) & \cdots & R(0) \end{bmatrix} \begin{pmatrix} 1 \\ a_1 \\ \vdots \\ a_M \end{pmatrix} = \begin{pmatrix} |b|^2 \\ 0 \\ \vdots \\ 0 \end{pmatrix}, \tag{3.11}$$

and $R(m)$ is the autocorrelation function,

$$R(m) = \int_0^1 I(v) e^{-i2\pi mv} dv. \tag{3.12}$$

Similarly, the complex valued nonlinear susceptibility can be described as

$$\chi^{(2)}(v) = \frac{b e^{i\varphi_v}}{1+\sum_{m=1}^{M} a_m e^{i2\pi mv}}, \tag{3.13}$$

where φ_v is the associated, frequency dependent, error phase. It is important to note that this phase is an internal value and not reflective of the actual phase of the intensities, however, the two parameters are directly related. Therefore a change in the error phase represents a change in the actual phase of the complex nonlinear susceptibility.

Since a_m and b are solutions from the intensity under the constraints listed above, the error phase is the only remaining unknown parameter, and therefore some physical knowledge of the system must be known to make an accurate prediction.[184-186] In this case, we are fortunate to consider the measured complex spectra of the silica/water and α-quartz/water interfaces from Tahara and coworkers[90] and Shen and coworkers,[82] respectively. In particular, using as a guide the zero cross over points observed in the real spectra, we select a constant error phase that yields similar results to the measured complex spectra of the silica/neat water interface and results in a $\chi^{(3)}$ spectrum that matches the recently reported spectrum.[101] The effect of varying the error phase

on the total, diffuse layer, and surface complex spectra was, in general, to redshift spectra with increasing phase angles and blueshift spectra with decreasing angles (Figure 3.2).

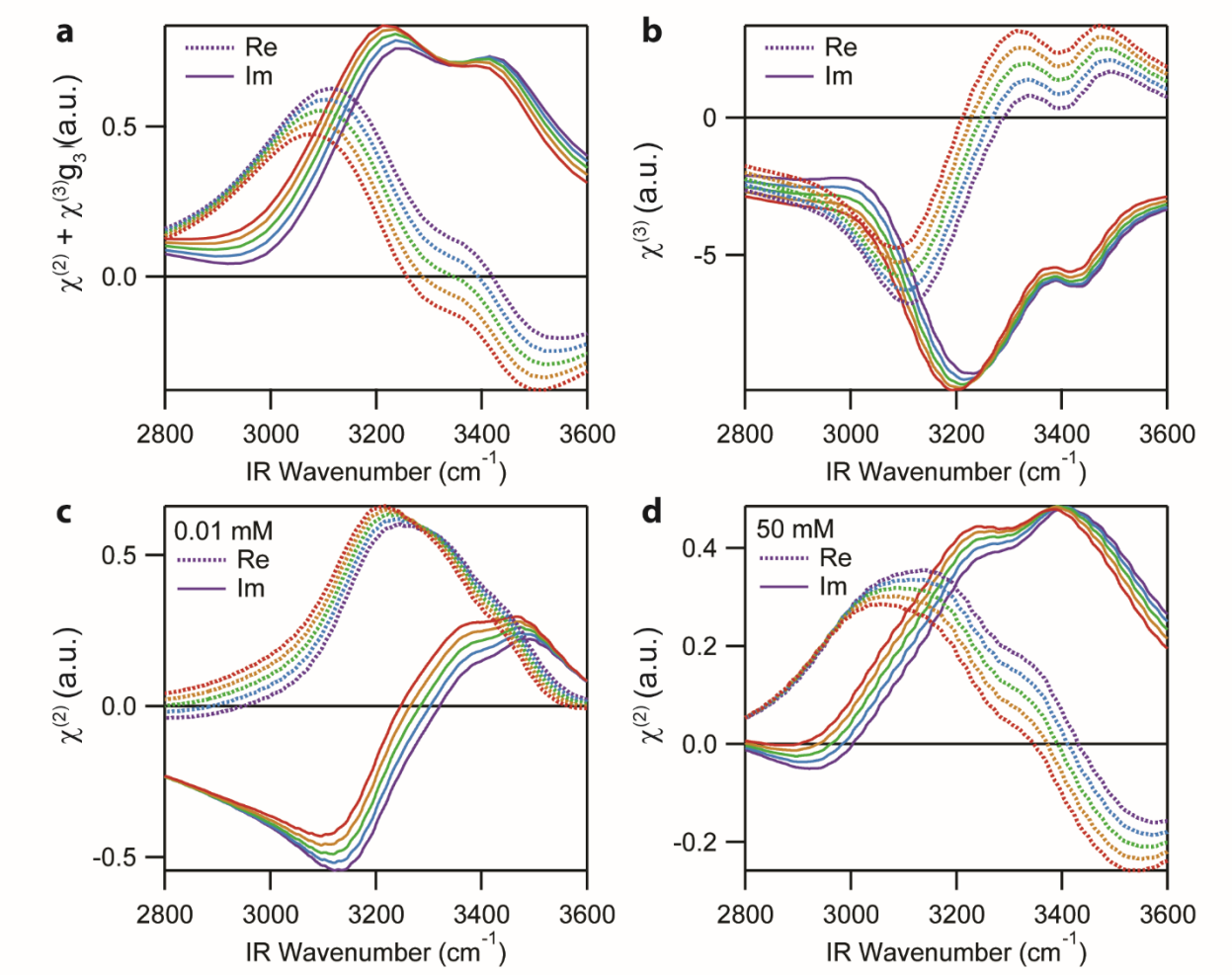

Figure 3.2 (a) Total complex nonlinear susceptibility at 50 mM NaCl, (b) third order nonlinear susceptibility, and surface nonlinear susceptibilities at (c) 0.01 mM and (d) 50 mM NaCl over a range of frequency-independent MEM error phases from 90° (red), 85° (orange), 80° (green), 75° (blue), and 70° (violet).

3.3.4 Approximating the Spectral Baseline and its Effect on the Nonlinear Susceptibility Determined by the MEM

Prior to applying the maximum entropy method, we corrected the intensity spectra for local field effects, the details of which can be found in Chapter 2.[58, 70] Furthermore, the MEM requires knowledge of the spectral baseline. Since our spectral window did not span from one baseline to the other, we first fit the local field-corrected SFG intensity to the square of a series of three Lorentzians (see Chapter 5 for equation 5.1, and see Appendix for fitting parameters) allowing us to approximate the SFG baseline at higher and lower wavenumber (Figure 3.3); this extrapolation agreed with reported intensity spectra for the silica/water interface at low wavenumber in particular.[188] We excluded the high wavenumber peak from our fit, observed around 3680 cm^{-1} by Tyrode and co-workers,[73] and Backus and co-workers,[75] although it was not very apparent in the phase-sensitive spectra.[90] We then performed the MEM on these fits to the data over the same wavenumber range as that measured and compared these MEM results with that performed directly on our measured SFG intensities (Figure 3.4). This comparison revealed excellent agreement between the complex spectra from the MEM of the measured and fit data. We then performed MEM on the Lorentzian fits over a larger range that captured the spectral baseline, which led to slight differences in the calculated complex spectra. These resulting complex spectra are shown in Figure 3.5, and they agree well with that measured by Tahara and coworkers using phase-sensitive SFG,[90] with the exception of the high wavenumber region beyond 3500 cm^{-1} which did not reach zero at 3600 cm^{-1} as in their measured spectra.

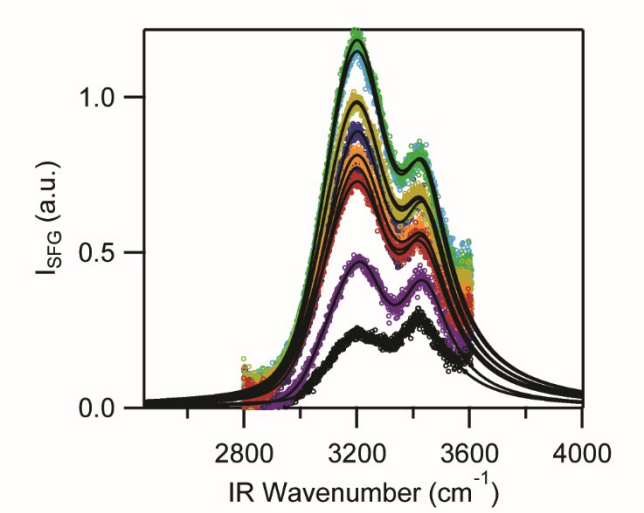

Figure 3.3 The fits (black lines) to the intensity data (circles), expanded from 2400 to 4000 cm^{-1} to approximate the baseline.

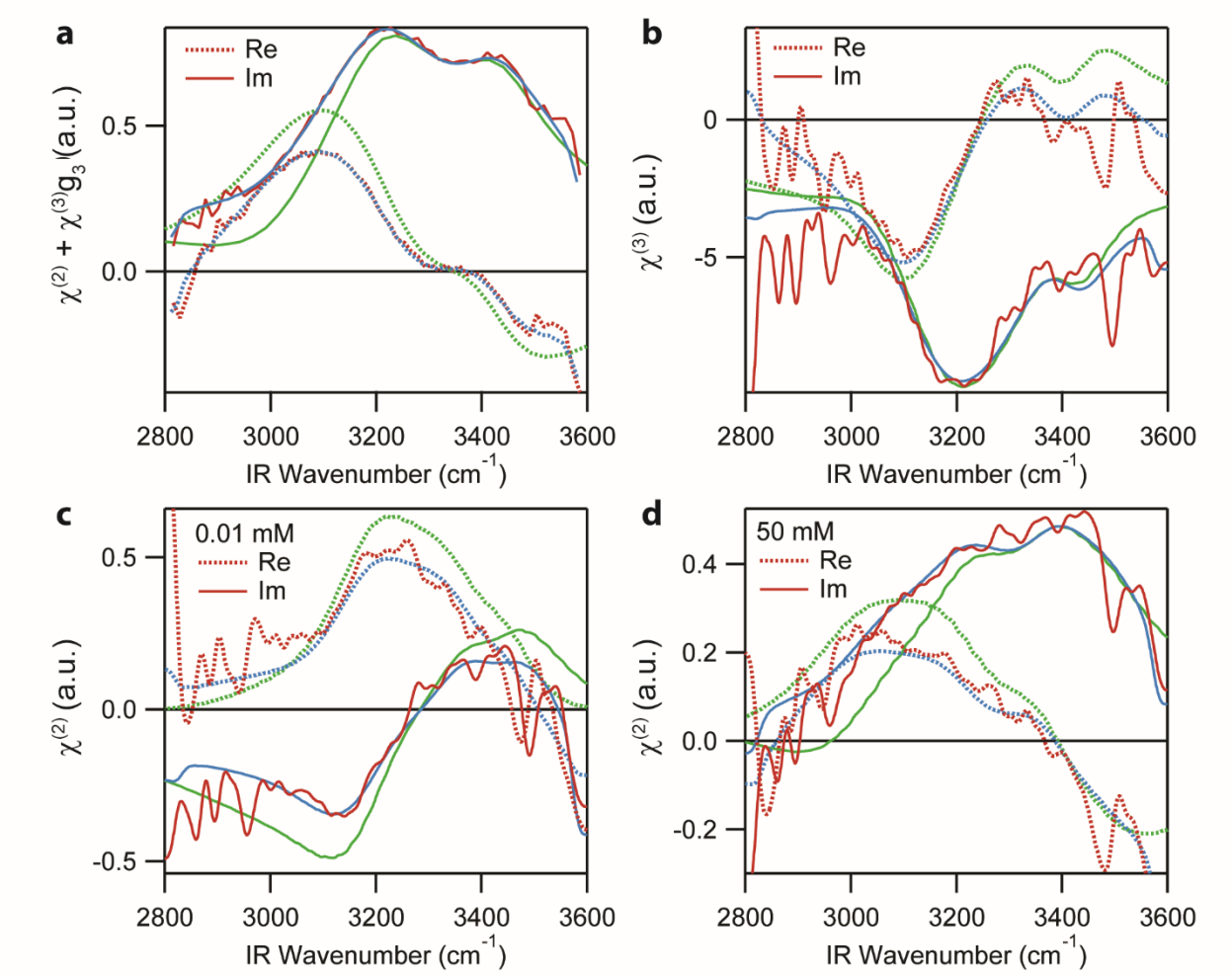

Figure 3.4 (a) Total complex nonlinear susceptibility at 50 mM NaCl, (b) third order nonlinear susceptibility, and surface nonlinear susceptibilities from (c) 0.01 mM and (d) 50 mM NaCl calculated from the MEM using the intensities (red), the fits (blue), and the expanded fits (green) at an error phase of 80°.

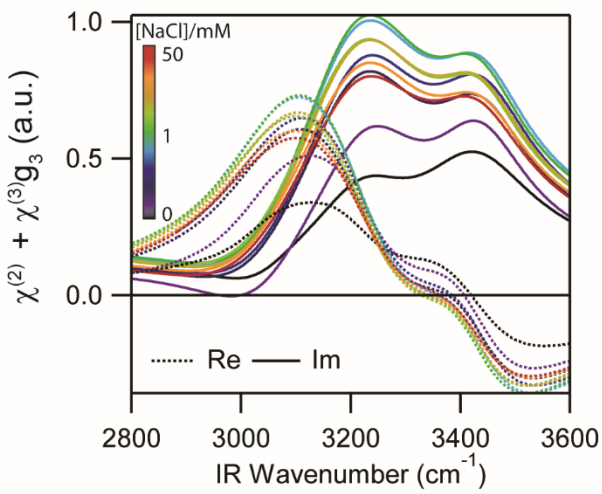

Figure 3.5 Real and imaginary spectra estimated by applying the maximum entropy method to the expanded fits of the measured SFG intensities at the silica/water interface from pure water (black) to 50 mM NaCl (red).

3.3.5 Extracting the Third Order Nonlinear Susceptibility

With the complex spectra and g_3 factor calculated from our measured zeta potential in hand, we can determine the complex third order nonlinear susceptibility, $\chi^{(3)}$. We do this by measuring the difference in the complex spectra over two salt concentrations, and assuming that the $\chi^{(2)}$ does not change between these two conditions; from this difference spectrum we can then use the g_3 factor to determine $\chi^{(3)}$. To choose two points that best meet this assumption, we referred to the recent work by Hore and Tyrode, which determined $\chi^{(2)}$ to be relatively unchanging from 10-50 mM NaCl.[128] The resulting complex third order nonlinear susceptibility is shown in Figure 3.6a. The shaded areas in Figure 3 depict the uncertainty due to variation in the zeta potential measurements between 10 and 50 mM ionic strength while the dashed lines show the complex

$\chi^{(3)}$ spectra measured by Tian, Shen and co-workers. For comparison, $\chi^{(3)}$ and the surface $\chi^{(2)}$ were also calculated using the difference between 10 and 25 mM ionic strength (Figure 3.7).

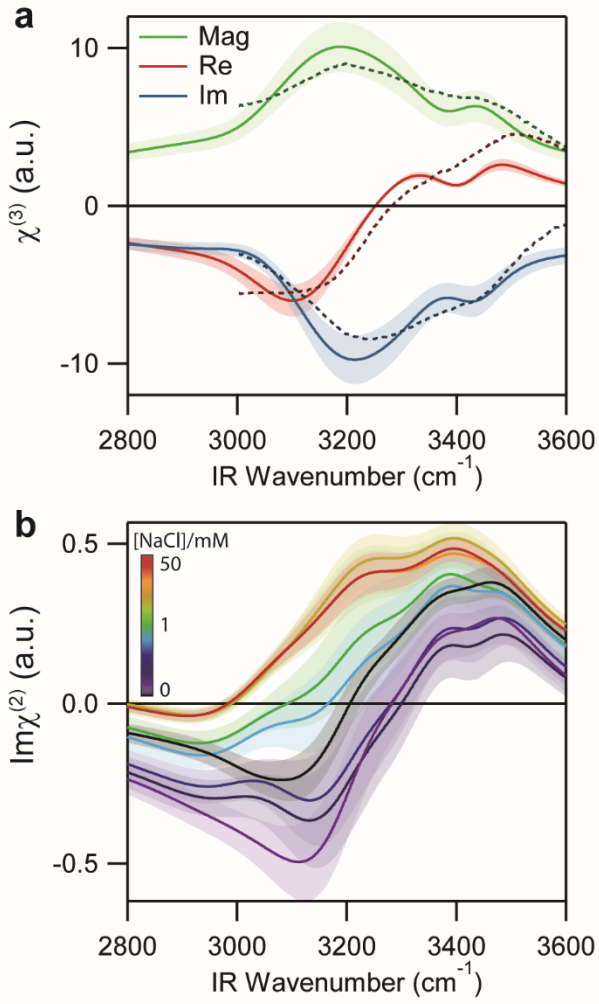

Figure 3.6 (a) The magnitude, real, and imaginary terms of the third order nonlinear susceptibility calculated from the complex spectra and the corrected zeta potential between 10 and 50 mM NaCl. The spectrum from Tian and coworkers (dashed line) is plotted for comparison. (b) The resulting imaginary surface spectra of the tightly bound waters from pure water (black) to 50 mM (red) ionic strengths. Shaded regions are the uncertainty propagated from the range in measured ζ potentials.

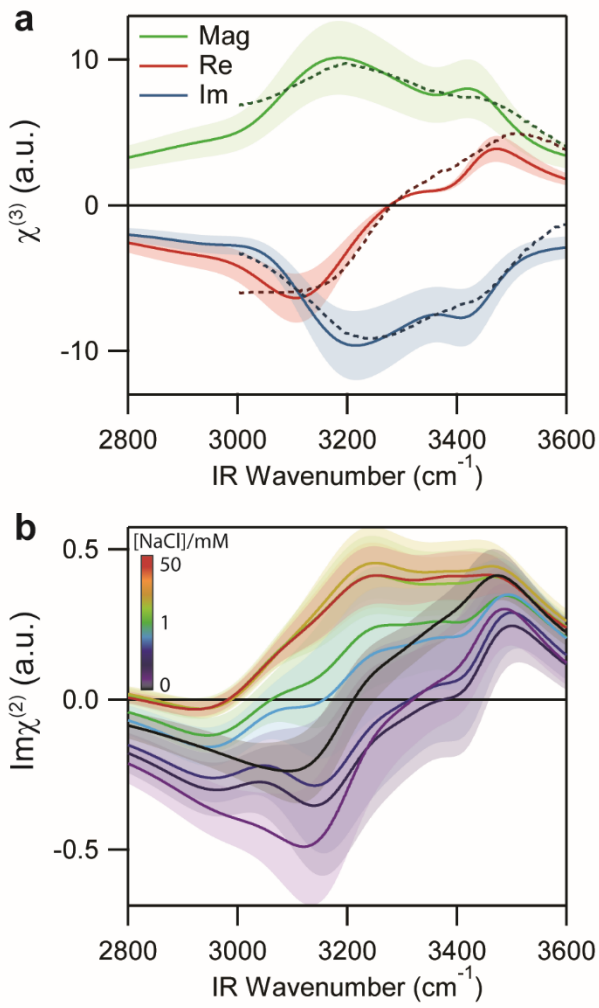

Figure 3.7 (a) The magnitude, real, and imaginary terms of the third order nonlinear susceptibility calculated from the complex spectra and the corrected zeta potential between 10 and 25 mM NaCl. The spectrum from Tian and coworkers (dashed line) is plotted for comparison. (b) The resulting imaginary surface spectra of the tightly bound waters from pure water (black) to 50 mM (red) ionic strengths. Shaded regions are the uncertainty propagated from the range in measured ζ potentials.

3.3.6 Calculating the Surface Nonlinear Susceptibility

The surface contribution may now be extracted from all complex spectra by subtracting the potential dependent component, which is the third order nonlinear susceptibility scaled by the g_3 factor. The result demonstrates a striking difference between the surface contributions as the ionic strength is increased (Figure 3.6b and 3.7b). At low salt concentration, we see two large modes of opposite phase. This suggests the presence of oppositely oriented water populations hydrogen bonded at the surface. Interestingly, the spectrum at low salt concentration and pH 6 is similar to the imaginary spectrum measured by Tahara and co-workers near the point of zero charge.[90] MD simulations of a neutral α-quartz/water interface (approximately equivalent to pH 2) resulted in a positive, high frequency band and a negative, low frequency band in the imaginary spectrum.[92] The former originated from waters which acted as H-bond donors to silanol, and the latter was due to waters accepting H-bonds from silanols. At a charged α-quartz/water interface in the absence of ions, the MD simulations revealed imaginary spectral contributions from these H-bond donors and acceptors were similar to the neutral surface, with the greatest difference in total spectral contribution originating from the potential dependent, $\chi^{(3)}$ term. As the ionic strength increases (Figure 3.6b and 3.7b), the surface contribution becomes dominantly positive suggesting an orientation flip of some water molecules induced by ions. At the highest ionic strength studied, 50 mM, the surface spectrum consists of two large modes centred around 3200 and 3400 cm^{-1} with a small, negative contribution at lower wavenumbers below 3000 cm^{-1}, similar to the total complex spectra themselves. With increasing ionic strength, the potential is reduced, and the total complex spectra (Figure 3.5) begin to take on the lineshape of the surface contribution at the given ionic strength.[100, 107, 182]

Additionally, the surface spectra extracted from the silica/water interface with increasing salt concentration indicated the effects of ionic strength to plateau at the higher concentrations studied. This plateau may be due to a saturation of ions at the surface, which was first suggested by Richmond and coworkers at the charged air/water interface,[159] where the SFG signal was observed to respond nonlinearly with respect to the potential, and then again by Bonn and coworkers,[189] where a saturation of ions was suggested. By comparison to screening studies by others,[108, 124] four regions of ionic strength were suggested, from pure water to ~ 1 mM, interference effects were dominant, whereas from ~ 1 to 10 mM, screening effects become more obvious. From ~ 10 mM to 1 M, there was relatively less change to the overall signal, and beyond 1 M, the signal dropped suddenly (Figure 1.11). It may be that in the 10 mM to 1 M regime there is a relative saturation of cations near the surface, accounting for the less drastic surface spectral changes observed at the higher salt concentrations studied (Figure 3.6b and 3.7b), while beyond 1 M NaCl, significant H-bond disruption occurs, as suggested by Hore and coworkers.[124] Such a disruption was observed by Tahara and coworkers at very high salt concentrations.[100]

3.3.7 The Effect of Using a Calculated Surface Potential Instead of a Measured Zeta Potential

To demonstrate the effect of using a zeta potential rather than a surface potential for the analysis, we applied the same treatment to the complex spectra acquired from the MEM using a surface potential calculated elsewhere.[128] Both $\chi^{(3)}$ and final $\chi^{(2)}$ surface spectra remained similar, although the former decreased in magnitude by approximately half its magnitude (Figure 3.8a) relative to that calculated using the zeta potentials. The decrease in $\chi^{(3)}$ magnitude is a result of the calculated surface potential which is nearly twice in magnitude as the measured zeta potential at high ionic strength (Figure 3.9b). The surface nonlinear susceptibilities resulting from the use

of the calculated surface potential remain relatively unchanged from those extracted using the measured zeta potential. This comparison highlights that the absolute value of the potential is less important than the relative difference between all potential values, given the arbitrary units. We note the similar trends between the measured zeta potential and calculated surface potential until higher potential values (Figure 3.9b). Despite the difference in magnitudes, both $\chi^{(2)}/\chi^{(3)}$ trends are qualitatively similar to that reported by Geiger and coworkers using heterodyne-detected second harmonic generation.[131] Interestingly, the plateau in zeta potential strength we measured at low ionic strength was not reproduced in the calculated surface potentials.

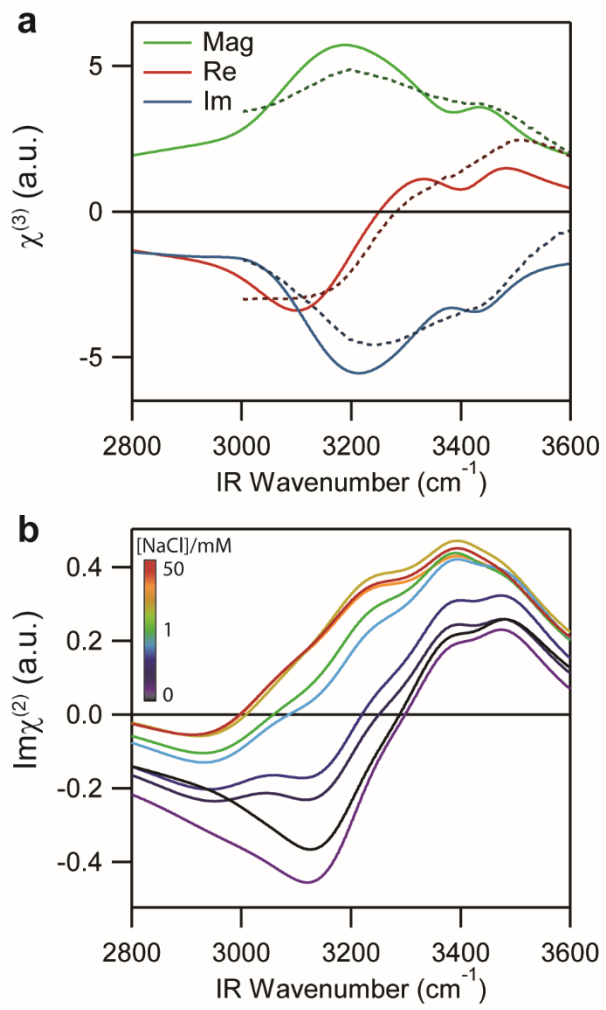

Figure 3.8 (a) The magnitude, real, and imaginary terms of the third order nonlinear susceptibility calculated from the complex spectra and the corrected, calculated surface potential between 10 and 50 mM NaCl. The spectrum from Tian and coworkers (dashed line) is plotted for comparison. (b) The resulting imaginary surface spectra of the tightly bound waters from pure water (black) to 50 mM (red) ionic strengths.

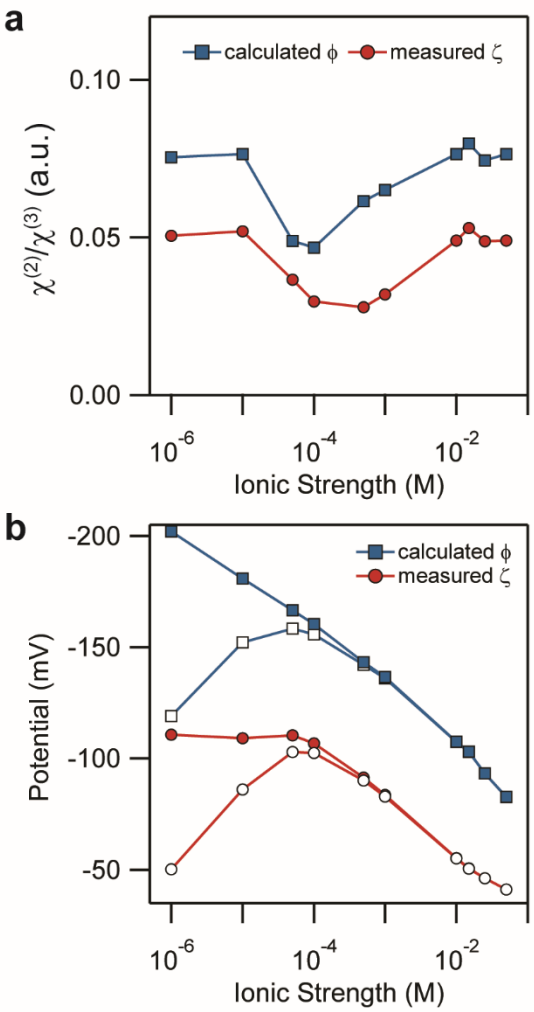

Figure 3.9 (a) The ratio of $\chi^{(2)}/\chi^{(3)}$ over the ionic strength range studied obtained from using a calculated surface potential and a measured zeta potential in the analysis. (b) The calculated surface potentials and measured zeta potentials (filled squares and circles, respectively) used in this study along with their respective g_3 values (open squares and circles, respectively).

3.4 Conclusion

In summary, we have shown how ionic strength affects the lineshape of surface bound waters at the silica/water interface using sum frequency generation spectroscopy, however, the

analysis and outcomes depend on the validity of the $\chi^{(3)}$ method. We found the maximum entropy method to be adequate in predicting the complex valued spectra from intensity measurements, given that some phase measurements were available for reference.[82, 90, 92, 101] The lineshape of the third order nonlinear susceptibility was extracted assuming an unchanging surface contribution between 10 and 50 mM ionic strength. The extracted $\chi^{(3)}$ lineshape appeared similar to that calculated by others.[92, 101] The measured zeta potential proved to be a valid potential for this analysis and indicated a similarity between the zeta potential trend to a calculated surface potential trend. Finally, given the differences observed to the surface water structure upon ionic strength increase, we predict a large dependence on the solution pH and hence the silica structure.

Chapter 4

On the Role of pH on Surface Bound Water Structure at the Silica/Water Interface

4.1 Introduction

Surface bound waters are often ascribed to the unique properties of silica, however little is known regarding their conformational structure. Under certain conditions, this surface layer of water on silica has been held accountable for some of the unique properties of silica among other mineral oxides. A striking example is the enhanced stability to aggregation of silica colloids experienced in solution near the point of zero charge, where there is predicted to be only a single monolayer of bonded waters.[1, 134-135] In contrast, the minimum stability is observed around a neutral pH of 7, with increasing stability with increasing pH until rapid dissolution occurs. This is in direct contrast to other materials, which generally do not exhibit enhanced stability with decreasing surface charge. Furthermore, the hydration of dehydrated silica is believed to occur more rapidly once water begins to adsorb,[1] suggesting surface waters catalyze the further hydration of other surface sites. However, studying these very thin layers amongst the vast sea of bulk water, including water within the so-called diffuse electrical double layer, is challenging even for surface specific nonlinear optical techniques like vibrational sum frequency generation spectroscopy (vSFG).

As discussed in Chapters 1 and 3, a methodology was developed for the deconvolution of vSFG signal into the spectral response of oscillators aligned by a potential and those aligned by other forces (i.e. hydrogen bonding).[101] This analysis takes root in the $\chi^{(3)}$ method, which postulates the separation of sum frequency signal from water into two components: the second-order nonlinear susceptibility, $\chi^{(2)}$, and the third-order nonlinear susceptibility, $\chi^{(3)}$.[59] The former term represents the interaction of water with the two probing electric fields, E_1 and E_2, while the latter term is the response of water when interacting with the above and an additional force, E_0, which is the electrostatic field induced by the presence of surface charges. Therefore all signal

from water molecules aligned or polarized by the static electric field of silica can be attributed to the $\chi^{(3)}$ term, while the remaining response is given to those waters not aligned by the field, rather, by other forces such as hydrogen bonding to the silica, and contribute to $\chi^{(2)}$. These waters not directly aligned by the field have been referred to as the bonded interfacial layer (BIL),[101] but we will refer to them as the surface bound waters. For relatively high salt concentrations (i.e. > 10 mM) the $\chi^{(3)}$ method can be described as the equation below

$$\sqrt{I_{SFG}} \propto \chi^{(2)}E_1E_2 + \chi^{(3)}E_1E_2\int_0^\infty E_0 dz = \chi^{(2)}E_1E_2 + \chi^{(3)}E_1E_2\Phi_0, \quad (4.1)$$

where I_{SFG} is the intensity of the sum frequency signal, and E_{SFG} is the sum frequency electric field. The static electric field that interacts with water in the diffuse layer is integrated from the surface to infinity along the surface normal (z-direction), yielding the surface potential, Φ_0. In the analysis by Tian and coworkers, $\chi^{(3)}$ was suggested to be constant and a property of bulk water, rather than an interface specific phenomenon.[101] This assumption was shown to be valid up to approximately 0.1 M ionic strength.[104] Therefore, with knowledge of the Stern layer potential, Φ_{SL}, the potential-dependent contribution, $\chi^{(3)}\Phi_0$, to the SFG signal can be extracted to yield the remaining potential-independent contributions, $\chi^{(2)}$.

Variations of this analysis have been applied to several interfaces,[101, 109-110, 182, 190] including that of silica/water,[100, 191] and have proven valuable as a tool for studying these interfacial regions of water. In particular, Tahara and coworkers measured the surface bound waters on silica and found a large contribution at 3200 cm^{-1} under high pH and high salt conditions.[100] We were interested in how the surface waters respond to changing ionic strength and solution pH since both are known to affect the properties of the silica/water interface. Very recently we have extracted the surface water contribution of silica from SFG intensities over the low to mid ionic strength

regime (pure water – 50 mM) at pH 6 and found a considerable salt-induced reorientation of surface waters.[191] We showed that we were able to use the maximum entropy method to approximate the complex spectra from the measured intensities, and retrieve the $\chi^{(3)}$ lineshape. Furthermore, by using a measured zeta potential in our analysis as an approximation of the Stern layer potential, we extracted the surface water contributions from the total spectra. Herein we apply a similar treatment to determine the effect of solution pH on the surface water structure. We find the water structure to change with pH, with a flip in sign of the imaginary $\chi^{(2)}$ surface at low wavenumbers. This sign change from negative to positive as the pH was increased was attributed to the deprotonation of silanols and the increase in association of waters to charged siloxides with their accompanying sodium cations.

4.2 Experimental Section

4.2.1 Materials

NaCl (99.99%, trace metals basis, Alfa Aesar) was used to prepare salt solutions and KCl (99.999%, trace metals basis, Acros Organics) was used to calibrate the SurPASS instrument. NaOH (99.99%, semiconductor grade, trace metals basis, Sigma-Aldrich) and HCl (trace metal grade, Fisher Chemical) were used for pH adjustments. HPLC-grade MeOH (Fisher Chemical) was used for substrate cleaning. Sulfuric acid (95.0-98.0%, Caledon Laboratories) and hydrogen peroxide (30% w/w in H_2O, Sigma-Aldrich) were mixed in a 3:1 ratio and used for piranha cleaning substrates. All materials were used without further purification. Ultrapure deionized water (18.2 MΩ·cm) was used after deionization from a Milli-Q Direct 8 Water Purification System (Millipore, ZR0Q008WW). IR-grade fused quartz hemispheres (Almaz Optics, KI, 1 in. diameter)

were used for SFG experiments. IR-grade fused quartz windows (Almaz Optics, KI, 2.5 in. diameter, 8 mm thickness) were used for zeta potential experiments. Sealing and spacer foils (Anton Paar, 97835 and 97834) were used to construct the flow channel along the fused quartz windows in the SurPASS clamping cell (Anton Paar, 22653).

4.2.2 Sample Preparation

The sample preparation is the same as that of Chapter 3, with the exception that the stock solution was 50 mM NaCl and titrants were prepared by dissolving NaOH or adding HCl to solutions containing 50 mM NaCl background electrolyte.

4.2.3 Laser Assembly

The laser assembly follows that described in Chapter 3 with no modifications.

4.2.4 SFG Experiments

The SFG experimental procedure is similar to that of Chapter 3, with some modifications. A fused quartz hemisphere (Almaz Optics, KI, 1 in. diameter) with a gold-coated planar side (200 nm) was mounted to the clean sample cell. The laser was aligned and the SFG signal was optimized using the signal from the silica/gold interface. A nonresonant reference spectrum was collected at a single delay setting using 6-7 IR pulses with centres ranging from ~2900-3500 cm^{-1}. A polystyrene calibration film (International Crystal Laboratories, 38 μm thick) was used to calibrate the detected frequency by comparison to three known polystyrene aromatic C-H absorptions

centred at 3026, 3059 and 3081 cm^{-1}. The gold-coated hemisphere was then exchanged for a freshly cleaned fused quartz hemisphere. The cell cavity was rinsed five times with ultrapure water and then allowed to equilibrate in ultrapure water for 30 minutes. Pure water was followed by a 10 mM NaCl solution and allowed to equilibrate for 30 minutes, the peak maximum of which at 3200 cm^{-1} we normalize our intensity data. The 10 mM NaCl solution was then exchanged for a 50 mM NaCl solution which was previously titrated to pH 10. The solution was allowed to equilibrate for 30 minutes before data collection. The solution pH was then decreased in situ using an HCl solution. Each subsequent solution was allowed to equilibrate with the fused quartz surface for at least 15 minutes before measurement. After collecting all sample spectra, the hemisphere was exchanged once more for the gold-coated hemisphere and a reference spectra was collected. Sample spectra were collected in ssp polarization (s-sum frequency, s-visible, p-infrared) for 120 s at each frequency used for the nonresonant reference. Reference spectra were collected in ppp polarization for 1s per centre frequency averaged over 10 acquisitions. All spectra were background corrected by subtraction with a background spectrum collected immediately prior to each sample or reference spectrum. Background spectra were collected by blocking the IR laser and acquiring signal at a single pulse. Final, gold normalized spectra were intensity normalized to the maximum observed at 10 mM NaCl in the ssp polarization combination.

4.2.5 Zeta Potential Experiments

The zeta potential experimental procedure is similar to that of Chapter 3, with some modifications. Measurements were performed on a SurPASS Electrokinetic Analyzer (Anton Paar) using the clamping cell. The conductivity probe (Anton Paar, 18116) was calibrated prior to each experiment with 0.1 M KCl solution. Before setting up the clamping cell, the electrodes were

connected by connection tube (Anton Paar, 100083) and the instrument was cleaned with ultrapure water four times (300 s for each cleaning cycle). After mounting the clamping cell to the instrument and connecting the electrodes, the instrument was filled with ultrapure water (200 s fill time) and a flow check was performed (500 mbar) to confirm linear flow rate with respect to pressure. The cell was then rinsed with ultrapure water (500 mbar for 500 s) and allowed to equilibrate for 30 minutes. Water was followed by 10 mM NaCl, which was finally exchanged for a 50 mM NaCl solution at pH 10. Both 10 mM NaCl and 50 mM NaCl at pH 10 were allowed to equilibrate for at least 30 minutes inside the instrument. Solution pH was decreased using a prepared HCl solution. At each solution pH, the cell was allowed to rinse (500 mbar for 500 s) and equilibrate for at least 15 minutes before measurement. Measurements were performed under streaming potential mode with a rinse target pressure of 500 mbar for 180 s and a ramp target pressure of 400 mbar for 20 s. The clean, calibrated conductivity probe was allowed to sit in the sample solution during the entire experiment.

4.3 Results and Discussion

4.3.1 Sum Frequency Spectra and Zeta Potentials of the Silica/Water Interface at 50 mM NaCl from pH 10 to 2

The sum frequency intensity of the silica/water interface in the presence of 50 mM NaCl exhibited bimodal behaviour from pH 10 to 2 with a minimum in the integrated SFG intensities occurring at pH 4 (Figure 4.1). This trend has been observed at several ionic strengths and was attributed to a flip in water molecules at lower pH by either overcharging of the silica surface by monovalent ions or hydration sphere asymmetry induced by proximity to the silica surface.[19, 99]

The overcharging mechanism would result in an isoelectric point (IEP) at the interface near pH 4, however, our zeta potential measurements performed under the same conditions indicated this was not the case (Figure 4.1b). Due to the constant lineshape of $\chi^{(3)}$, and the negative zeta values measured at all pH values, a net reorientation at low wavenumber in the current study may result from two scenarios: a large constant surface contribution opposite in phase to the potential-dependent contribution, or a surface contribution which experiences a net flip. If the surface contribution were constant, then this surface spectrum should closely resemble the spectrum measured near the point of zero charge (PZC) around pH 2, where ions are expected to play less of a role. Yet the complex spectra of silica/water[90] and α-quartz/water[82] near the PZC do not resemble the surface bound water spectrum recently measured at high pH and high salt concentration.[100] Therefore it is our hypothesis that the surface waters do indeed reorient with changing solution pH.

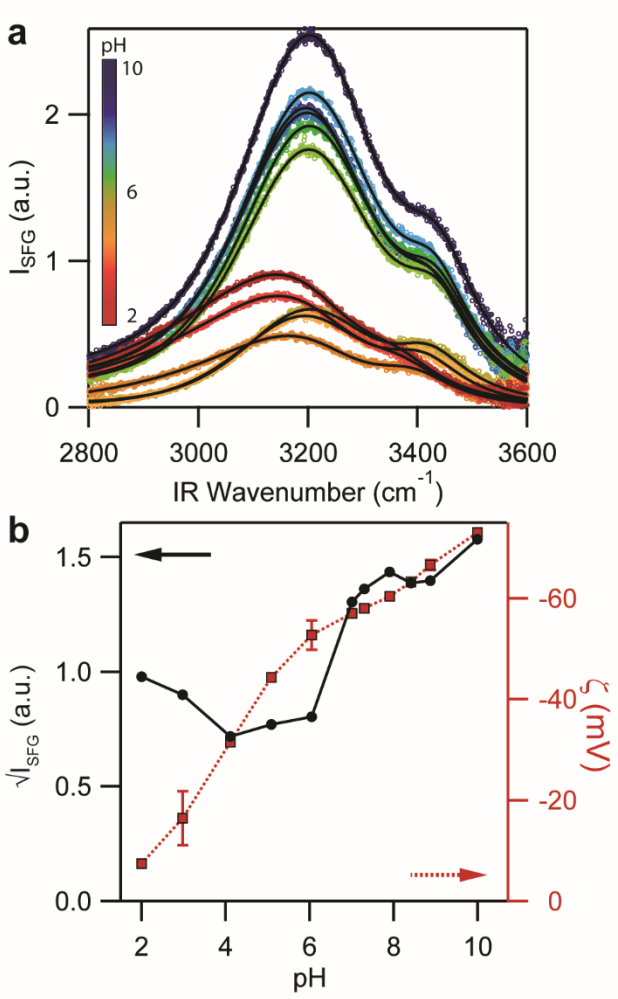

Figure 4.1 (a) Local field corrected sum frequency generation from 2800 to 3600 cm^{-1} at the silica/water interface with 50 mM NaCl from pH 10 to 2. Black lines are fits to the intensity. (b) The square root of the integrated SFG intensity (black circles, left) vs the zeta potential (red squares, right). Error bars on the zeta potential are the standard deviation between experiments.

4.3.2 Estimating the Nonlinear Susceptibilities from the Maximum Entropy Method

To test our hypothesis, we aimed to deconvolute the spectral contribution of the surface bound waters from the potential aligned waters. For this analysis, the phase of the SFG signal,

which is inherently lost in the intensity measurement, is required. To retrieve this phase information, we used the maximum entropy method (MEM), which has been previously used to predict the complex spectra from SFG intensity measurements.[184-186, 191] Prior to its application, we corrected the intensity spectra for local field effects (see Chapter 2) and fit the spectra to the square of the sum of Lorentzians (see Chapter 5 for equation 5.1, and see Appendix for fitting parameters) to estimate the baseline (Figure 4.2). A more in depth discussion of the MEM can be found in Chapter 3, but briefly, if we consider the spectral entropy, which is proportional to the integrated intensity spectrum, the MEM finds the most probable phase between the real and imaginary components without adding new information to the system (i.e. maximizing the spectral entropy). However, a remaining error phase modulates the final outcome which requires *a priori* knowledge of the system to estimate correctly. For this, we are fortunate to consider the measured heterodyne spectra of the silica/water[90] and α-quartz/water[82] interfaces. Our selection criteria have been described elsewhere (see Chapter 3),[191] however a modification to our previous methodology is in the phase change over the pH range studied. Where a single phase value was suitable in estimating the complex spectra over the salt concentrations previously studied, a gradually changing phase (with respect to pH) was required to reconstruct the measured complex spectra over the current pH range, particularly at the lower pH values. Furthermore, a frequency-independent phase was used, which we note may be a source of error at the high and low wavenumber extremes as the error phase has been known to vary at the edges of the spectral window due to the periodicity of the MEM.[184, 192-195] Although using our expanded frequency window will have a similar effect as the frequency squeezing procedure described in the literature which is to make the error phase more linear and shallow. Nevertheless, the reconstructed complex spectra from the intensity measurements closely resemble the phase measurements (Figure 4.3a).

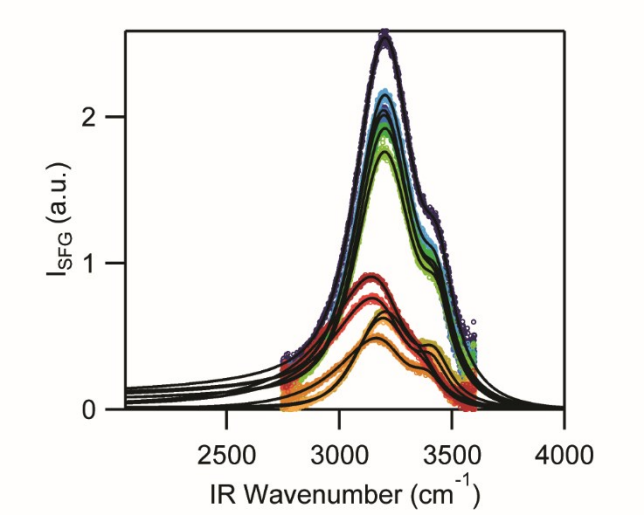

Figure 4.2 Fit of the local field corrected intensity spectra expanded from 2050 to 4000 cm^{-1}.

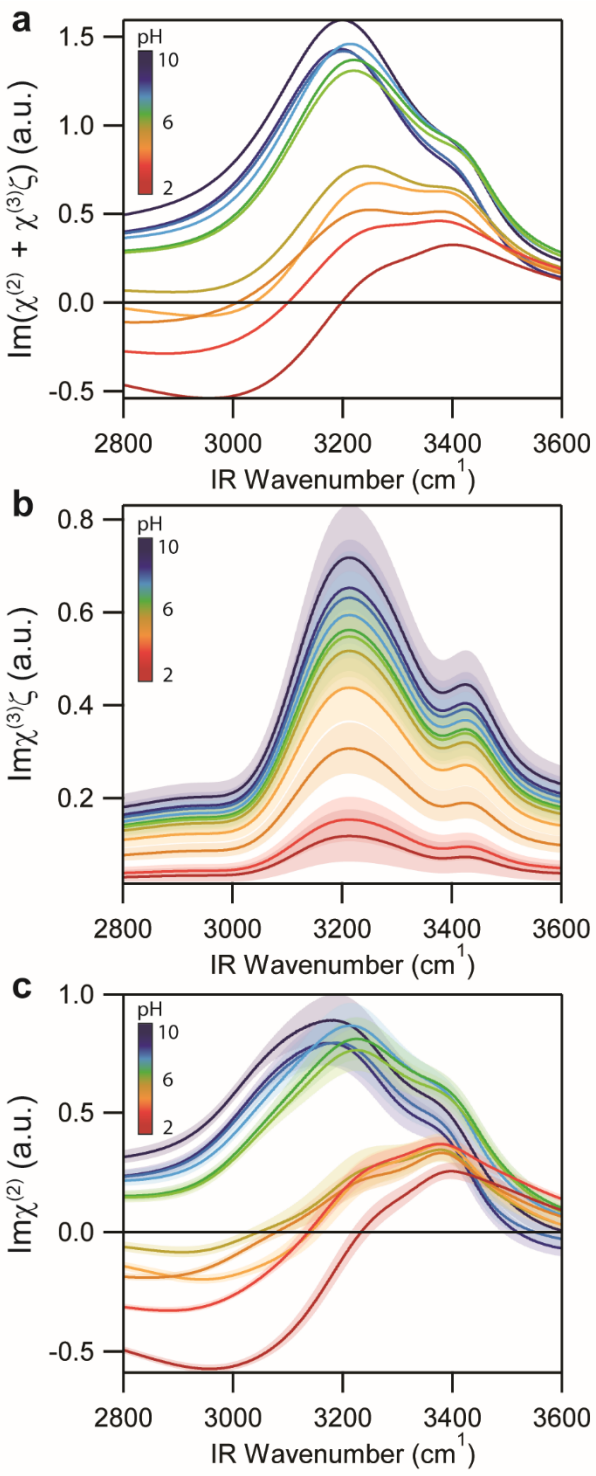

Figure 4.3 Imaginary component of (a) the total nonlinear susceptibility, $\chi^{(2)} + \chi^{(3)}\zeta$, (b) the potential aligned contribution, $\chi^{(3)}\zeta$, and (c) the surface nonlinear susceptibility, $\chi^{(2)}$. Shaded

regions are the uncertainty propagated from the range in measured ζ potentials for two separate experiments.

4.3.3 Extracting the Surface $\chi^{(2)}$ from the Nonlinear Susceptibilities Using the Zeta Potentials

In our previous work, we were able to calculate the $\chi^{(3)}$ lineshape under the assumption of an unchanging surface $\chi^{(2)}$ between 10 and 50 mM NaCl at pH 6 (see Chapter 3). While the presence of ions clearly affects the surface structure of silica[47, 51, 53-54, 175] and its surface bound waters,[191] the dominant change in this ionic strength regime (10-50 mM) seemed to result from surface charge screening,[80, 115, 124-125, 134] leading to a change in surface potential rather than a change in surface charge density due to sodium-induced deprotonation, which supports our assumption that the surface structure of water should not change over this range. Yet, for pH changes, this change in surface potential stems directly from changes to the surface charge density. Therefore the protonation/deprotonation of silica renders the assumption of an unchanging surface $\chi^{(2)}$ invalid. To overcome this problem, we used the $\chi^{(3)}$ lineshape produced in our previous work, which was in good agreement to that measured by Tian, Shen and coworkers.[101]

Coupling $\chi^{(3)}$ with the measured zeta potentials, and accounting for slight wavevector mismatch yields a diffuse layer component (Figure 4.3b) that can be subtracted from the total nonlinear susceptibility (Figure 4.2a) to yield the remainder, which is due to the surface bound waters (Figure 4.2c). At low pH, the surface spectrum appears similar to the total nonlinear susceptibility as the PZC is ~pH 2. This $Im\chi^{(2)}$ surface spectrum exhibits oppositely aligned modes centred around 3000 and 3400 cm^{-1}. As the pH was increased to near neutral values, the

large negative mode at low wavenumber became smaller in magnitude, while spectral contributions increased at 3200 cm^{-1}, accompanied by a small decrease in the magnitude at 3400 cm^{-1}. At even higher pH values, the surface imaginary spectrum is positive and consists largely of a broad feature centred around 3200 cm^{-1}. The magnitude around 3400 cm^{-1} also increased slightly, although this may be due to the tail of the growing 3200 cm^{-1} mode.

The imaginary spectrum of the surface waters at pH 6 is similar to our previous observations at 50 mM NaCl in CO_2-equilibrated water (pH 5.8),[191] indicating good compatibility with our previously extracted $\chi^{(3)}$. Furthermore the $Im\chi^{(2)}$ spectrum at pH 10 closely resembles that observed in heterodyne measurements by Tahara and coworkers at pH 12,[100] although we did not observe the very small negative features at high wavenumber they measured at high pH. This discrepancy may be due to the exclusion of a 3680 cm^{-1} mode in our fitting procedure (discussed in Chapter 3), or the difference in pH, since Tahara and coworkers measured their spectra at pH 12 while we measured up to pH 10. Furthermore, the trends we observed with increasing pH are similar to those observed recently at the gate-controlled silicon/native oxide/water interface with increasingly negative gate voltage.[129]

4.3.4 Reconstructing the Bimodal pH Dependence of SFG Intensity from the Silica/Water Interface at Varying Potential Values

It is now clear that the surface water structure is changing with pH in the $Im\chi^{(2)}$ surface spectra. Integrating the $Im\chi^{(2)}$ surface spectra (Figure 4.4f) results in a bimodal trend similar to that observed previously for the intensity spectra at 500 mM NaCl.[169] Interestingly, the integrated pH dependent intensities of the surface waters mirror the trend in aggregation time as a function

of pH observed for colloidal silica,[1] which suggests that the silica surface is less stable when there is less alignment of surface waters. Two factors generally affect the aggregation times of oxide particles: the surface charges and their counter ions, and the surface hydration waters.[1] Since pH 2 is approximately the PZC of silica, the metastability at low pH may originate entirely from the hydration waters, which resist the attack of hydroxide ions on silica that catalyze the aggregation. Although the concentration of hydroxide ions is fairly low at pH 2, the aggregation times were found to increase below this pH, suggesting more than one pathway for aggregation.[1]. Previous measurements observed a decrease in the pH where the minimum SFG intensity occurred when the salt concentration was decreased.[99] We now consider whether a flipping $Im\chi^{(2)}$ surface could account for the bimodal behaviour observed in the intensity spectra at all salt concentrations studied. If we briefly assume the surface structure (i.e. $Im\chi^{(2)}$ surface) is independent of ionic strength, and in the absence of any overcharging, we would expect the intensity minimum to shift to lower pH values with decreasing ionic strength (i.e. increasing potential) and to higher pH values with increasing ionic strength (i.e. decreasing potential). Of course, the surface structure is dependent on ionic strength, however, that dependence appeared weaker at ionic strengths above 10 mM.[128, 191] To demonstrate this general idea we used our surface $\chi^{(2)}$ collected at 50 mM NaCl and $\chi^{(3)}$ from our previous work[191] to reconstruct intensity spectra at varying potentials to simulate a changing ionic strength (Figure 4.4). We found that the intensity minimum did indeed shift to lower pH values with increasing potential strength (Figure 4.4e). However, we cannot completely rule out overcharging, which would lead to a flip in sign of $Im\chi^{(3)}\Phi_{SL}$. Due to limitations of our surface zeta potential analyzer, we could not measure the zeta potential at the high ionic strengths used in our other studies,[19, 99, 169] as there is some evidence for overcharging with monovalent salts. For example, Franks observed the IEP of amorphous silica shift to higher pH values with

increasing monovalent salt concentrations above 0.1 M,[49] Kosmulski observed positive electrokinetic potentials on fumed silica with increasing concentrations of monovalent, chloride-containing salts,[47] and Bolt observed positive charge densities at pH 2 with NaCl concentration above 1 M by titration.[196]

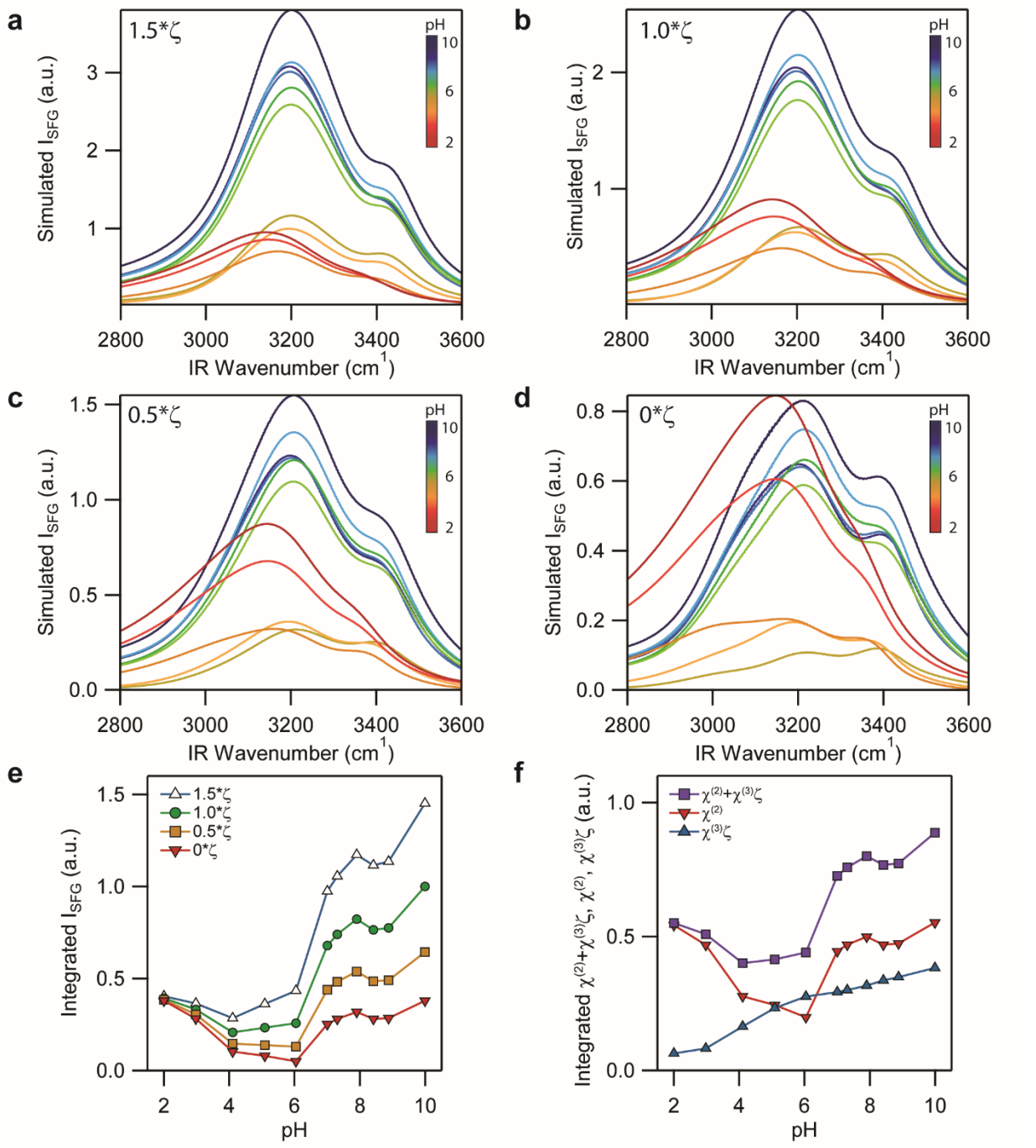

Figure 4.4 Reconstructed SFG intensities using the surface nonlinear susceptibility of 50 mM NaCl and (a) 1.5x, (b) 1x, (c) 0.5x, and (d) 0x the zeta potential. (e) Integrated simulated intensities from a-d, and (f) relative contributions to the total nonlinear susceptibilities at 50 mM NaCl.

4.3.5 Reinterpreting the Methodology with which to Calculate the Dissociation Constants of Silica

Since changes in surface water H-bond structure may be a direct consequence to changes occurring to the underlying silica structure, we consider the trend in surface water response to gain insight into the silica acid-base chemistry. The rapid decrease in signal from pH 2 to 6 may be correlated to the dissociation of silanols, in which case observe a pK_a to be around pH 3.5, which is consistent with that observed by us and others.[59, 121, 139] Beyond pH 6 the magnitude rises until a plateau ranging from pH 8 to 9, which may suggest a pKa around pH 7. The increase observed beyond pH 9 may then be due to a higher pKa. The possible presence of three pKa's is similar to that reported by SHG when initializing a titration at a high pH of 12.[139] Rather than the commonly reported two pKa's around pH 3.8 and 8.6, three pKa's were observed which were attributed to sample hysteresis.[139] In the current study, we initialized the pH titration at pH 10, and may be observing a similar behaviour.

4.3.6 Interpreting the Orientation of Surface Waters from the Imaginary Surface Spectra Over the pH Range Studied

Given the results of this study and the spectral contributions across the entire OH stretching region of water observed from the surface bound waters, we attempt to refine previous spectral assignments of the observed modes.[99-100] At pH 2, where the silica surface is predicted to be near neutral, fully hydrated, and consisting predominantly of silanols,[1, 40] we observe two modes of opposite phase. We attribute these modes to water acting as hydrogen bond donors and acceptors with the silanols. As a note, it might also be possible for water to hydrogen bond donate to the

oxygen of siloxane bridges, despite their hydrophobicity,[1] which has been suggested to occur spectrally at high wavenumbers around 3680 cm^{-1}.[75] As the pH is increased, silanols become deprotonated to yield charged siloxides. The appearance of charged sites will have multiple effects on the surface water structure. One is that the charges will attract counter ions (in this case, sodium), which themselves have been demonstrated to have an effect on the surface water structure of charged silica.[191] Another is that the ratio of hydrogen bond donor and acceptor sites on silica will change, with an increase expected for the latter. And finally, the strong electrostatic forces of the charged siloxides and sodium cations may shift the centre frequencies of the water resonances through the Stark Effect.[197]

Near the PZC.

The imaginary sign of $\chi^{(3)}\zeta$ reports on the absolute orientation of aligned diffuse layer waters. In our case, the positive value indicates waters with hydrogens pointed towards the surface (H-down). At the surface, the approximate bonding configuration of each silanol can accept two H-bonds and donate one H-bond (Figure 4.5a). Therefore twice as many waters can be H-bond donors than H-bond acceptors. The net orientation of H-bond donors will be in the H-down (towards the surface) orientation, although the extent depends highly on the angle of the Si-O bond with respect to the surface normal. For simplicity we assume an Si-O bond angle of less than 90° with respect to the surface normal. With this in mind, we assign the H-bond donors, which have the same net orientation as the potential-aligned diffuse waters (net H-down), to the 3400 cm^{-1} mode. The negative mode around 3000 cm^{-1} is then given to the H-bond acceptors, which should generally have an H-up orientation (away from the surface into the bulk). Although there are twice as many possible H-bond donor configurations of water to silica than H-acceptors, our previous simulations indicated that the low wavenumber mode was intrinsically more SFG active. In

particular, this simulation indicated 1.8 times the amount of oscillators contributing to the high wavenumber region than the low wavenumber region near the PZC, which supports our assignment.[169] Additionally, the bonding between the silanol oxygen and the H-bond donor waters may partially decouple the vibrational activity of those waters (i.e. two independent oscillators, or highly asymmetric character).[91] In this case, the OH groups donating hydrogens to the silanol would be dominantly pointing down (depending on the Si-O bond angle), while the other hydrogen of water, due to the freedom of rotation about the H-bond, may be randomly distributed. This random distribution, depending on the hydrogen bonding environment from neighbouring species, would lead to cancellation of signal from this OH bond.[91] Furthermore, the H-bond accepting water would likely not be decoupled and exhibit symmetric and asymmetric stretching and a Fermi resonance, which may be the cause of the differences observed between the spectra of the silica/water and silica/HOD interfaces at pH 2.[90]

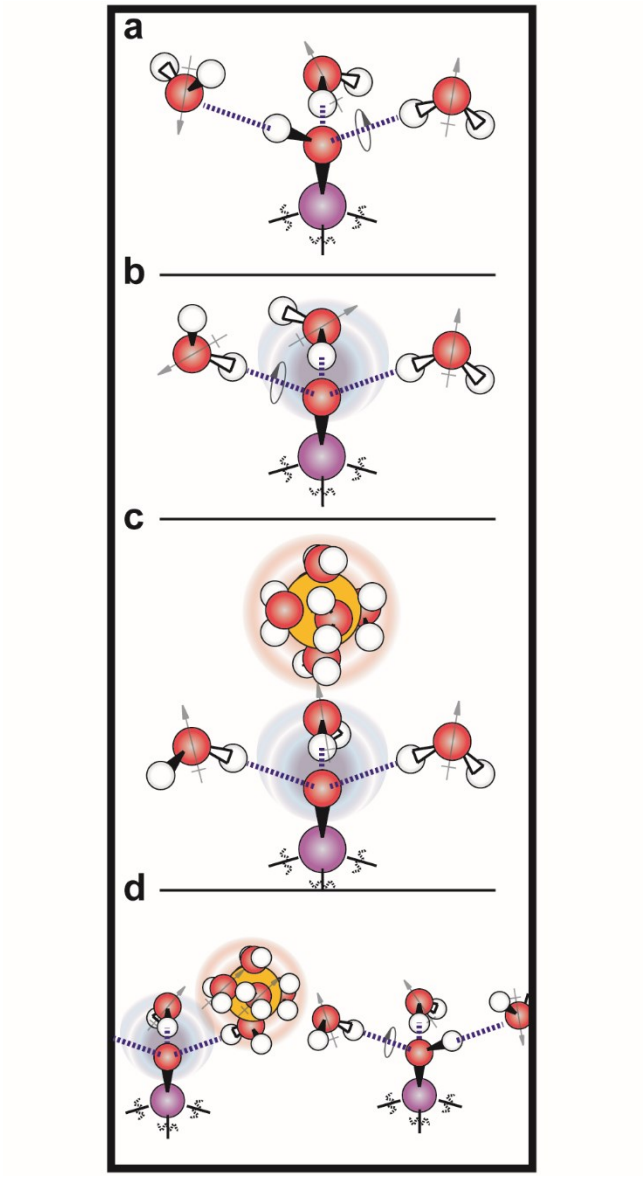

Figure 4.5. Water conformations about (a) a neutral silanol, and (b) a charged siloxide (c) which has attracted a sodium counter ion, and (d) which has exchanged a surface water for cation hydration water. Purple, red and white spheres are silicon, oxygen, and hydrogen atoms, respectively. The black and white wedges represent covalent bonds out of and into the page, respectively, while dashed blue lines represent H-bonds. Grey arrows represent the permanent dipole moment of water, and loops indicate freedom of rotation about H-bonds (not all rotations

are shown, for clarity). The orange sphere represents a sodium cation. Transparent blue and red halos about the siloxide and sodium represent negative and positive charge, respectively.

At higher pH.

Upon increasing the pH to near neutral, we observe the initial mode at pH 2 around 3000 cm^{-1} decrease in magnitude, while that around 3200 cm^{-1} increases. As the surface is deprotonated with increasing pH, the number of neutral silanol sites, and therefore the number of H-bond accepting sites decreases. The previously H-bond accepting waters would then reorient to H-bond donate with the siloxide. The loss in magnitude of the 3000 cm^{-1} mode is in agreement with this interpretation. The initial increase in magnitude around the 3400 cm^{-1} mode may be a result of an increasing number of H-bond donors to silica, accompanied by a decrease in destructive interference from the negative 3000 cm^{-1} mode. However, the resonance frequency of the H-bond donors to siloxides may be different than those to silanols, which may also be a cause of the 3400 cm^{-1} signal drop at higher pH values. The appearance and increase of the 3200 cm^{-1} mode appears to be related to the presence of the charged siloxides, which increases as the surface is further deprotonated.

The similarity between the observed surface water trends over the current pH range studied and those observed over the salt range studied in Chapter 3, invokes a comparison between the two studies. In the case of increasing salt concentration, a net flip in waters was observed with increasing ionic strength, and this flip was also observed as the pH was increased. If the potential at the slipping plane, ζ, is assumed to be equivalent to that at the OHP, Φ_{OHP}, the Grahame equation[23] can be used to calculate the charge density of the OHP, σ_{OHP}, according to

$$\sigma_{OHP} = -\sqrt{8\varepsilon_0\varepsilon_R CRT}\sinh\frac{zF\Phi_{OHP}}{2RT}, \tag{4.2}$$

where ε_0 and ε_R are the permittivity of free space and the relative permittivity of water, respectively, C is the concentration of ions, R is the gas constant, T is the temperature, z is the ion valency, and F is the Faraday constant. Using equation 4.2 under the assumption stated above, we find the charge density of the OHP to increase with increasing ionic strength (Figure 4.6). This may be explained by deprotonation of silanols induced by salt, leading to an increase in the charge density at the surface plane and by extension, the OHP. Similarly, from pH 2 to 10 at near constant ionic strengths, the charge density of the OHP also increased. Therefore we suggest the charge density at the surface plane, which reports on the number density of charged siloxides, to be closely linked to the orientation of surface waters. Comparing the OHP charge densities reveals similar magnitudes at high ionic strength at pH 2 and low ionic strength at pH 5.8. Differences in charge densities at 50 mM ionic strength and ~pH 6 between the salt and pH titrations may be explained by sample hysteresis since the pH titrations were initialized at pH 10. Yet the calculation through equation 4.2 is only an approximation since the position of the slipping plane may not coincide with the position of the OHP, and is expected to change with ionic strength.[41] In particular we point to the increasing charge densities from 10 to 50 mM ionic strength, where we observed little change to the surface water structure (Chapter 3), and others observed a plateau in SFG signal,[108, 124] and surface contribution.[128]

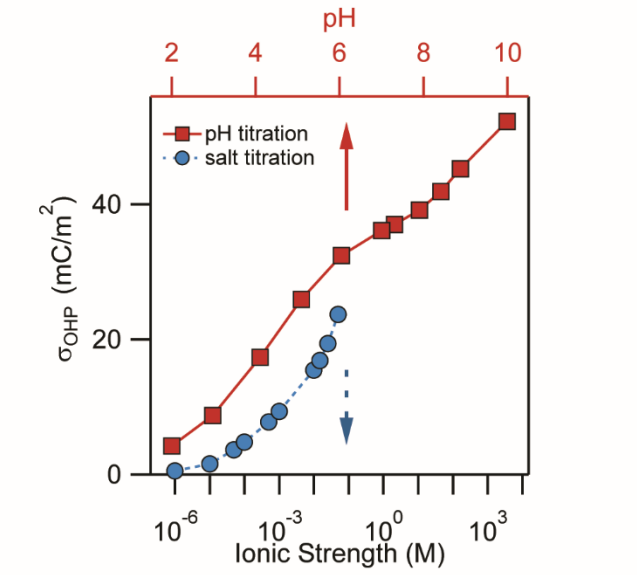

Figure 4.6 Charge densities of the OHP calculated from the zeta potentials from pH titrations at 50 mM ionic strength and salt titrations at pH 5.8.

Furthermore, where H-bond donor waters were assumed relatively free to rotate about their H-bonds with silanols at a neutral surface, these H-bond donors to charged siloxides may experience an aligning force leading to a preferential orientation of hydrogens pointed toward the surface, which would originate from the presence of negatively charged siloxides below. However, due to the presence of counter ions overhead, attracted by the negatively charged siloxides, a similar force acting on the surface waters, as suggested in Figures 4.5c and d, may also induce preferential orientation in the same direction. Additionally, we suspect some of the cation equatorial hydration waters, also free to rotate, to partially point their hydrogens down, further contributing to the number of aligned waters. Another case is that one of the surface H-bond donors is exchanged by a cation hydration water. Although such behaviour was suggested not to occur for sodium,[116, 198] recent MD simulations suggested that sodium does exchange hydration waters with those of silica and may form an additional bond to a neighbouring atom in a more side-on bonding orientation, rather than overhead (Figure 4.5d).[199] In either case, the surface waters and the cation

equatorial hydration waters would be reoriented preferentially between the two charges. Furthermore, in the case of a contact pair, in which a sodium cation bonds directly with the oxygen of a siloxide or silanol, we would expect similar reorientation behaviour of the hydration waters. Finally, the structure of the remaining H-bond acceptors from silanols may be disrupted by an increasing number of cations near the surface, resulting in the decrease observed at 3400 cm^{-1} at the highest pH values studied.

4.3.7 A Note on the Relation Between the Zeta Potential to the Surface Potential

The use of a measured zeta potential rather than a calculated surface potential has been discussed in Chapter 3, but in short, because of the arbitrary units involved, and since we calculate our own $\chi^{(3)}$, it is not the absolute value of the potential which is important. The magnitude of $\chi^{(3)}$ stems from the use of the zeta potentials which are generally lower than calculated Gouy-Chapman potentials, therefore it is the relative potential difference between all data points that determines the outcome (surface $\chi^{(2)}$). Yet as a note, because we have imported our $\chi^{(3)}$ from previous work, we maintain the same scale and normalization procedures. Furthermore, as demonstrated in Chapter 3, using a calculated surface potential rather than a zeta potential resulted in similar surface water spectra, it is possible the zeta potential to be nearly linearly related to the surface potential, which would depend on the position of the slipping plane.[41-42] However, calculations of the surface potential from XPS binding energies found the relationship deviates from linearity at higher pH values.[37, 41-42] Yet, similarities between SHG measurements and electrokinetic measurements of silica in 500 mM NaCl[42] may suggest the zeta potential adequately accounts for the waters aligned by the static electric field. Yet it may be more accurate to say the

Stern layer potential accounts for the aligned waters, since the slipping plane may be located some distance into the diffuse layer. Therefore nonlinearities between the Stern layer potential and the zeta potential may affect the analysis.

4.4 Conclusion

In summary, we have measured the silica/water interface using vibrational sum frequency generation spectroscopy in the presence of 50 mM NaCl over a pH range of 10 to 2. The bimodal pH dependent behaviour was revealed by complementary zeta potential measurements to not be the result of an isoelectric point. Through a deconvolution of the data, and the use of the maximum entropy method, we extracted the spectral contribution of the surface bound waters from the total SFG signal. This surface contribution was found to change over the pH range studied to arise from three frequency regions (3000, 3200, and 3400 cm^{-1}), depending on the pH. We speculated on the origin of the three dominant modes observed at the surface and hypothesized that the 3000 cm^{-1} and 3400 cm^{-1} modes were more associated with neutral silanols, while the 3200 cm^{-1} mode was closely linked to charged siloxides. The pH dependent behaviours of the surface waters presents a potential new method to determine the acid dissociation constants of silica, for which we found three: pH ~3.5, ~7, and greater than 9.

Chapter 5

Influence of High pH on the Organization of Acetonitrile at the Silica/Water Interface Studied by Sum Frequency Generation Spectroscopy

"*Influence of High pH on the Organization of Acetonitrile at the Silica/Water Interface Studied by Sum Frequency Generation Spectroscopy*" **Rehl, B.**; Li, Z.; Gibbs, J. M. *Langmuir* **2018**, *34*, 4445-4454.

5.1 Introduction

Acetonitrile (ACN) is one of the most widely used solvents in chemistry. The acetonitrile molecule contains a hydrophobic methyl group and a highly polar cyanide group; this unique hydrophobic/polar combination results in the capacity to dissolve a wide range of organic compounds. Moreover, these amphiphilic properties render acetonitrile important for heterogeneous catalysis, especially in aqueous media, in which interactions with a metal oxide surface play a key role in partitioning reactants among the various solvent phases.[200-201] As acetonitrile is also miscible in water at any ratio, the acetonitrile-water mixture is a commonly used mobile phase in chromatography and is effective in the separation of many chemical and biomolecular species.[202-209]

Hydrophilic interaction chromatography (HILIC) is one such example, in which silica is the stationary phase and the acetonitrile-water mixture is the mobile phase. The exact mode of action for HILIC is still not fully understood, but it is generally accepted that the enhanced separation arises from a phenomenon akin to liquid-liquid extraction. It is proposed that there exists a water-rich phase near the silica surface and an acetonitrile-rich phase further away from the silica; highly polar compounds will be attracted to the water-rich phase, while less polar compounds will gravitate towards the acetonitrile-rich phase.[210] Molecular dynamic simulations support that a monolayer of ordered water is present at the silica/acetonitrile-water interface.[211] However, nonlinear optical techniques suggest that ACN is also concentrated at the interface compared with the bulk liquid phase, supporting that an acetonitrile-rich layer is also present.[212] Moreover, evidence of direct hydrogen-bonding between ACN and silica has also been observed in these nonlinear optical studies on planar silica as well as in quasi-elastic neutron scattering

studies on mesoporous silica, suggesting some penetration of the water layer by acetonitrile at the interface.[212-213]

One method to tune HILIC selectivity and analyte retention times is by varying the pH of the ACN-water mixture. It has been observed that high pH directly affects the retention times of ionizable solutes in HILIC in ways that are not immediately apparent in terms of analyte hydrophilicity; for example, a HILIC study on the retention behaviour of peptides at various pH values demonstrated non-obvious trends between the aqueous pH and retention times of the neutral, acidic and basic amino acids.[214] Moreover, the authors concluded that the understanding of the separation mechanism of HILIC is incomplete, due to the difficulty in predicting retention times of amino acids at high pH using chromatographic retention models.[214] Indeed, while the ordering of water at the silica surface is known to be affected by pH,[19, 99] the influence of pH on acetonitrile order in ACN-water mixtures is unknown. In the case of the silica/water interface, increasing the solution pH results in more aligned water due to an increase of negative surface charges at the silica surface, which suggests that pH could strongly affect the ACN-water interfacial structure. It is therefore important to determine the pH-dependent structure of the interface at the molecular level, which should aid in predicting the pH-dependent behaviour of analytes during HILIC separations.

Based on simulations supported by experimental data, acetonitrile molecules are proposed to form patches of lipid-bilayer-like structures at the silica surface (at neutral pH), as a result of hydrophobic interactions between methyl groups.[211-212, 215-222] According to molecular dynamics (MD) simulations by Fourkas, Walker, Weeks, and coworkers, the first sublayer at the silica surface, or the inner leaflet, has the most ordered structure, in which the nitrogen of the nitrile groups point toward the silica surface while the methyl groups point toward bulk solution; the

second sublayer, or the outer leaflet, is less ordered than the first one, in which methyl groups interdigitate with methyl groups from the first sublayer and point towards the silica surface.[216] Additionally, in the presence of water and acetonitrile, MD simulations by Mountain reveal that this outer leaflet of the acetonitrile bilayer has a higher density of acetonitrile molecules than the inner leaflet.[211] For both ACN and aqueous mixtures, the bilayer pattern keeps repeating and becomes less and less ordered with distance from the surface.[216] In agreement with MD simulations, experimental evidence of this bilayer structure was found to exist not only at the silica/acetonitrile interface, but also at the silica/acetonitrile-water mixture interface, persisting even at very low acetonitrile concentrations in the form of patchy bilayers.[212]

In this work, vibrational SFG was employed to study the organization of acetonitrile molecules at the silica surface in the presence of water (ACN volume fraction = 0.4; ~20 mol%). Orientation analysis revealed that the net orientation of acetonitrile molecules in the second sublayer at the silica/acetonitrile-water interface did not change significantly as the solution pH of the water was increased from a natural pH of ~6 to a high pH of ~12. However, increasing solution pH resulted in a decreased number of ordered interfacial acetonitrile molecules around pH 10. This abrupt change in interfacial structure at higher pH provides insight into the unusual trends observed in pH-dependent retention times for charged analytes using HILIC.

5.2 Experimental Section

5.2.1 Materials and Sample Preparation

Acetonitrile (>99.9%, HPLC grade, Fisher), NaCl (>99.0%, Sigma-Aldrich) and NaOH (99.99%, Sigma-Aldrich) were purchased and used without further purification. Ultrapure

deionized (18.2 MΩ•cm) water was used shortly after deionization by a Milli-Q Plus ultrapure water purification system (Millipore). Prior to each experiment, a fused silica hemisphere (ISP Optics, 1-inch diameter, IR-grade) was sonicated in water and then methanol, followed by drying in an oven for 10 min at 90 °C, then cooling to room temperature. For probing the nitrile region, a calcium fluoride (CaF_2) hemisphere (ISP Optics, 1-inch diameter) was coated with a thin layer of of silicon (3 nm) and silica (125 nm) by electron beam vapor deposition, described elsewhere.[223]

5.2.2 Adjustment of Solution pH

1 L of 16.7 mM NaCl aqueous stock solution was prepared and used to make all aqueous fractions of the acetonitrile. The pH of each aqueous fraction was adjusted using a concentrated NaOH aqueous solution made from the stock. At each aqueous pH value, 6.0 mL aqueous solution was mixed with 4.0 mL acetonitrile, which corresponded to 18.6% mole fraction of acetonitrile. The total volume of the mixture was 9.9 mL, with a total concentration of 10.1 mM NaCl as background salt. All pH values reported in this paper correspond to pH of the aqueous fraction before mixing with acetonitrile.

5.2.3 Laser System and Experimental Setup

The laser setup was different during the collection of SFG for this project than in the other chapters. Our vibrational SFG experimental setup can be found in Figure 5.1. Our laser system consists of a Ti-sapphire oscillator (Spectra Physics, Maitai, 80 MHz), a Nd:YLF laser (Spectra Physics, Empower) and a regeneratively amplified laser (Spectra Physics, Spitfire Pro, 1 kHz, 120 fs, 3.3 W). The Maitai and the Empower were used to seed and pump the Spitfire to generate an

800 nm beam. The amplified 800 nm light from the Spitfire was passed through a 35/65 beam splitter, and 2.3 W of the output was used to pump a non-collinear optical parametric amplifier (TOPAS-C and NDFG, Light Conversion) to generate IR light, while some of the remaining 800 nm light passed through a Fabry-Perot etalon (TecOptics) to generate picosecond pulses (full width half maximum (FWHM) of 10 cm^{-1}). The IR and visible beams were focused at the sample using a CaF_2 (focal length = 500 mm, Thorlab) or BK7 (focal length = 400 mm, Thorlab) focusing lens, respectively. Pulse energies of 10-20 μJ/pulse of visible and ~14 μJ/pulse of IR were used, and the beams were slightly defocused to minimize sample damage. The infrared and visible pulses were directed through the IR grade silica hemisphere at incident angles of 64° and 60°, respectively, with respect to surface normal, and the SFG was collected in the reflection beam. SFG was detected using a spectrograph (Acton SP-2556 Imaging Spectrograph, grating: 1800 g/mm with 500 nm blaze wavelength) connected to a thermoelectrically cooled charged coupled device camera (Acton PIXIS 100B CCD digital camera system, 1340 x 100 pixels, 20 μm x 20 μm pixel size, Princeton Instruments).

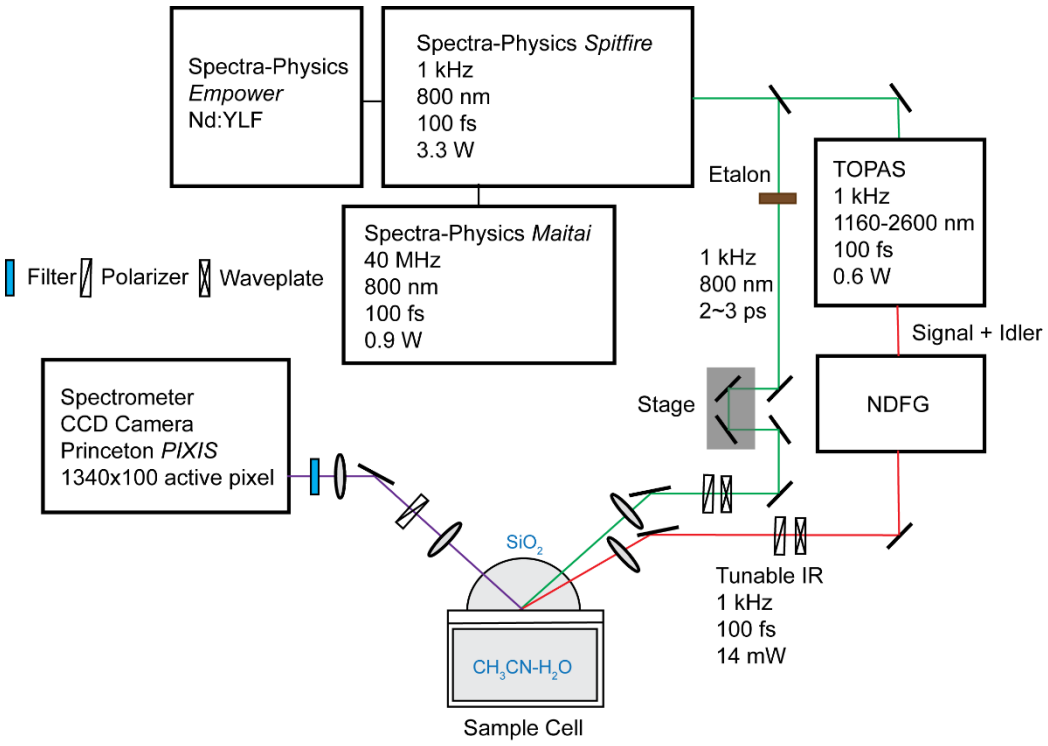

Figure 5.1. Experimental setup for broadband SFG experiments. Reprinted with permission from Gibbs and coworkers,[188] Copyright 2018 American Chemical Society.

The fused silica hemisphere was mounted on a custom-built Teflon cell. The flat side of the hemisphere was perpendicular to the laser table and in contact with the liquid phase in the sample cell; the top of the cell was exposed so solutions with different pH could be introduced. Our IR pulse is broad in the frequency domain (FWHM ~100 cm^{-1}), which covers the entire vibrational region of interest, so only one TOPAS-NDFG setting was used to collect spectra. Polarization-resolved experiments were done by selecting the polarization of each beam, and spectra were collected using ppp and ssp polarization combinations. In this type of polarization notation, the polarizations of SFG light, visible light and IR light are arranged in order of decreasing energy. For example, ssp polarization refers to s-polarized SFG, s-polarized visible light and p-polarized IR light. Data were acquired for 1 min per spectrum. The spectra shown in the figures are

representative of at least two experiments. The error in A/Γ represents the standard deviation from the fit for a single set of representative spectra.

5.2.4 Spectral Normalization and Fitting

The spectra shown in this paper were normalized to the SFG spectra from the silica/gold interface, as gold exhibits strong non-resonant SFG independent of IR wavelength, thus reflecting the shape of the broad IR pulse. In addition, both the sample and gold spectra were background corrected to subtract the signal from stray light entering the detector. To achieve normalization, the background-corrected spectrum from the sample interface was divided by the background-corrected spectrum measured immediately prior from a gold-coated fused silica hemisphere at the same TOPAS-NDFG settings.

The intensity of SFG signal (I_{SFG}) is proportional to the incident visible (I_{vis}) and IR (I_{IR}) intensities and the second-order susceptibility ($\chi^{(2)}$), which is specific to each interface. $\chi^{(2)}$ can be broken down into two terms: a non-resonant term, $\chi_{\mathrm{NR}}^{(2)}$, and vibrational resonant term, $\chi_{\mathrm{R}}^{(2)}$, summed over all possible frequencies. Each resonant mode is considered to possess a Lorentzian lineshape.[224-226] The intensity, I_{SFG}, is described in equation 5.1,

$$I_{SFG} \propto \left|\chi^{(2)}\right|^2 I_{vis} I_{IR} = \left|\chi_{NR}^{(2)} + \sum_v \chi_R^{(2)}\right|^2 I_{vis} I_{IR} = \left|\chi_{NR}^{(2)} + \sum_v \frac{A_v}{\omega_{IR} - \omega_v + i\Gamma_v}\right|^2 I_{vis} I_{IR}, \quad (5.1)$$

where ω_{IR} is the frequency of the incident IR beam, and A_v, ω_v and Γ_v are the amplitude, central frequency and damping coefficient of the v^{th} surface vibrational mode, respectively.

Equation 5.1 was fit to the normalized SFG spectra. The fitting was accomplished using Igor Pro and the function used was based on the number of expected vibrational modes in the

region; for each fitting, initial A_v, ω_v, Γ_v and $\chi_{NR}^{(2)}$, values were estimated and then the software was allowed to optimize all of them; the returned values from the previous run were used as initial values for a second run. The fitting stopped when the returned values were the same as the previous input values.

5.3 Results and Discussion

5.3.1 Basic Theory of Vibrational SFG

Sum frequency generation (SFG) has often been employed to study silica/solvent interfaces as it is well suited to probe interfacial molecules due to its intrinsic surface selectivity.[143, 149, 223, 227-231] SFG occurs when two incident laser beams are temporally and spatially overlapped in a non-centrosymmetric medium like an interface (Figure 5.2). New light is generated at a frequency that is the sum of the two incident frequencies. Generally, the frequency of one incident beam is held constant in the visible region and the other is tunable in the IR region. When the IR frequency is in resonance with a surface vibrational mode that is both IR and Raman active, there will be an enhancement in the observed SFG intensity if the corresponding molecule is ordered non-centrosymmetrically at the interface. Furthermore, by selecting the polarization of each incident beam and the collected SFG beam, polarization-resolved vibrational SFG provides information about the net orientation of interfacial molecules.[232-234]

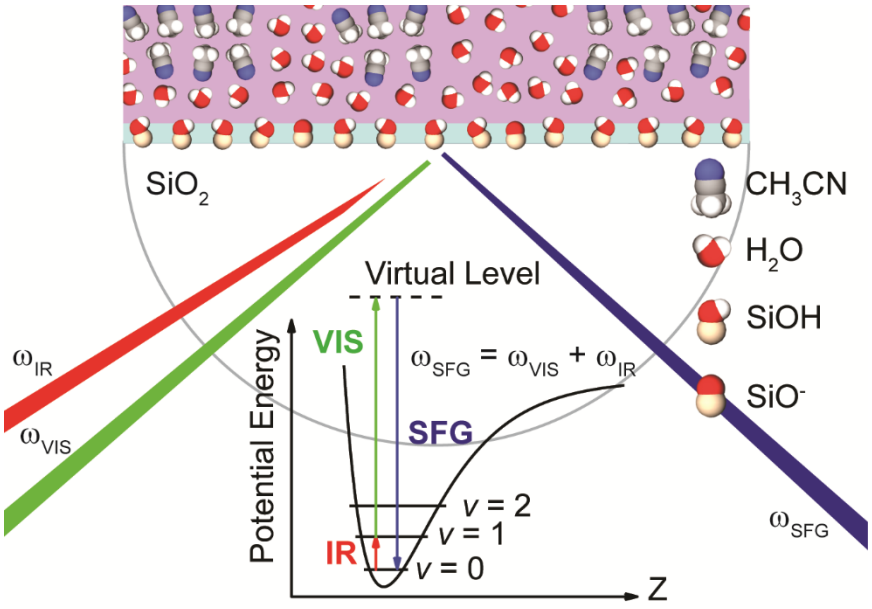

Figure 5.2 The organization of acetonitrile at the fused silica/water interface studied by vibrational sum frequency generation spectroscopy. Reprinted with permission from Gibbs and coworkers,[188] Copyright 2018 American Chemical Society.

5.3.2 Sum Frequency Spectra of the Silica/ACN-H_2O and Silica/ACN-D_2O Interfaces in the Presence of 10 mM NaCl from Mid to High Solution pH on Resonance with the Methyl Stretches

Using SFG, Fourkas and co-workers had previously examined the composition of the silica interface in the presence of ACN-water mixtures with varying mol % of ACN.[212] Between 100-80 mol% ACN, the analysis suggested that the composition of the interface reflected that of the mixture. Below 80 mol%, however, the acetonitrile partitioned more to the interface than water. Thus, we decided to utilize 19 mol% ACN as it fell into this region where ACN appeared to selectively partition to the interface. Additionally, this mole percent corresponds to a volume

fraction of 0.4 ACN, which lies in the range of ACN-water mixtures used in HILIC separations.[210, 235]

The C-H stretching region is useful for monitoring the extent of ordering of acetonitrile as the CH_3 symmetric mode in particular is very SFG active. However, this C-H stretching range (for ACN) of 2900-3040 cm^{-1} overlaps with the O-H stretching region of water, which should be significant given the large mole fraction of the latter. Therefore, in our first experiments we used D_2O to decrease the spectral overlap. SFG spectra of acetonitrile in the C-H stretching region were collected from the silica/acetonitrile-D_2O interface at various aqueous pD values in ppp and ssp polarization combinations (Figures 5.3A and 5.4A, respectively). Specifically, the pD of the aqueous phase was systematically increased prior to mixing with ACN using aqueous NaOH.[236] After a spectrum had been measured for a given pD, this mixture was replaced with a new acetonitrile mixture containing 0.60 volume fraction of the pD-adjusted D_2O. As expected, all of the resulting spectra exhibited a peak at 2943 cm^{-1}, which is the methyl symmetric stretch of acetonitrile, and a peak at ~3000 cm^{-1} in the ppp polarization combination (p-SFG, p-incident visible, p-incident IR), the corresponding asymmetric methyl stretch (Figure 5.3A). For the ssp polarization combination (s-SFG, s-incident visible, p-incident IR), the peak at ~3000 cm^{-1} was not discernable which is consistent with weaker contribution of asymmetric methyl stretches for this polarization combination (Figure 5.4A).

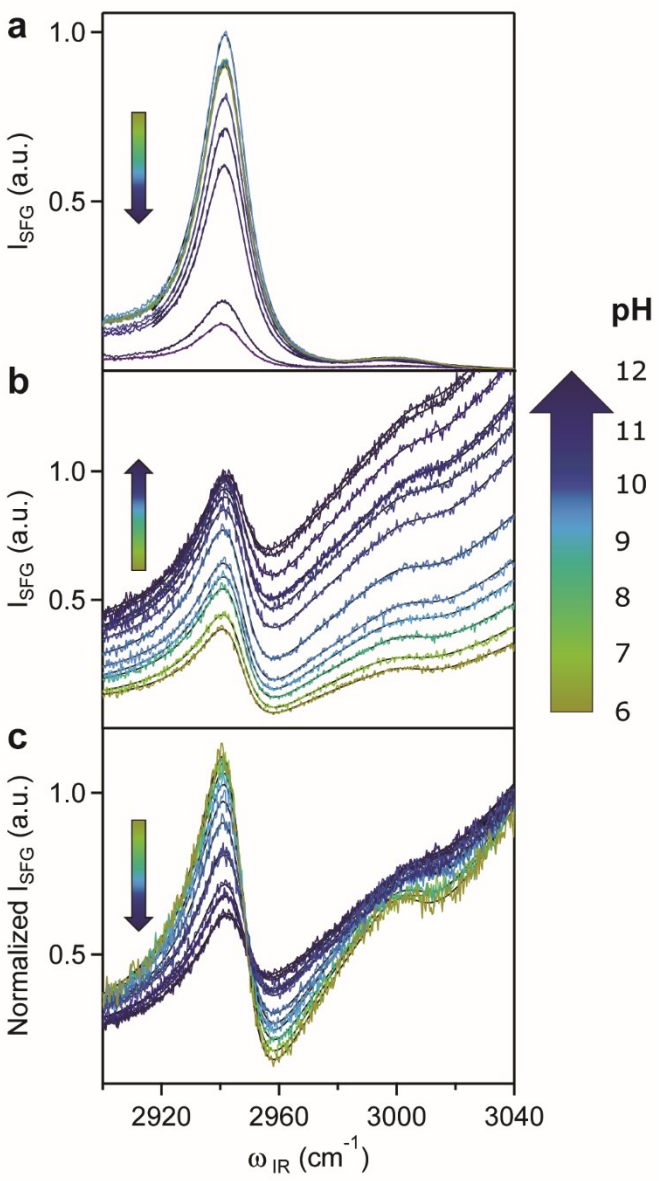

Figure 5.3 ppp-SFG spectra of acetonitrile in the C-H stretching region collected from the (a) silica/acetonitrile-deuterium oxide and (b) silica/acetonitrile-water interface (v:v=4:6) from aqueous pH 6 to 12. (c) The SFG spectra of the silica/acetonitrile-water interface normalized to the intensity at 3040 cm^{-1} stemming from the water to reveal the decreasing symmetric methyl mode. All acetonitrile-aqueous mixtures contained ~10 mM NaCl in addition to any Na^+ originating from the addition of NaOH. Black lines represent fits to the spectra. Reprinted with permission from Gibbs and coworkers,[188] Copyright 2018 American Chemical Society.

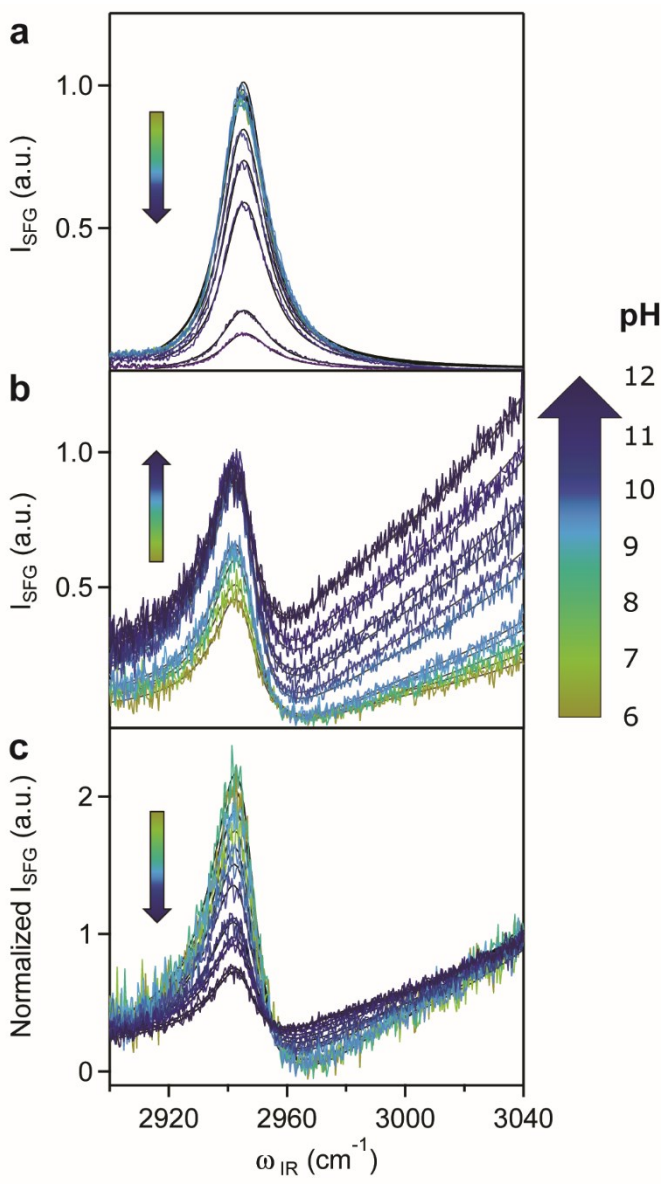

Figure 5.4 ssp-SFG spectra of acetonitrile in the C-H stretching region collected from the (a) silica/acetonitrile-deuterium oxide and (b) silica/acetonitrile-water interface (v:v=4:6) from aqueous pH 6 to 12. (c) The SFG spectra of the silica/acetonitrile-water interface normalized to the intensity at 3040 cm^{-1} stemming from the water to reveal the decreasing symmetric methyl mode. All acetonitrile-aqueous mixtures contained ~10 mM NaCl in addition to any Na^+ originating from the addition of NaOH. Black lines represent fits to the spectra. Reprinted with permission from Gibbs and coworkers,[188] Copyright 2018 American Chemical Society.

Prior to discussing the pH-dependent trends for ACN, we note that previous work at the silica/water interface at this salt concentration of 10 mM NaCl found that increasing the pH from pH 6 to pH 12 led to an increase in SFG in the O-H stretching region, indicating that the water became more ordered.[73, 99] This increase in order was attributed to the presence of more surface charges on silica with increasing pH, which aligned the interfacial water through electrostatic interactions.[73, 99, 124-125, 134, 147] In contrast to what had been observed for water, however, the SFG intensity of the ACN only increased slightly up to ~pD 10 and then decreased substantially as the pD was further increased (Figures 5.3A and 5.4A).

To determine whether this pH trend for ACN was general and would be observed in aqueous samples using H_2O rather than D_2O we performed the same experiment with regular water. In contrast to the D_2O experiments, the ppp- and ssp-SFG signal intensities increased over the wavenumber range as the pH was increased (Figures 5.3B and 5.4B, respectively). Yet, the presence of an O-H stretch arising from water at high wavenumber made it difficult to determine how much the signal from the methyl group was changing by a visual comparison of the spectra. If, however, the same spectra are shown normalized to the intensity at 3040 cm^{-1} that stems from interfacial water, it is apparent that the methyl contribution is becoming smaller and smaller in contrast to that from the water as the pH was increased (Figures 5.3C and 5.4C).

5.3.3 Spectral Assignments to the Methyl Stretching Region at the Silica/ACN-H_2O Interface

To more quantitatively determine the contribution from the methyl groups of ACN, the spectra were fitted using equation 5.1 that relates the SFG intensity to the second-order susceptibility $\chi^{(2)}$, modelled as the absolute square of the sum of a non-resonant contribution and

Lorentzian functions that represent each vibrational mode. The resulting Lorentzian peak amplitude and width ratios (A/Γ) are proportional to the number and net alignment of the corresponding interfacial molecules.[147, 237] From the fitting of the ppp-SFG spectra that corresponded to the ACN-H_2O mixture, we extracted two methyl symmetric stretch A/Γ values for each pH, which have been attributed to the two "leaflets" that form the ACN bilayer.[212] Based on previous reports, we assigned the higher frequency peak at near neutral pH to acetonitrile molecules that make up the inner leaflet (CH_3-ss2) and assigned the dominant peak at lower wavenumber at neutral pH to acetonitrile molecules that make up the outer leaflet (CH_3-ss1).[212, 216] This difference in frequency was attributed to the dissimilar local environments of the inner and outer leaflets.[212, 216] Furthermore as simulations and experiments have suggested, a repeatable bilayer structure leads to effective cancellation of SFG, thereby contributing little to the overall signal; therefore we assumed that most of the SFG signal originated from the first bilayer located closest to the silica interface.[211, 238] One methyl asymmetric stretch and a broad peak centred above 3100 cm^{-1} accounting for strongly hydrogen bonded water were also included in the spectral fitting of the ppp-SFG. We found the broad peak centred above 3100 cm^{-1} necessary to achieve satisfactory fits, as the dominant peaks in the water spectra (3200 cm^{-1} and 3400 cm^{-1}) lie outside of our spectral window (Figure 5.5).

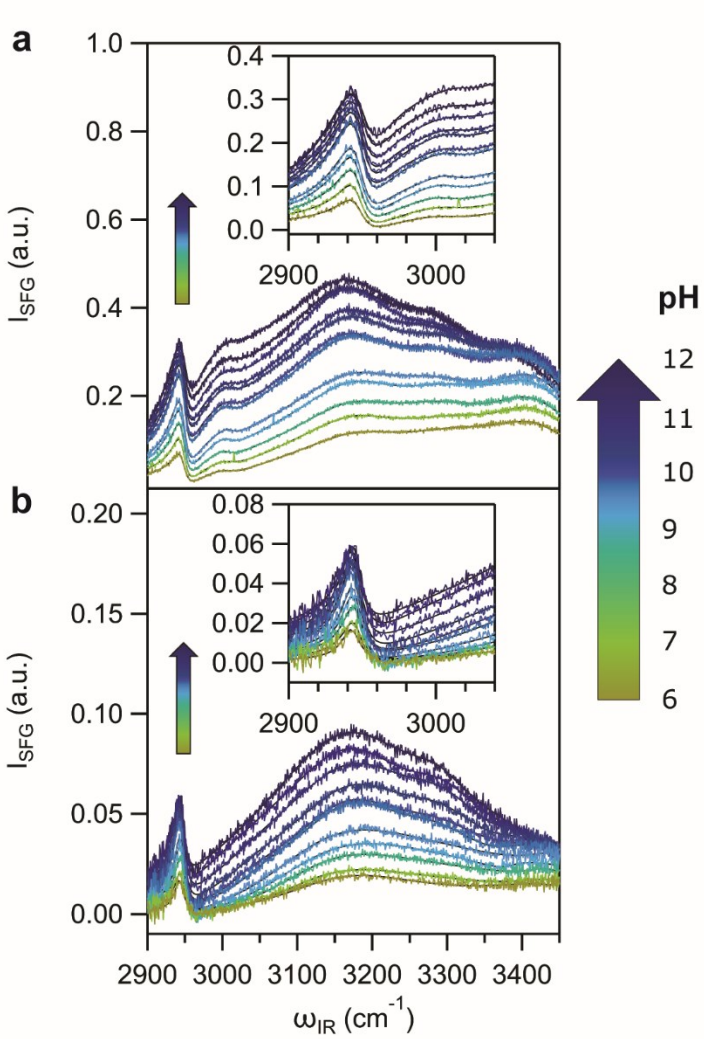

Figure 5.5 SFG spectra of the C-H and O-H stretching region from the silica/acetonitrile-water interface (v:v=4:6) from aqueous pH 6 to 12 collected in (a) ppp and (b) ssp polarization combinations. All acetonitrile-aqueous mixtures contained ~10 mM NaCl in addition to any Na^+ originating from the addition of NaOH. Black lines represent guides for the eyes. Inset: Magnified SFG spectra of the C-H stretching region of acetonitrile. Reprinted with permission from Gibbs and coworkers,[188] Copyright 2018 American Chemical Society.

For the ssp spectra (Figure 5.4B), fitting with two symmetric stretches and a broad peak at 3100 cm^{-1} were adequate, indicating the asymmetric mode did not contribute measurably to the

signal. However, we found that following our standard approach to fitting resulted in higher frequencies for CH_3-ss2 (ranging from 2971 to 2960 cm^{-1}). Yet if we held the CH_3-ss2 frequencies within a range of those values determined from the corresponding ppp spectrum (2952 to 2935 cm^{-1}), which were more within the expected range for a CH_3 symmetric stretch of ACN, we observed a similar goodness of fit. Moreover, the A/Γ values for both the CH_3-ss1 and CH_3-ss2 did not change substantially when either fitting protocol was used (Figure 5.6). Additionally, we always observed changes in the frequency of the CH_3-ss2 in both the ssp and ppp spectra upon changing the pH, while the CH_3-ss1 position remained relatively constant. This is consistent with significant changes in hydrogen-bonding or changes in the local static field experienced by the inner leaflet upon deprotonating the silica surface. The CH_3-ss2 frequency trends, however, were not consistent experiment to experiment, unlike the clear trends in A/Γ, which, for CH_3-ss1 in particular, were highly reproducible. We reason that our current spectral resolution and the overlap of the water tail and asymmetric mode make it difficult to fit the buried CH_3-ss2 peak with enough accuracy.

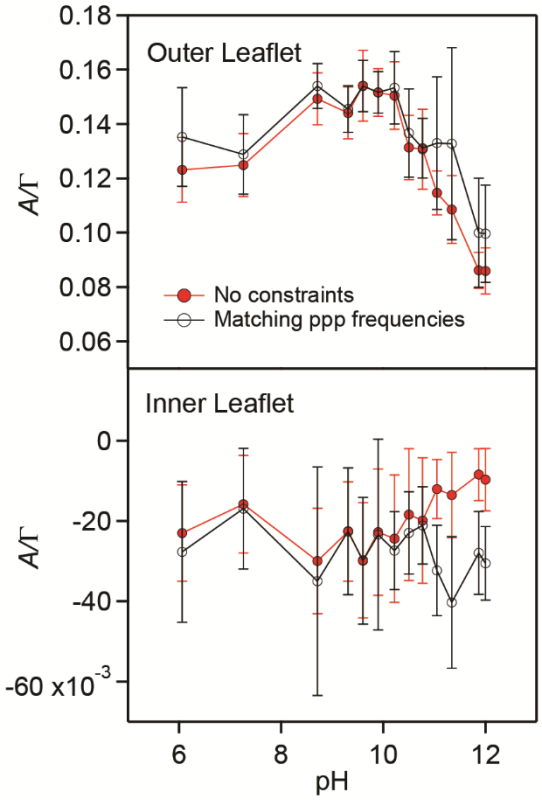

Figure 5.6 Comparison of outer and inner leaflet A/Γ values extracted from the silica/acetonitrile-water interface given different fitting protocols in ssp polarization combination. The red circles represent the fits where no constraints were held on frequencies. The black circles represent the fits where the CH_3-ss1 and CH_3-ss2 frequencies were constrained to the corresponding ppp polarization frequencies. Reprinted with permission from Gibbs and coworkers,[188] Copyright 2018 American Chemical Society.

Finally, for the ppp- and ssp-SFG spectra corresponding to the ACN-D_2O mixture, we were unable to fit two methyl symmetric stretches indicative of the bilayer, and instead the spectra could only be fit to one methyl symmetric stretch. We speculate that the presence of D_2O led to a similar hydrogen bonding experience by both the outer and inner leaflet. This similarity in hydrogen bonding led to a lack of difference in the symmetric stretch frequencies from the two leaflets of the bilayer.[239-244]

The A/Γ values corresponding to the more prominent CH_3-symmetric stretch at ~2945 cm^{-1} in the ppp spectra, attributed to the ACN sublayer not immediately adjacent to the surface (CH_3-ss1),[212] and those from the water OH stretch are plotted versus aqueous pH as well as A/Γ of the single CH_3-symmetric stretch in the ppp spectra for the ACN-D_2O system (Figure 5.7). Similar to our observations in the presence of D_2O, for the H_2O mixture the absolute values for the methyl peak at ~2945 cm^{-1} increased slightly as the pH increased from neutral to ~pH 10 and then underwent a dramatic decrease at pH > 10. The ssp-SFG analysis yielded similar results (Figure 5.6). As expected, this trend was in stark contrast to the pH-dependent A/Γ values for the water peak, which increased systematically as the pH increased, consistent with previous reports for the silica/water interface at this salt concentration.[99] From the fits of ppp-SFG spectra for the ACN-H_2O system, we observed that the methyl asymmetric stretch and the second methyl symmetric stretch, corresponding to the inner leaflet, did not exhibit clear pH dependence. For both modes, this is likely due to the larger errors in the fit parameters owing to these modes' weaker contributions to the overall spectra. Indeed, the ratio of A/Γ for the outer leaflet (CH_3-ss1) and the inner leaflet (CH_3-ss2) from the ppp spectra, which is proportional to the number density ratio of the outer and inner leaflet, varied from 2 to 6 (Figure 5.8), supporting the inner leaflet contributes less. Moreover these ratios are consistent with the simulations by Mountain which found the ratio to be 2 in the presence of neutral silica.[211] However, it is worthwhile to note that the simulations by Mountain were performed in the absence of both negatively charged siloxides and background salt, the effect of which on the ACN bilayer structure is unknown.

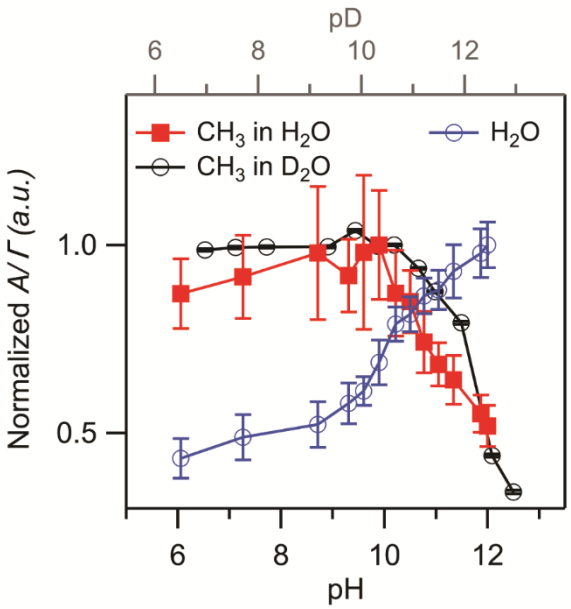

Figure 5.7. The pH dependent ratio of peak amplitude and peak width (A/Γ) from the ppp-SFG spectra for the: dominant methyl symmetric stretch from acetonitrile in water (CH_3-ss1, red closed squares) and in deuterium oxide (black open circles), and for the OH stretch at the silica/acetonitrile-water interface (blue open circles) in the ppp polarization combination. The pH values for the ACN/D_2O system were those measured with the pH probe in D_2O. The corresponding pD values (where $pD = 0.44 + pH_{measured}$) are shown in the upper axis. Reprinted with permission from Gibbs and coworkers,[188] Copyright 2018 American Chemical Society.

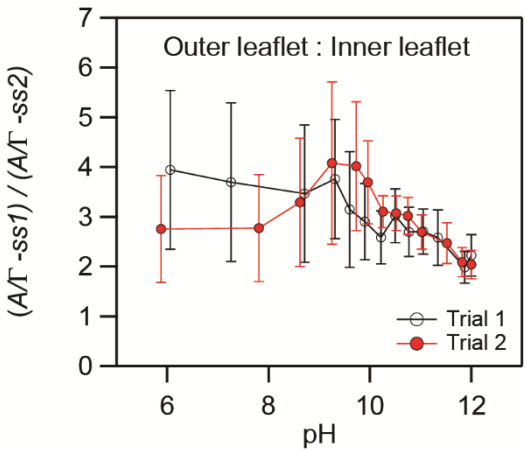

Figure 5.8. Ratio of outer leaflet to inner leaflet A/Γ values in ppp polarization combination. Two trials are shown for reproducibility.

5.3.4 The Effect of NaCl Concentration

In the pH variation experiments, the acetonitrile-aqueous mixture fraction always contained 10 mM NaCl background salt, so that in adjusting the aqueous pH with NaOH the concentration of Na^+ in the mixture remained relatively unchanged until ~pH 10 but increased to ~16 mM when the pH of the water fraction was increased to pH 12. This change in sodium cation concentration at higher pH, might influence the interfacial structure of the silica/ACN-water interface. Specifically, cations such as Na^+ are expected to accumulate at the negatively charged silica/water interface, partially screening the surface charge and disrupting the alignment of water.[80, 115] In order to explore the effect of Na^+ concentration on the SFG response of acetonitrile at the silica/aqueous interface, control experiments were performed by collecting SFG spectra with 10, 15 and 20 mM NaCl in acetonitrile-water mixtures using natural pH water (Figure 5.9). In the ~pH 6 acetonitrile-water mixture, we found that increasing [Na^+] from 10-20 mM suppressed the SFG signal from acetonitrile as it does for water, which is likely due to the disruption of the

acetonitrile bilayer by hydrated Na^+. However, as shown in Figure 5.8A and B, a comparison of A/Γ ratios of the CH_3-ss1 mode between pH variation and the salt variation experiments showed that the magnitude of this ratio dropped much more in pH variation experiments, indicating the increase in [Na^+] had a minimal effect on the ACN bilayer. As a result, we concluded the major contribution to the ACN SFG signal originated from the effect of pH on the silica surface rather than the increase in Na^+ concentration.

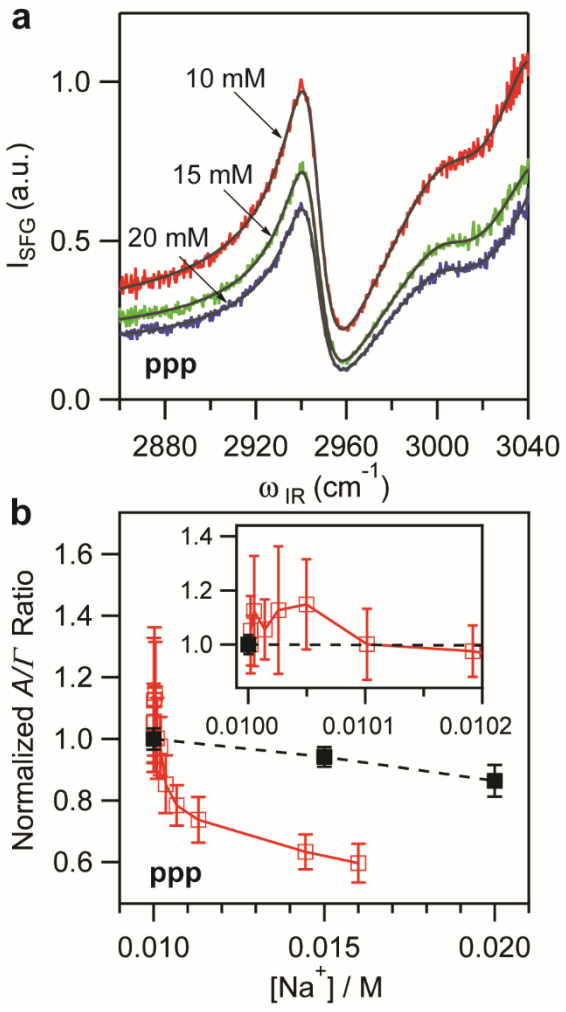

Figure 5.9 (a) ppp-SFG spectra at the silica/acetonitrile-water interface as a function of salt concentration. The acetonitrile-water mixture consisted of a pH 6 water fraction and total NaCl concentration of 10, 15 and 20 mM NaCl, respectively. Black lines represent fits to the spectra. (b)

The normalized A/Γ ratios of the CH_3-ss1 mode at different [Na^+] in the near neutral mixture from part A (black squares). The normalized A/Γ ratios of the CH_3-ss1 mode at different [Na^+] from the addition of NaOH (red hollow squares) corresponding to a pH increase from pH ~6 to ~12. Inset: A/Γ values from 0.0100 to 0.0102 M Na^+. Reprinted with permission from Gibbs and coworkers,[188] Copyright 2018 American Chemical Society.

5.3.5 Orientation Analysis of the ACN Bilayer

The observed decrease in A/Γ at higher pH for the dominant methyl symmetric stretch in both the H_2O and D_2O systems suggested that increasing the pH led to one or more of the following: the acetonitrile was expelled from the interface, it became less ordered, or the net orientation changed in such a way that the SFG activity decreased. To determine if the net orientation angle changed for the outer leaflet that in particular contributes most to the dominant peak, we took advantage of the sensitivity of SFG to the angle of orientation, which can be probed by comparing different polarization combinations.

The magnitude of $\chi^{(2)}$, and therefore the magnitude of A/Γ, may be influenced by two factors: number density of molecular oscillators, and the net orientation of the interfacial oscillators. In order to determine which factor plays a stronger role, we conducted orientation analysis based on the ratio of magnitudes of the CH_3-ss1 peak in ppp and ssp spectra.

For the acetonitrile molecule in the molecular coordinate frame, the *z* axis is defined along the transition dipole moment of the methyl symmetric stretch mode, which coincides with the C_3 symmetry axis; molecular *x* and *y* axes are defined along the transition dipole moments of two methyl asymmetric stretch modes, respectively. In the laboratory coordinate frame, the *Z* axis is

defined along the surface normal and the *X* axis is in the incidence plane perpendicular to *Z*. The relationship between *XYZ* and *xyz* frame are described by three angles: tilt angle θ, in-plane rotation angle ϕ and twist angle ψ (Figure 5.10).

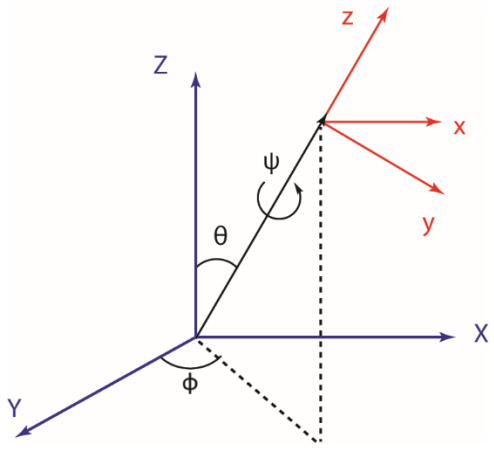

Figure 5.10 The relationship between the laboratory coordinate frame (*XYZ*) and molecular coordinate frame (*xyz*). Reprinted with permission from Gibbs and coworkers,[188] Copyright 2018 American Chemical Society.

The second-order susceptibility $\chi^{(2)}$ is a third-order tensor, which can be represented by $\chi^{(2)}_{\mathrm{IJK}}$ (*IJK* = *X*, *Y*, *Z*), where *X*, *Y* and *Z* are the defined laboratory axes. $\chi^{(2)}_{\mathrm{IJK}}$ can be related to the microscopic hyperpolarizability tensor elements $\beta^{(2)}_{\mathrm{IJK}}$ (*ijk* = *x*, *y*, *z*) of the vibrational mode in the molecular coordinate system through ensemble average over all possible molecular orientations as described in Equation 5.2,[224, 245]

$$\chi^{(2)}_{IJK} \propto N \sum_{ijk} \langle R_{Ii} R_{Jj} R_{Kk} \rangle \beta^{(2)}_{ijk}, \tag{5.2}$$

where *N* is the number density of molecular oscillators in resonance, $R_{\lambda\lambda'}$ (λ=*X*, *Y*, *Z*; λ'=*x*, *y*, *z*) is an element of the transformation matrix from the molecular coordinate system (*xyz*) to the laboratory coordinate system (*XYZ*) and the bracket denotes an orientationally averaged value.

For a rotationally isotropic interface like the silica/acetonitrile-water interface, which has $C_{\infty v}$ symmetry, there are only seven non-zero susceptibility tensor elements.[55, 148, 246] Expressions for the effective second-order nonlinear susceptibility, $\chi_{eff}^{(2)}$, under different polarization combinations are given by equations 2.5, 2.6, and 2.7 of Chapter 2.[57, 224, 247-248] The Fresnel coefficients were calculated based on equations 2.2, 2.3, and 2.4, In this study, we used: n_1(SFG)=1.46, n_1(visible)=1.45, n_1(IR)=1.41; n_2(SFG)=n′(SFG)=1.34, n_2(visible)= n′(visible)=1.34, n_2(IR)= n′(IR)=1.39. Here n_1 are refractive indices of silica, n_2 are the refractive indices of the solution. The incidence angles of IR, α_2 and visible, α_1, beams are 64° and 60°, respectively, and the reflection angle of SFG, α, was 61°. The calculated coefficients to equations 2.5, and 2.7 are summarized in Table 5.1.

Table 5.1. Calculated Coefficients Involved in the Polarization-Resolved SFG Experiments

Term	Magnitude
$L_{YY}(\omega_{SFG})L_{YY}(\omega_{Vis})L_{ZZ}(\omega_{IR})\sin\alpha_2$	1.48
$-L_{XX}(\omega_{SFG})L_{XX}(\omega_{Vis})L_{ZZ}(\omega_{IR})\cos\alpha\cos\alpha_1\sin\alpha_2$	0.16
$-L_{XX}(\omega_{SFG})L_{ZZ}(\omega_{Vis})L_{XX}(\omega_{IR})\cos\alpha\sin\alpha_1\cos\alpha_2$	0.20
$L_{ZZ}(\omega_{SFG})L_{XX}(\omega_{Vis})L_{XX}(\omega_{IR})\sin\alpha\cos\alpha_1\cos\alpha_2$	0.22
$L_{ZZ}(\omega_{SFG})L_{ZZ}(\omega_{Vis})L_{ZZ}(\omega_{IR})\sin\alpha\sin\alpha_1\sin\alpha_2$	1.38

The in-plane rotation angle ϕ, the tilt angle θ and the twist angle ψ are used to correlate laboratory and molecular coordinate frames (Figure 5.10). Considering the symmetry of the silica/acetonitrile-water interface and the highly symmetric structure of the acetonitrile molecule,

it is reasonable to assume that interfacial acetonitrile molecules have a random distribution in both the in-plane rotation angle ϕ and the twist angle ψ. Consequently, the tilt angle θ is the only parameter left to be determined, which represents the angle between the molecular axis *z*, along the C_{3v} axis of the methyl group, and the surface normal (*Z*). After simplification, the non-zero second-order susceptibility elements have the following expressions for the methyl symmetric stretch mode:[57, 224, 247-248]

$$\chi_{XXZ}^{(2)} = \chi_{YYZ}^{(2)} = \frac{1}{2}N\left[\beta_{ZZZ}^{(2)}(1-\cos^2\theta)\cos\theta + \beta_{XXZ}^{(2)}(1+\cos^2\theta)\cos\theta\right], \quad (5.3)$$

$$\chi_{XZX}^{(2)} = \chi_{ZXX}^{(2)} = \chi_{YZY}^{(2)} = \chi_{ZYY}^{(2)} = \frac{1}{2}N\left[\left(\beta_{ZZZ}^{(2)} - \beta_{XXZ}^{(2)}\right) \times (1-\cos^2\theta)\cos\theta\right], \quad (5.4)$$

$$\chi_{ZZZ}^{(2)} = N\left[\beta_{ZZZ}^{(2)}\cos^3\theta + \beta_{XXZ}^{(2)}(1-\cos^2\theta)\cos\theta\right]. \quad (5.5)$$

For a single methyl group, the non-zero hyperpolarizability elements of the symmetric stretch mode have the following relationship:[57]

$$\beta_{XXZ}^{(2)} = \beta_{YYZ}^{(2)} \approx R\beta_{ZZZ}^{2)}, \quad (5.6)$$

where the coefficient R is the molecular hyperpolarizability ratio, and is different for methyl groups in various molecules.

The ratio $\left|\chi_{\text{eff}}^{(2),\text{ppp}}/\chi_{\text{eff}}^{(2),\text{ssp}}\right|$ as a function of θ was calculated as described above using molecular hyperpolarizability ratio, values of 0.58 and 2.3 and assuming a narrow distribution in mean tilt angle θ (Figure 5.11A, bold and dashed lines, respectively). Theoretically, R can be calculated from the measured Raman depolarization ratio in bulk or by performing quantum calculations.[249-251] The magnitude of R is currently a subject of debate; generally, R is believed to be in the range of 1.66-4.0 for methyl groups, with a value of R=2.3 for the methyl in

acetonitrile;[232] however, values smaller than unity, such as 0.58, are also used in some studies.[249, 252] Next, we determined the experimental value of $\left|\chi_{\mathrm{eff}}^{(2),\mathrm{ppp}}/\chi_{\mathrm{eff}}^{(2),\mathrm{ssp}}\right|$ as a function of pH from the ratio of $\left|(A/\Gamma)_{\mathrm{ppp}}/(A/\Gamma)_{\mathrm{ssp}}\right|$ for the CH_3-ss1 mode in the ppp and ssp spectra (Figure 5.11, squares for H_2O and circles for D_2O). As shown in Figure 5.11, the measured tilt angle θ is located in the range of 0-30° (expected for the inner leaflet) or 150-180° (expected for the outer leaflet) when R=0.58; however when R=2.3, θ is likely close to 90°. The range of 0-30° is consistent with the values determined in previous studies for pure acetonitrile at other mineral oxide surfaces. For example, Rabinowitz and co-workers found that acetonitrile bound to zirconia with a tilt angle of around 20°,[253-254] and Williams and co-workers found that acetonitrile bound to alumina with a tilt angle of approximately 21° and to zirconia with a tilt angle of approximately 24°.[255] Accordingly, our result supports that the R value for methyl symmetric stretch in the acetonitrile molecule is likely smaller than unity, which is in agreement with Morita and coworkers[249] and Shultz and coworkers.[252]

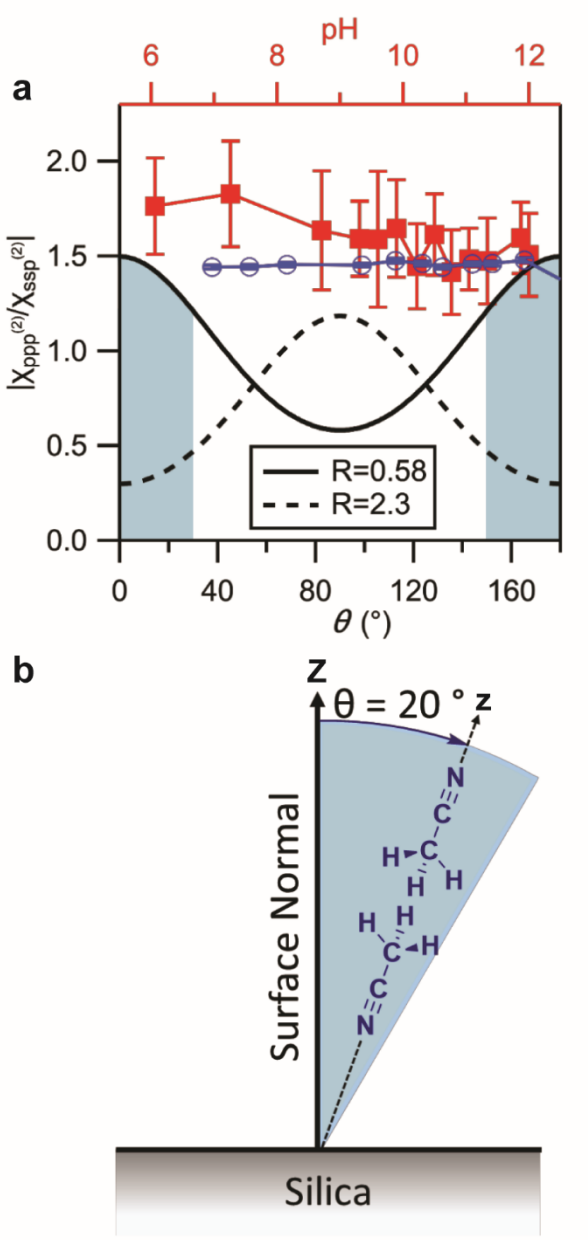

Figure 5.11 (a) Calculated $\left|\chi_{\mathrm{eff}}^{(2),\mathrm{ppp}}/\chi_{\mathrm{eff}}^{(2),\mathrm{ssp}}\right|$ values as a function of tilt angle θ with R=0.58 (solid black line) and 2.3 (dashed black line). The experimental $\left|\chi_{\mathrm{eff}}^{(2),\mathrm{ppp}}/\chi_{\mathrm{eff}}^{(2),\mathrm{ssp}}\right|$ value is plotted versus aqueous pH for ACN in water (CH_3-ss1, red squares) and for ACN in deuterium oxide (blue circles). Blue shaded regions indicate the proposed range in orientation angles. (b) Predicted tilt angle range (blue wedge) from the surface normal (vertical black arrow). The angle between the

surface normal and the dipole moment of the methyl of the outer leaflet is 200°, which is equivalent to 160°, given the azimuthal symmetry of the interface. Reprinted with permission from Gibbs and coworkers,[188] Copyright 2018 American Chemical Society.

Significantly, the $\left|\chi_{\mathrm{eff}}^{(2),\mathrm{ppp}}/\chi_{\mathrm{eff}}^{(2),\mathrm{ssp}}\right|$ ratio of the methyl symmetric stretch (corresponding to the outer leaflet) did not vary greatly with increasing pH for either the H_2O or D_2O systems, especially in the high pH region (pH > 10), indicating that any change in the orientation angle of interfacial acetonitrile molecules in the outer leaflet as the aqueous pH increased was insignificant. Therefore, the decrease is either due to a broadening in the orientation distribution (the acetonitrile becoming less ordered), which the above analysis does not account for, or a decrease in the number of ACN molecules present at the interface. One reason to reject the former is that the apparent tilt angle often changes as the distribution function increases (i.e., the interfacial molecules become less oriented).[234, 256] This magic angle for θ is 39°, which is the measured angle that all theoretical θ values converge to as the distribution in angles becomes very broad. As the angles we measured were closer to 20° (or 160°) and did not appear to increase, it is more likely that a decrease in the number density of interfacial acetonitrile molecules is the dominant reason why the SFG intensity changed. In other words, an increase in pH led to expulsion of ACN from the silica interface.

5.3.6 Possible Origin for the pH-Dependence of the Interfacial ACN Number Density

As the orientation analysis indicates that a change in number density of interfacial acetonitrile molecules is the dominant reason for the change in SFG magnitude, the question becomes why the acetonitrile bilayer, or at least the outer leaflet, is expelled at higher pH. At neutral pH, the silica surface is negatively charged, and this surface charge generates an electric

field, which we propose induces the alignment of water molecules in the interfacial region leading to the observed water tail in the C-H stretching region. As the solution pH is increased, more surface silanol groups become deprotonated resulting in a stronger static electric field and more aligned water molecules.[81] Consequently a stronger SFG signal in the water O-H stretching region is expected, which we confirmed experimentally (Figure 5.5). The increase in A/Γ determined from the water tail in the C-H stretching region is consistent with this interpretation, indicating more water molecules were aligned at the interface as the pH increased, even though acetonitrile existed in the mixture (Figure 5.7). Additionally, the sigmoidal shape of the A/Γ trend for the water from pH 6 to 12 is similar to the changes in the water spectrum for the silica/water interface containing only 10 mM NaCl[99] except that the inflection point for the sigmoid with ACN is slightly shifted towards higher pH values (Figure 5.12). This shift could be indicative of a change in effective pK_a of the silica surface sites in the presence of ACN, which has been suggested but never determined.[257-259]

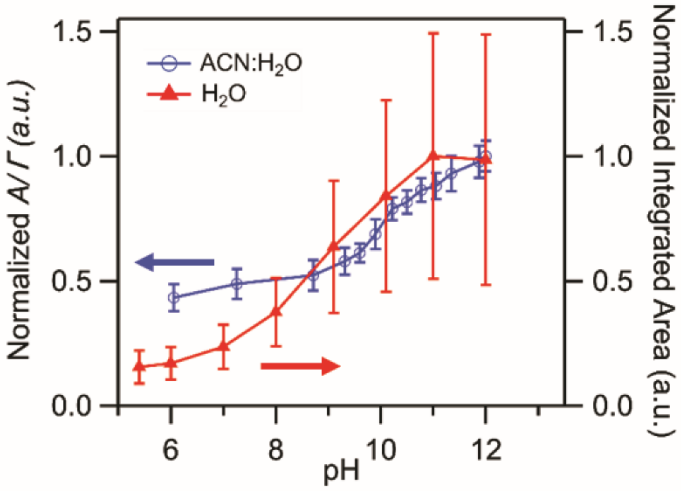

Figure 5.12 Comparison of the pH-dependent water signal at the silica/ACN:H_2O mixture in this study and at the silica/H_2O by Darlington et al.[99] in the presence of 10 mM NaCl at the silica

surface. The former corresponds to the A/Γ ratio of the mode at >3100 cm^{-1} while the latter is the intensity integrated from 2950 to 3550 cm^{-1}. Reprinted with permission from Gibbs and coworkers,[188] Copyright 2018 American Chemical Society.

Yet, while the water became more aligned, the amount of acetonitrile decreased above pH 10. We reason that the destabilization of the ACN bilayer stemmed from the deprotonation of the surface silanols by two complementary mechanisms. Firstly, as the static electric field emanating from the silica becomes larger in magnitude with increasing pH, it interacts unfavourably with the dipole moment of the inner leaflet of the acetonitrile bilayer, which points away from the negatively charged silica surface $\overset{\delta^-\ \delta^+}{\longrightarrow}$. As a result of this electrostatic repulsion of the inner leaflet, the bilayer structure could become unstable and be partially destroyed, which may account for the decrease in A/Γ for the methyl groups. Specifically the tilt angle from the surface normal of the inner leaflet could increase as the surface field increases which would destabilize interactions with the outer leaflet. In contrast as the outer leaflet of the acetonitrile bilayer is already favourably aligned with the interfacial static field, an increase in field strength may not result in a change of orientation, particularly as the outer leaflet has minimal tilt angle from surface normal (160 – 180°) according to our analysis. Secondly, the deprotonation of silanol groups to form siloxides could lead to increased water solvation of the surface sites, which would displace acetonitrile initially hydrogen bonded with, or near, the SiOH. Both effects separately or in conjunction could account for the observed signal changes. Although both mechanisms should affect the inner ACN leaflet at the silica surface, we reason that the outer leaflet is also destabilized as the formation of the outer leaflet requires hydrophobic interactions with the inner leaflet.[216, 219-220] Accordingly, if the inner leaflet is disrupted by the deprotonation of the surface, then the outer

leaflet is also perturbed which leads to significant changes in the SFG signal owing to our sensitivity to the latter given its greater number density.

Finally we note that according to the spectral analysis, only the outer leaflet exhibited a clear drop in A/Γ ratio as well as the invariant orientation with pH. More specifically, the pH-dependent changes in A/Γ observed for the inner leaflet were within error from the spectral fitting. Additionally, the relative error in the fit parameters for the inner leaflet were larger given the lower A/Γ values. Therefore, it is possible that charging the silica surface does not remove the inner leaflet but rather reorients it such that the outer leaflet is destabilized. As the inner leaflet is intrinsically lesser in ACN density according to the MD simulations and our experimental observations, it is difficult to determine how the inner leaflet changes from the measured spectra. Simulations of the aqueous acetonitrile/silica interface with increasing surface charge could isolate how the inner and outer leaflet respond.

5.3.7 Sum Frequency Spectra of the Nitrile Stretching Region at the CaF_2-Silica/ACN-H_2O Interface

To gain further insight into the behaviour of the nitrile molecules near the silica surface, we collected sum frequency spectra at the CaF_2-silica/ACN-H_2O interface (Figure 5.13). With increasing pH we observed a peak which increased in intensity until pH 10, at which point it suddenly vanished. Beyond pH 10, the mode reappeared and continued to increase in intensity, while exhibiting a similar interference pattern as observed with the methyl stretches. Furthermore, the baseline increased beyond pH 10. At the highest pH studied, the nitrile resonance appeared similar to that of the CaF_2-silica/ACN interface in the absence of water, although with a different

baseline. The lineshape observed at high pH may due to two nitrile modes, opposite in phase, however it may also depend on the origin of the strong background signal. If this strong background signal is a nonresonant one, then interference effects may be expected depending on its phase and magnitude. Given a recent study of water in contact with thin oxide films on CaF_2,[177] interference effects from a dual-interface system (i.e. CaF_2/silica and silica/solution), may be substantial. The ssp spectra did not exhibit the same strong background signal with increasing pH (Figure 5.14), however the total signal was much weaker than observed in the ppp spectra. Further investigation is required to elucidate the pH behaviour of the CaF_2-silica/ACN-H_2O interface.

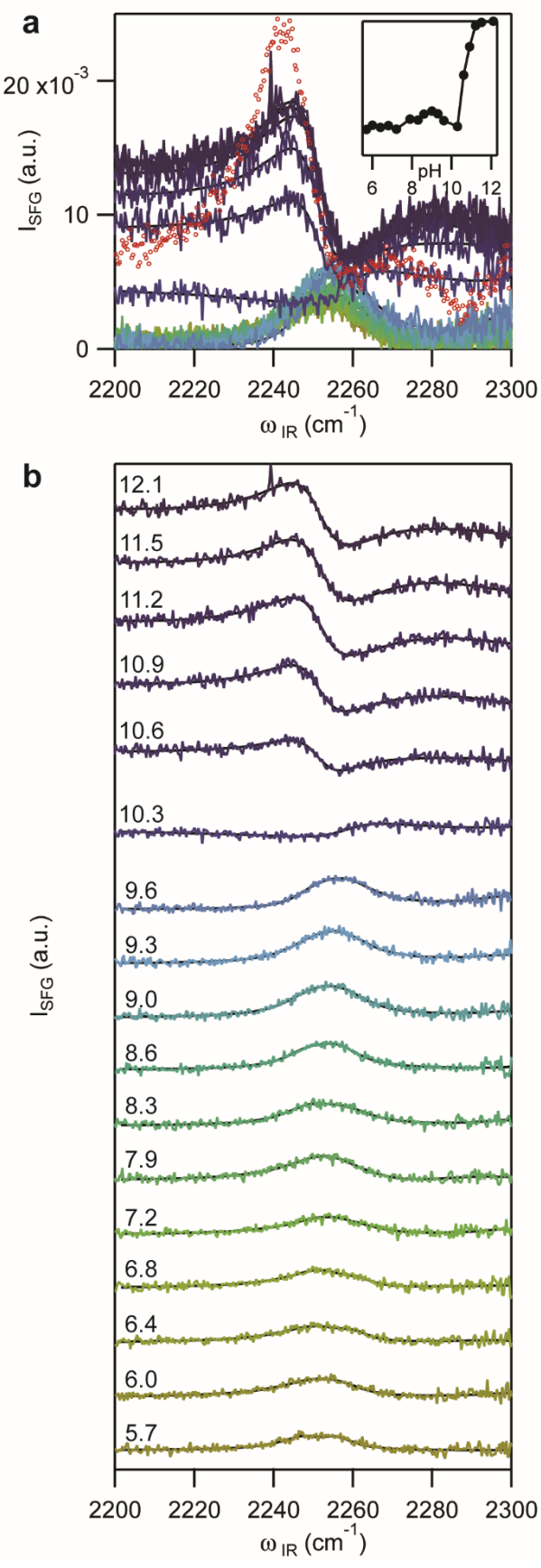
a
20 x10^-3
10
0
I_SFG (a.u.)
2200
2220
2240
2260
2280
2300
ω IR (cm^-1)
pH
6
8
10
12
b
12.1
11.5
11.2
10.9
10.6
10.3
9.6
9.3
9.0
8.6
8.3
7.9
7.2
6.8
6.4
6.0
5.7
I_SFG (a.u.)
2200
2220
2240
2260
2280
2300
ω IR (cm^-1)

Figure 5.13 (a) ppp-SFG intensities of the CaF_2-silica/ACN-H_2O interface in the presence of 10 mM NaCl from pH 5.8 to 12 over a spectral window of 2200 to 2300 cm^{-1}. The red dots denote the spectrum of the CaF_2-silica/ACN interface. Inset: SFG intensity at 2250 cm^{-1}. (b) The same spectra (without that of pure ACN), vertically offset for clarity. Colours follow the same scheme as Figure 5.3, although pH values are provided. Black lines are guides for the eye.

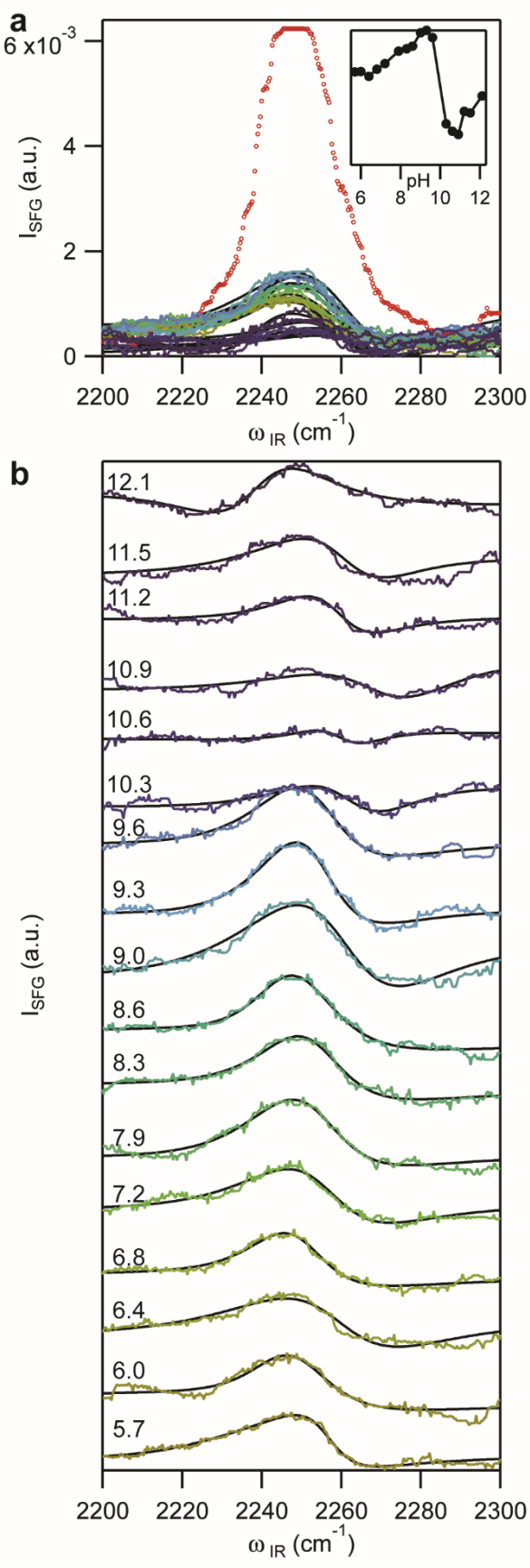
a
6 x10^-3
4
2
0
I_SFG (a.u.)
6
8
pH
10
12
2200
2220
2240
2260
2280
2300
ω IR (cm^-1)
b
12.1
11.5
11.2
10.9
10.6
10.3
9.6
9.3
9.0
8.6
8.3
7.9
7.2
6.8
6.4
6.0
5.7
I_SFG (a.u.)
2200
2220
2240
2260
2280
2300
ω IR (cm^-1)

Figure 5.14 (a) ssp-SFG intensities of the CaF_2-silica/ACN-H_2O interface in the presence of 10 mM NaCl from pH 5.8 to 12 over a spectral window of 2200 to 2300 cm^{-1}. The red dots denote the spectrum of the CaF_2-silica/ACN interface. Inset: SFG intensity at 2250 cm^{-1}. (b) The same spectra (without that of pure ACN), vertically offset for clarity. Colours follow the same scheme as Figure 5.3, although pH values are provided. Black lines are guides for the eye.

5.4 Conclusion

In conclusion, the SFG spectra of acetonitrile in the C-H stretching region were collected from the silica/acetonitrile-water interface from pH 6 to 12 in the presence of H_2O and D_2O. Spectral fitting of the former revealed two types of methyl groups, which have been attributed to acetonitrile with different chemical environments. Orientation analysis indicated that the net orientation of acetonitrile molecules in the outer leaflet of the interfacial bilayer did not change significantly as the pH increased. Yet increasing the solution pH from neutral to basic pH significantly decreased the number density of interfacial acetonitrile molecules. We attributed this expulsion of acetonitrile to the static field present at aqueous pH values (pH > 10) when a substantial fraction of the acidic silanols were deprotonated that repels or reorients the inner leaflet, which destabilizes the outer leaflet that contains a higher density of acetonitrile molecules. This disruption of the acetonitrile-rich layer near the interface abruptly at pH > 10 sheds light on the unpredictable pH dependence of analyte retention times in HILIC separations.

Chapter 6

Conclusion

6.1 Conclusions

This thesis focuses on disentangling the interactions occurring at the silica/water interface. Key among these interactions are those of the waters bound to the surface, which are difficult to measure by conventional spectroscopies or electrochemical methods. Nonlinear optical techniques, such as sum frequency generation and second harmonic generation, demonstrate the surface selectivity required to probe such buried interfaces. The many forces at play at the silica/water interface have large effects on the signal measured by SHG or SFG. However, discrepancies still exist in this rapidly growing field. In the seminal work by Eisenthal and coworkers,[59] it was suggested that water plays a large role in signal generation by SHG at the silica/water interface. From this, the $\chi^{(3)}$ method was established, which accounts for the SHG signal in terms of aligned water. However, when the water stretching region of the silica/water interface was measured using vibrational sum frequency generation,[60] the trends did not match those observed by SHG.

Chapter 2 aimed to directly compare the pH dependent trends observed by nonresonant second harmonic generation and resonant sum frequency generation. When the $\chi^{(3)}$ method was developed,[59] it was assumed that the potential independent term at the silica/water interface, $\chi^{(2)}$, was small, because the signal at the expected point of zero charge, was small. At other interfaces such as titania/water[158, 164] and alumina/water,[156, 162] the SHG signal also only decreased with decreasing pH. Given the larger signal measured at the PZC of these mineral oxides, the behaviour was explained by an interference between $\chi^{(2)}$ and $\chi^{(3)}\Phi$, where the sign of the latter term was expected to flip upon passing through the PZC due to a change in sign of the potential.[18] SFG signal exhibited a minimum near the PZCs of titania[164] and alumina,[162] which is in support of this argument. However, on silica, $\chi^{(2)}$ was considered small, and therefore interference could not account for the minimum in SFG signal observed at higher pH values. We measured a substantial

SHG signal from the silica/air interface, where it was assumed the dominant contribution to be from silanols and siloxides. By subtracting the electric field of this signal from the total SHG electric field measured at the silica/water interface, we obtained bimodal behaviour in the nonresonant SHG trend. However, large differences in relative SHG intensities at low and high pH with respect to that measured by SFG were still apparent. These differences were explained by invoking a flip in orientation of some water molecules near the SFG minimum. SHG, which cannot spectrally resolve such contributions, would therefore be affected by destructive interference to the water signal at low pH where different populations of water are in opposite orientation. This theory follows from observations made previously,[19, 99] which suggested a flip at low pH due to either overcharging or asymmetric hydration spheres. Furthermore, the idea of oppositely aligned waters is supported by phase measurements.[82, 90] In a further attempt to explain the difference between SHG and SFG trends, molecular dynamics simulations of silica/water at neutral charge suggested the intrinsic SFG activity of the low wavenumber SFG mode to be higher than that of the high wavenumber mode despite 1.8 times the amount of oscillators contributing to the latter, indicating some disorder of waters contributing to the former. At the high salt concentrations of this study, the surface waters were expected to play a relatively large role in signal generation, since the Debye length was reduced to only a few nanometers.

Chapter 3 was aimed at determining how ionic strength affects the surface water structure. This study served to establish a methodology for obtaining surface water complex spectra from intensity measurements. The maximum entropy method has been used previously to extract phase information at other interfaces,[184-186] however, solving for the unknown error phase requires some additional knowledge of the system. Reference to phase measurements of the silica/water interface,[82, 90] allowed us to determine the correct error phase for the MEM. Under the assumption

of an unchanging $\chi^{(2)}$ between two salt concentrations, any spectral changes between their respective spectra must be due to the potential component, $\chi^{(3)}\Phi$. By measuring the zeta potential at each ionic strength at the same interface, the relative value of $\chi^{(3)}$ was determined. The surface spectra were then extracted at each ionic strength, which demonstrated a sign inversion in the imaginary spectra at low wavenumber as salt was increased from 0.01 mM to 50 mM NaCl. This project spectrally demonstrated that ionic strength plays a large role in the alignment of surface waters on silica.

Chapter 4 follows up on the previous chapter by investigating the role of pH on the orientation of surface waters on silica. SFG intensities and zeta potentials were measured at the silica/water interface at 50 mM NaCl from pH 10 to 2. The phase of the intensity measurements was determined through the MEM as in Chapter 3. Although, to obtain the $\chi^{(3)}$ spectrum, we could not make the assumption of an unchanging $\chi^{(2)}$ over any of the pH points studied because of the dissociation of silanols expected over the pH range. For this reason, the $\chi^{(3)}$ spectrum from Chapter 3 was used. At low pH, two modes of opposite phase were observed in the surface spectrum, which were assigned to H-bond acceptor (low wavenumber) and H-bond donor (high wavenumber) waters. This assignment was supported by the sign of $\chi^{(3)}\Phi$, which was representative of waters with their hydrogens pointing towards the surface, and in phase with the high wavenumber mode at low pH. As the pH was increased, the low wavenumber mode became less negative, and a new positive mode centred around 3200 cm^{-1} grew until the entire spectrum was positive. The 3400 cm^{-1} region did not change very much over the pH titration. The net flip in signal contributing to low wavenumbers was attributed to an increase in number density of siloxides. The increasingly negative charge of the siloxides was suggested to induce a favourable alignment of water with their hydrogens pointed towards the surface, additionally, the proximity

of cations to the surface may also lend to this preference. The bimodal behaviour of the SFG signal over the pH range studied was considered and reconstructed over a wide range of potential magnitudes suggesting the bimodal behaviour can be rationalized by interfering surface and diffuse layer contributions. Comparisons of the surface spectral trends were made to the pH dependent behaviour of certain properties of silica such as solubility and aggregation rates.

Chapter 5 was a study on the interactions of acetonitrile, an amphiphilic, polar molecular, and water in the contact with silica with increasing pH. This solvent mixture is used in hydrophilic interaction chromatography for the separation of charged or polar compounds. However, the behaviour in retention time is difficult to predict at higher pH and is likely due to interfacial processes occurring near the silica, which is the stationary phase oF HILIC. To determine the behaviour of the water and acetonitrile, SFG spectra of the silica/ACN-H_2O were collected in the methyl, hydroxyl, and nitrile stretching regions. As solution pH was increased above 10, a sudden spectral change was observed in all regions measured. In the methyl region, this change was in the form of an increase in total intensity, however, fitting the spectra revealed that the methyl stretch was actually decreasing, whereas the total intensity increase was due to an increase in the alignment of water molecules. This was supported by the spectra in the water stretching region, which increased with pH, and the spectra of the silica/ACN-D_2O interface which lacked the interference from the OH modes and clearly demonstrated a loss in methyl signal. This decrease in methyl signal was attributed to a displacement of ACN from the surface as the orientation analysis revealed little net rearrangement. The nitrile stretching region was measured at the CaF_2-silica/ACN-H_2O interface and also exhibited pH dependent behaviour with a sudden change occurring around pH 10.

6.2 Future Work

An interesting observation of the surface water spectra of silica obtained through the $\chi^{(3)}$ method is its similarity to that extracted from the negatively charged, lipid/water interface.[101] In both cases, two oppositely signed modes were observed when the surface was expected to be neutral (Figures 1.12 and 4.3c). As the surface was deprotonated, the low wavenumber mode flipped in sign, and a 3200 cm^{-1} mode grew in. In both circumstances, sodium ions were present. It would be interesting to determine if this behaviour is common to all neutral interfaces containing H-bond donor and acceptor sites. Furthermore, if the increase in 3200 cm^{-1} intensity was related to the presence of cations near the negative surface, it would be interesting to observe the spectral features of anions near a positive surface. Following the model laid out in Chapters 3 and 4, this would be straightforward following SFG intensity and zeta potential measurements of a surface with a higher pK_a, such as alumina or titania.[18] However, this procedure would require phase knowledge of the system, and therefore would have to be measured. Furthermore, specific ion effects have already been demonstrated on the surface waters of silica through heterodyne SHG measurements,[132] and it would be insightful to measure the corresponding spectral changes.

On the behaviour of silica near the PZC, studies of cation adsorption are often discussed in terms of adsorption to neutral silanol sites.[1, 199] For titania[158] and alumina,[156-157] the PZC was estimated by determining the point of zero salt effect (PZSE), where the addition of salt had no effect on the NLO signal because of a lack of charged sites with which to bind. However, if cations bind with neutral sites, as suggested for silica,[1, 199] then there should be no PZSE, yet, a study to determine the PZSE on silica has never been performed. An SFG study comparing the effect of pure water and 0.1 M NaCl on silica indicated little spectral changes at pH 2.[134] However, as demonstrated in Chapter 3, the dominant changes to the surface water spectra at a charged surface

were observed below 10 mM ionic strength. Though the ionic strength is already quite large at pH 2 (10 mM), it may be possible to extrapolate the PZSE (if it exists) from measurements at higher pH. Furthermore, as sodium is often described as having unique binding affinities to silica, relative to other cations,[1] a change might still be observed as the total sodium concentration is increased. In this case, a comparison to other cations would be prudent. Furthermore, XPS studies on quartz suggest that the silica surface does not only consist of neutral silanols at pH 2, but rather an equal proportion of negatively charged $Si\text{-}O^-$ and positively charged $Si\text{-}OH_2^+$ sites.[40] At such a mixed surface, attraction of cations by charged sites would still be expected at pH 2, and similarly, anions should also be attracted to the surface. Therefore it would be very insightful to measure the SFG spectra of silica/water at pH 2 in the presence of different cations and anions, and may shed further light on why the surface spectrum of the silica/water interface in the presence of very low ionic strengths at pH 5.8 appears similar to that at pH 2 (Figures 3.6b and 4.3c)

Temperature also affects SFG spectra from the silica/water interface.[83-84, 260] In general, the SFG spectra of the silica/ice interface exhibited a dominant feature centred around 3200 cm^{-1}, attributed to the strong hydrogen bonding of ice. In fact, in both the SFG spectra of silica/ice and silica/water at low and high pH, a strong mode around 3200 cm^{-1} is observed. There is likely a wealth of information to be gained by studying the silica/ice interface in the presence of salts and varying solution pH. For example, due to the kosmotropic and chaotropic nature of different salts, it may be expected that ice formation is affected by the presence of various ions. Furthermore, the structure of water on silica may be affected when frozen in the presence of strong or weak static electric fields. Conversely, the presence of static electric fields may affect ice melting.

The question remains whether the zeta potential, rather than the surface potential, is the dominant force influencing the potential-aligned waters observed by SFG, which has been

suggested by others.[42, 154] This may indicate the surface potential is not obtainable by comparing changes to the net alignment of diffuse layer waters. However, in this light, there may yet be a spectroscopic method to obtain the surface potential from insulators like silica. Simulations predict the electronic component of the SFG signal, the second hyperpolarizability, γ, is much smaller than the first hyperpolarizability, β.[92] However, this was only found true in the resonant regime. In the nonresonant case, the magnitude of γ was comparable to that of β. This γ accounts for the signal generation due to the polarization of molecules, rather than their reorientation (Equation 1.6). In other words, surface waters which are not reoriented by the electric field, may still be highly polarized. Therefore, the actual surface potential may be coupled to the γ of the surface waters and might be accessed by comparing the surface water behaviour observed by resonant SFG and nonresonant SHG techniques. Additionally, the large electric fields interacting with the surface bound waters may lead to a Stark shift, where the resonance frequencies would be expected to redshift with increasingly negative potentials.[197] If spectral contributions from neighbouring modes, intermolecular coupling, and changes to H-bonding strength can be determined, frequency shifts may be assigned to such a Stark effect.

Finally, all results were analyzed under the electric dipole approximation, which assumes quadrupole effects to be negligible. However, recent studies have indicated this is not always the case.[261] It may be worthwhile to revisit some of the studies performed herein to investigate for quadrupole effects, particularly for those where signal contribution from the silica was considered.

6.2 Perspectives

Nonlinear optical techniques such as SFG and SHG are very useful in studying buried interfaces such as that of silica/water. However, the techniques themselves are not fool-proof. It goes without saying that the proper alignment of optics is of utmost importance in obtaining useful data. For SFG of silica/water spectra, making use of polarization-resolved SFG can aid in assessing whether the alignment is accurate. In particular, misalignments will have drastic effects on the pss spectrum from silica/water. For the silica/water interface at a natural pH of 5.8, a misalignment is often observed in the pss spectrum as an apparent mode around 3200 cm^{-1}, which is likely contribution from other polarization combinations (i.e. ssp or ppp), that exhibit a large 3200 cm^{-1} mode. Additionally, the high laser powers required to generate SFG and SHG can damage the interface being measured. For this reason, laser powers are often attenuated before reaching the sample,[121-123, 231, 262] however, the effect of beam damage to silica on SFG spectra is unclear. Similarly, if the high intensity beams are changing the temperature within the probing region at the interface, changes to the resulting spectra would be expected, as the spectrum of $\chi^{(3)}$ has been shown to be very sensitive to temperature,[104] and temperature directly affects equilibrium constants (i.e. the acid dissociation of silica). Furthermore, fluctuations in laser power can occur very regularly over time, and must be carefully monitored as this directly affects the intensity of the sum frequency light (Equation 1.3). It is important not to confuse power changes with changes to the nonlinear susceptibility, for example while waiting for interfacial equilibrium. On this note, processes at the silica/water interface have been demonstrated to take long periods of time to reach equilibrium (Figure 2.1), especially under flow conditions.[137-138] Therefore when any changes to solution are made, the resulting signal should be immediately monitored for changes until equilibrium is reached before acquiring data.

Spectral fitting is often necessary to gain further insight into interfacial processes or to interpret SFG data. However, be aware that one can spend days attempting to fit spectra and make no real progress. A quote attributed to John von Neumann,[263] "*...with four parameters I can fit an elephant, and with five I can make him wiggle his trunk,"* is of special consideration here. When necessary, care must always be taken to ensure a certain robustness of fit. When in doubt, consider the fitting procedures used by others in the literature.

It is always at the author's discretion to interpret his or her own data, and interpretation is never an absolute. Underlying models and assumptions play a large role in the perceived outcome. For example, the early screening studies at the silica/water interface interpreted the trend in SFG signal at very low ionic strengths in terms of a surface charge density increase which countered screening effects.[124] Yet, it is now more common, at those low salt concentrations, to invoke interference from signal generation outside of the coherence length.[107-108] However, if SFG studies were compared to screening effects measured by streaming potential, one might make a connection between the decrease in SFG intensity to the decrease in streaming potential measured at low ionic strengths (see Figure 4.5 of the following reference[264]). Although this trend does not occur in streaming current measurements, and is attributed to an increase in surface conductance due to a "diffuse cloud of ions".[264] Perhaps there is a connection yet to be made between SFG and surface conductance that will change the current models? In this thesis, the $\chi^{(3)}$ model is often invoked to explain spectral changes observed at the silica/water interface, and is therefore subject to its accuracy. However, experimental measurements made with all-good intent, peer-reviewed, and reproducible, do not lie, and are the foundations of theories that are malleable. It is not often the intention of the author to mislead the reader. If interpretations are deemed incorrect, there is usually an underlying observation or assumption that led to that interpretation. Therefore the interpretation

may eventually fail, but the measurement will not. In summary, use caution to understand underlying assumptions and theories, take good measurements, and make up your own mind.

References

1. Iler, R. K., *The Chemistry of Silica: Solubility, Polymerization, Colloid and Surface Properties, and Biochemistry*. New York: Wiley: 1979.

2. Jugdaohsingh, R., Silicon and Bone Health. *J. Nutr. Health Aging* **2007,** *11* (2), 99-110.

3. Berner, R. A.; Lasaga, A. C.; Garrels, R. M., The Carbonate-Silicate Geochemical Cycle and its Effect on Atmospheric Carbon Dioxide Over the Past 100 Million Years. *Am. J. Sci.* **1983,** *283* (7), 641-683.

4. Frings, P. J.; Clymans, W.; Fontorbe, G.; De La Rocha, C. L.; Conley, D. J., The Continental Si Cycle and its Impact on the Ocean Si Isotope Budget. *Chem. Geol.* **2016,** *425*, 12-36.

5. Tréguer, P. J.; De La Rocha, C. L., The World Ocean Silica Cycle. *Annu. Rev. Mar. Sci.* **2013,** *5* (1), 477-501.

6. Tréguer, P.; Bowler, C.; Moriceau, B.; Dutkiewicz, S.; Gehlen, M.; Aumont, O.; Bittner, L.; Dugdale, R.; Finkel, Z.; Iudicone, D.; Jahn, O.; Guidi, L.; Lasbleiz, M.; Leblanc, K.; Levy, M.; Pondaven, P., Influence of Diatom Diversity on the Ocean Biological Carbon Pump. *Nat. Geosci.* **2017**.

7. Malviya, S.; Scalco, E.; Audic, S.; Vincent, F.; Veluchamy, A.; Poulain, J.; Wincker, P.; Iudicone, D.; de Vargas, C.; Bittner, L.; Zingone, A.; Bowler, C., Insights into Global Diatom Distribution and Diversity in the World's Ocean. *P. Natl. Acad. Sci. USA* **2016,** *113* (11), E1516-E1525.

8. Conley, D. J., Terrestrial Ecosystems and the Global Biogeochemical Silica Cycle. *Global Biogeochem. Cy.* **2002,** *16* (4), 68-1-68-8.

9. Currie, H. A.; Perry, C. C., Silica in Plants: Biological, Biochemical and Chemical Studies. *Ann. Bot.* **2007,** *100* (7), 1383-1389.

10. Sahebi, M.; Hanafi, M. M.; Siti Nor Akmar, A.; Rafii, M. Y.; Azizi, P.; Tengoua, F. F.; Nurul Mayzaitul Azwa, J.; Shabanimofrad, M., Importance of Silicon and Mechanisms of Biosilica Formation in Plants. *Biomed Res. Int.* **2015,** *2015*, 396010.

11. Price, C. T.; Koval, K. J.; Langford, J. R., Silicon: A Review of its Potential Role in the Prevention and Treatment of Postmenopausal Osteoporosis. *Int. J. Endocrinol.* **2013,** *2013*, 316783-316783.

12. Griot, O.; Kitchener, J. A., Ageing of Silica Suspensions in Water and its Influence on Flocculation by Polyacrylamide. *Nature* **1963,** *200* (491), 1004.

13. Volkov, A. V.; Kiselev, A. V.; Lygin, V. I., Spectroscopic Study of Water on Aerosil Without Heating of Sample by Infrared Radiation .3. Water Adsorption on Highly Dehydroxylated Aerosil Surface. *Zh. Fiz. Khim.* **1974,** *48* (5), 1214-1218.

14. Wirzing, G., Die Bestimmung von Wasser + SiOH-Gruppen in Aerosil + Silicagel Durch Spektroskopie im Nahen Ultrarot. *Naturwissenschaften* **1964,** *51* (9), 211-&.

15. de Boer, J. H., Untersuchungen Über Mikroporöse Salz- und Oxyd-Systeme. *Angew. Chem.* **1958,** *70* (13), 383-389.

16. Bermudez, V. M., Proton Nuclear Magnetic Resonance Technique for Determining the Surface Hydroxyl Content of Hydrated Silica Gel. *J. Phys. Chem.* **1970,** *74* (23), 4160-4161.

17. Chertov, V. M.; Dzhambae.Db; Plachind.As; Neimark, I. E., Hydroxy-Groups on Surface of and Within Silica Gel Globules Obtained by Hydrothermal Treatment of Hydrogels. *Russ. J. Phys. Ch.* **1966,** *40* (3), 282-&.

18. Kosmulski, M., The pH-dependent surface charging and points of zero charge: V. Update. *Journal of Colloid and Interface Science* **2011,** *353* (1), 1-15.

19. DeWalt-Kerian, E. L.; Kim, S.; Azam, M. S.; Zeng, H.; Liu, Q.; Gibbs, J. M., pH-Dependent Inversion of Hofmeister Trends in the Water Structure of the Electrical Double Layer. *J. Phys. Chem. Lett.* **2017,** *8*, 2855-2861.

20. Helmholtz, H., Ueber Einige Gesetze der Vertheilung Elektrischer Ströme in Körperlichen Leitern mit Anwendung auf die Thierisch-Elektrischen Versuche. *Ann. Phys.-Berlin* **1853,** *165* (6), 211-233.

21. Chapman, D. L., LI. A Contribution to the Theory of Electrocapillarity. *Philos. Mag.* **1913,** *25* (148), 475-481.

22. Stern, O., Zur Theorie der Elektrolytischen Doppelschicht. *Z. Elktrochem. Angew. P.* **1924,** *30* (21-22), 508-516.

23. Grahame, D. C., The Electrical Double Layer and the Theory of Electrocapillarity. *Chem. Rev.* **1947,** *41* (3), 441-501.

24. Yates, D. E.; Levine, S.; Healy, T. W., Site-Binding Model of the Electrical Double Layer at the Oxide/Water Interface. *J. Chem. Soc., Faraday Trans. 1* **1974,** *70* (0), 1807-1818.

25. Jørgensen, S. S., Solubility and Dissolution Kinetics of Precipitated Amorphous Silica in 1 M $NaClO_4$ at 25 Degrees C. *Acta. Chem. Scand.* **1968,** *22* (335), 335-341.

26. Greenberg, S. A.; Price, E. W., The Solubility of Silica in Solutions of Electrolytes. *J. Phys. Chem.* **1957,** *61* (11), 1539-1541.

27. Stober, W., Formation of Silicic Acid in Aqueous Suspensions of Different Silica Modifications. *Adv. Chem. Ser.* **1967,** (67), 161-&.

28. Alexander, G. B.; Heston, W. M.; Iler, R. K., The Solubility of Amorphous Silica in Water. *J. Phys. Chem.* **1954,** *58* (6), 453-455.

29. Lier, J. A. V.; Bruyn, P. L. D.; Overbeek, J. T. G., The Solubility of Quartz. *J. Phys. Chem.* **1960,** *64* (11), 1675-1682.

30. Bacon, F. R.; Raggon, F. C., Promotion of Attack on Glass and Silica by Citrate and Other Anions in Neutral Solution. *J. Am. Ceram. Soc.* **1959,** *42* (4), 199-205.

31. Jephcott, C. M.; Johnston, J. H., Solubility of Silica and Alumina. *Arch. Indhyg. Occ. Med.* **1950,** *1* (3), 323-340.

32. Baumann, H., The Dissolving Process of Solid SiO_2 Modifications. *Beitr. Silikose-Forsch.* **1955,** *1*, 31-41.

33. Iler, R. K., Polymerization of Silicic Acid: Catalytic Effect of Fluoride. *J. Phys. Chem.* **1952,** *56* (6), 680-683.

34. Baxter, S.; Bryant, K. C., 577. Silica Sols. Part II. Conditions of Stability. *J. Chem. Soc.* **1952,** (0), 3021-3024.

35. Baxter, S.; Bryant, K. C., 578. Silica Sols. Part III. Accelerated Gelation, and Particle Size. *J. Chem. Soc.* **1952,** (0), 3024-3027.

36. Iler, R. K.; Dalton, R. L., Degree of Hydration of Particles of Colloidal Silica in Aqueous Solution. *J. Phys. Chem.* **1956,** *60* (7), 955-957.

37. Preočanin, T.; Namjesnik, D.; Brown, M. A.; Lützenkirchen, J., The Relationship Between Inner Surface Potential and Electrokinetic Potential from an Experimental and Theoretical Point of View. *Environ. Chem.* **2017,** *14* (5), 295-309.

38. McDonald, R. S., Study of the Interaction between Hydroxyl Groups of Aerosil Silica and Adsorbed Non-Polar Molecules by Infrared Spectrometry[1]. *J. Am. Chem. Soc.* **1957,** *79* (4), 850-854.

39. McDonald, R. S., Surface Functionality of Amorphous Silica by Infrared Spectroscopy. *J. Phys. Chem.* **1958,** *62* (10), 1168-1178.

40. Duval, Y.; Mielczarski, J. A.; Pokrovsky, O. S.; Mielczarski, E.; Ehrhardt, J. J., Evidence of the Existence of Three Types of Species at the Quartz−Aqueous Solution Interface at pH 0−10: XPS Surface Group Quantification and Surface Complexation Modeling. *J. Phys. Chem. B* **2002,** *106* (11), 2937-2945.

41. Brown, M. A.; Goel, A.; Abbas, Z., Effect of Electrolyte Concentration on the Stern Layer Thickness at a Charged Interface. *Angew. Chem. Int. Ed.* **2016,** *55*, 3790 - 3794.

42. Brown, M. A.; Abbas, Z.; Kleibert, A.; Green, R. G.; Goel, A.; May, S.; Squires, T. M., Determination of Surface Potential and Electrical Double-Layer Structure at the Aqueous Electrolyte-Nanoparticle Interface. *Phys. Rev. X* **2016,** *6* (1), 011007.

43. Kondo, S.; Muroya, M. A., Dehydration of Surface Silanol on Silica Gel. *B. Chem. Soc. Jpn.* **1970,** *43* (8), 2657.

44. Li, I.; Bandara, J.; Shultz, M. J., Time Evolution Studies of the H_2O/Quartz Interface Using Sum Frequency Generation, Atomic Force Microscopy, and Molecular Dynamics. *Langmuir* **2004,** *20* (24), 10474-10480.

45. Gusev, I.; Horváth, C., Streaming Potential in Open and Packed Fused-Silica Capillaries. *J. Chromatogr. A* **2002,** *948* (1), 203-223.

46. Scales, P. J.; Grieser, F.; Healy, T. W.; White, L. R.; Chan, D. Y. C., Electrokinetics of the Silica-Solution Interface: A Flat Plate Streaming Potential Study. *Langmuir* **1992,** *8* (3), 965-974.

47. Kosmulski, M., Positive Electrokinetic Charge of Silica in the Presence of Chlorides. *J. Colloid Interf. Sci.* **1998,** *208* (2), 543-545.

48. Kosmulski, M.; Rosenholm, J. B., High Ionic Strength Electrokinetics. *Adv. Colloid Interface Sci.* **2004,** *112* (1), 93-107.

49. Franks, G. V., Zeta Potentials and Yield Stresses of Silica Suspensions in Concentrated Monovalent Electrolytes: Isoelectric Point Shift and Additional Attraction. *J. Colloid Interf. Sci.* **2002,** *249* (1), 44-51.

50. Jalil, A. H.; Pyell, U., Quantification of Zeta-Potential and Electrokinetic Surface Charge Density for Colloidal Silica Nanoparticles Dependent on Type and Concentration of the Counterion: Probing the Outer Helmholtz Plane. *J. Phys. Chem. C* **2018,** *122* (8), 4437-4453.

51. Karlsson, M.; Craven, C.; Dove, P. M.; Casey, W. H., Surface Charge Concentrations on Silica in Different 1.0 M Metal-Chloride Background Electrolytes and Implications for Dissolution Rates. *Aquat. Geochem.* **2001,** *7* (1), 13-32.

52. Kitamura, A.; Fujiwara, K.; Yamamoto, T.; Nishikawa, S.; Moriyama, H., Analysis of Adsorption Behavior of Cations onto Quartz Surface by Electrical Double-layer Model. *J. Nucl. Sci. Technol.* **1999,** *36* (12), 1167-1175.

53. Salis, A.; Parsons, D. F.; Boström, M.; Medda, L.; Barse, B.; Ninham, B. W.; Monduzzi, M., Ion Specific Surface Charge Density of SBA-15 Mesoporous Silica. *Langmuir* **2010,** *26* (4), 2484-2490.

54. Icenhower, J. P.; Dove, P. M., The Dissolution Kinetics of Amorphous Silica into Sodium Chloride Solutions: Effects of Temperature and Ionic Strength. *Geochim. Cosmochim. Ac.* **2000,** *64* (24), 4193-4203.

55. Boyd, R. W., *Nonlinear Optics, 3rd ed.* Burlington, MA: Academic Press: 2008.

56. Franken, P. A.; Hill, A. E.; Peters, C. W.; Weinreich, G., Generation of Optical Harmonics. *Phys. Rev. Lett.* **1961,** *7* (4), 118-119.

57. Lu, R.; Gan, W.; Wu, B.-h.; Zhang, Z.; Guo, Y.; Wang, H.-f., C-H Stretching Vibrations of Methyl, Methylene and Methine Groups at the Vapor/Alcohol (n = 1−8) Interfaces. *J. Phys. Chem. B* **2005,** *109*, 14118-14129.

58. Gan, W.; Wu, D.; Zhang, Z.; Feng, R.-r.; Wang, H.-f., Polarization and Experimental Configuration Analyses of Sum Frequency Generation Vibrational Spectra, Structure, and Orientational Motion of the Air/Water Interface. *J. Chem. Phys.* **2006,** *124* (11), 114705.

59. Ong, S.; Zhao, X.; Eisenthal, K. B., Polarization of Water Molecules at a Charged Interface: Second Harmonic Studies of the Silica/Water Interface. *Chem. Phys. Lett.* **1992,** *191*, 327-335.

60. Du, Q.; Freysz, E.; Shen, Y. R., Vibrational Spectra of Water Molecules at Quartz/Water Interfaces. *Phys. Rev. Lett.* **1994,** *72*, 238-241.

61. Corcelli, S. A.; Lawrence, C. P.; Skinner, J. L., Combined Electronic Structure/Molecular Dynamics Approach for Ultrafast Infrared Spectroscopy of Dilute HOD in Liquid H_2O And D_2O. *J. Chem. Phys.* **2004,** *120* (17), 8107-8117.

62. Paesani, F.; Voth, G. A., The Properties of Water: Insights from Quantum Simulations. *J. Phys. Chem. B* **2009,** *113* (17), 5702-5719.

63. Møller, K. B.; Rey, R.; Hynes, J. T., Hydrogen Bond Dynamics in Water and Ultrafast Infrared Spectroscopy: A Theoretical Study. *J. Phys. Chem. A* **2004,** *108* (7), 1275-1289.

64. Lawrence, C. P.; Skinner, J. L., Ultrafast Infrared Spectroscopy Probes Hydrogen-Bonding Dynamics in Liquid Water. *Chem. Phys. Lett.* **2003,** *369* (3), 472-477.

65. Bakker, H. J.; Skinner, J. L., Vibrational Spectroscopy as a Probe of Structure and Dynamics in Liquid Water. *Chem. Rev.* **2010,** *110* (3), 1498-1517.

66. Kumar, R.; Schmidt, J. R.; Skinner, J. L., Hydrogen Bonding Definitions and Dynamics in Liquid Water. *J. Chem. Phys.* **2007,** *126* (20), 204107.

67. Nibbering, E. T. J.; Elsaesser, T., Ultrafast Vibrational Dynamics of Hydrogen Bonds in the Condensed Phase. *Chem. Rev.* **2004,** *104* (4), 1887-1914.

68. Du, Q.; Freysz, E.; Shen, Y. R., Surface Vibrational Spectroscopic Studies of Hydrogen Bonding and Hydrophobicity. *Science* **1994,** *264* (5160), 826.

69. Du, Q.; Superfine, R.; Freysz, E.; Shen, Y. R., Vibrational Spectroscopy of Water at the Vapor/Water Interface. *Phys. Rev. Lett.* **1993,** *70*, 2313-2316.

70. Liljeblad, J. F. D.; Tyrode, E., Vibrational Sum Frequency Spectroscopy Studies at Solid/Liquid Interfaces: Influence of the Experimental Geometry in the Spectral Shape and Enhancement. *J. Phys. Chem. C* **2012,** *116* (43), 22893-22903.

71. Tyrode, E.; Liljeblad, J. F. D., Water Structure Next to Ordered and Disordered Hydrophobic Silane Monolayers: A Vibrational Sum Frequency Spectroscopy Study. *J. Phys. Chem. C* **2013,** *117* (4), 1780-1790.

72. Zhang, L.; Singh, S.; Tian, C.; Shen, Y. R.; Wu, Y.; Shannon, M. A.; Brinker, C. J., Nanoporous Silica-Water Interfaces Studied by Sum-Frequency Vibrational Spectroscopy. *J. Chem. Phys.* **2009,** *130* (15), 154702.

73. Dalstein, L.; Potapova, E.; Tyrode, E., The Elusive Silica/Water Interface: Isolated Silanols Under Water as Revealed by Vibrational Sum Frequency Spectroscopy. *Phys. Chem. Chem. Phys.* **2017,** *19*, 10343-10349.

74. Sheth, N.; Ngo, D.; Banerjee, J.; Zhou, Y.; Pantano, C. G.; Kim, S. H., Probing Hydrogen-Bonding Interactions of Water Molecules Adsorbed on Silica, Sodium Calcium Silicate, and Calcium Aluminosilicate Glasses. *J. Phys. Chem. C* **2018,** *122* (31), 17792-17801.

75. Cyran, J. D.; Donovan, M. A.; Vollmer, D.; Siro Brigiano, F.; Pezzotti, S.; Galimberti, D. R.; Gaigeot, M.-P.; Bonn, M.; Backus, E. H. G., Molecular Hydrophobicity at a Macroscopically Hydrophilic Surface. *P. Natl. Acad. Sci. USA* **2019,** *116* (5), 1520.

76. Hare, D. E.; Sorensen, C. M., Interoscillator Coupling Effects on the OH Stretching Band of Liquid Water. *J. Chem. Phys.* **1992,** *96* (1), 13-22.

77. Morita, A.; Hynes, J. T., A Theoretical Analysis of the Sum Frequency Generation Spectrum of the Water Surface. *Chem. Phys.* **2000,** *258* (2), 371-390.

78. Schnitzer, C.; Baldelli, S.; Shultz, M. J., Sum Frequency Generation of Water on NaCl, $NaNO_3$, $KHSO_4$, HCl, HNO_3, and H_2SO_4 Aqueous Solutions. *J. Phys. Chem. B* **2000,** *104* (3), 585-590.

79. Richmond, G. L., Molecular Bonding and Interactions at Aqueous Surfaces as Probed by Vibrational Sum Frequency Spectroscopy. *Chem. Rev.* **2002,** *102*, 2693-2724.

80. Jena, K. C.; Hore, D. K., Variation of Ionic Strength Reveals the Interfacial Water Structure at a Charged Mineral Surface. *J. Phys. Chem. C* **2009,** *113*, 15364-15372.

81. Ostroverkhov, V.; Waychunas, G. A.; Shen, Y. R., Vibrational Spectra of Water at Water/α-Quartz(0001) Interface. *Chem. Phys. Lett.* **2004,** *386*, 144-148.

82. Ostroverkhov, V.; Waychunas, G. A.; Shen, Y. R., New Information on Water Interfacial Structure Revealed by Phase-Sensitive Surface Spectroscopy. *Phys. Rev. Lett.* **2005,** *94* (4), 046102.

83. Shen, Y. R., 1998 Frank Isakson Prize Address Sum Frequency Generation for Vibrational Spectroscopy: Applications to Water Interfaces and Films of Water and Ice. *Solid State Commun.* **1998,** *108* (7), 399-406.

84. Liljeblad, J. F. D.; Furo, I.; Tyrode, E. C., The Premolten Layer of Ice Next to a Hydrophilic Solid Surface: Correlating Adhesion with Molecular Properties. *Phys. Chem. Chem. Phys.* **2017,** *19* (1), 305-317.

85. Sovago, M.; Campen, R. K.; Wurpel, G. W. H.; Müller, M.; Bakker, H. J.; Bonn, M., Vibrational Response of Hydrogen-Bonded Interfacial Water is Dominated by Intramolecular Coupling. *Phys. Rev. Lett.* **2008,** *100* (17), 173901.

86. Nihonyanagi, S.; Yamaguchi, S.; Tahara, T., Water Hydrogen Bond Structure near Highly Charged Interfaces Is Not Like Ice. *J. Am. Chem. Soc.* **2010,** *132* (20), 6867-6869.

87. Isaienko, O.; Nihonyanagi, S.; Sil, D.; Borguet, E., Observation of the Bending Mode of Interfacial Water at Silica Surfaces by Near-Infrared Vibrational Sum-Frequency Generation Spectroscopy of the [Stretch + Bend] Combination Bands. *J. Phys. Chem. Lett.* **2013,** *4* (3), 531-535.

88. Kananenka, A. A.; Skinner, J. L., Fermi Resonance in OH-Stretch Vibrational Spectroscopy of Liquid Water and the Water Hexamer. *J. Chem. Phys.* **2018,** *148* (24), 244107.

89. Sovago, M.; Kramer Campen, R.; Bakker, H. J.; Bonn, M., Hydrogen Bonding Strength of Interfacial Water Determined with Surface Sum-Frequency Generation. *Chem. Phys. Lett.* **2009,** *470* (1), 7-12.

90. Myalitsin, A.; Urashima, S.; Nihonyanagi, S.; Yamaguchi, S.; Tahara, T., Water Structure at the Buried Silica/Aqueous Interface Studied by Heterodyne-Detected Vibrational Sum-Frequency Generation. *J. Phys. Chem. C* **2016,** *120* (17), 9357-9363.

91. Roy, S.; Hore, D. K., Simulated Structure and Nonlinear Vibrational Spectra of Water Next to Hydrophobic and Hydrophilic Solid Surfaces. *J. Phys. Chem. C* **2012,** *116* (43), 22867-22877.

92. Joutsuka, T.; Hirano, T.; Sprik, M.; Morita, A., Effects of Third-Order Susceptibility in Sum Frequency Generation Spectra: A Molecular Dynamics Study in Liquid Water. *Phys. Chem. Chem. Phys.* **2018,** *20* (5), 3040-3053.

93. Lyu, Y.; Wang, Y.; Wang, S.; Liu, B.; Du, H., Potassium Hydroxide Concentration-Dependent Water Structure on the Quartz Surface Studied by Combining Sum-Frequency Generation (SFG) Spectroscopy and Molecular Simulations. *Langmuir* **2019,** *35* (36), 11651-11661.

94. Pezzotti, S.; Galimberti, D. R.; Shen, Y. R.; Gaigeot, M.-P., Structural Definition of the BIL and DL: A New Universal methodology to Rationalize Non-Linear $\chi^{(2)}(\omega)$ SFG Signals at Charged Interfaces, Including $\chi^{(3)}(\omega)$ Contributions. *Phys. Chem. Chem. Phys.* **2018,** *20* (7), 5190-5199.

95. Gaigeot, M.-P.; Sprik, M.; Sulpizi, M., Oxide/Water Interfaces: How the Surface Chemistry Modifies Interfacial Water Properties. *J. Phys. Condens. Mat.* **2012,** *24* (12), 124106.

96. Sthoer, A.; Hladílková, J.; Lund, M.; Tyrode, E., Molecular Insight into Carboxylic Acid–Alkali Metal Cations Interactions: Reversed Affinities and Ion-Pair Formation Revealed by Non-Linear Optics and Simulations. *Phys. Chem. Chem. Phys.* **2019,** *21* (21), 11329-11344.

97. Pegram, L. M.; Wendorff, T.; Erdmann, R.; Shkel, I.; Bellissimo, D.; Felitsky, D. J.; Record, M. T., Why Hofmeister Effects of Many Salts Favor Protein Folding but bot DNA Helix Formation. *P. Natl. Acad. Sci. USA* **2010,** *107* (17), 7716.

98. Okur, H. I.; Hladílková, J.; Rembert, K. B.; Cho, Y.; Heyda, J.; Dzubiella, J.; Cremer, P. S.; Jungwirth, P., Beyond the Hofmeister Series: Ion-Specific Effects on Proteins and Their Biological Functions. *J. Phys. Chem. B* **2017,** *121* (9), 1997-2014.

99. Darlington, A. M.; Jarisz, T. A.; DeWalt-Kerian, E. L.; Roy, S.; Kim, S.; Azam, M. S.; Hore, D. K.; Gibbs, J. M., Separating the pH-Dependent Behavior of Water in the Stern and Diffuse Layers with Varying Salt Concentration. *J. Phys. Chem. C* **2017,** *121*, 20229-20241.

100. Urashima, S.-h.; Myalitsin, A.; Nihonyanagi, S.; Tahara, T., The Topmost Water Structure at a Charged Silica/Aqueous Interface Revealed by Heterodyne-Detected Vibrational Sum Frequency Generation Spectroscopy. *J. Phys. Chem. Lett.* **2018,** *9* (14), 4109-4114.

101. Wen, Y.-C.; Zha, S.; Liu, X.; Yang, S.; Guo, P.; Shi, G.; Fang, H.; Shen, Y. R.; Tian, C., Unveiling Microscopic Structures of Charged Water Interfaces by Surface-Specific Vibrational Spectroscopy. *Phys. Rev. Lett.* **2016,** *116* (1), 016101.

102. Pezzotti, S.; Galimberti, R. D.; Shen, R. Y.; Gaigeot, M.-P., What the Diffuse Layer (DL) Reveals in Non-Linear SFG Spectroscopy. *Minerals* **2018,** *8* (7).

103. Chen, Y.; Okur, H. I.; Gomopoulos, N.; Macias-Romero, C.; Cremer, P. S.; Petersen, P. B.; Tocci, G.; Wilkins, D. M.; Liang, C.; Ceriotti, M.; Roke, S., Electrolytes Induce Long-Range Orientational Order and Free Energy Changes in the H-Bond Network of Bulk Water. *Sci. Adv.* **2016,** *2* (4), e1501891.

104. Joutsuka, T.; Morita, A., Electrolyte and Temperature Effects on Third-Order Susceptibility in Sum-Frequency Generation Spectroscopy of Aqueous Salt Solutions. *J. Phys. Chem. C* **2018,** *122* (21), 11407-11413.

105. Boamah, M. D.; Ohno, P. E.; Geiger, F. M.; Eisenthal, K. B., Relative Permittivity in the Electrical Double Layer from Nonlinear Optics. *J. Chem. Phys.* **2018,** *148* (22), 222808.

106. Behrens, S. H.; Grier, D. G., The Charge of Glass and Silica Surfaces. *J. Chem. Phys.* **2001,** *115* (14), 6716-6721.

107. Gonella, G.; Lütgebaucks, C.; de Beer, A. G. F.; Roke, S., Second Harmonic and Sum-Frequency Generation from Aqueous Interfaces Is Modulated by Interference. *J. Phys. Chem. C* **2016,** *120* (17), 9165-9173.

108. Schaefer, J.; Gonella, G.; Bonn, M.; Backus, E. H. G., Surface-Specific Vibrational Spectroscopy of the Water/Silica Interface: Screening and Interference. *Phys. Chem. Chem. Phys.* **2017,** *19* (25), 16875-16880.

109. Ohno, P. E.; Wang, H.-f.; Geiger, F. M., Second-Order Spectral Lineshapes from Charged Interfaces. *Nat. Commun.* **2017,** *8* (1), 1032.

110. Ohno, P. E.; Wang, H.-f.; Paesani, F.; Skinner, J. L.; Geiger, F. M., Second-Order Vibrational Lineshapes from the Air/Water Interface. *J. Phys. Chem. A* **2018,** *122* (18), 4457-4464.

111. Mifflin, A. L.; Gerth, K. A.; Geiger, F. M., Kinetics of Chromate Adsorption and Desorption at Fused Quartz/Water Interfaces Studied by Second Harmonic Generation. *J. Phys. Chem. A* **2003,** *107*, 9620-9627.

112. Hayes, P. L.; Chen, E. H.; Achtyl, J. L.; Geiger, F. M., An Optical Voltmeter for Studying Cetyltrimethylammonium Interacting with Fused Silica/Aqueous Interfaces at High Ionic Strength. *J. Phys. Chem. A* **2009,** *113* (16), 4269-4280.

113. Malin, J. N.; Holland, J. G.; Saslow, S. A.; Geiger, F. M., U(VI) Adsorption and Speciation at the Acidic Silica/Water Interface Studied by Resonant and Nonresonant Second Harmonic Generation. *J. Phys. Chem. C* **2011,** *115*, 13353-13360.

114. Jordan, D. S.; Geiger, F. M., Interaction of Aluminum Ions with Fused Silica/Water Interfaces in the Presence of Oxalic Acid Tracked by Second Harmonic Generation. *J. Phys. Chem. C* **2014,** *118* (50), 28970-28977.

115. Yang, Z.; Li, Q.; Chou, K. C., Structures of Water Molecules at the Interfaces of Aqueous Salt Solutions and Silica:Cation Effects. *J. Phys. Chem. C* **2009,** *113*, 8201-8205.

116. Lovering, K. A.; Bertram, A. K.; Chou, K. C., New Information on the Ion-Identity-Dependent Structure of Stern Layer Revealed by Sum Frequency Generation Vibrational Spectroscopy. *J. Phys. Chem. C* **2016,** *120* (32), 18099-18104.

117. Flores, S. C.; Kherb, J.; Konelick, N.; Chen, X.; Cremer, P. S., The Effects of Hofmeister Cations at Negatively Charged Hydrophilic Surfaces. *J. Phys. Chem. C* **2012,** *116* (9), 5730-5734.

118. Flores, S. C.; Kherb, J.; Cremer, P. S., Direct and Reverse Hofmeister Effects on Interfacial Water Structure. *J. Phys. Chem. C* **2012,** *116* (27), 14408-14413.

119. Campen, R. K.; Pymer, A. K.; Nihonyanagi, S.; Borguet, E., Linking Surface Potential and Deprotonation in Nanoporous Silica: Second Harmonic Generation and Acid/Base Titration. *J. Phys. Chem. C* **2010,** *114* (43), 18465-18473.

120. Zhao, X.; Ong, S.; Wang, H.; Eisenthal, K. B., New Method for Determination of Surface pK_a Using Second Harmonic Generation. *Chem. Phys. Lett.* **1993,** *214* (2), 203-207.

121. Azam, M. S.; Weeraman, C. N.; Gibbs-Davis, J. M., Specific Cation Effects on the Bimodal Acid-Base Behavior of the Silica/Water Interface. *J. Phys. Chem. Lett.* **2012,** *3*, 1269-1274.

122. Azam, M. S.; Darlington, A.; Gibbs-Davis, J. M., The Influence of Concentration on Specific Ion Effects at the Silica/Water Interface. *J. Phys. Condens. Mat.* **2014,** *26*, 244107.

123. Azam, M. S.; Weeraman, C. N.; Gibbs-Davis, J. M., Halide-Induced Cooperative Acid-Base Behavior at a Negatively Charged Interface. *J. Phys. Chem. C* **2013,** *117*, 8840-8850.

124. Jena, K. C.; Covert, P. A.; Hore, D. K., The Effect of Salt on the Water Structure at a Charged Solid Surface: Differentiating Second- and Third-order Nonlinear Contributions. *J. Phys. Chem. Lett.* **2011,** *2*, 1056-1061.

125. Covert, P. A.; Jena, K. C.; Hore, D. K., Throwing Salt into the Mix: Altering Interfacial Water Structure by Electrolyte Addition. *J. Phys. Chem. Lett.* **2014,** *5*, 143-148.

126. Achtyl, J. L.; Vlassiouk, I. V.; Fulvio, P. F.; Mahurin, S. M.; Dai, S.; Geiger, F. M., Free Energy Relationships in the Electrical Double Layer over Single-Layer Graphene. *J. Am. Chem. Soc.* **2013,** *135* (3), 979-981.

127. Ohno, P. E.; Saslow, S. A.; Wang, H.-f.; Geiger, F. M.; Eisenthal, K. B., Phase-Referenced Nonlinear Spectroscopy of the α-Quartz/Water Interface. *Nat. Commun.* **2016,** *7*, 13587.

128. Hore, D. K.; Tyrode, E., Probing Charged Aqueous Interfaces Near Critical Angles: Effect of Varying Coherence Length. *J. Phys. Chem. C* **2019,** *123* (27), 16911-16920.

129. Wang, H.; Xu, Q.; Liu, Z.; Tang, Y.; Wei, G.; Shen, Y. R.; Liu, W.-T., Gate-Controlled Sum-Frequency Vibrational Spectroscopy for Probing Charged Oxide/Water Interfaces. *J. Phys. Chem. Lett.* **2019**.

130. Inoue, K.-i.; Nihonyanagi, S.; Singh, P. C.; Yamaguchi, S.; Tahara, T., 2D Heterodyne-Detected Sum Frequency Generation Study on the Ultrafast Vibrational Dynamics of H_2O and HOD Water at Charged Interfaces. *J. Chem. Phys.* **2015,** *142*, 212431.

131. Ohno, P. E.; Chang, H.; Spencer, A. P.; Liu, Y.; Boamah, M. D.; Wang, H.-f.; Geiger, F. M., Beyond the Gouy–Chapman Model with Heterodyne-Detected Second Harmonic Generation. *J. Phys. Chem. Lett.* **2019,** *10* (10), 2328-2334.

132. Boamah, M. D.; Ohno, P. E.; Lozier, E.; Van Ardenne, J.; Geiger, F. M., Specifics about Specific Ion Adsorption from Heterodyne-Detected Second Harmonic Generation. *J. Phys. Chem. B* **2019,** *123* (27), 5848-5856.

133. Marchioro, A.; Bischoff, M.; Lütgebaucks, C.; Biriukov, D.; Předota, M.; Roke, S., Surface Characterization of Colloidal Silica Nanoparticles by Second Harmonic Scattering: Quantifying the Surface Potential and Interfacial Water Order. *J. Phys. Chem. C* **2019,** *123* (33), 20393-20404.

134. Dewan, S.; Yeganeh, M. S.; Borguet, E., Experimental Correlation Between Interfacial Water Structure and Mineral Reactivity. *J. Phys. Chem. Lett.* **2013,** *4*, 1977-1982.

135. Dove, P. M.; Nix, C. J., The Influence of the Alkaline Earth Cations, Magnesium, Calcium, and Barium on the Dissolution Kinetics Of Quartz. *Geochim. Cosmochim. Ac.* **1997,** *61* (16), 3329-3340.

136. Schaefer, J.; Backus, E. H. G.; Bonn, M., Evidence for Auto-Catalytic Mineral Dissolution from Surface-Specific Vibrational Spectroscopy. *Nat. Commun.* **2018,** *9* (1), 3316.

137. Lis, D.; Backus, E. H. G.; Hunger, J.; Parekh, S. H.; Bonn, M., Liquid Flow along a Solid Surface Reversibly Alters Interfacial Chemistry. *Science* **2014,** *344*, 1138-1142.

138. Gibbs-Davis, J. M.; Kruk, J. J.; Konek, C. T.; Scheidt, K. A.; Geiger, F. M., Jammed Acid−Base Reactions at Interfaces. *J. Am. Chem. Soc.* **2008,** *130* (46), 15444-15447.

139. Darlington, A. M.; Gibbs-Davis, J. M., Bimodal or Trimodal? The Influence of Starting pH on Site Identity and Distribution at the Low Salt Aqueous/Silica Interface. *J. Phys. Chem. C* **2015,** *119* (29), 16560-16567.

140. Han, H.; Peng, M.; Hu, Y.; Nguyen, A. V.; Sun, W., An SFG Spectroscopy Study of the Interfacial Water Structure and the Adsorption of Sodium Silicate at the Fluorite and Silica Surfaces. *Miner. Eng.* **2019,** *138*, 178-187.

141. Covert, P. A.; Hore, D. K., Geochemical Insight from Nonlinear Optical Studies of Mineral–Water Interfaces. *Annu. Rev. Phys. Chem.* **2016,** *67* (1), 233-257.

142. Björneholm, O.; Hansen, M. H.; Hodgson, A.; Liu, L.-M.; Limmer, D. T.; Michaelides, A.; Pedevilla, P.; Rossmeisl, J.; Shen, H.; Tocci, G.; Tyrode, E.; Walz, M.-M.; Werner, J.; Bluhm, H., Water at Interfaces. *Chem. Rev.* **2016,** *116* (13), 7698-7726.

143. Geiger, F. M., Second Harmonic Generation, Sum Frequency Generation, and $\chi^{(3)}$: Dissecting Environmental Interfaces with a Nonlinear Optical Swiss Army Knife. *Annu. Rev. Phys. Chem.* **2009,** *60*, 61-83.

144. Schrödle, S.; Richmond, G. L., *In Situ* Non-Linear Spectroscopic Approaches to Understanding Adsorption at Mineral–Water Interfaces. *J. Phys. D. Appl. Phys.* **2008,** *41* (3), 033001.

145. de Beer, A. G. F.; Campen, R. K.; Roke, S., Separating Surface Structure and Surface Charge with Second-Harmonic and Sum-Frequency Scattering. *Phys. Rev. B* **2010,** *82* (23), 235431.

146. Nihonyanagi, S.; Yamaguchi, S.; Tahara, T., Ultrafast Dynamics at Water Interfaces Studied by Vibrational Sum Frequency Generation Spectroscopy. *Chem. Rev.* **2017,** *117* (16), 10665-10693.

147. Shen, Y. R.; Ostroverkhov, V., Sum-Frequency Vibrational Spectroscopy on Water Interfaces: Polar Orientation of Water Molecules at Interfaces. *Chem. Rev.* **2006,** *106*, 1140-1154.

148. Shen, Y. R., *The Principles of Nonlinear Optics*. New York: J. Wiley: 1984.

149. Shen, Y. R., Surface Properties Probed by Second-Harmonic and Sum-Frequency Generation. *Nature* **1989,** *337*, 519-525.

150. Shen, Y. R., Optical Second Harmonic Generation at Interfaces. *Annu. Rev. Phys. Chem.* **1989,** *40* (1), 327-350.

151. Shen, Y. R., *Fundamentals of Sum-Frequency Spectroscopy*. Cambridge University Press: Cambridge, 2016.

152. Eisenthal, K. B., Liquid Interfaces Probed by Second-Harmonic and Sum-Frequency Spectroscopy. *Chem. Rev.* **1996,** *96*, 1343-1360.

153. Konek, C. T.; Musorrafiti, M. J.; Al-Abadleh, H. A.; Bertin, P. A.; Nguyen, S. T.; Geiger, F. M., Interfacial Acidities, Charge Densities, Potentials, and Energies of Carboxylic Acid-Functionalized Silica/Water Interfaces Determined by Second Harmonic Generation. *J. Am. Chem. Soc.* **2004,** *126* (38), 11754-11755.

154. Lützenkirchen, J.; Scharnweber, T.; Ho, T.; Striolo, A.; Sulpizi, M.; Abdelmonem, A., A Set-Up for Simultaneous Measurement of Second Harmonic Generation and Streaming Potential and Some Test Applications. *J. Colloid Interf. Sci.* **2018,** *529*, 294-305.

155. Malin, J. N.; Holland, J. G.; Saslow, S. A.; Geiger, F. M., U(VI) Adsorption and Speciation at the Acidic Silica/Water Interface Studied by Resonant and Nonresonant Second Harmonic Generation. *J. Phys. Chem. C* **2011,** *115* (27), 13353-13360.

156. Fitts, J. P.; Shang, X.; Flynn, G. W.; Heinz, T. F.; Eisenthal, K. B., Electrostatic Surface Charge at Aqueous/α-Al_2O_3 Single-Crystal Interfaces as Probed by Optical Second-Harmonic Generation. *J. Phys. Chem. B* **2005,** *109* (16), 7981-7986.

157. Stack, A. G.; Higgins, S. R.; Eggleston, C. M., Point of Zero Charge of a Corundum-Water Interface Probed with Optical Second Harmonic Generation (SHG) And Atomic Force Microscopy (AFM): New Approaches to Oxide Surface Charge. *Geochim. Cosmochim. Ac.* **2001,** *65* (18), 3055-3063.

158. Fitts, J. P.; Machesky, M. L.; Wesolowski, D. J.; Shang, X.; Kubicki, J. D.; Flynn, G. W.; Heinz, T. F.; Eisenthal, K. B., Second-Harmonic Generation and Theoretical Studies of Protonation at the Water/α-TiO_2 (110) Interface. *Chem. Phys. Lett.* **2005,** *411* (4), 399-403.

159. Gragson, D. E.; McCarty, B. M.; Richmond, G. L., Ordering of Interfacial Water Molecules at the Charged Air/Water Interface Observed by Vibrational Sum Frequency Generation. *J. Am. Chem. Soc.* **1997,** *119* (26), 6144-6152.

160. Gragson, D. E.; Richmond, G. L., Potential Dependent Alignment and Hydrogen Bonding of Water Molecules at Charged Air/Water and CCl_4/Water Interfaces. *J. Am. Chem. Soc.* **1998,** *120* (2), 366-375.

161. Gragson, D. E.; Richmond, G. L., Investigations of the Structure and Hydrogen Bonding of Water Molecules at Liquid Surfaces by Vibrational Sum Frequency Spectroscopy. *J. Phys. Chem. B* **1998,** *102* (20), 3847-3861.

162. Yeganeh, M. S.; Dougal, S. M.; Pink, H. S., Vibrational Spectroscopy of Water at Liquid/Solid Interfaces: Crossing the Isoelectric Point of a Solid Surface. *Phys. Rev. Lett.* **1999,** *83* (6), 1179-1182.

163. Sung, J.; Zhang, L.; Tian, C.; Shen, Y. R.; Waychunas, G. A., Effect of pH on the Water/α-Al_2O_3 ($1\bar{1}02$) Interface Structure Studied by Sum-Frequency Vibrational Spectroscopy. *J. Phys. Chem. C* **2011,** *115* (28), 13887-13893.

164. Kataoka, S.; Gurau, M. C.; Albertorio, F.; Holden, M. A.; Lim, S.-M.; Yang, R. D.; Cremer, P. S., Investigation of Water Structure at the TiO_2/Aqueous Interface. *Langmuir* **2004,** *20* (5), 1662-1666.

165. Zhao, X.; Ong, S.; Eisenthal, K. B., Polarization of Water Molecules at a Charged Interface. Second Harmonic Studies of Charged Monolayers at the Air/Water Interface. *Chem. Phys. Lett.* **1993,** *202*, 513-520.

166. Dreier, L. B.; Bernhard, C.; Gonella, G.; Backus, E. H. G.; Bonn, M., Surface Potential of a Planar Charged Lipid–Water Interface. What Do Vibrating Plate Methods, Second Harmonic and Sum Frequency Measure? *J. Phys. Chem. Lett.* **2018,** *9* (19), 5685-5691.

167. Sauerbeck, C.; Braunschweig, B.; Peukert, W., Surface Charging and Interfacial Water Structure of Amphoteric Colloidal Particles. *J. Phys. Chem. C* **2014,** *118* (19), 10033-10042.

168. Segelstein, D. J. The Complex Refractive Index of Water. Master Thesis, University of Missouri, USA, Kansas City, 1981.

169. Rehl, B.; Rashwan, M.; DeWalt-Kerian, E. L.; Jarisz, T. A.; Darlington, A. M.; Hore, D. K.; Gibbs, J. M., New Insights into $\chi(3)$ Measurements: Comparing Nonresonant Second Harmonic Generation and Resonant Sum Frequency Generation at the Silica/Aqueous Electrolyte Interface. *J. Phys. Chem. C* **2019,** *123* (17), 10991-11000.

170. Smith, A. M.; Lee, A. A.; Perkin, S., The Electrostatic Screening Length in Concentrated Electrolytes Increases with Concentration. *J. Phys. Chem. Lett.* **2016,** *7* (12), 2157-2163.

171. Zhang, H.; Hassanali, A. A.; Shin, Y. K.; Knight, C.; Singer, S. J., The Water–Amorphous Silica Interface: Analysis of the Stern Layer and Surface Conduction. *J. Chem. Phys.* **2011,** *134* (2), 024705.

172. Hartkamp, R.; Siboulet, B.; Dufrêche, J.-F.; Coasne, B., Ion-Specific Adsorption and Electroosmosis in Charged Amorphous Porous Silica. *Phys. Chem. Chem. Phys.* **2015,** *17* (38), 24683-24695.

173. Haria, N. R.; Lorenz, C. D., Atomistic Description of Pressure-Driven Flow of Aqueous Salt Solutions through Charged Silica Nanopores. *J. Phys. Chem. C* **2015,** *119* (22), 12298-12311.

174. Roy, S.; Naka, T. L.; Hore, D. K., Enhanced Understanding of Amphipathic Peptide Adsorbed Structure by Modeling of the Nonlinear Vibrational Response. *J. Phys. Chem. C* **2013,** *117* (47), 24955-24966.

175. Dove, P. M.; Craven, C. M., Surface Charge Density on Silica in Alkali and Alkaline Earth Chloride Electrolyte Solutions. *Geochim. Cosmochim. Ac.* **2005,** *69* (21), 4963-4970.

176. Piontek, S. M.; Tuladhar, A.; Marshall, T.; Borguet, E., Monovalent and Divalent Cations at the α-Al_2O_3(0001)/Water Interface: How Cation Identity Affects Interfacial Ordering and Vibrational Dynamics. *J. Phys. Chem. C* **2019,** *123* (30), 18315-18324.

177. Schlegel, S. J.; Hosseinpour, S.; Gebhard, M.; Devi, A.; Bonn, M.; Backus, E. H. G., How Water Flips at Charged Titanium Dioxide: An SFG-Study on the Water–TiO_2 Interface. *Phys. Chem. Chem. Phys.* **2019,** *21* (17), 8956-8964.

178. Uosaki, K.; Yano, T.; Nihonyanagi, S., Interfacial Water Structure at As-Prepared and UV-Induced Hydrophilic TiO2 Surfaces Studied by Sum Frequency Generation Spectroscopy and Quartz Crystal Microbalance. *J. Phys. Chem. B* **2004,** *108* (50), 19086-19088.

179. Sanders, S. E.; Vanselous, H.; Petersen, P. B., Water at Surfaces with Tunable Surface Chemistries. *J. Phys. Condens. Matter.* **2018,** *30* (11), 113001.

180. Dalchand, N.; Cui, Q.; Geiger, F. M., Electrostatics, Hydrogen Bonding, and Molecular Structure at Polycation and Peptide:Lipid Membrane Interfaces. *ACS Appl. Mater. Inter.* **2019**.

181. Yamaguchi, S.; Tahara, T., Heterodyne-Detected Electronic Sum Frequency Generation: "Up" Versus "Down" Alignment of Interfacial Molecules. *J. Chem. Phys.* **2008,** *129* (10), 101102.

182. García Rey, N.; Weißenborn, E.; Schulze-Zachau, F.; Gochev, G.; Braunschweig, B., Quantifying Double-Layer Potentials at Liquid–Gas Interfaces from Vibrational Sum-Frequency Generation. *J. Phys. Chem. C* **2019,** *123* (2), 1279-1286.

183. Rashwan, M.; Rehl, B.; Sthoer, A.; Darlington, A. M.; Azam, M. S.; Zeng, H.; Liu, Q.; Tyrode, E.; Gibbs, J. M., Structure of the Silica/Divalent Electrolyte Interface: Molecular Insight into Charge Inversion with Increasing pH. **In Preparation**.

184. Yang, P.-K.; Huang, J. Y., Phase-Retrieval Problems in Infrared–Visible Sum-Frequency Generation Spectroscopy by the Maximum-Entropy Method. *J. Opt. Soc. Am. B* **1997,** *14* (10), 2443-2448.

185. Sovago, M.; Vartiainen, E.; Bonn, M., Determining Absolute Molecular Orientation at Interfaces: A Phase Retrieval Approach for Sum Frequency Generation Spectroscopy. *J. Phys. Chem. C* **2009,** *113* (15), 6100-6106.

186. de Beer, A. G. F.; Samson, J.-S.; Hua, W.; Huang, Z.; Chen, X.; Allen, H. C.; Roke, S., Direct Comparison of Phase-Sensitive Vibrational Sum Frequency Generation with Maximum Entropy Method: Case Study of Water. *J. Chem. Phys.* **2011,** *135* (22), 224701.

187. Burg, J. P. Maximum Entropy Spectral Analysis Ph.D. Thesis, Stanford University, USA, Stanford, 1975.

188. Rehl, B.; Li, Z.; Gibbs, J. M., Influence of High pH on the Organization of Acetonitrile at the Silica/Water Interface Studied by Sum Frequency Generation Spectroscopy. *Langmuir* **2018,** *34* (15), 4445-4454.

189. Dreier, L. B.; Nagata, Y.; Lutz, H.; Gonella, G.; Hunger, J.; Backus, E. H. G.; Bonn, M., Saturation of Charge-Induced Water Alignment at Model Membrane Surfaces. *Sci. Adv.* **2018,** *4* (3).

190. Chiang, K.-Y.; Dalstein, L.; Wen, Y.-C., Intrinsic pH of Water/Vapor Interface Revealed by Ion-Induced Water Alignment. *arXiv* **2019**, 1908.09433.

191. Rehl, B.; Gibbs, J. M., On the Role of Ionic Strength on Surface Bound Water Structure at the Silica/Water Interface. *in preparation* **2020**.

192. Yang, P.-K.; Huang, J. Y., Model-Independent Maximum-Entropy Method for the Analysis of Sum-Frequency Vibrational Spectroscopy. *J. Opt. Soc. Am. B* **2000,** *17* (7), 1216-1222.

193. Vartiainen, E. M.; Peiponen, K. E.; Asakura, T., Maximum Entropy Model in Reflection Spectra Analysis. *Opt. Commun.* **1992,** *89* (1), 37-40.

194. Vartiainen, E. M., Phase Retrieval Approach for Coherent Anti-Stokes Raman Scattering Spectrum Analysis. *J. Opt. Soc. Am. B* **1992,** *9* (8), 1209-1214.

195. Vartiainen, E. M.; Peiponen, K. E.; Kishida, H.; Koda, T., Phase Retrieval in Nonlinear Optical Spectroscopy by the Maximum-Entropy Method: An Application to the $|X^{(3)}|$ Spectra of Polysilane. *J. Opt. Soc. Am. B* **1996,** *13* (10), 2106-2114.

196. Bolt, G. H., Determination of the Charge Density of Silica Sols. *J. Phys. Chem.* **1957,** *61* (9), 1166-1169.

197. Ge, A.; Videla, P. E.; Lee, G. L.; Rudshteyn, B.; Song, J.; Kubiak, C. P.; Batista, V. S.; Lian, T., Interfacial Structure and Electric Field Probed by in Situ Electrochemical Vibrational Stark Effect Spectroscopy and Computational Modeling. *J. Phys. Chem. C* **2017,** *121* (34), 18674-18682.

198. Kim, J.; Chou, K. C.; Somorjai, G. A., Structure and Dynamics of Acetonitrile at the Air/Liquid Interface of Binary Solutions Studied by Infrared-Visible Sum Frequency Generation. *J. Phys. Chem. B* **2003,** *107*, 1592-1596.

199. Döpke, M. F.; Lützenkirchen, J.; Moultos, O. A.; Siboulet, B.; Dufrêche, J.-F.; Padding, J. T.; Hartkamp, R., Preferential Adsorption in Mixed Electrolytes Confined by Charged Amorphous Silica. *J. Phys. Chem. C* **2019,** *123* (27), 16711-16720.

200. Hidalgo-Acosta, J. C.; Mendez, M. A.; Scanlon, M. D.; Vrubel, H.; Amstutz, V.; Adamiak, W.; Opallob, M.; Girault, H. H., Catalysis of Water Oxidation in Acetonitrile by Iridium Oxide Nanoparticles. *Chem. Sci.* **2015,** *6*, 1761-1769.

201. Hidalgo-Acosta, J. C.; Scanlon, M. D.; Mendez, M. A.; Peljo, P.; Opallo, M.; Girault, H. H., Enhanced Reactivity of Water Clusters towards Oxidation in Water/Acetonitrile Mixtures. *ChemElectroChem* **2016,** *3*, 2003-2007.

202. Amiri, A. A.; Hemmateenejad, B.; Safavi, A.; Sharghi, H.; Beni, A. R. S.; Shamsipur, M., Structure-Retention and Mobile Phase-Retention Relationships for Reversed-Phase High-Performance Liquid Chromatography of Several Hydroxythioxanthone Derivatives in Binary Acetonitrile-Water Mixtures. *Anal. Chim. Acta* **2007,** *605*, 11-19.

203. Barbosa, J.; Sanz-Nebot, V.; Toro, I., Solvatochromic Parameter Values and pH in Acetonitrile-Water Mixtures. Optimization of Mobile Phase for the Separation of Peptides by High-Performance Liquid Chromatography. *J. Chromatogr. A* **1996,** *725*, 249-260.

204. Emel'yanova, N. S.; Kurbatova, S. V.; Saifutdinov, B. R.; Yudashkin, A. V., Regularities of the Sorption of Cycloalkenyl-Substituted Thiophenes and 2,2′-Bithiophenes from Water-Acetonitrile Solutions on Hexadecyl Silica Gel under Conditions of High-Performance Liquid Chromatography. *Russ. J. Phys. Chem. A* **2011,** *85*, 1440-1449.

205. Guillaume, Y.; Cavalli, E. J.; Peyrin, E.; Guinchard, C., A New Approach to Study Benzodiazepine Separation and the Differences between a Methanol/Water and Acetonitrile/Water

Mixture on Column Efficiency in Liquid Chromatography. *J. Liq. Chromatogr. R. T.* **1997,** *20*, 1741-1756.

206. Hemmateenejad, B.; Shamsipur, M.; Safavi, A.; Sharghi, H.; Amiri, A. A., Reversed-Phase High Performance Liquid Chromatography (RP-HPLC) Characteristics of Some 9,10-Anthraquinone Derivatives Using Binary Acetonitrile-Water Mixtures as Mobile Phase. *Talanta* **2008,** *77*, 351-359.

207. Kukusamude, C.; Burakham, R.; Chailapakul, O.; Srijaranai, S., High Performance Liquid Chromatography for the Simultaneous Analysis of Penicillin Residues in Beef and Milk Using Ion-Paired Extraction and Binary Water-Acetonitrile Mixture. *Talanta* **2012,** *92*, 38-44.

208. Saifutdinov, B. R.; Emel'yanova, N. S.; Kurbatova, S. V.; Pimerzin, A. A., The Adsorption of Hetero- and Alicyclic Thiophene Derivatives from Water-Acetonitrile Solutions on the Surface of Porous Graphitic Carbon under High-Performance Liquid Chromatography Conditions. *Russ. J. Phys. Chem. A* **2012,** *86*, 1152-1160.

209. Subirats, X.; Bosch, E.; Roses, M., Retention of Ionisable Compounds on High-Performance Liquid Chromatography XVI. Estimation of Retention with Acetonitrile/Water Mobile Phases from Aqueous Buffer pH and Analyte pK_a. *J. Chromatogr. A* **2006,** *1121*, 170-177.

210. Buszewski, B.; Noga, S., Hydrophilic Interaction Liquid Chromatography (HILIC)—A Powerful Separation Technique. *Anal Bional Chem* **2012,** *402*, 231-247.

211. Mountain, R. D., Molecular Dynamics Simulation of Water-Acetonitrile Mixtures in a Silica Slit. *J. Phys. Chem. C* **2013,** *117*, 3923-3929.

212. Rivera, C. A.; Bender, J. S.; Manfred, K.; Fourkas, J. T., Persistence of Acetonitrile Bilayers at the Interface of Acetonitrile/Water Mixtures with Silica. *J. Phys. Chem. A* **2013,** *117*, 12060-12066.

213. Kittaka, S.; Iwashita, T.; Serizawa, A.; Kranishi, M.; Takahara, S.; Kuroda, Y.; Mori, T.; Yamaguchi, T., Low Temperature Properties of Acetonitrile Confined in MCM-41. *J. Phys. Chem. B* **2005,** *109*, 23162-23169.

214. Gilar, M.; Jaworski, A., Retention Behavior of Peptides in Hydrophilic-Interaction Chromatography. *J. Chromatogr. A* **2011,** *1218*, 8890-8896.

215. Cheng, L.; Morrone, J. A.; Berne, B. J., Structure and Dynamics of Acetonitrile Confined in a Silica Nanopore. *J. Phys. Chem. C* **2012,** *116*, 9582-9593.

216. Ding, F.; Hu, Z.; Zhong, Q.; Manfred, K.; Gattass, R. R.; Brindza, M. R.; Fourkas, J. T.; Walker, R. A.; Weeks, J. D., Interfacial Organization of Acetonitrile: Simulation and Experiment. *J. Phys. Chem. C* **2010,** *114*, 17651-17659.

217. Gulmen, T. S.; Thompson, W. H., Grand Canonical Monte Carlo Simulations of Acetonitrile Filling of Silica Pores of Varying Hydrophilicity/Hydrophobicity. *Langmuir* **2009,** *25*, 1103-1111.

218. Hu, Z.; Weeks, J. D., Acetonitrile on Silica Surfaces and at Its Liquid-Vapor Interface: Structural Correlations and Collective Dynamics. *J. Phys. Chem. C* **2010,** *114*, 10202-10211.

219. Loughnane, B. J.; Farrer, R. A.; Fourkas, J. T., Evidence for the Direct Observation of Molecular Exchange of a Liquid at the Solid/Liquid Interface. *J. Phys. Chem. B* **1998,** *102*, 5409-5412.

220. Loughnane, B. J.; Farrer, R. A.; Scodinu, A.; Fourkas, J. T., Dynamics of a Wetting Liquid in Nanopores: An Optical Kerr Effect Study of the Dynamics of Acetonitrile Confined in Sol-Gel Glasses. *J. Chem. Phys.* **1999,** *111*, 5116-5123.

221. Morales, C. M.; Thompson, W. H., Simulations of Infrared Spectra of Nanoconfined Liquids: Acetonitrile Confined in Nanoscale, Hydrophilic Silica Pores. *J. Phys. Chem. A* **2009,** *113*, 1922-1933.

222. Berne, B. J.; Fourkas, J. T.; Walker, R. A.; Weeks, J. D., Nitriles at Silica Interfaces Resemble Supported Lipid Bilayers. *Acc. Chem. Res.* **2016,** *49*, 1605-1613.

223. Li, Z.; Weeraman, C. N.; Gibbs-Davis, J. M., Following the Azide-Alkyne Cycloaddition at the Silica/Solvent Interface with Sum Frequency Generation. *ChemPhysChem* **2014,** *15*, 2247-2251.

224. Liu, W.-T.; Zhang, L.; Shen, Y. R., Interfacial Structures of Methanol:Water Mixtures at a Hydrophobic Interface Probed by Sum-Frequency Vibrational Spectroscopy. *J. Chem. Phys.* **2006,** *125*, 144711.

225. Miranda, P. B.; Pflumio, V.; Saijo, H.; Shen, Y. R., Chain-Chain Interaction between Surfactant Monolayers and Alkanes or Alcohols at Solid/Liquid Interfaces. *J. Am. Chem. Soc.* **1998,** *120*, 12092-12099.

226. Rao, Y.; Turro, N. J.; Eisenthal, K. B., Water Structure at Air/Acetonitrile Aqueous Solution Interfaces. *J. Phys. Chem. C* **2009,** *113*, 14384-14389.

227. Chen, Z.; Shen, Y. R.; Somorjai, G. A., Studies of Polymer Surfaces by Sum Frequency Generation Vibrational Spectroscopy. *Annu. Rev. Phys. Chem.* **2002,** *53*, 437-465.

228. Ding, B.; Jasensky, J.; Li, Y.; Chen, Z., Engineering and Characterization of Peptides and Proteins at Surfaces and Interfaces: A Case Study in Surface-Sensitive Vibrational Spectroscopy. *Acc. Chem. Res.* **2016**.

229. Yan, E. C. Y.; Wang, Z.; Fu, L., Proteins at Interfaces Probed by Chiral Vibrational Sum Frequency Generation Spectroscopy. *J. Phys. Chem. B* **2015,** *119*, 2769-2785.

230. Li, Z.; Weeraman, C. N.; Gibbs-Davis, J. M., Ketone Binding at Amino and Ureido Monolayer/Solvent Interfaces Studied by Nonlinear Optical Techniques. *J. Phys. Chem. C* **2014,** *118*, 28662-28670.

231. Li, Z.; Weeraman, C. N.; Azam, M. S.; Osman, E.; Gibbs-Davis, J. M., The Thermal Reorganization of DNA Immobilized at the Silica/Buffer Interface: A Vibrational Sum Frequency Generation Investigation. *Phys. Chem. Chem. Phys.* **2015,** *17*, 12452-12457.

232. Wang, H.-F.; Gan, W.; Lu, R.; Rao, Y.; Wu, B.-H., Quantitative Spectral and Orientational Analysis in Surface Sum Frequency Generation Vibrational Spectroscopy (SFG-VS). *Int. Rev. Phys. Chem.* **2005,** *24*, 191-256.

233. Wang, H.-F.; Velarde, L.; Gan, W.; Fu, L., Quantitative Sum-Frequency Generation Vibrational Spectroscopy of Molecular Surfaces and Interfaces: Lineshape, Polarization, and Orientation. *Annu. Rev. Phys. Chem.* **2015,** *66*, 189-216.

234. Li, Z.; Wang, J.; Li, Y.; Xiong, W., Solving the "Magic Angle" Challenge in Determining Molecular Orientation Heterogeneity at Interfaces. *J. Phys. Chem. C* **2016,** *120*, 20239-20246.

235. Irgum, P. H. K., Hydrophilic Interaction Chromatography. *J. Sep. Sci.* **2006,** *29*, 1784-1821.

236. A stock solution containing 16.7 mM NaCl was adjusted to the desired pH with an NaOH solution containing 16.7 mM NaCl to avoid dilution. A 6 mL aqueous aliquot was then mixed with a 4 mL acetonitrile aliquot to yield a 10 mM NaCl acetonitrile:water mixture, which was disposed after measurement, and replaced with a fresh mixture.

237. Backus, E. H. G.; Abrakhi, S.; Péralta, S.; Teyssié, D.; Fichet, O.; Cantin, S., Sum-Frequency Generation Spectroscopy of Cinnamate Modified Cellulosic Polymer at the Air-Water Interface. *J. Phys. Chem. B* **2012,** *116*, 6041-6049.

238. Holman, J.; Davies, P. B., Sum Frequency Generation from Langmuir-Blodgett Multilayer Films on Metal and Dielectric Substrates. *J. Phys. Chem. B* **2005,** *109*, 18723-18732.

239. Buckingham, A. D.; Fan-Chen, L., Differences in the Hydrogen and Deuterium Bonds. *Int. Rev. Phys. Chem.* **1981,** *1*, 253-269.

240. Thomas, M. R.; Scheraga, H. A.; Schrier, E. E., A Near-Infrared Study of Hydrogen Bonding in Water and Deuterium Oxide. *J. Phys. Chem.* **1965,** *69*, 3722-3726.

241. Rao, C. N. R., Effect of Deuteration on Hydrogen Bonds. *J. Chem. Soc., Faraday Trans. 1* **1975,** *71*, 980-983.

242. Schott, H., Direct Comparison of the Strength of Hydrogen Bonds Formed by H_2O and D_2O. *J. Macromol. Sci. B* **1988,** *27*, 119-123.

243. Scheiner, S.; Cuma, M., Relative Stability of Hydrogen and Deuterium Bonds. *J. Am. Chem. Soc.* **1996,** *118*, 1511-1521.

244. Sobczyk, L.; Obrzud, M.; Filarowski, A., H/D Isotope Effects in Hydrogen Bonded Systems. *Molecules* **2013,** *18*, 4467-4476.

245. Wampler, R. D.; Moad, A. J.; Moad, C. W.; Heiland, R.; Simpson, G. J., Visual Methods for Interpreting Optical Nonlinearity at the Molecular Level. *Acc. Chem. Res.* **2007,** *40*, 953-960.

246. Verbiest, T.; Clays, K.; Rodriguez, V., *Second-Order Nonlinear Optical Characterization Techniques: An Introduction*. Boca Raton: CRC Press: 2009.

247. Wang, J.; Chen, C.; Buck, S. M.; Chen, Z., Molecular Chemical Structure on Poly(methyl methacrylate) (PMMA) Surface Studied by Sum Frequency Generation (SFG) Vibrational Spectroscopy. *J. Phys. Chem. B* **2001,** *105*, 12118-12125.

248. Zhuang, X.; Miranda, P. B.; Kim, D.; Shen, Y. R., Mapping Molecular Orientation and Conformation at Interfaces by Surface Nonlinear Optics. *Phys. Rev. B* **1999,** *59*, 12632-12640.

249. Saito, K.; Peng, Q.; Qiao, L.; Wang, L.; Joutsuka, T.; Ishiyama, T.; Ye, S.; Morita, A., Theoretical and Experimental Examination of SFG Polarization Analysis at Acetonitrile-Water Solution Surfaces. *Phys. Chem. Chem. Phys.* **2017,** *19* (13), 8941-8961.

250. Zhang, D.; Gutow, J.; Eisenthal, K. B., Vibrational Spectra, Orientations, and Phase Transitions in Long-Chain Amphiphiles at the Air/Water Interface: Probing the Head and Tail Groups by Sum Frequency Generation. *J. Phys. Chem.* **1994,** *98*, 13729-13734.

251. Martin, J.; Montero, S., Raman Intensities of Ethane and Deuterated Derivatives. *J. Chem. Phys.* **1984,** *80*, 4610-4619.

252. Shultz, M. J.; Bisson, P.; Groenzin, H.; Li, I., Multiplexed Polarization Spectroscopy: Measuring Surface Hyperpolarizability Orientation. *J. Chem. Phys.* **2010,** *133* (5), 054702.

253. Hatch, S. R.; Polizzotti, R. S.; Dougal, S.; Rabinowitz, P., Surface Vibrational Spectroscopy of the Vapor/Solid and Liquid/Solid Interface of Acetonitrile on ZrO_2. *Chem. Phys. Lett.* **1992,** *196*, 97-102.

254. Hatch, S. R.; Polizzotti, R. S.; Dougal, S.; Rabinowitz, P., In Situ Surface Vibrational Spectroscopy of the Vapor/Solid and Liquid/Solid Interfaces of Acetonitrile on ZrO_2. *Vac. Sci. Technol.* **1993,** *11*, 2232-2238.

255. Strunk, M. R.; Williams, C. T., Aliphatic Nitrile Adsorption on Al_2O_3 and ZrO_2 As Studied by Total Internal Reflection Sum-Frequency Spectroscopy. *Langmuir* **2003,** *19*, 9210-9215.

256. Simpson, G. J.; Rowlen, K. L., An SHG Magic Angle: Dependence of Second Harmonic Generation Orientation Measurements on the Width of the Orientation Distribution. *J. Am. Chem. Soc.* **1999,** *121*, 2635-2636.

257. McCalley, D. V., Is Hydrophilic Interaction Chromatography with Silica Columns a Viable Alternative to Reversed-Phase Liquid Chromatography for the Analysis of Ionisable Compounds? *J. Chromatogr. A* **2007,** *1171*, 46-55.

258. Jordan, F., Acidity Scales in Mixed Water-Acetonitrile Buffer Solutions. *J. Phys. Chem.* **1973,** *77*, 2681-2683.

259. Bosch, E.; Bou, P.; Allemann, H.; Roses, M., Retention of Ionizable Compounds on HPLC. pH Scale in Methanol-Water and the pK and pH Values of Buffers. *Anal. Chem.* **1996,** (3651-3657).

260. Wei, X.; Miranda, P. B.; Zhang, C.; Shen, Y. R., Sum-Frequency Spectroscopic Studies of Ice Interfaces. *Phys. Rev. B* **2002,** *66* (8), 085401.

261. Matsuzaki, K.; Nihonyanagi, S.; Yamaguchi, S.; Nagata, T.; Tahara, T., Quadrupolar Mechanism for Vibrational Sum Frequency Generation at Air/Liquid Interfaces: Theory and Experiment. *J. Chem. Phys.* **2019,** *151* (6), 064701.

262. Azam, M. S.; Gibbs-Davis, J. M., Monitoring DNA Hybridization and Thermal Dissociation at the Silica/Water Interface Using Resonantly Enhanced Second Harmonic Generation Spectroscopy. *Anal. Chem.* **2013,** *85*, 8031-8038.

263. Dyson, F., A Meeting with Enrico Fermi. *Nature* **2004,** *427* (6972), 297-297.

264. Luxbacher, T.; Anton Paar Gmb, H., *The Zeta Potential for Solid Surface Analysis : A Practical Guide to Streaming Potential Measurement*. Anton Paar GmbH: Austria, 2014.

Appendix:

Tables A.1 and A.2 are the parameter corresponding to the fits shown in Chapters 3 and 4, respectively. Tables A.3 to A.10 are the parameters corresponding to the fits shown in Chapter 5.

Table A.1 Fitting Parameters to the Water Spectra at the Silica/Water Interface at pH 5.8 with Varying Ionic Strength

	$1x10^{-6}$ M	**$1x10^{-5}$ M**	**$5x10^{-5}$ M**	**$1x10^{-4}$ M**	**$5x10^{-4}$ M**	**$1x10^{-3}$ M**	**$1x10^{-2}$ M**	**1.5x1 0^{-2} M**	**2.5x1 0^{-2} M**	**$5x10^{-2}$ M**
ω_1	3032 +/- 2	3042 +/- 4	3031 +/- 5	3036 +/- 6	3031 +/- 4	3041 +/- 5	3029 +/- 6	3034 +/- 6	3014 +/- 5	3013 +/- 7
A_1	12 +/- 9	42 +/- 5	59 +/- 8	68 +/- 9	74 +/- 8	82 +/- 9	74 +/- 10	75 +/- 10	60 +/- 9	60 +/- 11
Γ_1	97 +/- 1	135 +/- 6	166 +/- 8	175 +/- 9	171 +/- 7	176 +/- 7	186 +/- 10	179 +/- 8	176 +/- 10	181 +/- 13
ω_2	3223 +/- 2	3235 +/- 1	3221 +/- 1	3223 +/- 1	3219 +/- 1	3217 +/- 1	3216 +/- 1	3217 +/- 1	3221 +/- 1	3222 +/- 1
A_2	-34 +/- 5	-71 +/- 3	-124 +/- 4	-135 +/- 6	-168 +/- 6	-184 +/- 7	-169 +/- 7	-165 +/- 7	-138 +/- 5	-124 +/- 5
Γ_2	111 +/- 1	127 +/- 3	147 +/- 2	149 +/- 3	157 +/- 2	161 +/- 3	163 +/- 3	161 +/- 3	157 +/- 3	154 +/- 3
ω_3	3419 +/- 2	3430 +/- 1	3430 +/- 1	3432 +/- 1	3429 +/- 1	3425 +/- 1	3426 +/- 1	3426 +/- 1	3428 +/- 1	3424 +/- 1
A_3	-58 +/- 3	-53 +/- 2	-50 +/- 2	-58 +/- 2	-54 +/- 2	-47 +/- 1	-42 +/- 1	-46 +/- 2	-45 +/- 2	-50 +/- 3
Γ_3	130 +/- 0	109 +/- 2	108 +/- 2	112 +/- 2	107 +/- 2	102 +/- 2	100 +/- 2	105 +/- 2	108 +/- 2	113 +/- 2
$\chi^{(2)}_{NR}$	0	0	0	0	0	0	0	0	0	0

Table A.2 Fitting Parameters to the Water Spectra at the Silica/Water Interface at 50 mM NaCl with Varying pH

	pH 10	**pH 8.9**	**pH 8.4**	**pH 7.9**	**pH 7.3**	**pH 7**	**pH 6**	**pH 5.1**	**pH 4.1**	**pH 3**	**pH 2**
ω_1	3100	3100	3100	3100	3100	3100	3100	3100	3100	3100	3100
A_1	196 +/- 3	208 +/- 3	204 +/- 3	200 +/- 3	206 +/- 3	192 +/- 3	146 +/- 4	169 +/- 6	291 +/- 7	422 +/- 14	465 +/- 17
Γ_1	236 +/- 2	239 +/- 2	239 +/- 2	233 +/- 2	241 +/- 2	239 +/- 2	227 +/- 3	233 +/- 3	350 +/- 14	314 +/- 10	312 +/- 8
ω_2	3230	3230	3230	3230	3230	3230	3230	3230	3230	3230	3230
A_2	-367 +/- 4	-329 +/- 4	-341 +/- 4	-349 +/- 3	-338 +/- 4	-312 +/- 4	-192 +/- 5	-177 +/- 6	-180 +/- 14	-262 +/- 25	-286 +/- 30
Γ_2	187 +/- 1	185 +/- 1	189 +/- 1	187 +/- 1	188 +/- 1	185 +/- 1	179 +/- 2	173 +/- 3	172 +/- 4	175 +/- 5	175 +/- 6
ω_3	3434 +/- 1	3433 +/- 1	3426 +/- 1	3428 +/- 1	3430 +/- 1	3430 +/- 1	3420 +/- 1	3413 +/- 2	3393 +/- 2	3369 +/- 2	3364 +/- 2
A_3	-39 +/- 1	-37 +/- 1	-29 +/- 1	-31 +/- 1	-32 +/- 1	-35 +/- 1	-30 +/- 1	-36 +/- 2	-45 +/- 6	-47 +/- 10	-49 +/- 12
Γ_3	88 +/- 1	89 +/- 1	79 +/- 1	81 +/- 1	83 +/- 1	86 +/- 1	88 +/- 2	95 +/- 3	102 +/- 5	107 +/- 7	107 +/- 8
$\chi_{NR}^{(2)}$	0.224 +/- 0.004	0.24 +/- 0.005	0.229 +/- 0.004	0.202 +/- 0.004	0.173 +/- 0.004	0.179 +/- 0.004	0.068 +/- 0.006	0.074 +/- 0.009	0.013 +/- 0.015	-0.076 +/- 0.012	-0.083 +/- 0.011

Table A.3 Peak Frequency Fitting Parameters

Exp	**pH**	ω_1	ω_2	ω_3	ω_4
H_2O-ACN (ppp)	6.1	2945.2 ± 0.3	2952 ± 3	3004 ± 0.8	3110 ± 1
	7.3	2945.2 ± 0.3	2952 ± 3	3002.3 ± 0.9	3116 ± 1
	8.7	2945.5 ± 0.2	2948 ± 2	3004.7 ± 0.8	3118 ± 2
	9.3	2945.6 ± 0.3	2948 ± 3	3004.6 ± 0.9	3120 ± 1
	9.6	2945.7 ± 0.2	2946 ± 1	3005.7 ± 0.7	3123 ± 2
	9.9	2945.5 ± 0.3	2945 ± 2	3004.6 ± 0.8	3129 ± 2
	10.2	2945.9 ± 0.2	2942 ± 1	3005.7 ± 0.7	3135 ± 3
	10.5	2945.6 ± 0.2	2941 ± 1	3005.1 ± 0.7	3137 ± 3
	10.8	2945.9 ± 0.2	2939 ± 2	3007.3 ± 0.7	3139 ± 4
	11.1	2945.8 ± 0.2	2938 ± 2	3006.1 ± 0.8	3139 ± 3
	11.3	2946 ± 0.3	2939 ± 2	3005.5 ± 1	3143 ± 4
	11.9	2946.4 ± 0.3	2935 ± 1	3006.7 ± 0.8	3148 ± 4
	12.0	2945.9 ± 0.3	2935 ± 2	3006.8 ± 0.7	3151 ± 5
H_2O-ACN (ssp)	6.1	2944.5 ± 0.3	2971 ± 5	-	3106 ± 5
	7.3	2944.9 ± 0.3	2973 ± 8	-	3108 ± 6
	8.7	2944.9 ± 0.3	2977 ± 5	-	3110 ± 6
	9.3	2945.2 ± 0.3	2975 ± 6	-	3116 ± 6
	9.6	2944.7 ± 0.3	2967 ± 6	-	3103 ± 3
	9.9	2945.1 ± 0.3	2971 ± 7	-	3126 ± 9
	10.2	2944.6 ± 0.4	2961 ± 8	-	3112 ± 4
	10.5	2944.7 ± 0.4	2963 ± 10	-	3130 ± 8
	10.8	2944.4 ± 0.4	2960 ± 9	-	3124 ± 5
	11.1	2944.7 ± 0.2	2966 ± 4	-	3127 ± 5
	11.3	2944.2 ± 0.3	2963 ± 6	-	3128 ± 6
	11.9	2944.4 ± 0.3	2966 ± 3	-	3143 ± 7
	12.0	2944.3 ± 0.3	2964 ± 4	-	3136 ± 6
D_2O-ACN (ppp)	6.5	2942.5 ± 0.02	-	2994.2 ± 0.4	-
	7.1	2942.6 ± 0.03	-	2994 ± 0.4	-
	7.7	2942.6 ± 0.03	-	2994.3 ± 0.4	-
	8.9	2942.5 ± 0.03	-	2994.3 ± 0.4	-
	9.4	2942.8 ± 0.02	-	2994.5 ± 0.4	-
	9.9	2942.6 ± 0.03	-	2994.5 ± 0.4	-
	10.2	2942.5 ± 0.02	-	2994.6 ± 0.4	-
	10.7	2942.5 ± 0.02	-	2994.1 ± 0.4	-
	11.0	2942.7 ± 0.03	-	2993.8 ± 0.4	-
	11.5	2942.7 ± 0.03	-	2993.4 ± 0.4	-
	12.1	2942.6 ± 0.05	-	2998.9 ± 0.5	-
	12.5	2942.8 ± 0.07	-	2999.6 ± 0.7	-
D_2O-ACN (ssp)	6.5	2944.7 ± 0.05	-	-	-

7.1	2944.8 ± 0.05	-	-	-
7.7	2944.8 ± 0.05	-	-	-
8.9	2944.7 ± 0.05	-	-	-
9.4	2945 ± 0.06	-	-	-
9.9	2944.8 ± 0.06	-	-	-
10.2	2944.8 ± 0.05	-	-	-
10.7	2944.9 ± 0.06	-	-	-
11.0	2945.1 ± 0.06	-	-	-
11.5	2945.2 ± 0.06	-	-	-
12.1	2945 ± 0.06	-	-	-
12.5	2945.2 ± 0.08	-	-	-

Table A.4 Peak Amplitude Fitting Parameters

Exp	pH	A_1	A_2	A_3	A_4
H_2O-ACN (ppp)	6.1	2.0 ± 0.2	-1.6 ± 0.4	0.46 ± 0.07	22 ± 2
	7.3	2.2 ± 0.3	-1.6 ± 0.5	0.57 ± 0.09	28 ± 3
	8.7	2.4 ± 0.4	-1.9 ± 0.3	0.52 ± 0.07	30 ± 3
	9.3	2.2 ± 0.2	-2.0 ± 0.4	0.68 ± 0.12	35 ± 2
	9.6	2.5 ± 0.5	-2.0 ± 0.3	0.55 ± 0.06	39 ± 2
	9.9	2.6 ± 0.4	-2.3 ± 0.3	0.64 ± 0.09	49 ± 3
	10.2	2.2 ± 0.3	-2.3 ± 0.2	0.53 ± 0.07	59 ± 3
	10.5	2.1 ± 0.2	-2.0 ± 0.2	0.68 ± 0.09	68 ± 3
	10.8	1.8 ± 0.2	-2.0 ± 0.2	0.56 ± 0.09	68 ± 3
	11.1	1.7 ± 0.1	-2.0 ± 0.2	0.52 ± 0.08	72 ± 3
	11.3	1.6 ± 0.1	-2.0 ± 0.3	0.62 ± 0.12	81 ± 5
	11.9	1.3 ± 0.1	-2.3 ± 0.3	0.41 ± 0.07	86 ± 5
	12.0	1.2 ± 0.1	-1.8 ± 0.2	0.47 ± 0.07	94 ± 5
H_2O-ACN (ssp)	6.1	1.07 ± 0.09	-0.56 ± 0.22	-	10 ± 1
	7.3	1.10 ± 0.09	-0.48 ± 0.29	-	11 ± 1
	8.7	1.30 ± 0.07	-1.33 ± 0.46	-	11 ± 1
	9.3	1.27 ± 0.07	-0.97 ± 0.42	-	13 ± 1
	9.6	1.37 ± 0.10	-1.03 ± 0.38	-	12 ± 1
	9.9	1.34 ± 0.07	-1.14 ± 0.64	-	20 ± 2
	10.2	1.39 ± 0.10	-0.81 ± 0.42	-	20 ± 1
	10.5	1.21 ± 0.10	-0.67 ± 0.48	-	26 ± 2
	10.8	1.20 ± 0.12	-0.58 ± 0.38	-	28 ± 1
	11.1	1.00 ± 0.06	-0.17 ± 0.08	-	31 ± 2
	11.3	0.98 ± 0.10	-0.22 ± 0.15	-	35 ± 2
	11.9	0.71 ± 0.04	-0.09 ± 0.05	-	42 ± 3
	12.0	0.71 ± 0.06	-0.11 ± 0.07	-	42 ± 2
D_2O-ACN (ppp)	6.5	8.00 ± 0.02	-	2.68 ± 0.08	-
	7.1	8.08 ± 0.02	-	2.72 ± 0.09	-
	7.7	8.11 ± 0.02	-	2.67 ± 0.09	-
	8.9	8.11 ± 0.02	-	2.60 ± 0.09	-
	9.4	8.46 ± 0.02	-	2.55 ± 0.09	-
	9.9	8.12 ± 0.02	-	2.46 ± 0.08	-
	10.2	8.12 ± 0.02	-	2.41 ± 0.08	-
	10.7	7.66 ± 0.02	-	2.26 ± 0.07	-
	11.0	7.17 ± 0.02	-	2.53 ± 0.09	-
	11.5	6.52 ± 0.03	-	2.97 ± 0.10	-
	12.1	3.65 ± 0.03	-	3.28 ± 0.11	-
	12.5	2.85 ± 0.03	-	3.50 ± 0.14	-
D_2O-ACN (ssp)	6.5	5.33 ± 0.02	-	-	-

7.1	5.38 ± 0.02	-	-	-
7.7	5.36 ± 0.02	-	-	-
8.9	5.38 ± 0.02	-	-	-
9.4	5.51 ± 0.02	-	-	-
9.9	5.38 ± 0.02	-	-	-
10.2	5.42 ± 0.02	-	-	-
10.7	5.07 ± 0.02	-	-	-
11.0	4.73 ± 0.02	-	-	-
11.5	4.23 ± 0.02	-	-	-
12.1	2.61 ± 0.01	-	-	-
12.5	2.10 ± 0.01	-	-	-

Table A.5 Peak Width Fitting Parameters

Exp	pH	Γ_1	Γ_2	Γ_3	Γ_4
H_2O-ACN (ppp)	6.1	9.4 ± 0.4	28 ± 8	14 ± 1	56 ± 5
	7.3	9.8 ± 0.4	26 ± 8	17 ± 2	65 ± 5
	8.7	9.9 ± 0.6	27 ± 9	15 ± 1	65 ± 5
	9.3	9.5 ± 0.4	32 ± 8	18 ± 2	68 ± 4
	9.6	10.1 ± 0.7	26 ± 7	16 ± 1	71 ± 3
	9.9	10.3 ± 0.5	27 ± 5	17 ± 1	80 ± 4
	10.2	10.3 ± 0.5	27 ± 3	17 ± 2	84 ± 3
	10.5	9.9 ± 0.4	29 ± 3	19 ± 2	92 ± 3
	10.8	9.9 ± 0.5	30 ± 3	17 ± 2	88 ± 3
	11.1	9.7 ± 0.4	31 ± 2	17 ± 2	91 ± 3
	11.3	9.9 ± 0.4	32 ± 3	19 ± 2	97 ± 5
	11.9	9.6 ± 0.4	34 ± 2	16 ± 2	98 ± 4
	12.0	9.6 ± 0.5	31 ± 2	16 ± 2	105 ± 4
H_2O-ACN (ssp)	6.1	8.7 ± 0.4	24 ± 8	-	69 ± 4
	7.3	8.8 ± 0.4	30 ± 15	-	65 ± 4
	8.7	8.7 ± 0.3	45 ± 12	-	65 ± 5
	9.3	8.8 ± 0.3	43 ± 15	-	64 ± 4
	9.6	8.9 ± 0.3	34 ± 11	-	63 ± 3
	9.9	8.9 ± 0.3	50 ± 20	-	80 ± 5
	10.2	9.3 ± 0.3	33 ± 13	-	82 ± 4
	10.5	9.2 ± 0.4	36 ± 19	-	94 ± 5
	10.8	9.2 ± 0.4	29 ± 13	-	98 ± 4
	11.1	8.7 ± 0.4	14 ± 5	-	100 ± 4
	11.3	9.0 ± 0.5	17 ± 7	-	111 ± 4
	11.9	8.2 ± 0.4	10 ± 5	-	115 ± 4
	12.0	8.2 ± 0.5	12 ± 6	-	117 ± 5
D_2O-ACN (ppp)	6.5	9.47 ± 0.02	-	20.9 ± 0.7	-
	7.1	9.49 ± 0.02	-	20.9 ± 0.7	-
	7.7	9.52 ± 0.02	-	20.6 ± 0.7	-
	8.9	9.51 ± 0.02	-	20.4 ± 0.7	-
	9.4	9.52 ± 0.02	-	20.2 ± 0.8	-
	9.9	9.51 ± 0.02	-	19.7 ± 0.7	-
	10.2	9.48 ± 0.02	-	19.4 ± 0.7	-
	10.7	9.54 ± 0.02	-	19.2 ± 0.6	-
	11.0	9.56 ± 0.02	-	21.3 ± 0.8	-
	11.5	9.59 ± 0.03	-	24.5 ± 0.8	-
	12.1	9.69 ± 0.04	-	33.6 ± 1.2	-
	12.5	9.68 ± 0.07	-	37.0 ± 1.6	-
D_2O-ACN (ssp)	6.5	9.09 ± 0.05	-	-	-

7.1	9.12 ± 0.05	-	-	-
7.7	9.16 ± 0.05	-	-	-
8.9	9.16 ± 0.05	-	-	-
9.4	9.14 ± 0.05	-	-	-
9.9	9.19 ± 0.05	-	-	-
10.2	9.11 ± 0.05	-	-	-
10.7	9.20 ± 0.06	-	-	-
11.0	9.20 ± 0.06	-	-	-
11.5	9.20 ± 0.06	-	-	-
12.1	9.49 ± 0.06	-	-	-
12.5	9.73 ± 0.08	-	-	-

Table A.6 Nonresonant Fitting Parameters

Exp	**pH**	$\chi_{NR}^{(2)}$
H_2O-ACN (ppp)	6.1	-0.045 ± 0.014
	7.3	-0.027 ± 0.018
	8.7	-0.048 ± 0.016
	9.3	-0.038 ± 0.015
	9.6	-0.041 ± 0.009
	9.9	-0.03 ± 0.017
	10.2	-0.029 ± 0.011
	10.5	-0.017 ± 0.011
	10.8	-0.019 ± 0.01
	11.1	-0.002 ± 0.013
	11.3	0.008 ± 0.019
	11.9	0.002 ± 0.015
	12.0	0.029 ± 0.014
H_2O-ACN (ssp)	6.1	0.0064 ± 0.0035
	7.3	-0.0004 ± 0.0039
	8.7	-0.0034 ± 0.0035
	9.3	-0.0048 ± 0.0038
	9.6	-0.0004 ± 0.0043
	9.9	0.0016 ± 0.0046
	10.2	0.0093 ± 0.0071
	10.5	0.0193 ± 0.0081
	10.8	0.0323 ± 0.0078
	11.1	0.0333 ± 0.0056
	11.3	0.0498 ± 0.0065
	11.9	0.0591 ± 0.0081
	12.0	0.064 ± 0.0079
D_2O-ACN (ppp)	6.5	-0.0659 ± 0.0009
	7.1	-0.0669 ± 0.0009
	7.7	-0.0678 ± 0.0009
	8.9	-0.0652 ± 0.0009
	9.4	-0.0722 ± 0.0009
	9.9	-0.0641 ± 0.0009
	10.2	-0.0639 ± 0.0009
	10.7	-0.058 ± 0.0008
	11.0	-0.0578 ± 0.0009
	11.5	-0.0606 ± 0.001
	12.1	-0.0417 ± 0.001
	12.5	-0.0428 ± 0.0013

D_2O-ACN (ssp)	6.5	0.016 ± 0.001
	7.1	0.016 ± 0.001
	7.7	0.015 ± 0.001
	8.9	0.016 ± 0.001
	9.4	0.017 ± 0.001
	9.9	0.017 ± 0.001
	10.2	0.017 ± 0.001
	10.7	0.02 ± 0.001
	11.0	0.02 ± 0.001
	11.5	0.02 ± 0.001
	12.1	0.013 ± 0.001
	12.5	0.012 ± 0.001

Table A.7 ssp Peak Frequency Fitting Parameters While Constraining Frequency to Match ppp

Exp	**pH**	ω_1	ω_2	ω_3	ω_4
H_2O-ACN (ssp)	6.1	2945.2 ± 0.6	2954 ± 8	-	3105 ± 5
	7.3	2945.6 ± 0.5	2945 ± 13	-	3115 ± 7
	8.7	2945.7 ± 0.3	2950 ± 19	-	3105 ± 5
	9.3	2946.0 ± 0.3	2950 ± 13	-	3110 ± 5
	9.6	2945.6 ± 0.3	2948 ± 10	-	3103 ± 3
	9.9	2945.8 ± 0.2	2947 ± 17	-	3117 ± 7
	10.2	2945.5 ± 0.3	2944 ± 5	-	3108 ± 3
	10.5	2945.5 ± 0.4	2943 ± 7	-	3119 ± 5
	10.8	2945.3 ± 0.3	2941 ± 7	-	3119 ± 4
	11.1	2945.9 ± 0.4	2940 ± 4	-	3119 ± 4
	11.3	2945.6 ± 0.5	2941 ± 4	-	3121 ± 5
	11.9	2945.7 ± 0.5	2937 ± 4	-	3128 ± 6
	12.0	2946.0 ± 0.5	2937 ± 4	-	3124 ± 5

Table A.8 ssp Peak Amplitude Fitting Parameters While Constraining Frequency to Match ppp

Exp	pH	A_1	A_2	A_3	A_4
H_2O-ACN (ssp)	6.1	1.25 ± 0.15	-1.0 ± 0.4	-	10 ± 1
	7.3	1.16± 0.11	-0.8 ± 0.5	-	10 ± 1
	8.7	1.35 ± 0.06	-3.5 ± 2.4	-	12 ± 2
	9.3	1.27 ± 0.06	-1.8 ± 1.0	-	11 ± 1
	9.6	1.34 ± 0.07	-2.2 ± 0.9	-	11 ± 1
	9.9	1.32 ± 0.05	-2.2 ± 1.8	-	17 ± 3
	10.2	1.42 ± 0.11	-1.2 ± 0.3	-	17 ± 1
	10.5	1.28 ± 0.14	-0.9 ± 0.2	-	21 ± 2
	10.8	1.18 ± 0.09	-1.0 ± 0.3	-	24 ± 2
	11.1	1.27 ± 0.22	-0.8 ± 0.2	-	23 ± 2
	11.3	1.34 ± 0.33	-1.0 ± 0.3	-	27 ± 3
	11.9	0.92 ± 0.17	-0.7 ± 0.2	-	30 ± 4
	12.0	0.92 ± 0.15	-0.8 ± 0.2	-	29 ± 3

Table A.9 ssp Peak Width Fitting Parameters While Constraining Frequency to Match ppp

Exp	pH	Γ_1	Γ_2	Γ_3	Γ_4
H_2O-ACN (ssp)	6.1	9.3 ± 0.6	37 ± 18	-	65 ± 6
	7.3	9.0 ± 0.5	47 ± 31	-	60 ± 5
	8.7	8.8 ± 0.3	101 ± 46	-	65 ± 10
	9.3	8.7 ± 0.3	79 ± 35	-	56 ± 5
	9.6	8.7 ± 0.3	74 ± 25	-	58 ± 4
	9.9	8.7 ± 0.3	94 ± 56	-	71 ± 8
	10.2	9.2 ± 0.4	44 ± 13	-	70 ± 4
	10.5	9.4 ± 0.5	40 ± 15	-	78 ± 6
	10.8	9.0 ± 0.4	49 ± 17	-	84 ± 5
	11.1	9.6 ± 0.7	25 ± 5	-	77 ± 7
	11.3	10.1 ± 0.9	24 ± 6	-	87 ± 9
	11.9	9.2 ± 0.8	24 ± 4	-	88 ± 8
	12.0	9.2 ± 0.7	27 ± 4	-	87 ± 8

Table A.10 ssp Nonresonant Fitting Parameters While Constraining Frequency to Match ssp

Exp	**pH**	$\chi_{NR}^{(2)}$
H_2O-ACN (ssp)	6.1	0.0015 ± 0.0069
	7.3	-0.0070 ± 0.0062
	8.7	0.0004 ± 0.0124
	9.3	-0.0125 ± 0.0057
	9.6	-0.0068 ± 0.0054
	9.9	-0.0087 ± 0.0091
	10.2	-0.0084 ± 0.0052
	10.5	-0.0015 ± 0.0089
	10.8	-0.0094 ± 0.0069
	11.1	-0.0076 ± 0.0113
	11.3	0.0053 ± 0.0149
	11.9	0.0068 ± 0.0146
	12.0	0.0071 ± 0.0137